



DISSERTATION

Ablation and micro/nano structuring with ultrashort laser pulses of 10 fs - 550 fs duration

Ausgeführt zum Zwecke der Erlangung des akademischen
Grades eines Doktors der technischen Wissenschaften
unter der Leitung von

Ao.Univ.Prof.Dipl.-Ing. Dr.techn. Wolfgang Husinsky

eingereicht an der Technischen Universität Wien
Faculty of Physics

von

Chandra Sekher Reddy Nathala

Matr. No. 1228434

Donaufelderstrasse 73/4/4

1210 Vienna

Zusammenfassung

Im Rahmen dieser Dissertation werden einige wesentlichen Konsequenzen für die Dynamik der Laserablation und ihre Abhängigkeit von den wichtigsten Laserparametern im Detail untersucht, wobei vor allem der bis dato nicht untersuchte Bereich der Laserpulsbreiten von typisch einigen zig-fsec bis in den heute mit kommerziellen Lasersystemen erreichbaren sub 10fsec Bereich von Interesse war.

Der Schwellwert des Laserflusses, bei dem Ablation auftritt (wobei der Begriff Schwellwert durchaus einen Interpretationsspielraum offen lässt) ist einer der wichtigsten Parameter, da er in vielen Fällen einen Einblick in die vielfältigen physikalischen Prozesse, die sich im Material abspielen, ermöglicht ist. Diese Schwellwerte sind aber meist keine "gegebene" physikalische Größe, sondern hängen natürlich essentiell von der Art des Materials aber auch dynamisch von der Laserpulsbreite und der Anzahl der verwendeten Laserpulse ab. In dieser Arbeit wurde eine systematische Studie der Abhängigkeit der Ablationsschwellwerte vom Laserfluss, der Laserpulsbreite (10fs-550fs) sowie der Anzahl der Pulse für drei verschiedenen Materialtypen durchgeführt: Metall (Cu), Halbleiter (Si) und Biopolymere (Gelatin) durchgeführt. Diese Messungen ergeben, dass der Schwellwert generell für kleinere Pulszeiten abnimmt. Im speziellen konnte eine Abhängigkeit $F_{th} \propto \tau^{0.05}$ for Cu, $F_{th} \propto \tau^{0.12}$ for Si and $F_{th} \propto \tau^{0.22}$ für Gelatin ermittelt werden.

Eine wichtige Informationsquelle für die verschiedenen möglichen, involvierten Prozesse ist die Messung der Masse sowie der Energie (Geschwindigkeit) der bei der Laser-Materialwechselwirkung "ablierten" emittierten Teilchen (Ionen, Neutrale) sowohl als atomare Teilchen als auch als größere Moleküle und Cluster oder sogar ganzer "Teilchenjunks". Mittels eines Flugzeitmassenspektrometers mit integrierter Laser-Nachionisation konnten diese Größen bestimmt werden. Wiederum wurde die Abhängigkeit dieser Größen (Massenzusammensetzung, Ionen-Neutralenanteil sowie Energie) als Funktion des Laserflusses als auch der Laserpulszeit (100-550fsec) untersucht. Insbesondere die relativ hohen Teilchenenergien von einigen eV lassen auf Prozesse schließen, die auf eine lasererzeugte ultraschnelle Ladungstrennung (Plasma) basieren.

Bei der Bestrahlung von Materialoberflächen mit ultrakurzer Laserstrahlung im 10-550fsec Bereich kann man sich dabei ausbildende Oberflächenstrukturen beobachten, die unter gewissen Bedingungen (Laserfluss, Pulszeit und Pulsanzahl) periodischer Natur sind. Man bezeichnet diese als LIPSS (Laser-Induced-Periodic-Surface-Structures). Besonders interessant und weitgehendst noch nicht im Detail verstanden sind dabei solche Strukturen, deren Periodizität wesentlich kleiner als die Laserwellenlänge (bis einige nm) sind. Deren Abhängigkeit von den Laserparametern wurde detailliert für einige Materialien untersucht. Bei Biopolymeren z.B. ermöglicht eine geschickte Wahl von Laserparametern die Ausbildung von "schwammartigen" Strukturen, die eine hohe Biokompatibilität solcher Materialien als Zellersatz ermöglichen.

Besondere Beachtung wurde in dieser Arbeit darauf gelegt, die komplexen Vorgänge und die oben erwähnten Ablationsgrößen und ihre Abhängigkeit von den Laserparametern in Zusammenhang zu bringen und so die relevanten Prozesse für die einzelnen Materialbearbeitungsgrößen einem besseren Verständnis zuzuführen.

Abstract

In this thesis, the dependence of the ablation dynamics on the most important laser parameters and the implied consequences for micro/nano structuring was studied in detail. Of particular interest was the dependence on the pulse durations which are in the range of 10's of femtoseconds to <10 femtoseconds, now deliverable by commercially available laser systems.

Ablation threshold fluence is an important parameter that can give insight into the physical processes taking place in a material. Knowing the values is also necessary to deposit a defined amount of energy for precision material processing applications. The value is dependent on the type of material, on the laser pulse duration and on the number of pulses. In this work a systematic study was done to investigate the influence of pulse duration and pulse number on the ablation thresholds for three different types of materials: metal (copper), semiconductor (silicon) and bio-polymer (gelatin) in 10 fs - 550 fs range. The results indicate that the threshold fluence reduces with decreasing the pulse duration. The dependence of the threshold fluence on the pulse duration was determined as $F_{th} \propto \tau^{0.05}$ for copper, $F_{th} \propto \tau^{0.12}$ for silicon and $F_{th} \propto \tau^{0.22}$ for gelatin.

The processes that take place when an ultrashort laser pulse irradiates a material are complex and is material dependent. By detecting the particles (ions, clusters, neutrals) and measuring the energies with which they are emitted, the underlying physical mechanisms can be identified. By using a time-of-flight mass spectrometer (TOFMS) the ions and neutrals emitted from metal and semiconductor targets upon an ultrashort laser pulse irradiation are detected. The dependence of ion emission on fluence and pulse duration was measured. Extensive measurements were done to find the velocities of the neutral particles that are emitted when irradiated with pulses of 10 fs to 550 fs. The results show that neutrals with energies in excess of few eV are detected. This cannot be explained if the fast non-thermal processes like coulomb explosion and ultrafast melting are not considered. The velocities (energies) with which neutrals are emitted from different metals and semiconductors is reported.

When an ultrafast laser irradiates a material, a wide variety of structures are formed. The most interesting structures are conical structures and periodic ripples. In bio-polymers, scaffold-like structures are formed. As part of this work, structures were produced on a wide variety of materials (titanium, steel, tin, nickel, copper, molybdenum, silicon etc., and on bio-polymers like gelatin and collagen etc.). A systematic study was done to characterize the laser-induced periodic surface structures (LIPSS), both the low-spatial frequency LIPSS (LSFLs) and the high-spatial frequency LIPSS (HSFLs), and their dependence on various laser parameters. Scaffold-like structures that mimic the extracellular matrix, were produced on bio-polymer films and were studied for the suitability of tissue engineering. The cell seeding experiments showed that cell mobility and adaptability were dependent on the topography. It has been demonstrated that the micro-pores', dimensions formed on the scaffolds can be tuned in a controllable way by altering the laser parameters.

Dedication

I dedicate this thesis to my beloved parents

Acknowledgements

It has been a wonderful experience for me to have enrolled for a Ph.D at the Faculty of Physics, Vienna University of Technology and reaching the completion stage. Having done M.Sc(Physics) and M.Tech(Laser Science and Application) over a decade ago and working as a laser engineer since then, I have always longed to do a Ph.D. I thank my employer Femtolasers Produktions GmbH (now Spectra-Physics Vienna) for recognizing my dream and giving me an opportunity to realize it. I am indebted and grateful to Priv.Doiz. Dr. Andreas Assion for choosing me to work on the research project he penned, which gave me an opportunity to enrol for the Ph.D. Despite his busy schedule, he was always available for me. I thank him for all his advices and guidance. I also thank the Österreichische Forschungsfördergesellschaft (FFG) agency for the funding.

What else could be a blessing when one enrolls for a Ph.D? Well, to have a compassionate and encouraging supervisor who would never-ever lose his cool. I got more than a blessing in this regard. I thank my thesis adviser ao.Univ.-Prof. Dipl.-Ing. Dr.techn. Wolfgang Husinsky for this. In the first place, I thank him for accepting me as his student and supervising me. He has always stood by me, giving total freedom in choosing problems and type of experiments while seeing to it that I did not deviate from the main goal. I learned a lot from the many lengthy discussion I had with him. I also thank the group head, who is also the head of the institute ("Institut für Angewandte physik"), Univ.Prof. Mag.rer.nat. Dipl.Ing. Dr.techn. Friedrich Aumayr and the former head of the institute, ao. Univ. Prof. Dr. Herbert Störi for all the help and support.

I thank Ms. Karin Whitmore from the USTEM division for the training on the Scanning Electron Microscope, without which the characterization wouldn't have been possible. I thank Mr. Rainer Gärtner and Mr. Herbert Schmidt from the workshop for making the parts needed for the experiments. I found them to be very helpful and genuinely interested in making the required parts. Similarly, I thank Mr. Paul Berlinger (now retired) and Ms. Marie Christin Preimesberger of the electronics lab for the help in making the electronic circuits needed for the

experiments and troubleshooting the TOF electronics.

A good start, particularly for a Ph.D, happens only when one has the support of the seniors in the lab. I was fortunate to have unfettered support of Dr. Shazia Bashir, Dr. Shahid Bashir, and Dr. Albena Daskalova who actually completed their Ph.Ds and left the lab, but were visiting the lab from time to time. The experiments I did with them introduced me to the world of ablation and structuring. I thank our collaborators in Russia, Dr.Sergey Vladimirovich Makarov and Prof. Sergey Kudryashov with whom we worked closely.

A ton of thanks go to Dr. Ali Ajami who finished his Ph.D and is working as a PostDoc in the lab, for all his help. Ali and I did many experiments together in the purview of this project and also spent many hours troubleshooting lasers and different equipment from time to time in last 3.5 year. I deeply appreciate the help Ali extended during my thesis writing phase.

I thank my colleagues at the company, Harald Frei, Peter Bimminger, Thomas Hüller, Thomas Ganz (now left), Mikayel Musheghyan, Fabian Lücking, Tuan Le, Manfred Riemer , Thomas Prikozovits, Christian Warmuth and Andreas Stingl, for all the help and support during the last few years.

Last but not the least, I thank my family: my parents, who even at an age of 65+, were enquiring about my study every week since the day I enrolled for a Ph.D, and my wife 'Ramaa' and daughter 'Ritvika' for all their support, patience and understanding.

Contents

1	Synopsis	11
2	Introduction:Laser Matter Interaction	20
2.1	Laser absorption and Ionization of matter	22
2.1.1	Collisional absorption	24
2.1.2	Collisionless absorption and properties of plasma	28
2.2	Interplay between different processes: Some models	29
2.3	Formation of double layers and ion acceleration	34
2.4	Laser Ablation	35
2.4.1	Nonthermal processes	35
2.4.2	Thermal processes	37
2.4.3	The Two temperature model	38
2.5	Laser Induced Periodic Surface Structures (LIPSS)	39
2.5.1	LSFLs	41
2.5.2	HSFLs	43
2.5.3	Sipe Model	43
2.5.4	Self-organization model	47
2.6	Conclusion	50
3	Experimental Setup	52
3.1	The laser system and diagnostics	53
3.1.1	Femtosecond laser oscillator	53
3.1.2	Femtosecond laser amplifier	54
3.1.3	Laser Diagnostics	60
3.2	Optical schematics	61
3.2.1	Optical set-up for creating structures	61
3.2.2	Set up for White light generation and structuring in liquid environment	63
3.2.3	Set up for measuring ablation thresholds in vacuum environ- ment :	64

3.2.4	Set up for measuring electron emission	64
3.2.5	Set up for measuring ion emission:	65
3.2.6	Set up for measuring of neutral particles	66
3.3	Detection system and Diagnostics	68
3.3.1	Time of flight mass spectrometer	68
3.3.2	Scanning Electron Microscope	71
3.3.3	Atomic Force Microscope (AFM)	71
3.3.4	Raman Spectroscopy	72
3.4	Summary	73
4	Ablation Threshold Measurements	74
4.1	Copper	77
4.2	Silicon	80
4.3	Gelatin	80
4.4	Pulse Width dependence	83
4.5	Conclusions	84
5	Time of Flight Measurements	86
5.1	Silicon	87
5.1.1	Ion/Clusters Emission	87
5.1.2	Neutrals Emission	91
5.1.3	Velocity spectrum	94
5.2	Copper	99
5.2.1	Ion Emission	100
5.2.2	Neutral Emission	102
5.2.3	Velocity spectrum	102
5.3	Titanium	103
5.3.1	Ion Emission	104
5.3.2	Neutral Emission	105
5.3.3	Velocity spectrum	105
5.4	Silver	106
5.5	Discussion	108
5.6	Conclusion	111
6	Laser Induced Structuring	112
6.1	Laser Induced Periodic Surface Structures on Titanium	113
6.1.1	Fluence dependence	114
6.1.2	Scanning Speed / Pulse Number Dependence	116
6.1.3	Pulse Duration Dependence	119
6.1.4	Wavelength Dependence	121

6.1.5	Polarization Dependence	122
6.1.6	Surface-roughness Dependence	122
6.1.7	Discussion	125
6.2	Structuring in liquid environment and Raman Analysis	128
6.2.1	Raman spectrographs	129
6.3	Some observations	130
6.3.1	Structuring with 10 fs laser pulses	130
6.3.2	Structures formed on titanium surface at higher repetition rate	131
6.3.3	Split in periodicity	132
6.3.4	Nano tips formation on Aluminium	133
6.4	Summary and Conclusions	134
7	Laser Induced Structuring on Bio-Polymer Films	135
7.1	Pulse number and pulse duration dependence	139
7.2	Conclusions	141
8	White Light Generation in Water	142
8.1	Conclusions	147
9	Conclusions	148

Chapter 1

Synopsis

The work documented in this thesis is the work carried out at Vienna University of Technology and is based on the experimental investigations of femtosecond laser pulse interaction with materials. The study deals with the measurement of laser parameters to ablate materials and understand the basic phenomena and process that take place when an ultrashort laser pulse with as short as 10 fs duration is incident on a material. The results give more insight into the underlying physics of laser-matter interactions. When irradiated on materials, ultrashort laser pulses create different kinds of structures on them. The kind of structures formed depends on the laser parameters and, to a certain extent, on the type of material. This work focuses on studying the impact of laser parameters on the physical processes and the micro- and nanoscopic surface modifications that take place.

Thanks to the advent of Ti:sapphire lasers, chirp pulse amplification technique, Kerr-lens mode-locking technique and chirp dielectric mirrors, ultrafast lasers are now capable of producing pulses of gigantic fluxes in durations as short as 10 -30 fs. The laser pulses of 1.5 mJ and 25 fs when focussed to a spot size of 20 microns results in an intensity of 10^{16} W/cm^2 . Such high intensities correspond to electric field strength in excess of 10^9 V/cm , which is the order of the coulomb field binding the electrons to a Hydrogen nucleus. Availability of such high intensity pulses and the ability to drive matter to extreme states opened up an exciting field of light-matter interactions.

Apart from studying the physics of light-matter interactions, ultrafast lasers have been of increasing interest in material processing applications too due to their capability of precise micromachining of a large variety of materials: metals, semiconductors, polymers, dielectrics, biological materials etc. The processes that occur

when a laser pulse irradiates a material could be categorized into two domains: the non-thermal domain (for processes that take place up to few ps) and the thermal domain (for longer durations). The laser-matter interaction processes that happen with laser pulses of durations greater than characteristic electron–phonon relaxation times ($\tau_{ep} \sim 10$ ps) seems to have been fairly understood. However, when an ultra-short laser pulse irradiates a material, the non-thermal processes that occur depends on the class of the material irradiated as well as the intensity of the irradiation. The precise processes and the sequence at which they take place are far from understood. Laser ablation refers to removal of macroscopic amounts of material from the surface of a medium under irradiation of laser pulses. Depending on the class of the material, different processes take place preceding laser ablation. For example, in metals which have abundant free electrons, absorption of photons creates hot electrons in a cold lattice as the electron and the phonon processes takes place on different time scales. After electron-electron scattering, electron-phonon-scattering sets in, followed by melting, boiling and ablation. To a certain extent these processes can be described by a Two Temperature Model (TTM). In case of dielectrics and wide-bandgap semiconductors, absorption of radiation can be understood by multi-photon excitation and impact ionization with subsequent avalanche ionization. These carriers then thermalize to a Fermi-Dirac distribution while transferring their excess energy to phonons. These phonons then recombine to a Bose-Einstein distribution and thermal processes follow. It is worth mentioning that upon irradiation with high peak intensities, dielectrics can exhibit metal-like properties. Hence, understanding the exact mechanisms that take place upon femtosecond laser irradiation are complex and involve linear and several non-linear processes taking place simultaneously. Ablation threshold fluence, usually defined as the minimum laser fluence necessary to initiate the ablation process (material removal), is an important parameter which can give insight into the physical processes taking place in the material. Knowing these values is also necessary to deposit a defined amount of energy for precision material processing applications. The single-shot ablation threshold for ultrashort pulsed laser ablation depends on the thermal and dynamical properties of the material. In multi-pulse regime it is well established that the ablation threshold depends on the number of laser pulses exciting the same spot. The threshold fluence normally decreases with laser shot number. This phenomenon is referred to as material incubation, and the origin of the incubation is still under debate. The reduction in ablation threshold fluence follows a power law equation which holds for all materials and can be ascribed to higher energy coupling efficiency. An increase of surface roughness after multi-shot irradiation due to ripples formation or accumulation of surface defects results in reduction in the reflectance and thus leads to enhance the absorption and then a decrease in ablation threshold. It has also been suggested

that the incubation behaviour for metals can be due to the accumulation of plastic deformation resulting from laser induced thermal stress fields. The ablation threshold is usually determined by inspection of the exposed area with a microscope or by detecting changes in the scattering pattern produced by a probe laser or by detecting the ion emission using time of flight spectrometers. In Chapter 2 we give a brief introduction on the physics of laser-matter interaction and in Chapter 3, we briefly describe the the generation of ultrashort laser pulses and the different experimental setups used for the works reported in this thesis.

It has been observed that the damage threshold depends on the pulse duration. For long pulses (eg. $\tau > 10$ ps), where damage on the surface of a medium results from conventional heating and melting, the damage threshold scales as $\tau^{0.5}$ with pulse duration. However, a deviation from this scaling has been observed for shorter pulses where damage results from plasma formation and ablation. Although the ablation threshold in the short pulse regime reduces with decreasing the pulse duration, this dependency is weaker than what is observed in the long pulse regime. Till date, many authors have investigated the dependence of ablation threshold fluence on various laser parameters, but most studies were limited to a particular pulse duration or number of shots or material. A comprehensive study for different type of materials under identical experimental conditions was missing. In this thesis a systematic study was done to investigate the influence of pulse duration on the ablation thresholds and the incubation coefficients for three different types of materials: metal (copper), semiconductor (silicon) and bio-polymer (gelatin) in 10 fs - 550 fs range. The thresholds were measured by plotting the squared crater diameters versus the fluence values and extrapolating the curve to zero crater diameter. The results indicate that the threshold fluence reduces with decreasing the pulse duration. The dependence of the threshold fluence on the pulse duration was determined as $F_{th} \propto \tau^{0.05}$ for Copper, $F_{th} \propto \tau^{0.12}$ for Silicon and $F_{th} \propto \tau^{0.22}$ for Gelatin as shown in the Fig.1.1. The results are discussed in detail in Chapter 4.

The values of ablation thresholds can be measured to a good accuracy that is needed for material processing applications by the technique mentioned above and detailed in Chapter 4. But the exact physical mechanisms taking place and the real time evolution and response of various physical process taking place inside a material can only be studied by detecting the basic atomic particles emitted by the material after irradiating it with the laser pulses. In Chapter 5 we detail the results of our time-of-flight mass spectrometry measurements wherein we studied the emission of ions and neutrals as a function of laser parameters like fluence and pulse duration. The velocities with which neutral particles are emitted from various semiconductors and metals is studied.

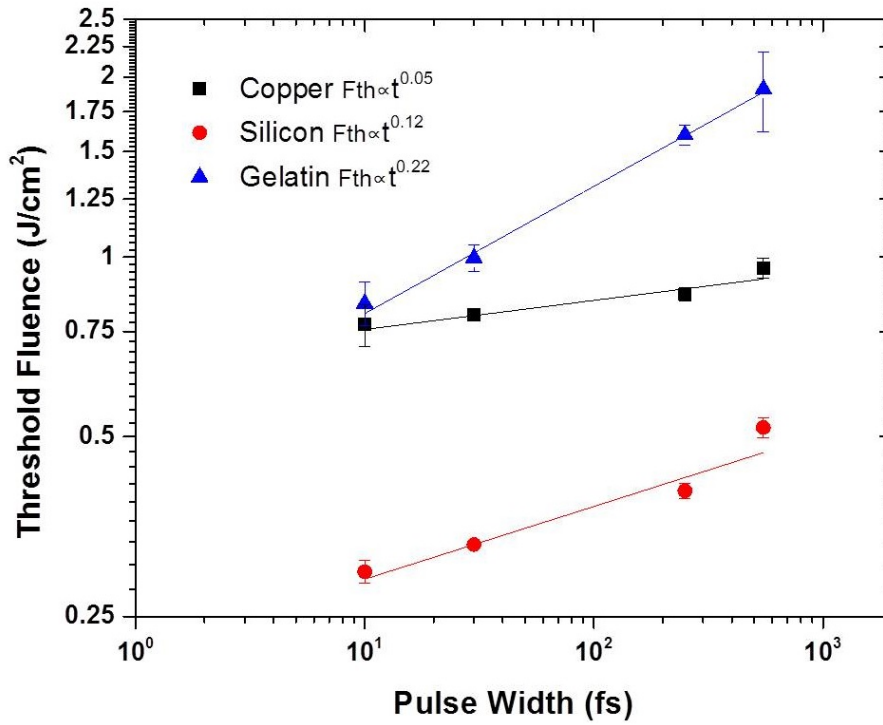


Figure 1.1: Derived single-shot threshold fluence versus pulse width for Copper, Silicon and Gelatin film samples

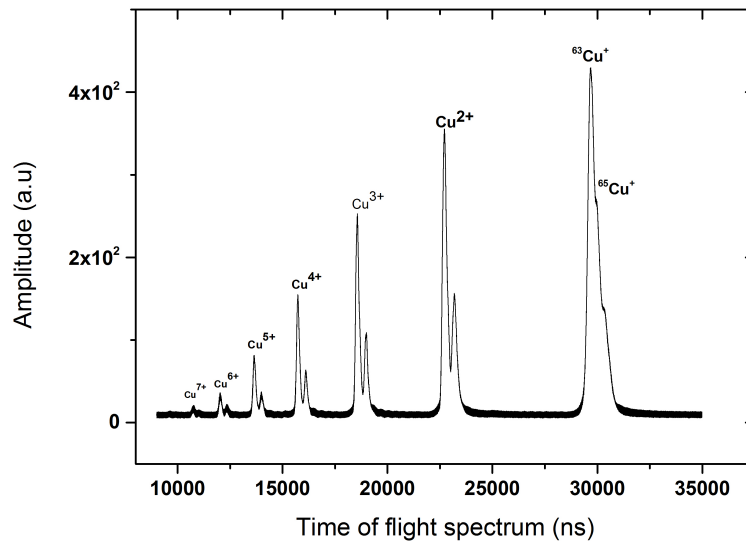


Figure 1.2: Time-of-flight spectrum of copper sample when irradiated with 10 fs pulses of fluence $\approx 1.4 J/cm^2$.

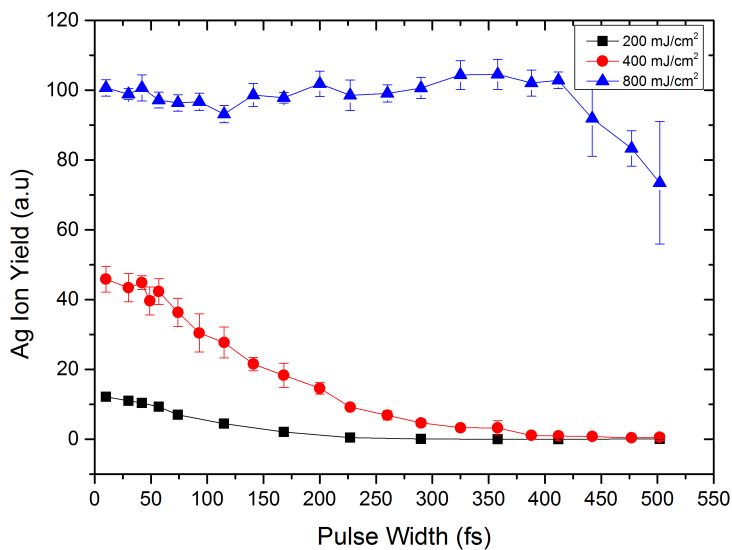


Figure 1.3: Pulse duration dependence of Ag ion emission from silver targets for three different fluence values.

Fig.1.2 shows the time-of-flight spectrum recorded from a 99.99% Cu sample when irradiated with 10fs pulses of $1.4J/cm^2$. As can be seen from the picture, the technique allows us to detect particles based on their mass and charge state. Measuring the emitted ions with respect to the laser fluence and pulse duration can give an insight into the mechanisms that are responsible for ion emission. For example, Fig.1.3 shows the dependence of Ag ion emission on laser pulse duration. The dependence is studied for 3 different fluence values. It can be seen from the plot that for low fluence values close to the threshold, the ion emission is strongly dependent on the pulse duration. This indicates that even in metals, at energies closer to the threshold, processes like multiphoton ionization take place and is primarily responsible for ion emission. For higher energies, though, the emission is independent of pulse duration. This indicates that impact ionization is a dominant mechanism at these fluence values. Apart from ions, the neutral particles ejected from the target upon irradiating with femtosecond laser pulses can be detected by using the TOF spectrometer. For detecting the neutrals, the emitted neutrals are ionized by a second laser beam and the so ionized neutrals (secondary ions) are detected by the TOF spectrometer. Fig.1.4 shows the time-of-flight spectrum of neutral particles emitted from titanium target when irradiated with 10 fs. The potential of reflectron type of mass spectrometer can be noticed by observing the spectrum. Particles with even 1 a.m.u spacing can be detected with good accuracy and their emission behaviour can be studied. Fig.1.4 not only shows the emitted titanium neutral atoms but also the stable isotopes of titanium are detected.

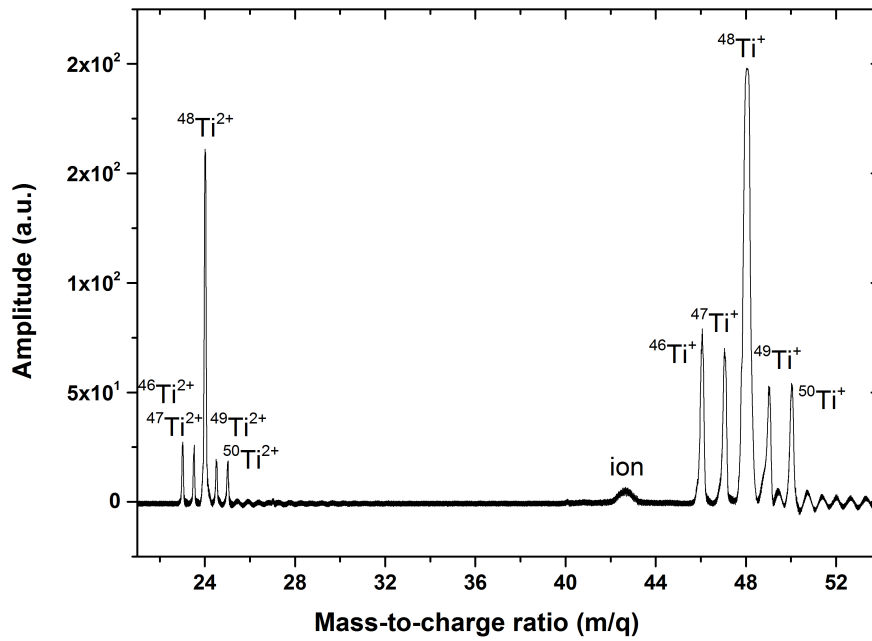


Figure 1.4: Time-of-flight mass spectrum of neutral atoms emitted from titanium sample when irradiated with 10 fs pulses of fluence $\approx 300 \text{ mJ/cm}^2$.

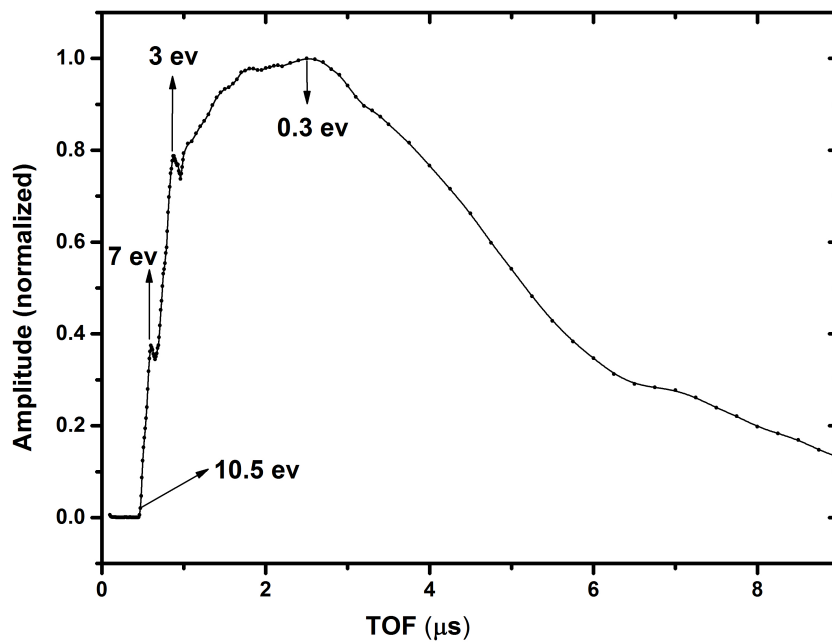


Figure 1.5: Velocity distribution of neutral particles emitted from a titanium target upon irradiating with 10 fs laser pulses of $\approx 100 \text{ mJ/cm}^2$.

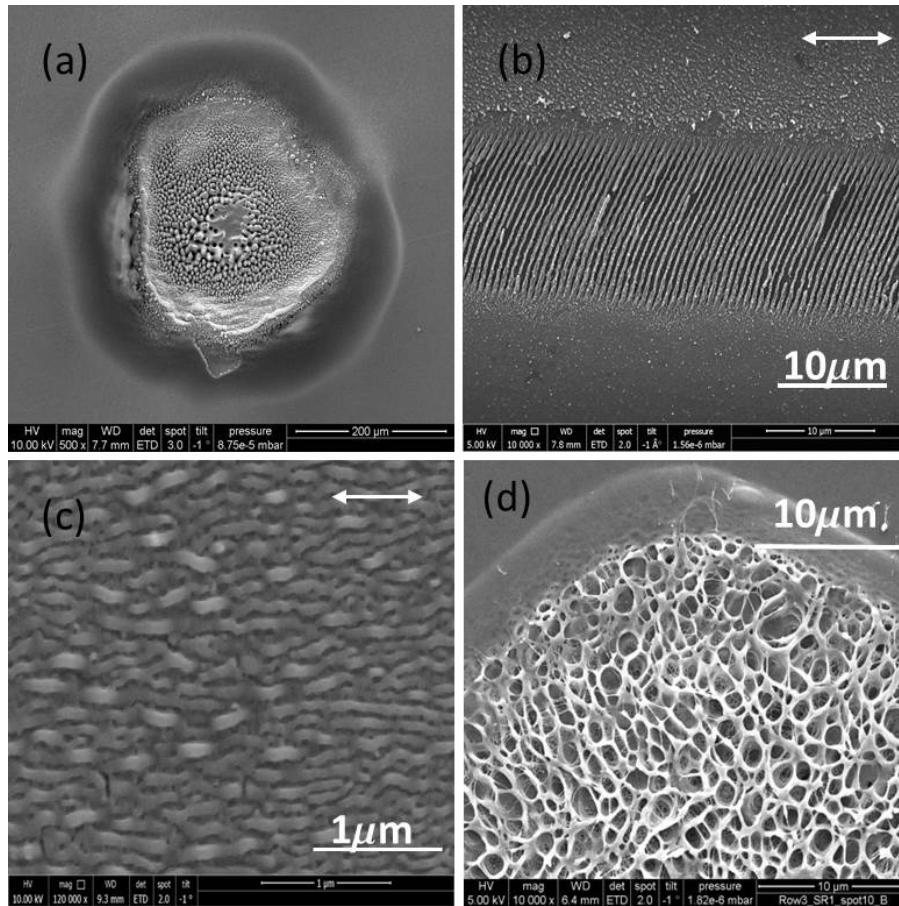


Figure 1.6: Different kinds of structures formed on materials when irradiated with ultrashort laser pulses. (a) Conical structures formed on steel sample after irradiating with 500 pulses of 500 mJ/cm^2 . (b) Laser induced low spatial frequency ripples formed on titanium surface after irradiating with 36 pulses of 65 mJ/cm^2 . (c) Laser induced high spatial frequency ripples formed on titanium surface after irradiating with 220 pulses of 30 fs pulses duration and 42 mJ/cm^2 . (d) Structures formed on collagen-elastin film when irradiated with a single pulse of 30 fs duration and 3.92 J/cm^2 .

The velocity (energy) of the neutral particles emitted from the target can be also measured by the reflectron type of mass spectrometer by scanning the delay between the post-ionizing pulses and the ablating pulses. This corresponds to the time the neutrals take to travel from the target surface to the post-ionizing point. By scanning the delay between the two laser pulses by several microseconds in steps of few tens of nanoseconds and detecting the secondary ions, the velocity (and hence the energy) of the emitted neutrals can be measured. Fig.1.5 shows the time distribution of the neutrals emitted from a titanium target irradiated by 10 fs pulses of 100 mJ/cm^2 . It can be seen that apart from the low energy particles detected beyond $1 \mu\text{s}$ delay, there are peaks corresponding to energies of 7 eV and 3 eV. These high energy particles are emitted as a result of non-thermal process like Coulomb explosion, ultrafast melting and optical rectification processes. In Chapter 5 we report the results obtained from the time-of-flight mass spectrometry studies.

Micro- and nanostructures are formed on a wide variety of materials when an ultrafast laser irradiates a material. The most well-known of them are regular arrays of conical structures (Fig.1.6(a)) and periodic structures. Two kinds of periodic structures are formed with ultrafast lasers: structures with periods close to the wavelength of the incident laser radiation (Fig.1.6(b)) and periods $\sim 1/10$ th the wavelength (Fig.1.6(c)). The exact mechanism of periodic structure formation is still under debate. There are principally two different models that try to explain the formation of these structures. One, which is called the *Sipe model* suggests that the ripples are a consequence of an inhomogeneous absorption of radiation by the surface because of the interference between the incident laser beam and some kind of surface waves. The other model, called the *self-organization model* is based on the instabilities caused by the incident radiation. The absorbed energy causes a perturbation and softening of the crystal binding leading to an unstable surface region which relaxes via self-organization. By all modest means it can be stated that both models are complex but strong in explaining certain experimental observations. In this thesis we produced the periodic structures on many materials, but we report on the systematic studies we did on titanium metal. Specifically, we did a detailed study on the high spatial frequency ripples which were only recently reported. The results of our experiments are reported in Chapter 6.

Different kind of structures are formed on bio-polymer materials like collagen and gelatin, when they are irradiated with femtosecond laser pulses. Scaffold-like structures are formed on them (Fig.1.6(d)). These structures can be used in regenerative medicine, where the goal is to regenerate a tissue after injury or disease. Moreover, these biopolymers, collagen and gelatin already exist in the human body, so they are bio-compatible. In collaboration with a group in Sofia, we produced scaffold like structures on many bio-polymers. We found out that the morphology of the structures formed on these materials can be modified by tuning the laser parameters. Accordingly scaffolds that are good for cell proliferation, viability and mobility were created and tested. The results of these experiments are reported in Chapter 7.

Supercontinuum emission or white light generation is the manifestation of a host of nonlinear processes that take place when an ultrashort laser pulse interacts with matter. In Chapter 8 we report the results of our systematic investigation of white light generation in water. Over the last many decades, many authors have studied the SCE in wide variety of materials. In our study we focussed on the pulse duration dependence of the process and the geometrical focussing effect on the generated white light. Fig.1.7 shows the spectra of white light generated in water with femtosecond laser pulses of 30 - 300 fs duration. Detailed results are reported in

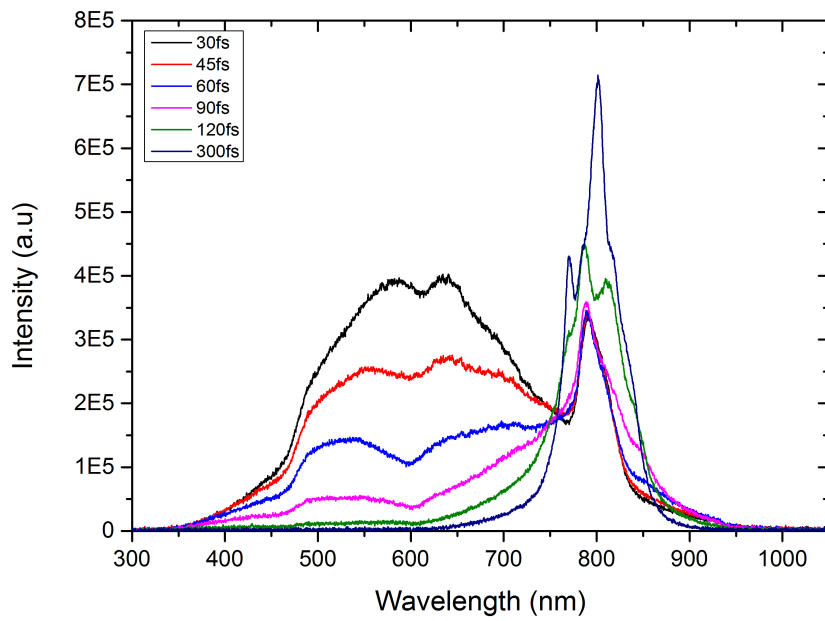


Figure 1.7: SCE spectra from water when incident with fs pulses of duration 30-300fs.

Chapter 8.

Chapter 2

Introduction: Laser Matter Interaction

From the day the first Ruby laser was invented in 1960 by T. H. Maiman [1], lasers have grown more powerful year after year. In the 1980s, most labs around the world had few GW class of lasers and today peta-watt class of lasers are commercially sold. That's a factor of $10^5 - 10^6$ increase of available peak powers of laser radiation for researchers. There are two factors that made this possible: 1. Chirp pulse amplification technique [2], where low energy pulses are stretched in time, amplified and then compressed producing pulses of gigantic fluxes and 2. Shortening the pulses in time to almost the limits set by the bandwidth of the gain medium [3]. Robust systems producing pulses as short as few femtoseconds are produced and commercially sold now while generation of attosecond (10^{-18} s) pulses are demonstrated and routinely used to control electronic processes [4, 5]. Availability of such high intensity pulses opened up an exciting field of *light-matter interactions* or *laser-solid interactions*. LASER ABLATION is an important phenomenon resulting from the interaction of intense laser light with solids. The interaction process in which atoms are selectively driven off by thermal or nonthermal mechanisms, resulting in transient or permanent modifications to the material topography, is defined as *laser ablation*. The field of laser ablation physics is advancing so rapidly that its principal results are seen only in specialized journals, conferences (eg. Conference On Laser Ablation (COLA)) and dedicated books [6]. Laser ablation has many practical applications ranging from inertial confinement fusion to pollution monitoring to material processing. Laser ablation is characterized by the laser fluence called *ablation threshold fluence*. Even though this definition of *laser ablation* seems to be straightforward, it is worth noting that one might distinguish between desorption (fluence below 'ablation threshold fluence' where normally only emission of particles

is observed without any noticeable surface modifications), spallation, fragmentation and similar terms by the physical processes taking place. However, it has turned out that regarding many practical applications it is not useful to divide them. Both, the particle emission and the change in material properties can be a clue to the specific processes that take place inside the material upon laser irradiation. The processes involved are complicated and the mechanisms of interactions are different depending on the type of the material and the laser parameters (photon energy, fluence and peak intensity). Metals have abundant free electrons, so they absorb photons and gain energy irrespective of the photon energy. In semiconductors, depending on the photon energy, electrons in the valance band are excited to the conduction band. In dielectrics whose band gaps are normally much larger than the IR lasers' photon energy, multiple photons are required to promote electrons from the valence band to the conduction band.

The interaction of light with matter can be described in simple terms as a spring-mass system : an electron is attached by a spring (Coulomb potential) to a heavy mass nucleus. The nucleus being much heavier than the electron, is fixed when the interaction with light takes place. The electron vibrates along the mean position. Though this analogy is valid in low flux regime, it is not at high intensities. At higher intensities, the motion is anharmonic and many interesting nonlinear phenomena arise. When high intensity pulses are focussed, it produces gigantic electric fields which will ionize the matter completely. Consider the example of Hydrogen atom. The electric field strength between the electron and the proton in Hydrogen atom can be written as:

$$E_H = \frac{e}{4\pi\epsilon_0 a_B} \approx 5 \times 10^9 \text{Vm}^{-1} \quad (2.1)$$

Here, a_B is the Bohr radius, $a_B = \frac{\hbar^2}{m_e c^2} \approx 5.3 \times 10^{-11} \text{m}$.

Now, the intensity of the laser, where the laser field matches this binding strength of the atom can be calculated using:

$$I_H = \frac{1}{2}\epsilon_0 c E_H^2 \approx 3.5 \times 10^{16} \text{Wcm}^{-2} \quad (2.2)$$

So evidently if the laser intensity is more than this value, the incident radiation will directly ionise the atoms.

There are three main pathways to ionise matter with optical field, called optical field ionization (OFI). They are: multi-photon ionization (MPI), tunnelling ionization (TI) and over-the-barrier ionization (OTBI). They are discussed in detail in the next section.

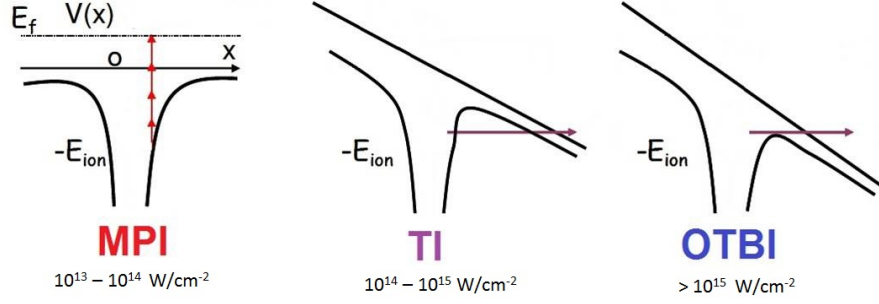


Figure 2.1: Schematic representation of ionization mechanisms. MPI-Multi-Photon Ionization, TI-Tunnel Ionization, OTBI:Over The Barrier Ionization.

2.1 Laser absorption and Ionization of matter

In semiconductors / dielectrics, the individual photon energy $E = \hbar\omega$ (1.55 eV for 800 nm) is very less compared to typical band gap of materials, (≈ 10 eV), so the normal photoelectric ionization can not occur. Particularly, in dielectrics, the electron density in the conduction band at room temperature is small (typically $10^8 - 10^{10} \text{cm}^{-3}$) and mostly a consequence of thermal and defect induced charge carrier excitation. However, at large intensities on the order $10^{13} - 10^{14} \text{W}\cdot\text{cm}^{-2}$, multiple photons act together to cover the energy required to ionize the atom and this process is called multiphoton ionization (MPI).

This process is expressed as:

$$E_f = (n + s)\hbar\omega - E_{ion} \quad (2.3)$$

where n is the number of photons required for multiphoton process to occur and s is the excess absorbed. Using perturbation theory, the ionization rate Γ can be calculated using:

$$\Gamma = \sigma_n I^n \quad (2.4)$$

where σ_n is the cross-section, which decreases with n , but the I^n dependence ensures that an n -th order ionization event will eventually occur provided that the intensity is high enough and sufficient atoms or ions are left. The process is schematically represented in Fig.2.1a.

In deducing the physical picture of MPI, an assumption is made that the external laser electric field does not perturb the atomic electric field, an assumption valid till the external field is very small compared to the atomic field. As the laser intensity is increased ($> 10^{14} \text{W}/\text{cm}^2$) the external electric field starts distorting the atomic field and the bound state electrons have a finite probability to tunnel through the atomic potential barrier as illustrated in Fig.2.1b showing the instantaneous distortion in the

atomic potential. In time, the width and the inclination of the barrier oscillate with the laser frequency. An electron can successfully tunnel through, only if it can do so before the polarity of the oscillating electric field is reversed, i.e. if the tunnelling frequency (inverse of the tunnelling time) is higher than the laser frequency. Since the laser intensity essentially controls the width of the barrier and the frequency of the laser field determines the time available for tunneling, they both become important parameters controlling the rate of tunnel ionization (TI). Keldysh [7] and Perelomov et.al. [8] introduced a parameter γ called the Keldysh parameter, and showed that its value controls the competition between MPI and TI regimes. The Keldysh parameter is expressed as:

$$\gamma = \frac{\omega}{\omega_T} = \sqrt{\frac{I_P}{2U_p}} \quad (2.5)$$

where, ω is the frequency of the laser, ω_T is the tunnelling frequency, I_P is the ionization potential, and U_P is the *ponderomotive energy* of the electrons ¹, expressing the effective quiver energy associated with their oscillatory motion in the laser field. As a rule of thumb, tunnelling applies to strong fields and long wavelengths ($\gamma < 1$) and multiphoton applies for the case of $\gamma > 1$

According to Keldysh [7], for Hydrogen-like atoms (atoms stripped down to the last 1s electron), the rate of ionization by tunneling is given by:

$$\alpha_i = 4\omega_a (E_i/E_H)^{5/2} E_a/E_L \exp \left[-2/3 (E_i/E_H)^{3/2} E_a/E_L \right] \quad (2.6)$$

Where E_i and E_H are the ionization potentials of the atoms and Hydrogen respectively, E_a is the atomic electric field given by equation 2.1, E_L is the instantaneous laser field and ω_a is the atomic frequency defined by:

$$\omega_a = me^4/\hbar^3 = 4.16 \times 10^{16} S^{-1} \quad (2.7)$$

When averaged over a complete laser cycle, the ionization rate conforms with

$$W = \left(\frac{3}{\pi} \right)^{1/2} \left[\frac{E_L}{E_a} \left[\frac{E_H}{E_i} \right] \right]^{1/2} \alpha_i. \quad (2.8)$$

When an external field of amplitude E is applied, the modified Coulomb potential

¹A simple expression for the energy given to the electron by light, called ponderomotive energy is given by, $U_P = e^2 E^2 \lambda^2 / m^2 c^2$

$V(x)$ can be written as:

$$V(x) = \frac{-Ze^2}{x} - eEx. \quad (2.9)$$

At still higher intensities, when the Coulomb barrier falls below the bound electron's energy (Fig. 2.1c), the electron is exposed to the continuum directly. This ionization mechanism is called over-the-barrier-ionization (OTBI) or barrier suppression ionization (BSI).

2.1.1 Collisional absorption

Unlike in single particle behaviour discussed above, when a laser pulse irradiates the surface of a solid, because of large densities involved, the electron-ion interaction play a significant role. At first only the electronic subsystem of the target reacts to the incident radiation. Energy is absorbed only by the electronic subsystem and any transfer of energy to the lattice system is a subsequent process. In metals the optical absorption is usually dominated by free carrier absorption. Light is almost exclusively absorbed by conduction band electrons. Electron scattering events can take place within a few femtoseconds and electronic thermalization can be extremely fast. Using Drude model, the electron scattering time τ_D can be deduced as [9]:

$$\tau_D = m\sigma_{el}/Ne^2 \quad (2.10)$$

Where σ_{el} is the electrical conductivity, N is the conduction electron density, e is the electron charge and m is the electron mass.

Typical values of τ_D are a few fs. However, Drude model provides the electron scattering time under equilibrium conditions and an ultrashort laser pulse irradiation induces a non-equilibrium electronic distribution. So more sophisticated approaches must be employed to deduce the electron scattering times. Using Fermi liquid theory [10], the lifetime τ_{ee} of excited electrons can be written as [9]

$$\tau_{ee} = \tau_0 \left(\frac{E_F}{E - E_F} \right)^2 \quad (2.11)$$

Where τ_0 is of the order of a femtosecond, E_F is the Fermi energy, and E is the excited electron energy. With laser photons in the visible-UV range and with a typical Fermi energy of ≈ 10 eV, τ_{ee} is of the order 1- 10 fs and it rapidly increases as the electron energy relaxes towards the Fermi level. This lifetime dependence has been experimentally confirmed by several time-resolved photoemission experiments using femtosecond lasers. It is to be noted that due to the ultrafast character of

electron-electron interactions these processes can only be revealed by using laser pulses of duration comparable with τ_{ee} . With longer pulses, the electron-electron thermalization occurs within the pulse duration and the electron dynamics substantially follow the time evolution of the laser pulse. So with the ultrashort pulses, the electronic subsystem exclusively absorb the incident radiation and thermalize within few femtoseconds. Because of large densities involved, the electron-ion interactions kicks in and several other ionization and absorption mechanisms unique to this state emerge. One such ionization mechanism is the Collisional ionization (CI) or Impact ionization (IO). When the laser encounters a solid with density $\sim 10^{23}$ atoms cm^{-3} , the light can drive electrons not only on its own, but can also use the freed electrons, which gain enough kinetic energy in the laser field, to efficiently cause other excitations in the medium. This leads to an avalanche breakdown of the solids in the laser irradiated portion.

Collisional ionization can be due to both thermal electrons, i.e., the electrons equilibrated through collisions, and the electrons oscillating with laser fields under ponderomotive potential. The rate of this process can be described using the semi-empirical Lotz formula [11, 12].

In case of thermal electrons, this ionization rate is determined using the semi-empirical Lotz formula for electron impact ionization averaged over a Maxwellian energy distribution,

$$W_{kT} = n_e \frac{a_i q_i}{I_p (kT_e)^{1/2}} \int_{I_p/kT_e}^{\infty} \frac{e^{-x}}{x} dx \quad (2.12)$$

where, n_e is the electron number density, I_p is the ionization potential in eV, a_i is an empirical constant ($= 4.5 \times 10^{-14} eV^2$), and q_i is the number of electrons in the outer shell of the ion.

The collisional ionization rate, due to electrons oscillating in the laser field, is calculated using the following equation while treating the electron velocity in the laser field as sinusoidal:

$$W_{laser}(t) = n_e \sigma_i \frac{eE}{m_e \omega} \sin \omega t, \quad (2.13)$$

where σ_i is the ionization cross section and E is the laser field in atomic units. As is evident from equations 2.12 and 2.13, collisional ionization process contributes more and more with increasing electron density.

For metals, P.B.Allen [13] has proposed a simplified approach for the interaction of electrons with the lattice subsystem based on the rate of change of the electron and phonon distributions due to collisions. Allen derived an expression for the energy

transfer between the photo-excited electrons and the lattice that allows to evaluate the variation of the electronic temperature T_e as a simple rate equation [9]:

$$\frac{\partial T_e}{\partial t} = \frac{(T_l - T_e)}{\tau_{ep}} \quad (2.14)$$

Where T_l and T_e are lattice and electron temperatures. The electron-phonon coupling time τ_{ep} is given by :

$$\tau_{ep} = (2\pi k_B T_e) / (3\hbar \lambda_p \omega_D^2) \quad (2.15)$$

For $T_e \sim 10^3 K$ and using typical values of the Debye frequency for metals ($\hbar\omega_D$ of a few tens of meV), $\tau_{ep} \sim 0.1 - 1 ps$. Thus, the energy transfer from the electronic subsystem to the lattice subsystem occurs on the picosecond time scale. So it is roughly two orders of magnitude slower than the electron-electron scattering time.

By the ionization processes mentioned above, the free electron densities of semiconductors and dielectrics under ultrashort laser pulse irradiation can increase drastically and hence exhibit metal like behaviours. Also, owing to the short duration of the pulses, the lattice subsystem is unaffected during the irradiation.

We can summarize the ionization processes discussed above as follows:

1. With light intensities $\approx 10^{13} - 10^{16} W/cm^2$ matter can be completely ionized, independent of light wavelength and the energy of individual photon by processes such as MPI, TI and OTBI.
2. The femtosecond laser pulse is almost impulsive to matter, meaning except for the electronic response, all other motions in the matter are frozen.
3. The already present free electrons or the electrons ionized (freed) during the rising edge of the light pulse can absorb enormous amounts of energy from the remainder of the laser pulse. The energies of such electrons can thus reach a few MeV.
4. By electron-phonon interactions further ionization takes place.
5. The interaction is highly transient and equilibrium is not established until few ps.

From these considerations, it is clear that the electrons and the lattice can develop distinct dynamics upon fs laser irradiation, and the time evolution of the energy (temperature) of the electron subsystem and lattice can be described by two separate but coupled heat transport equations, known as two-temperature model (TTM)[14] (discussed separately in sec.2.3.3). It is evident from the above discuss that using ultrashort laser pulses below 1 ps the laser light interacts only with a passive target and all significant target modifications (transient changes, removal of particles) occur

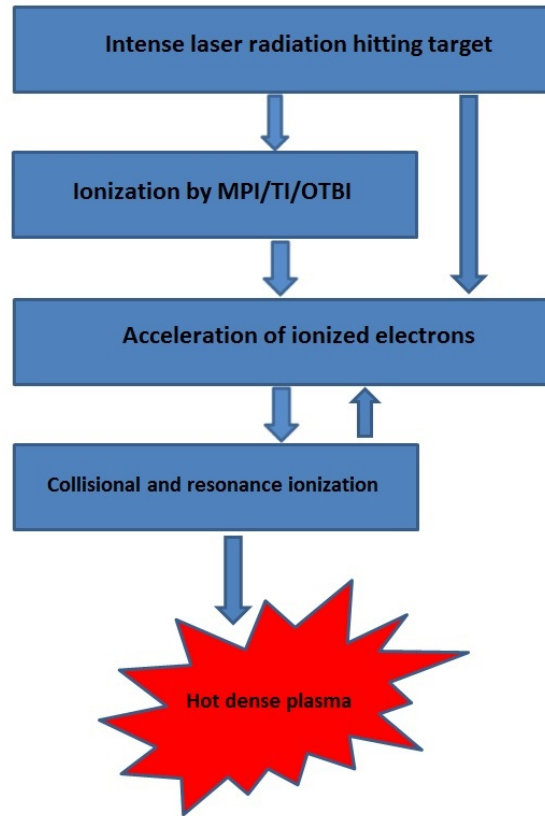


Figure 2.2: Basic mechanism of plasma formation in intense laser fields

only after the laser pulse. In non-metals, there is a significantly higher variation of the absorption mechanisms and the thermalization time typically range from 10^{-12} to 10^{-6} s. Polymers and dielectric materials are typically on the slower end of this range. Excitations of localized electronic states associated with defects, impurities or surfaces play a significant role in slowing down this thermalization time.

Because of all the above mentioned processes, the matter in the focal volume of the intense laser is severely ionized and exists in the form of electrons and ions exhibiting *quasi-neutrality* and *collective behaviour*. Matter in such a state exhibiting quasi-neutrality and collective behaviour is called **plasma**. Once plasma is formed the radiation interacts with the plasma. For short laser pulses it is reasonable to assume that the plasma forms during the initial part of the rising edge of the laser pulse. As the pulse reaches its peak amplitude and crosses it, it is the collisional ionization which starts to dominate the further ionizations. Fig.2.2 shows the process of the plasma formation.

2.1.2 Collisionless absorption and properties of plasma

Without going too much into plasma physics, collisionless absorption process and some of the basic plasma properties and their parameters are summarized below:

1. The plasma exhibits *collective behaviour* and *quasi-neutrality* beyond a length and time scale given by Debye length (λ_D) and inverse electron plasma frequency (ω_p) respectively.

$$\lambda_D = \sqrt{\frac{\epsilon_0 k_B T_e}{N e^2}} \quad (2.16)$$

$$\omega_p = \sqrt{\frac{4\pi N e^2}{m_e}} = 5.64 \times 10^4 n_e^{1/2} (\text{rad/sec}) \quad (2.17)$$

Where, ϵ_0 is the permittivity of free space, k_B is the Boltzmann's constant, T_e is the plasma temperature, N is the electron density and e is the electronic charge. It can be seen that the plasma frequency is independent of the wave vector and is dependent only on the electron density. It is also a measure of the length of time required for an electron moving with thermal speed to travel a Debye length. As ω_p varies as $(N/m)^{1/2}$, the denser the plasma, the higher is ω_p .

2. Only if the considered length scales $L \gg \lambda_D$, can the system be regarded as a plasma.
3. There should be enough electrons in a Debye Sphere (a sphere with radius λ_D for it to be a statistically valid. $N_{De} = (4/3)\pi\lambda_D^3 n_e \gg 1$).
4. The dielectric function of plasma can be written as:

$$\epsilon = n^2 = 1 - \frac{\omega_p^2}{\omega(\omega + i\nu)} \quad (2.18)$$

where, ω_p is the plasma characteristic oscillation given by Eq.2.17, ω is the incident laser frequency, ν is the damping frequency because of electron-ion collisions. It is then clear that the plasma allows propagation of only those frequencies ω for which n^2 is positive. Negative values make n imaginary and such a light wave is attenuated. In other words, the incident electromagnetic wave will propagate up to a density called critical density n_{cr} before it suffers specular reflection. At this interface some amount of radiation can tunnel in to the critical density layer, leading to collision-less absorption.

5. As the incident laser radiation is absorbed completely, the plasma wave grows and the damping processes would attenuate the wave, so that the energy is transferred to the plasma electrons, preferentially to some group of plasma electrons which are termed as '*hot electrons*'. The hot electrons can have temperatures 100 - 1000 times

larger than the bulk plasma electrons.

2.2 Interplay between different processes: Some models

Following ionization the laser energy is absorbed by free electrons due to Inverse Brehmstrahlung and resonance absorption mechanisms and does not depend on the initial state of the target. Consequently, the interaction with both metals and dielectrics proceeds in a similar way, which contrasts to the situation with a long pulse where ablation of metals occurs at a relatively low intensity compared with that for a transparent dielectric whose absorption is negligibly small. For dielectrics and semiconductors photoionization and electron-electron impact ionization are two competing processes which may lead to an avalanche. Rethfeld [15] developed a model describing the free-electron generation in transparent solids under high-intensity laser irradiation. She introduced a multiple rate equation (MRE) consisting of a set of coupled ordinary differential equations. According to Rethfeld, the transient free electron density in this regard is a fundamental parameter and is described by simple rate equation, combining the rate of photoionization \dot{n}_{pi} with the rate of impact ionization, assumed to depend on the total free-electron density n_{total} as:

$$\frac{dn_{total}}{dt} = \dot{n}_{pi}(E_L) + \alpha(E_L)n_{total} \quad (2.19)$$

As Rethfeld explains, because the photoionization is dependent directly on the amplitude of the laser electric field E_L , electrons are shifted from the valence band into the conduction band. In contrast, electron-electron impact ionization is caused by a free electron already existing in the conduction band. If the kinetic energy of such electron is sufficiently large, it may transfer part of it to an electron in the valence band, such that the latter is enabled to overcome the ionization potential. The parameter α called avalanche coefficient depends on the effective energy gain of the free electron in the laser field E_L and can be estimated by approximative models or is taken as a fit parameter. Equation 2.19 was verified with nanosecond pulses, but gave contradictory results with picosecond and sub-picosecond pulses. One basic assumption of equation 2.19 is that the impact ionization depends on the total density of the free electrons. However, the energy of a particular electron plays an important role as photo-ionization generates electrons with low kinetic energy in the conduction band and impact ionization requires electrons of high kinetic energy. This additional energy required by the low energy electron in the conduction band to initiate impact ionization, is absorbed from the laser light by intraband

absorption. If this absorption process takes times comparable to the laser pulse duration, then determining the energy distribution of the electrons becomes crucial for the probability of impact ionization. The MRE model introduced by Rethfeld [15] overcomes this issue and provides direct possibility for estimating the role of the impact ionization avalanche. Rethfeld describes the cycle of ionization as follows: Photo-ionization generates electrons with a certain ionization rate \dot{n}_{pi} at the lower edge of the conduction band, i.e., with energy $\varepsilon_0 \approx 0$. An electron at energy $\varepsilon_0 \approx 0$ may absorb a single photon from the laser light with probability $W_{1pt}(\varepsilon_0)$. The resulting kinetic energy of the electron reads $\varepsilon_1 := \varepsilon_0 + \hbar\omega_L$, where ω_L is the laser frequency. In the same manner, further discrete energy levels $\varepsilon_{j+1} := \varepsilon_j + \hbar\omega_L$ are defined. When $k = \lceil \varepsilon_{crit}/\hbar\omega_L \rceil$ photons have been absorbed, the electrons energy $\varepsilon_k = \varepsilon_0 + k\hbar\omega_L$ exceeds the critical energy for impact ionization ε_{crit} . For electrons with $\varepsilon > \varepsilon_{crit}$ impact ionization occurs with a probability $\tilde{\alpha}$. Through this process the kinetic energy of the electron will be reduced and a second electron is shifted from the valence band (VB) into the conduction band. Both electrons will then have a small kinetic energy, which can be assumed to be comparable to ε_0 .

Defining the density n_j as the density of electrons at energy ε_j , and writing the rate equations for n_j for $j=1$ to k and adding them yields:

$$\frac{dn_{total}}{dt} = \dot{n}_{pi}(E_L) + \tilde{\alpha}n_k \quad (2.20)$$

with $n_{total} = \sum_{j=1}^k n_j$. The difference in the last term of Eq.2.19 compared to Eq. 2.20 is substantial: while in Eq. 2.19 the impact ionization is assumed to depend on the total free-electron density n_{total} , Eq. 2.20 considers the fact that only those electrons which bear sufficiently high energy may produce impact ionization. By solving the rate equation, the temporal evolution of the shape of the free-electron distribution function for ultrashort times can be deduced. Fig.2.3 shows the transient fraction of high-energy electrons n_k/n_{total} multiplied with $\tilde{\alpha}$ (thereby being independent on the choice of $\tilde{\alpha}$). It shows the temporal evolution of the shape of the free-electron distribution function for ultrashort times and its development towards the asymptotic stationary long-time behaviour. Depending on the laser electric field, the time to reach the stationary regime and thus a constant fraction of high-energy electrons is in the range of several hundreds of femtoseconds. Below this time scale, the fraction of the high-energy electrons is much lower than its asymptotic value.

Kaiser et.al., have investigated theoretically the role of ionization processes in a defect-free crystal, including two competing processes: strong-electric field ionization and electron impact ionization [16] by solving numerically a system of time

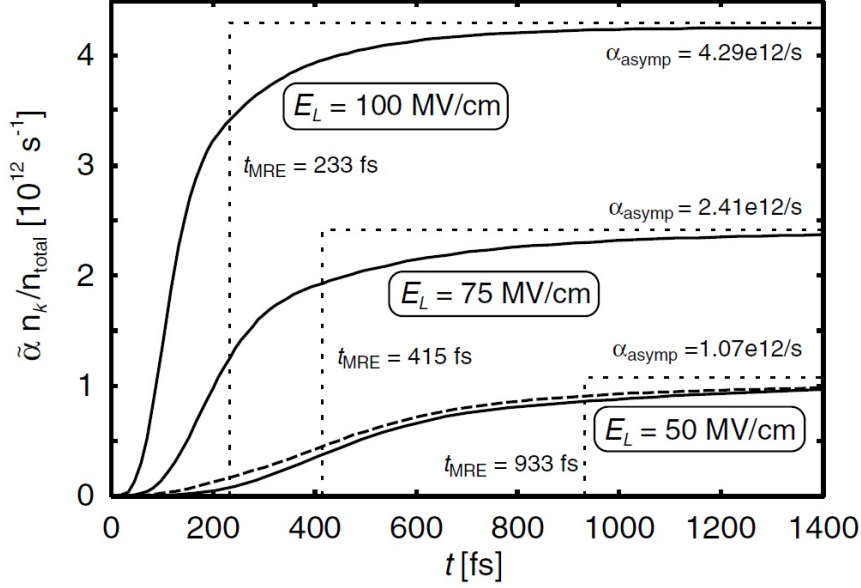


Figure 2.3: Temporal evolution of the fraction of high-energy electrons for different laser field amplitudes calculated by the MRE (solid lines). (from Ref.[15]).

dependent Boltzmann equations. Their results of the full kinetic calculations are shown in the following figures.

Fig.2.4 shows the time dependence of the free-electron density evolution, during and after the laser pulse, and the contributions of strong-electric-field ionization and impact ionization, respectively for four different pulse lengths, all at laser field of 150 MV/cm. As can be seen in the Fig.2.4, the rate of strong -electric-field ionization is directly connected with the laser field. In contrast, impact ionization becomes important only when a sufficient number of high-energy electrons is present in the conduction band. Therefore this process starts much later than strong-electric-field ionization. As each striking electron shifts a second electron into the conduction band, the density contribution of electrons created by impact ionization grows exponentially. However, for very short pulses of 25 fs, free electrons have not enough time to absorb laser energy to reach above the critical energy for impact ionization. In this case, the contribution of impact ionization to the total electron density is negligible. If the laser pulse length is increased, the number of free electrons created by impact ionization also increases. Only for pulse lengths of 200 fs and more is the contribution of impact electrons is comparable to the contribution of the strong electric field ionization.

Kaiser et.al., have attributed the sharp rise in impact ionization at the end of laser irradiation as an artifact caused by assuming a box shaped pulse. By varying increasing effective electron mass in valence band or decreasing band gap, leads to an increase of impact ionization. However, strong-electric-field ionization still remains

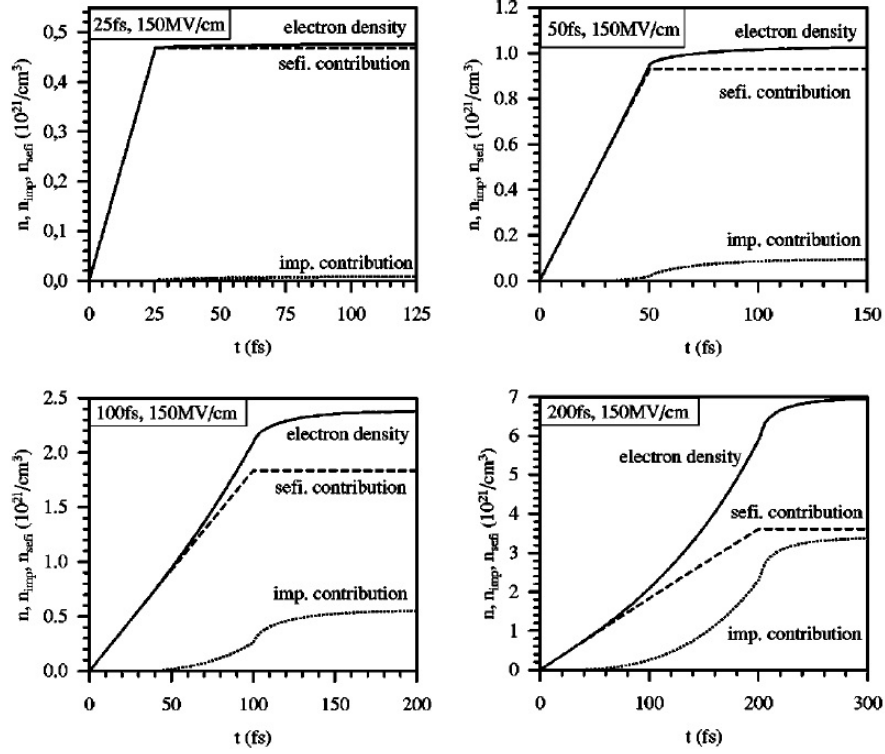


Figure 2.4: Time dependence of free-electron density and the contributing processes, i.e., strong-electric-field ionization (sefi) and impact ionization. A 500 nm laser pulse impinging on SiO_2 with an electric field of 150 MV/cm is assumed. (from Ref.[16]).

the dominant ionization process for laser pulses below 150 fs.

Fig.2.5 shows the maximum electron density dependence on the laser field and the individual contributions of strong-electric-field ionization and impact ionization to the free electron density. For all pulse lengths, the electron density increases with increasing laser field. Strong-electric field ionization is directly proportional to the laser pulse intensity, whereas the impact ionization rate increases because of the avalanche effect. As can be seen in the Fig.2.4, for pulse lengths below ≈ 100 fs the contribution of impact ionization is negligible compared to strong-electric-field ionization. Only for a pulse length of 200 fs do both processes provide similar contributions. Thus the pulse length determines predominantly which ionization process is mainly responsible for the formation of a free electron gas.

Kaiser et.al., have also theoretically calculated the ablation threshold using the criterion of plasma formation, where the dielectric is assumed to change to plasma state when the electron density exceeds a critical value. Fig.2.6 shows the calculated damage threshold for an assumed laser pulse of wavelength of 500 nm irradiating on SiO_2 .

In this dissertation work, we studied the dependence of pulse duration on the emission of ions and neutrals to understand which of the above two processes: strong field

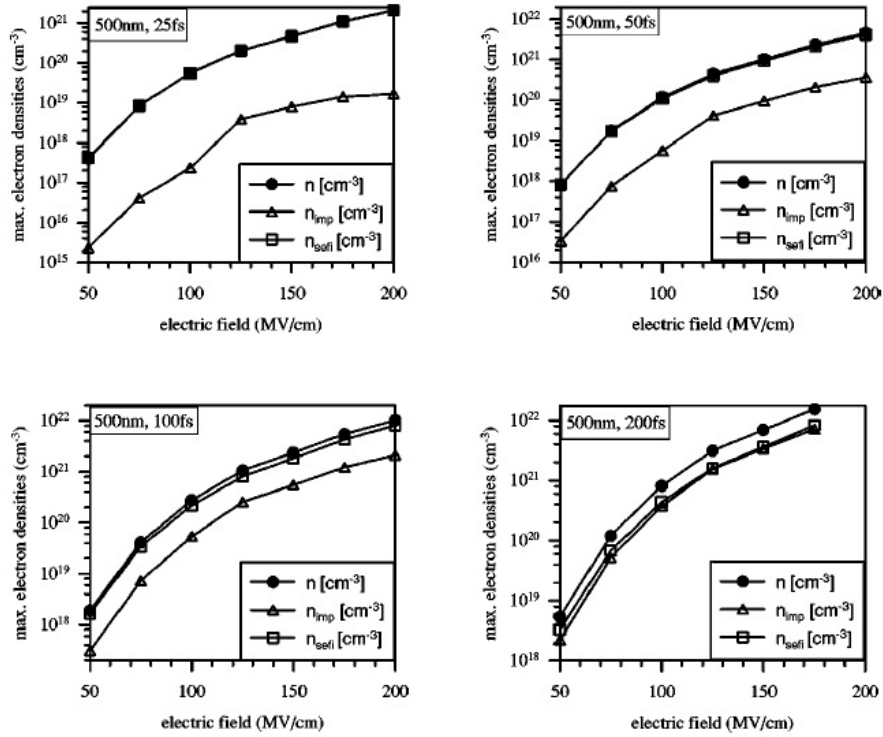


Figure 2.5: Maximum electron density in the conduction band after laser irradiation for varying electric laser fields, together with contributions from the two considered ionization processes for four different laser pulse durations. (from Ref.[16]).

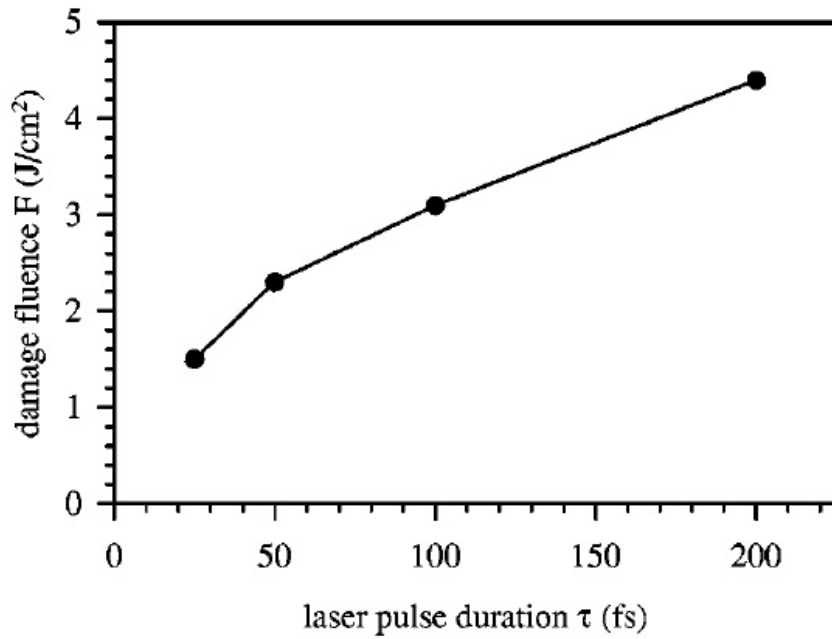


Figure 2.6: Calculated damage threshold values for different pulse durations with an assumed pulse of wavelength 500 nm. (from Ref.[16]).

ionization, impact ionization, is predominant and in what pulse duration range. Dependence of ablation threshold fluence on pulse duration is also measured for certain materials.

2.3 Formation of double layers and ion acceleration

When an intense laser radiation is incident on matter, plasma is formed by the process explained in the above sections where electrons play a crucial role. But apart from their role in the formation of energetic plasma, the electrons are also crucial in determining the energetics of ion expansion. The formed plasma simultaneously starts to expand and at any instant, the density of electrons falls off exponentially towards the vacuum. The heavy ions follow the outgoing electrons thus forming a double layer. This double layer consists of equal but oppositely charged layers. The electric field is much stronger inside the double layer than outside and quasi neutrality is locally violated in both space charge layers. Traditionally this has been treated as a hydrodynamic model and the planar 1D expansion of plasma is treated by assuming that the electrons and the ions are separate fluids with different temperatures [17]. The ions are described in terms of the continuity and momentum equations, while the electrons are assumed to be in isothermal equilibrium with the electron density given by the Boltzmann relation. Introducing the quasi-neutrality condition, $n_e = Zn_i$, where n_e and n_i are the electron and ion densities, respectively, and z is the ion charge number yields,

$$\frac{\partial n_i}{\partial t} + \frac{\partial}{\partial x}(n_i v_i) = 0, \quad (2.21)$$

$$\frac{\partial v_i}{\partial t} + v_i \frac{\partial v_i}{\partial x} = \frac{c^2}{n_i} \frac{\partial n_i}{\partial x}, \quad (2.22)$$

Where v_i is the ion velocity, $c = (zT_e/m_i)^{1/2}$ is the ion acoustic speed, T_e is the electron temperature, and m_i is the ion mass.

A self-similar solution for equations 2.21 and 2.22 is obtained by assuming a space-time dependence of n_i and v_i through the variable $\xi = x/t$. The solutions are:

$$n_i = n_o \exp \left[- \left(1 + \frac{x}{ct} \right) \right], \quad (2.23)$$

$$v_i = c + x/t \tag{2.24}$$

and the electric field accelerating the electric field ,

$$E = \frac{T_e}{ect} \tag{2.25}$$

2.4 Laser Ablation

As mentioned earlier, *laser ablation* is defined as the process of removing macroscopic amounts of matter from the surface of targets by the interaction of laser, where transient or permanent modifications to the material topography takes place. The processes which govern the interaction of ultrashort laser radiation with matter and subsequent removal of macroscopic amounts of material can be a complex interplay between *fast* processes and *slow* processes which one traditionally calls as the *non-thermal* and *thermal* processes respectively. When an ultrashort laser pulse irradiates a solid, ionization takes places by the processes mention in the previous sections. Following ionization, the laser energy is absorbed by the free electrons due to inverse Bremsstrahlung and resonance absorption mechanisms and does not depend on the initial state of the target. Hence the interaction of the radiation with both metals and dielectrics proceeds in the same way. In the following sections we briefly describe the non-thermal and thermal processes.

2.4.1 Nonthermal processes

2.4.1.1 Coulomb explosion (CE)

Coulomb explosion (CE) is an ultrafast nonthermal process responsible for particle emission within few 100s of femtoseconds and occur when parts of the lattice disintegrate when their low mass outer valence electrons responsible for chemical bonding are stripped from atoms, leaving the atoms positively charged. When the charge density is sufficiently large, the repulsive state between atoms whose chemical bonds are broken, explodes into a small cloud of energetic ions having velocities higher than that normally seen in the thermal emission. This is called Coulomb explosion (CE). Fingerprints of Coulomb explosion was noticed in experimental studies on dielectrics [18–21], semiconductors[22, 23] and even in metals[24–27]. The velocities of charged particles emitted from the target following Coulomb explosion is determined by the

repulsive Coulomb forces while neutral particles obtain their velocities by collisions with the fast ions. Besides positive ions, ion clusters, neutral clusters have also been observed [24]. While the process of Coulomb emission happening in dielectrics is not disputed, for semiconductors and metals the subject is still controversial[28]. The occurrence of Coulomb explosion in semiconductors has been debated extensively in the literature[22–24, 29, 30]. Stoian et al[30] model shows that on dielectric surfaces, sufficient charge can be accumulated to initiate Coulomb explosion within 100 fs time scale. In semiconductors and metals, because of the higher electron mobility and higher density of available free electrons, which ensure effective screening, a much smaller net positive charge accumulates, which is not enough by orders of magnitude to induce a macroscopic electrostatic breakup.

2.4.1.2 Femtosecond Field Ion Emission by Surface Optical Rectification

Vella et al[31] have developed a model based on the surface optical rectification effect associated with the nonlinear response of free electrons to explain quantitatively the observations of ultrafast laser assisted field-ion emission from metals. According to the model, THz optical rectification occurs by nearly degenerate difference frequency mixing between the frequency components of an ultra-short pulse in the second order nonlinear optical medium. This process is capable of producing very broadband THz pulses by an intense optical beam. The spectral bandwidth associated with ultrashort pulses is very large and mixing of different frequency components produces a beating polarization, which results in the emission of electromagnetic waves in the terahertz regime. The efficiency of THz generation depends on the second order nonlinear susceptibility of the medium. A direct detection of surface optical rectification is very difficult and an undisputable evidence of its occurrence is still needed.

2.4.1.3 Ultrafast melting (UFM)

An other non-thermal pathway in semiconductors which allows melting within a few femtosecond is *ultrafast melting* [32]. This non-thermal melting process is ascribed to the massive excitation of charge carriers into the conduction band, converting the interatomic forces into antibonding states. It has been experimentally observed that after rapid femtosecond excitation of silicon or germanium the lattice order disappears within about a hundred femtoseconds [33], which has been interpreted as an initial ballistic atom disordering due to the lack of remaining binding forces.

This ultrafast melting is considered to be one important aspect in the laser ablation mechanisms of semiconductors.

2.4.2 Thermal processes

Ablation process that is characterized by the transfer of the energy deposited by the laser beam on the target to the lattice through electron-phonon interactions resulting in lattice heating, melting, and evaporation of the material is defined as thermal ablation process. Within this thermal regime different mechanisms have been proposed to explain laser ablation. Vaporization, boiling and explosive boiling/phase explosion are the most discussed ones. Which process is significant depends on the laser pulse duration and the temperature attained by the focal volume of the target upon laser irradiation. Thermal ablation is the dominant mechanism when the laser pulsewidth is more than the electron-lattice relaxation time. In metals, for such long pulses, the ablated mass can be calculated by [34]:

$$m = \frac{N \cdot E_{pulse}}{c_p \cdot (T_v - T_o) + \Delta H_m + \Delta H_v} \quad (2.26)$$

Where, m is the ablated mass, N is the number of number of laser pulses, E_{pulse} is the pulse energy, c_p is the heat capacity, T_v is the evaporation temperature, T_o is the ambient temperature, ΔH_m is the melting enthalpy and ΔH_v is the evaporation enthalpy.

For ultrashort pulses, the dynamics of laser absorption and ablation mechanisms are totally different. The laser energy is absorbed by the electron subsystem and the energy transfer from the electronic subsystem to the lattice occurs on the picosecond timescale. So the electron subsystem and the lattice develop distinct dynamics that can be described by the two temperature model (TTM)[14]. So for ultrashort laser pulses, the TTM is used to explain the thermal phenomena. Based on this model, Chichkov et al [35] derived a formula for the ablation depth and is given by:

$$m = N \cdot \rho \cdot A \cdot \alpha^{-1} \cdot \ln \left(\frac{F_a}{F_{th}} \right) \quad (2.27)$$

Where, m is the ablated mass, N is the number of laser pulses, ρ is the density, A is the focal spot area, α is the optical penetration depth, F_a is the laser fluence and F_{th} is the threshold fluence for ablation.

2.4.3 The Two temperature model

The two-temperature model (TTM) [14] is a three-dimensional temperature diffusion model that attempts to describe the transport of the laser energy from the electron subsystem to the lattice subsystem of a metal after irradiation with a femtosecond laser pulse. Upon irradiation of a solid with a femtosecond laser pulse, the energy transport mechanism consists of two stages: 1. The absorption of laser energy through photon-electron interactions within the ultrashort pulse duration. It takes a few femtoseconds (called the electron relaxation time) for the electrons to re-establish the Fermi distribution. 2. The energy distribution to the lattice through electron-phonon interactions, which takes typically on the order of tens of picoseconds (called thermalization time). Although the electron-phonon collision time may be comparable to the electron-electron collision time, it takes much longer to transfer energy from free electron to phonons, because the phonon mass is much greater than the electron mass.

Since the time of the energy relaxation within the electron subsystem is much smaller than the time necessary to transfer the energy to the lattice subsystem, the thermal conductivity of the lattice can therefore be neglected on the time scale of the electron-phonon coupling and the electron subsystem and the lattice subsystem are described by two different temperatures: T_e (temperature of electrons) and T_l (temperature of lattice). The temporal and spatial evolution of the electron and lattice temperatures can be estimated by solving the following coupled three-dimensional differential equations:

$$C_e(T_e) \frac{\partial T_e}{\partial t} = \nabla \cdot \{K_e(T_e) \nabla T_e\} - G(T_e) \{T_e - T_l\} + S \quad (2.28)$$

$$C_l(T_l) \frac{\partial T_l}{\partial t} = \nabla \cdot \{K_l(T_l) \nabla T_l\} + G(T_e) \{T_e - T_l\} \quad (2.29)$$

Where C and K are respectively the heat capacity and the thermal conductivity of the electrons (subscript e) and the lattice (subscript l).

G is the electron-phonon coupling factor, and is given by [36]:

$$G = \frac{\pi^2 m_e n_e c_s^2}{6\tau(T_e) T_e} \quad (2.30)$$

Where m_e is the nonrelativistic mass of a free electron; n_e is the density of the free

electron; c_s is the speed of sound in bulk material calculated by:

$$C_s = \sqrt{\frac{B}{\rho_m}} \quad (2.31)$$

Where B is the bulk modulus and ρ_m is the density.

S in Eqn. 1.1 is the laser source term accounting for the energy deposition by the laser and is given by[37]:

$$S(z, t) = \frac{0.94(1 - R)J}{t_p\delta} \exp\left[-\frac{z}{\delta} - 2.77\left(\frac{t}{t_p}\right)^2\right] \quad (2.32)$$

Where R is the reflectivity, J is the laser energy density, t_p is the laser pulse duration, δ is the laser penetration depth.

If the laser spot size is much larger than the depth of the ablated structures, the three-dimensional equations (Eq.2.28 & Eq.2.29) can be reduced to two coupled one dimensional equations, since it can be assumed that all the energy is propagating into the material and not along the surface.

An often applied simplification of the TTM is the assumption of temperature independent heat capacities and a constant electron-phonon coupling factor. However neither the electronic heat capacity C_e nor the electron-phonon coupling factor G are well approximated by a constant.

2.5 Laser Induced Periodic Surface Structures (LIPSS)

While studying the surface damage of semiconductor materials using Ruby laser Birnbaum et.al.,n 1965 [38] have observed that semiconductor materials when irradiated with a laser, produced strikingly periodic structures on the surface. Since then, many researchers studying the interaction of intense laser beams with solids have observed the periodic damage patterns that produce on various surfaces when the fluence of the beam is near the damage threshold. These laser produced periodic structures are commonly referred to as ripples or Laser-induced periodic surface structures (LIPSSs). Since their discovery, this phenomenon was observed on many different types of materials: metals [28, 39–44], semiconductors [44–47] and dielectrics [48–50] and with different lasers having pulse durations from continuous wave to few femtoseconds. It has been observed that when irradiated with a linearly polarized laser beam, the periodicity of the observed ripples was close to the laser wavelength ($\Lambda \approx \lambda$). Such ripples are referred to as low spatial frequency LIPSSs

(LSFLs). Interestingly, when irradiated with femtosecond laser pulses, the periodicity of these ripples, in most cases, is found to be smaller than the wavelength of the incident laser radiation and their orientation is perpendicular to the laser polarization. The spatial characteristics of the formed LIPSSs i.e., periodicity, and orientation depends on the material properties and on the laser parameters (wavelength, fluence, pulse duration, number of pulses, etc). Fig.2.7 shows the geometry of the light incident on a rough surface and the main parameters used to describe LIPSSs and laser parameters. In fact, if the surface has a scratch which is oriented normal to the polarization of a p-polarized beam, two sets of fringes parallel to the scratch with spacing $\lambda(1 + \sin\theta)^{-1}$ and $\lambda(1 - \sin\theta)^{-1}$ are observed, where θ is the angle of incidence of the beam. Apart from these, at large angles of incidence and only with p-polarized light, ripples having a spacing of $\lambda/\cos\theta$ and running parallel to the polarization of the incident light are also produced. Various theories were proposed to explain the formation of these ripples. Emmony et al. suggested that LSFLs were a consequence of interference between the incident laser beam and surface-scattered waves [51]. However, the theory fails to explain few inconsistencies like observed ripple spacing of λ in some materials (eg. GaAs) and λ/n in some materials (eg. NaCl), dependence of the fringe patterns on the polarization of the incident light etc. In 1983 Sipe et al [52] have proposed a theory, called as η theory, or Sipe theory, which predicts a inhomogeneous energy absorption of the linearly polarized electromagnetic plane waves below the material's rough surface. It is assumed that the ripples grow where the absorbed energy is the largest. Some authors termed the Sipe theory to be the most rigorous and comprehensive theory that can explain all the observed LIPSS [53]. In spite of its wide acceptance, the Sipe theory has several limitations and cannot explain all the kinds of LIPSS produced by ultrashort laser-matter interaction.

Another theory that is slowly gaining popularity is the *Self-organization model* which is inspired by the similarity of the laser generated patterns to that produced in nature, for example on a beach, on Mars [54] or that produced on a surface by energetic ions [55]. As per the *self-organization model*, the absorbed laser energy causes a perturbation and softening of the crystal binding, leading to an unstable surface region, which relaxes via self-organization resulting in a spontaneous formation of surface structures in the laser irradiated region. The chain of processes that takes place according to this model are: After a metal is irradiated with an ultrashort laser pulse, the laser light is absorbed by electrons whose temperature increase during the time equal to that of the pulse width of the laser, while the lattice remains at the initial temperature. The thermal equilibrium between electrons and lattice is established in picosecond time scale. The surface then melts and remains in the molten state for

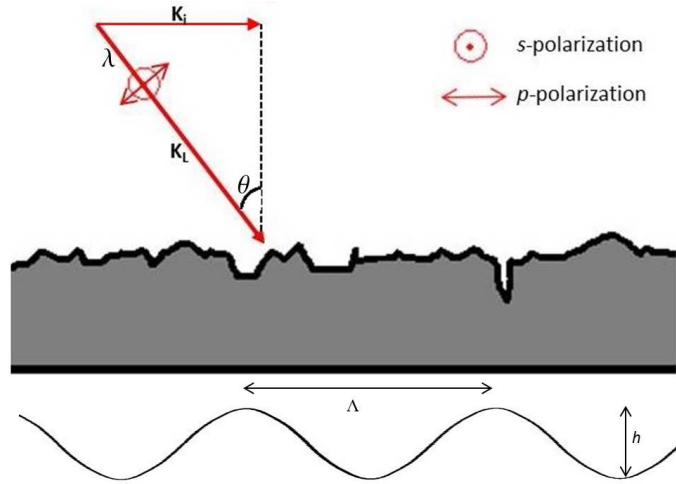


Figure 2.7: Geometry of the light incident on a rough surface and the main parameters used to describe LIPSSs and laser parameters.

upto a nanosecond. During this time, the system relaxes by self-organization and after re-solidification the self-organized ripples are frozen into the surface.

In recent femtosecond laser ablation studies [56, 57, 39], ripples with spatial periods much smaller than wavelengths ($\Lambda \ll \lambda$) with direction either parallel or orthogonal to the polarization were observed. Sipe theory cannot explain the formation of these ripples and the origin of these ripples is still under debate. In the following sections the LSFLs (sec.2.5.1), HSFLs (sec.2.5.2), Sipe theory (sec.2.5.3), and self-organization model (sec.2.5.4) are discussed. Over the last few decades, many groups have published papers reporting LIPSS on many different kind of materials, however, even for a same material, the results reported in the literature vary considerably and cannot be compared because of experimental differences. In this thesis, systematic experiments were conducted to find the dependence of these structures on various laser parameters. The results are presented and discussed in Chapter 4.

2.5.1 LSFLs

As defined in the introduction section, LSFLs are ripples with periodicity Λ close to the laser wavelength, direction orthogonal to the polarization of the laser radiation and height in the range of a few hundreds of nanometers [58, 59]. LSFLs are obtained with continuous wave lasers and pulsed lasers. When pulse lasers are used, several pulses (30 - 100 pulses) are needed to clearly see the LSFLs. LSFLs are observed when the sample is stationary or when moved such that several pulses overlap partially. Thus LSFLs can be produced over any length.

The LIPSS patterns formed on a material can be complex and a convenient way

Table 2.1: Literature survey of LSFLs reported on different type of materials upon laser pulse irradiation. Class of Material: M - metal, S - semiconductor, D - dielectric. \parallel - aligned parallel to laser polarization, \perp - ripples aligned perpendicular to laser polarization.

Material	Class	Pulse duration	Periodicity Λ_{LSFLs} (nm)	Orientation	References
Melted quartz	M	ns	$\approx 0.71\lambda$	\perp	[41]
Al	M	fs	$\approx 0.66\lambda$	\perp	[42]
Au	M	fs	$\approx 0.74\lambda$	\perp	[40]
Cu	M	fs	$\approx (0.64 - 0.9)\lambda$	\perp	[28]
Pt	M	fs	$\approx (0.70 - 0.79)\lambda$	\perp	[40]
Pt	M	fs	$\approx (0.77 - 0.89)\lambda$	\perp	[43]
Ti	M	fs	$\approx (0.65 - 0.86)\lambda$	\perp	[44]
Ti	M	fs	$\approx (0.64 - 0.89)\lambda$	\perp	[43]
Ti	M	fs	$\approx (0.78 - 0.9)\lambda$	\perp	[39] (this work)
Si	S	ns	$\approx 0.94\lambda$	\perp	[45]
Si	S	fs	$\approx (0.72 - 0.98)\lambda$	\perp	[44]
InP	S	fs	$\approx (0.75 - 0.96)\lambda$	\perp	[46]
GaP	S	fs	$\approx (0.66 - 0.87)\lambda$	\perp	[47]
Diamond	D	fs	$\approx 0.96\lambda$	\perp	[48]
BaF_2	D	fs	$\approx (0.77 - 1.15)\lambda$	\parallel	[49]
Al_2O_3	D	fs	$\approx 95\lambda$	\perp	[50]

to study their properties is to characterize the patterns in the frequency domain. J.F.Young et.al., [60] used a simple method to study the formed LIPSS in the frequency domain. They analyzed the diffraction pattern produced by an Ar^+ beam upon reflection from the surface containing the LIPSSs.

The periodicity and orientation of the LSFLs depend on several parameters such as incident angle, laser fluence, number of laser pulses, polarization of the laser beam and the laser pulse duration. The angle of incidence of the laser beam has a strong influence on the periodicity and orientation of LSFLs. For p-polarized laser radiation, two sets of periodicities are observed in the direction orthogonal to the laser beam for angle of incidence, $\theta \lesssim 45^\circ$, given by $\Lambda = \lambda/(1 \pm \sin\theta)$ [60]. For larger angles of incidence, LIPSS patterns are formed parallel to the polarization and the periodicity is given by $\Lambda = \lambda/\cos\theta$. However, for s-polarized laser radiation, the periodicity $\Lambda = \lambda/\cos\theta$ for $\theta \lesssim 45^\circ$ [60]. For larger angles of incidence, the LIPSS pattern is neither parallel nor orthogonal to the polarization. Another parameter that has strong influence on the periodicity is the number of pulses N , incident on the surface. The periodicity of LSFLs decreases with increasing number of pulses and the rate of this decrease is material dependent [39, 61, 62, 40]. Table 2.1 provides a literature survey on the spatial periods and orientation with respect of laser polarization of LSFLs in various materials.

2.5.2 HSFLs

HSFLs are defined as LIPSSs with a periodicity Λ significantly smaller than the laser wavelength λ . HSFLs are reported to be produced on metals, semiconductors and dielectrics with their orientation either parallel or perpendicular to the laser polarization. HSFLs are reportedly developed only with pulsed lasers with pulse durations in the picosecond/femtosecond regime. Due to their distinct properties compared to LSFLs, the mechanism responsible for their formation could be different to that of LSFLs formation and their origin is still under debate. Though there were studies to characterize the dependence of HSFLs properties on laser parameters, a systematic study was missing. In this work we characterized in detail the HSFLs dependence on laser fluence, pulse number, pulse duration, and polarization. The results are discussed in Chapter 6.

2.5.3 Sipe Model

J.E. Sipe et.al., have developed a theory in 1983 [52] to explain the formation of laser-induced periodic surface structures by associating each Fourier component of induced structure with the corresponding Fourier component of inhomogeneous energy deposition just beneath the surface. It was assumed that the surface roughness is confined to a region of height much less than the wavelength of light, and is responsible for the symmetry breaking leading to inhomogeneous deposition of energy. The model estimates strong peaks in energy deposition in Fourier space which leads to predictions of induced fringe patterns with spacing and orientation dependent on the angle of incidence and polarization of the incident beam. The model results show that the induced structures depend on the two parameters, shape and filling factors, introduced to characterize surface roughness, in case of p -polarized beam but essentially independent of these parameters in case of s -polarized beam.

The efficacy factor is defined as:

$$\boldsymbol{\eta}(\mathbf{k}, \mathbf{k}_i) = 2\pi|v(\mathbf{k}_+) + v^*(\mathbf{k}_-)| \quad (2.33)$$

For the two cases of s and p -polarized light, incident under an angle of θ and having polarization vectors and a wave vector component \mathbf{k}_i , as shown in the Fig.2.7, the complex function v is given by:

$$v(\mathbf{k}_\pm, s - pol.) = [h_{ss}(k_\pm)(\hat{\mathbf{k}}_\pm \cdot \hat{\mathbf{y}})^2 + h_{kk}(k_\pm) \times (\hat{\mathbf{k}}_\pm \cdot \hat{\mathbf{x}})^2] \gamma_t |t_s(\mathbf{k}_i)|^2, \quad (2.34)$$

$$\begin{aligned}
 v(\mathbf{k}_\pm, p-pol.) = & [h_{ss}(k_\pm)(\hat{\mathbf{k}}_\pm \cdot \hat{\mathbf{x}})^2 + h_{kk}(k_\pm) \times (\hat{\mathbf{k}}_\pm \cdot \hat{\mathbf{y}})^2] \gamma_t |t_x(\mathbf{k}_i)|^2 \\
 & + h_{kz}(k_\pm) * \times (\hat{\mathbf{k}}_\pm \cdot \hat{\mathbf{y}}) \gamma_z \varepsilon t_x^*(\mathbf{k}_i) t_z(\mathbf{k}_i) \\
 & + h_{zk}(k_\pm) \times (\hat{\mathbf{k}}_\pm \cdot \hat{\mathbf{y}}) \gamma_t t_x(\mathbf{k}_i) t_z^*(\mathbf{k}_i) \\
 & + h_{zz}(k_\pm) \gamma_z \varepsilon |t_z(\mathbf{k}_i)|^2
 \end{aligned} \tag{2.35}$$

with the inner products

$$(\hat{\mathbf{k}}_\pm \cdot \hat{\mathbf{y}}) = (\sin\theta \pm \kappa_y) / \kappa_\pm \tag{2.36}$$

$$(\hat{\mathbf{k}}_\pm \cdot \hat{\mathbf{x}}) = \kappa_x / \kappa_\pm \tag{2.37}$$

where,

$$\kappa_\pm = \sqrt{\kappa_x^2 + (\sin\theta \pm \kappa_y)^2} \tag{2.38}$$

$$h_{ss}(\kappa_\pm) = \frac{2i}{\sqrt{1 - \kappa_\pm^2} + \sqrt{\varepsilon - \kappa_\pm^2}} \tag{2.39}$$

$$h_{kk}(\kappa_\pm) = \frac{2i\sqrt{(\varepsilon - \kappa_\pm^2)(1 - \kappa_\pm^2)}}{\varepsilon\sqrt{1 - \kappa_\pm^2} + \sqrt{\varepsilon - \kappa_\pm^2}} \tag{2.40}$$

$$h_{kk}(\kappa_\pm) = \frac{2i\kappa_\pm\sqrt{\varepsilon - \kappa_\pm^2}}{\varepsilon\sqrt{1 - \kappa_\pm^2} + \sqrt{\varepsilon - \kappa_\pm^2}} \tag{2.41}$$

$$h_{zk}(\kappa_\pm) = \frac{2i\kappa_\pm\sqrt{1 - \kappa_\pm^2}}{\varepsilon\sqrt{1 - \kappa_\pm^2} + \sqrt{\varepsilon - \kappa_\pm^2}} \tag{2.42}$$

and

$$h_{zz}(\kappa_\pm) = \frac{2i\kappa_\pm^2}{\varepsilon\sqrt{1 - \kappa_\pm^2} + \sqrt{\varepsilon - \kappa_\pm^2}} \tag{2.43}$$

The complex functions t_s , t_x , and t_z are given by:

$$t_s(\mathbf{k}_i) = \frac{2|\cos\theta|}{|\cos\theta| + \sqrt{\varepsilon - (\sin\theta)^2}} \tag{2.44}$$

$$t_x(\mathbf{k}_i) = \frac{2\sqrt{\varepsilon - (\sin\theta)^2}}{\varepsilon|\cos\theta| + \sqrt{\varepsilon - (\sin\theta)^2}} \quad (2.45)$$

and

$$t_z(\mathbf{k}_i) = \frac{2\sin\theta}{\varepsilon|\cos\theta| + \sqrt{\varepsilon - (\sin\theta)^2}} \quad (2.46)$$

The surface roughness is included in the theory in the factors γ_t and γ_z via two numerical factors, s (shape factor) and f (filling factor) by:

$$\gamma_t = \frac{\varepsilon - 1}{4\pi\{1 + (\frac{1}{2})(1 - f)(\varepsilon - 1)[F(s) - R \times G(s)]\}} \quad (2.47)$$

$$\gamma_z = \frac{\varepsilon - 1}{4\pi\{\varepsilon - (1 - f)(\varepsilon - 1)[F(s) - R \times G(s)]\}} \quad (2.48)$$

with $R = (\varepsilon - 1)/(\varepsilon + 1)$ and the scalar functions

$$F(s) = \sqrt{s^2 + 1} - s \quad (2.49)$$

and

$$G(s) = \left(\frac{1}{2}\right) \left(\sqrt{s^2 + 4} + s\right) - \sqrt{s^2 + 1} \quad (2.50)$$

Using Eqs.2.39 to 2.56, it is possible to calculate numerically the efficacy factor $\boldsymbol{\eta}$ as a function of the normalized LIPSS wave vector components κ_x, κ_y for any given values of incidence angle θ , wavelength of the incidence radiation λ , polarization direction, optical dielectric constant ε and the surface roughness properties (s and f). Fig.2.8 shows the calculated $\boldsymbol{\eta}$ plots for various incidence angles for s-polarized beam. The patterns obtained by the model are consistent with the experimentally observed diffraction patterns (for ex. see[60]).

2.5.3.1 Sipe Model : Strengths, limitations and updates

In this section the strengths and limitations of Sipe theory are summarized. To overcome the limitations several modifications/updates were made to the theory. These updates are also discussed briefly.

1. Sipe theory could for the first time quantitatively explain the periodicity ($\Lambda \leq \lambda$), orientation, and angle dependence of the observed LSFLs.
2. The rigorous treatment of Maxwell's equations lead to the inclusion of not only the surface electromagnetic waves (SEW) generated on the rough surface but also

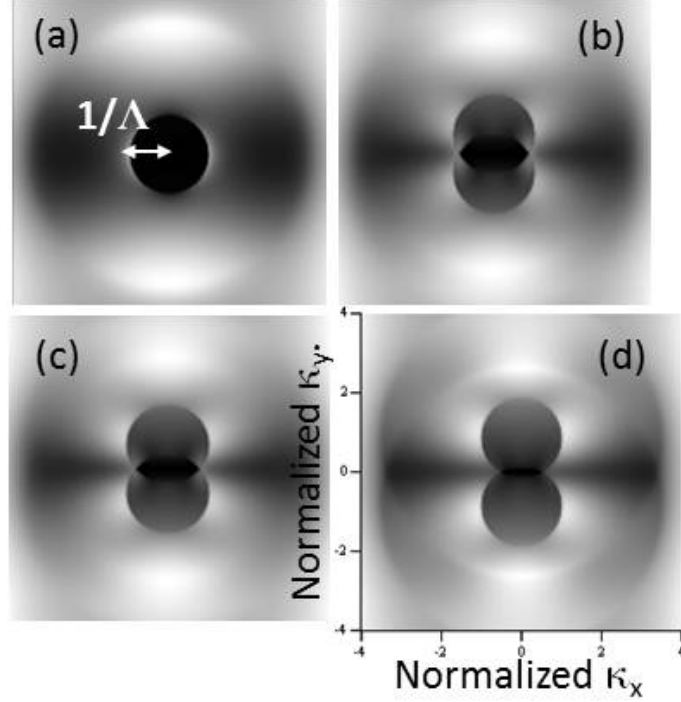


Figure 2.8: Grayscale map of the efficacy factor η for different incidence angles: (a) 0° (b) 30° (c) 40° (d) 60° for s-polarized radiation.

excitation of surface plasmon polaritons (SPP).

3. The theory fails to explain the observed HSFLs ($\Lambda \ll \lambda$), ripples with periodicity greater than the wavelength ($\Lambda > \lambda$) and the dependence of periodicity on fluence and number of pulses.

4. The Sipe model considered light-matter interaction in the framework of linear optics and the optical dielectric function was considered to be a constant. Under the influence of ultrashort laser radiation there would be transient changes in the optical properties of the material and so the dielectric function cannot be taken as a constant. To overcome this, Bonse et al [63] modelled the optical properties of the material using Drude model in order to account for the transient changes in the optical properties. As per this model, the complex dielectric function is given by:

$$\tilde{\epsilon}^* = \tilde{\epsilon} + \tilde{\epsilon}_{Drude} \quad (2.51)$$

Where, $\tilde{\epsilon}^*$ is the complex dielectric constant of the non-excited material and $\tilde{\epsilon}_{Drude}$ is the contribution from the Drude model and is given by :

$$\tilde{\epsilon}_{Drude} = - \left(\frac{\omega_p}{\omega} \right)^2 \frac{1}{1 + i \frac{1}{\omega \tau_D}} \quad (2.52)$$

Where, $\omega_p = \sqrt{N_e e^2 / \epsilon_0 m_{opt}^* m_e}$ is the plasma frequency with e , the electron charge, N_e the carrier density, ϵ_0 , the vacuum dielectric permittivity, m_{opt}^* the optical ef-

fective electron mass and m_e the free electron mass, τ_D the Drude damping time accounting for $e - e$ and $e - h$ scattering.

5. Several authors attributed the excitation of surface plasmon polaritons as the reason for the periodic enhancement of local fields in the surface layer [63–66]. By considering the formation of SPPs and following the Sipe model, an expression for periodicity has been derived as [66]:

$$\Lambda = \frac{\lambda_{laser}}{\eta \pm \sin\theta} \quad (2.53)$$

Where, λ_{laser} is the wavelength of laser radiation, θ is the angle of incidence, and $\eta = \Re e [\tilde{\epsilon}_m \tilde{\epsilon}_d / (\tilde{\epsilon}_m + \tilde{\epsilon}_d)]^{1/2}$. However, some authors have argued that the excitation of the surface plasmons is impossible in the laser ablation experiments, since the excitation conditions are not fulfilled [67]

2.5.4 Self-organization model

The *Self-organization model* is inspired by the similarities seen between the structures produced on a surface by ultrafast laser irradiation and for example, of structures produced by energetic ion beam sputtering [55]: Bifurcation of ripples, periodicity of produced ripples, dependence of periodicity on laser fluence (ion beam energy) and number of laser pulses (ion beam irradiation time), co-existence of LSFLs and HSFLs, abrupt period doubling near threshold, and strong positive feedback in the development process, all indicate in the direction that the physical mechanism of ripple formation is the same in laser induced structuring and like in ion beam sputtering technique. Patterns are formed when a system is driven into an instability and the nonlinear mechanisms that take place in the system for it to move towards a new stable state results in a pattern formation ([68] and references therein).

Figure 2.9 shows the schematic of the self-organization model. A femtosecond laser beam induces a high degree of instability at the surface, perturbing the irradiated area. The perturbed surface relaxes through reorganization that leads to formation of self-organized patterns in the laser irradiated region.

Figure 2.10 explains the formation process of a thin corrugulated layer on the surface of an irradiated target upon multiple ultrashort laser pulses. When a laser beam hits the surface of a plain target, a stochastic charge distribution establishes on the surface and hence ions are emitted from randomly located sites, resulting in the creation of local defects. A higher probability of absorption in the defect sites

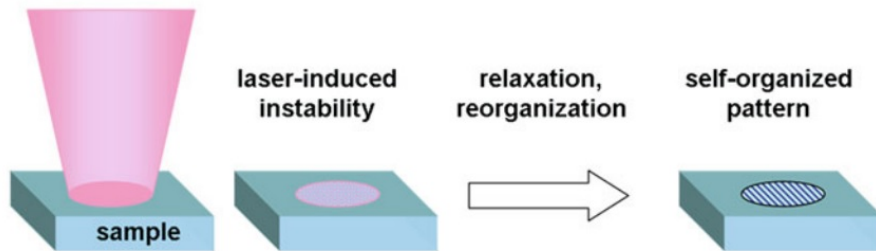


Figure 2.9: Schematic of *self-organization model*. A femtosecond laser beam induces a high degree of instability in the region of irradiation. The perturbed surface relaxes through reorganization that leads to the formation of self-organized patterns in the laser irradiated region (figure taken from ref. [68])

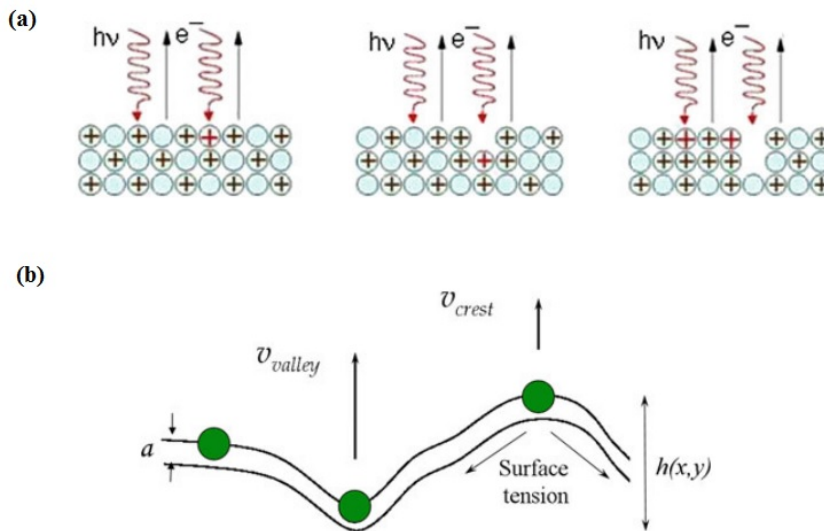


Figure 2.10: (a) Development of a corrugated surface layer upon multiple laser irradiation. (b) Model for surface height evolution: a is the thickness and $h(x,y)$ is the modulation height of an unstable surface film induced upon repetitive laser irradiation. Velocities of the desorbed ions from the valley (v_{valley}) and from the crest (v_{crest}) are indicated with arrows. (figure taken from ref. [68])

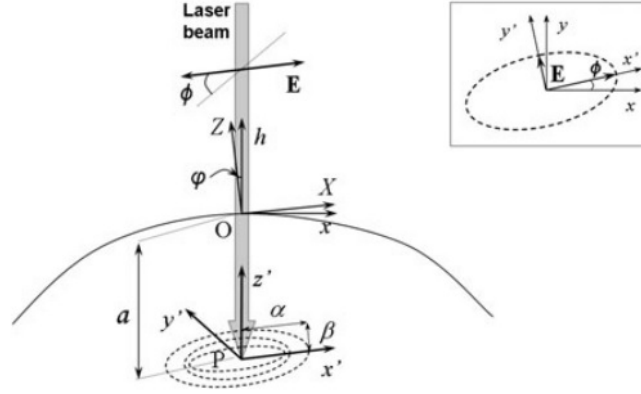


Figure 2.11: Geometry of the Self-organization model. Reference frames for the computation of the erosion velocity: (x', y', z') in the reference frame of the incoming beam. x' is parallel to the vector E of the electromagnetic field; (X, Y, Z) corresponds to the local coordinate frame, where Z is parallel to the local normal to the surface, while (x, y, h) denotes the laboratory frame of coordinates with h perpendicular to the flat substrate surface. The dotted ellipse is a Gaussian distribution of deposited energy with half-width α, β along x', y' , respectively. The energy distribution along z' with half-width γ is not shown here. ϕ is the angle between the local and the laboratory reference frames (corrugation) and denotes the local incidence angle; ϕ is orientation of E in the plane of incidence (x, y) . Inset View from top along h . (figure taken from ref.[68])

will result in a progressively inhomogeneous surface ionization during the next laser pulses. After several laser pulses, a modulated thin surface film of thickness a and modulation height $h(x, y)$ builds up as shown in Fig.2.10(b). Absorption becomes homogeneous while desorption is not homogeneous and depends on local surface-curvature. The escape velocity of valley-ions, (V_{valley}) becomes larger, compared to that from crests, (V_{crest}) , so valleys will be eroded faster than crests. This causes instability in the thin surface. Balancing the surface erosion processes, thermally activated self-diffusion tends to smooth the surface again by filling the valleys with diffused crest-atoms. Moreover, the tension gradient forces the particles to move downhill and thereby balance the instability on the surface.

In this model, the physics of pattern formation is described within the theoretical framework of nonlinear dynamics. Spatial and temporal evolution of the perturbed system is represented by nonlinear partial differential equations like Kuramoto-Sivashinsky/Kardar-Parisi-Zhang type [69–71]. The solution of such equations with corresponding boundary conditions results in periodic pattern formation. The geometry of the model is illustrated in the Fig.2.11 and the equation that describes the time evolution of the surface profile $h(x, y, t)$ is given by equation 2.54, known as an anisotropic noisy Kuramoto-Sivanshinsky equation:[69, 70].

$$\begin{aligned}
 \frac{\partial h}{\partial t} = & -\mathcal{V}_0 + \mathcal{V}_x \frac{\partial^2 h}{\partial x^2} + \mathcal{V}_y \frac{\partial^2 h}{\partial y^2} + \mathcal{V}_{xy} \frac{\partial^2 h}{\partial x \partial y} + \frac{\lambda_x}{2} \left(\frac{\partial h}{\partial x} \right)^2 \\
 & + \frac{\lambda_y}{2} \left(\frac{\partial h}{\partial y} \right)^2 + \frac{\lambda_{xy}}{2} \left(\frac{\partial h}{\partial x} \right) \left(\frac{\partial h}{\partial y} \right) \\
 & - K \Delta^2 (\Delta^2 h) + \eta(x, y, z)
 \end{aligned} \tag{2.54}$$

Where, $\eta(x, y, z)$ is the statistical fluctuations of initial surface roughness and the coefficients are given by the following equations for the case of normal incidence.

$$\begin{aligned}
 \mathcal{V}_x &= -\frac{Fa}{2\gamma} \left(\frac{\alpha^2}{\gamma^2} \cos^2 \phi + \frac{\beta^2}{\gamma^2} \sin^2 \phi \right), \\
 \mathcal{V}_y &= -\frac{Fa}{2\gamma} \left(\frac{\alpha^2}{\gamma^2} \sin^2 \phi + \frac{\beta^2}{\gamma^2} \cos^2 \phi \right), \\
 \mathcal{V}_{xy} &= -\frac{Fa}{2\gamma} \left(\frac{\alpha^2}{\gamma^2} + \frac{\beta^2}{\gamma^2} \right) \sin 2\phi, \\
 \lambda_x &= -\frac{F}{\gamma} \left[1 + \left(\frac{\alpha^2}{\gamma^2} - 1 \right) \left(\frac{\alpha^2}{\gamma^2} \cos^2 \phi + \frac{\beta^2}{\gamma^2} \sin^2 \phi \right) \right], \\
 \lambda_y &= -\frac{F}{\gamma} \left[1 + \left(\frac{\alpha^2}{\gamma^2} - 1 \right) \left(\frac{\alpha^2}{\gamma^2} \sin^2 \phi + \frac{\beta^2}{\gamma^2} \cos^2 \phi \right) \right], \\
 \lambda_{xy} &= -\frac{F}{\gamma} \left(\frac{\alpha^2}{\gamma^2} - 1 \right) \left(\frac{\beta^2}{\gamma^2} - \frac{\alpha^2}{\gamma^2} \right) \sin 2\phi, \\
 \mathcal{V}_0 &= \frac{F}{\gamma} \text{ and} \\
 F &= \frac{I_0 \xi A}{\sqrt{2\pi}} \exp \left(\frac{\alpha^2}{2\gamma^2} \right).
 \end{aligned} \tag{2.55}$$

Surface patterns obtained by numerical integration of equation.2.55 (Fig.2.12(a-d)) for various ϕ describing the orientation of the laser electric field \mathbf{E} in the plane of incidence (x,y) are in excellent agreement with those obtained experimentally (Fig.2.12(e-h)).

2.6 Conclusion

In this chapter we detailed the mechanisms that occur when an ultrashort laser pulse irradiates a material. The initial processes that take place depend on the type of material: metal, semiconductor and dielectric. However once ionized, the further mechanisms does not depend on the initial state of the target and the interaction

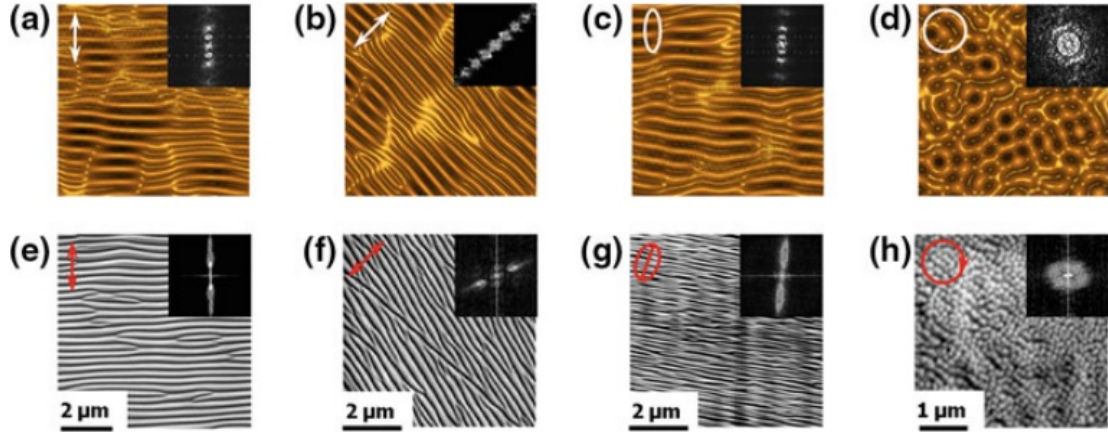


Figure 2.12: The upper panel shows the numerically calculated surfaces using Eqn.2.55, showing surface morphologies for different polarizations as indicated by the white arrow. The bottom panel shows the patterns produced on CaF_2 after irradiated it by 5000 pulses of intensity $8TW/cm^2$. The red-arrows indicate the polarization. (figure taken from ref. [68])

with both metals, semiconductors and dielectrics proceed in a similar way. In this dissertation, we tried to investigate and identify the type of physical processes that take place when an ultrashort laser pulse of duration 10 fs to 550 fs is used to ablate metals and semiconductor targets. We used a reflectron-type of mass spectrometer for this. The results are detailed in chapter 4.

When a laser, particularly an ultrashort laser, irradiates a target, various kinds of structures are formed (grooves, conical structures, periodic structures of high and low frequency, scaffold kind of structures etc). Despite of two decades of research it is modest to say that the mechanism that are responsible for the formation of these structures are still under debate. We discussed the two promising models that try to explain the formation of the periodic structures. A systematic experimental study was done to characterize the properties of the formed periodic structures and their dependence on various laser parameters, in an attempt to identify the mechanisms that are responsible for these structure formation.

Chapter 3

Experimental Setup

In the works presented in this thesis, the interaction mechanisms leading to ablation of materials and structuring of materials upon incidence of ultrashort pulses of 10 fs to 550 fs duration is studied. Emphasis was on the pulse duration dependence of various processes that occur when an ultrashort laser pulse is irradiated on metals, semi-conductors or dielectrics. This chapter describes the experimental setups used in general. The other relevant specifics of the experimental parameters are given at appropriate places in the next chapters where the results are discussed. The experimental setups are different for different experiments conducted, but broadly, each experimental setup can be divided into three parts: (i) the laser source(s) with relevant diagnostics, (ii) optical set-up, which steers the beam to the target, the target along with the associated motion control, and (iii) the detection system where experimentally measured parameters are obtained. The laser systems used for the works presented here are described in section 3.1. There we briefly describe the technique of generating ultra-short laser pulses, the typical laser parameters and the diagnostics used to characterize the femtosecond laser pulses. In section 3.2 the various setups used for different experiments, the targets used, the details of the vacuum chamber, and the motion control are described along with the layouts. In section 3.3 the details about the detection system where the experimentally measured parameters are obtained, is discussed. In case of post-exposure studies, the relevant diagnostic tools used to study the exposure are discussed.

The targets used in all the experiments that are discussed in the present thesis are metals, semiconductors and bio-polymers. A significant portion of this thesis deals with the measurements of ions and neutrals emission using time of flight mass spectrometer. Emphasis was put on to measure the dependence of ions/neutrals emission on fluence and pulse duration of ultrashort pulses.

3.1 The laser system and diagnostics

Different kinds of Ti:sapphire-based laser systems were used for the works presented in this thesis: Oscillators (500 mW, 80 MHz, 10 fs), extended cavity oscillators (800 nJ, 4 MHz, 50 fs) and amplifiers (800 μ J, 1 KHz, 30 fs). The laser beams used for most part of the works presented in this thesis were extracted from two multipass Ti:Sapphire amplifier systems (Femtopower Pro, Femtolasers Produktions GmbH), which will be referred to as 'Amplifier 1' and 'Amplifier 2' in this thesis. The two amplifiers are identically similar, except for that the 'Amplifier 1' has a Dazzler installed in it for pulse shaping to reduce the gain narrowing in the amplifier and achieve shorter pulses. The two amplifiers were seeded by a common chirp-mirror based Ti:Sapphire oscillator (FemtoSource Pro; FemtoLasers Produktions GmbH). For this the beam from the oscillator is split into two beams by a beam splitter. Two thirds of the power was used for seeding 'Amplifier 1' and the other third of the power is used to seed 'Amplifier 2'.

3.1.1 Femtosecond laser oscillator

To generate electromagnetic energy in femtosecond durations, an extremely broad bandwidth spectrum is necessary. Titanium doped sapphire is an excellent broadband laser material available which supports bandwidth of ≈ 100 THz. However, exploiting a substantial part of this bandwidth became possible only after the discovery of Kerr-lens mode locking (or self-mode locking) [72] technique. The refractive index experienced by a Gaussian beam is greater in the center of the beam than at the edges. Hence the laser medium acts as a lens for high intensity light. Thus in a cavity with active Kerr medium, short bursts of light will be focused differently from continuous waves. To favour pulsed mode over cw, a hard aperture can be introduced inside the cavity which the beam must pass in each resonator round trip. Kerr lensing will introduce losses to cw beam at the aperture while the high intensity beam passes through the aperture without losses. Another way is to introduce a soft aperture inside the gain medium. This can be done by carefully designing the cavity to overlap the pumped region of the gain medium with the pulsed beam. Both techniques will initiate the modelocking mechanism. However because of various elements inside the cavity, a positive group delay dispersion (GDD) is introduced in the cavity which needs to be compensated by additional negative GDD scheme. For a long time, a pair of Brewster-angled prisms were used as a source of negative GDD in the cavity [73, 74] and dispersion-controlled self-modelocked Ti:sapphire lasers were put into operation. It was soon realised that

the bandwidth $\Delta\nu_{GDD}$ over which the overall negative GDD is approximately constant, is very critical on system performance. The highly dispersive SF 10 prisms used in the first demonstrations and commercial oscillators typically limits $\Delta\nu_{GDD}$ to less than 10 THz due to strong third order dispersion of the prism pair itself. By substituting the SF-10 prisms with fused-silica prisms, which introduced the lowest third-order dispersion, allowed to achieve nearly ideal, bandwidth-limited, secant-hyperbolic pulses as short as 15 fs. Pulses slightly below 10 fs can be achieved with prism pair but only at the expense of pulse quality characterized by time-bandwidth product of ≈ 0.6 . Another problem using prism pair for dispersion compensation is the increased sensitivity to alignment. A small cavity realignment necessitates subsequent readjustment of the prism position and orientation to compensate for the glass path length inside the prism. Addressing these drawbacks, Szipöcs et.al., have introduced chirped multilayer mirrors for dispersion control which can exhibit constant negative GDD over a frequency range as broad as 80 THz [75]. Chirped mirrors or dispersion-controlled mirrors are essentially modified quarter-wave dielectric mirrors in which the multilayer period is modulated across the mirror structure, creating a wavelength-dependent optical field penetration depth. With careful design, higher-order contributions to the mirror phase dispersion is kept low or chosen in such a way that high-order phase errors introduced by other cavity components are cancelled. Using this Mirror-dispersion controlled (MDC) scheme Stingl et.al., have demonstrated bandwidth-limited, secant-hyperbolic pulses from a Ti:sapphire oscillator with pulse durations as low as 8 fs, and a time-bandwidth product of 0.38 [3].

The oscillator used in the experiments presented here is a mirror dispersion- controlled, self modelocked (Kerr-lens) Ti:sapphire oscillator (FemtoSource Pro; FemtoLasers Produktions GmbH). It is pumped by a Continuous-wave (CW) 5 W frequency doubled, diode pumped Nd:YVO₄ laser ("Verdi", Coherent Inc) and delivers pulses with spectral width greater than 100 nm at a repetition rate of 80 MHz with an output power of $\approx 500mW$. With proper dispersion compensation after the oscillator, sub-10 fs pulses can be extracted. However, since the oscillator pulses are anyway needed to be stretched in the amplifier for further amplification, they were not compensated.

3.1.2 Femtosecond laser amplifier

Typical modelocked oscillators like the one described above provide ultra-short pulses of few nanoJoules energy. For many applications pulses with higher peak powers are required. Amplifiers can boost the peak powers of the seed beam using

the same broadband gain medium as the seed laser. However, the high peak powers in such an amplifier can damage the optical components in the amplifier. To avoid optical damage and nonlinear effects in the amplifier, Mourou et.al., have proposed chirped pulse amplification technique [2], where the peak power of the seed pulses are reduced by pulse broadening (chirped). The chirped pulses are amplified using multi-pass configuration in a gain medium (Ti:sapphire) pumped by a pulsed (typically 1 KHz to 10 KHz) green laser. The amplified pulses are subsequently compressed in a compressor.

In our case, the broadband (FWHM >100 nm)), 80 MHz pulse train from the mirror-dispersion controlled Ti: sapphire oscillator "FemtoSource Pro" is seeded to a multipass amplifier "Femtopower PRO, Femtolasers Produktions GmbH", which is a 1 kHz repetition rate, multi-pass titanium-sapphire amplifier, based on a modified version of the chirped-pulse amplification scheme. Fig. 3.1 and Fig. 3.2 show the functional block diagram and the schematic of the multi-pass amplifier. It consists of a (i) stretcher (ii) an amplification unit and (iii) a compressor. These three units are briefly described in the following sub-sections.

3.1.2.1 Stretcher

In the original "chirp-pulse amplification" set-up demonstrated by Mourou et.al., pulse stretching was accomplished by a pair of gratings. In the amplifier we used (Femtopower-PRO, Femtolasers Produktions GmbH), a modified scheme of "chirp-pulse amplification" was used, wherein pulse stretching was accomplished by introducing a 10-cm-long block of heavy flint-glass (SF57). This glass block along with other system components like Faraday isolator, Pockels cell, wave plates and polarizers introduces a small amount of dispersion and thanks to the large bandwidth spectrum, the seed pulses are stretched to a duration of ~ 5 ps after passing through these optical components. This stretching factor of around ≈ 500 is enough to avoid damage while amplifying the seed pulse energies to ≈ 1 mJ per pulse at 1 KHz.

3.1.2.2 Amplification

Pulses from the stretcher are fed into the amplification unit which consists of a Brewster-cut 2.5 mm long titanium sapphire crystal, two curved mirrors (AFM1 & APM7), and two retroreflectors (ARR1A/B & ARR2A/B) placed in a multi-pass arrangement as shown in Fig. 3.2. The highly doped 2.5 mm long Ti: sapphire crystal is placed in a vacuum chamber and is thermo-electrically cooled down to -15 °C to reduce the effect of thermal lensing. One of the retroreflectors is made up of two

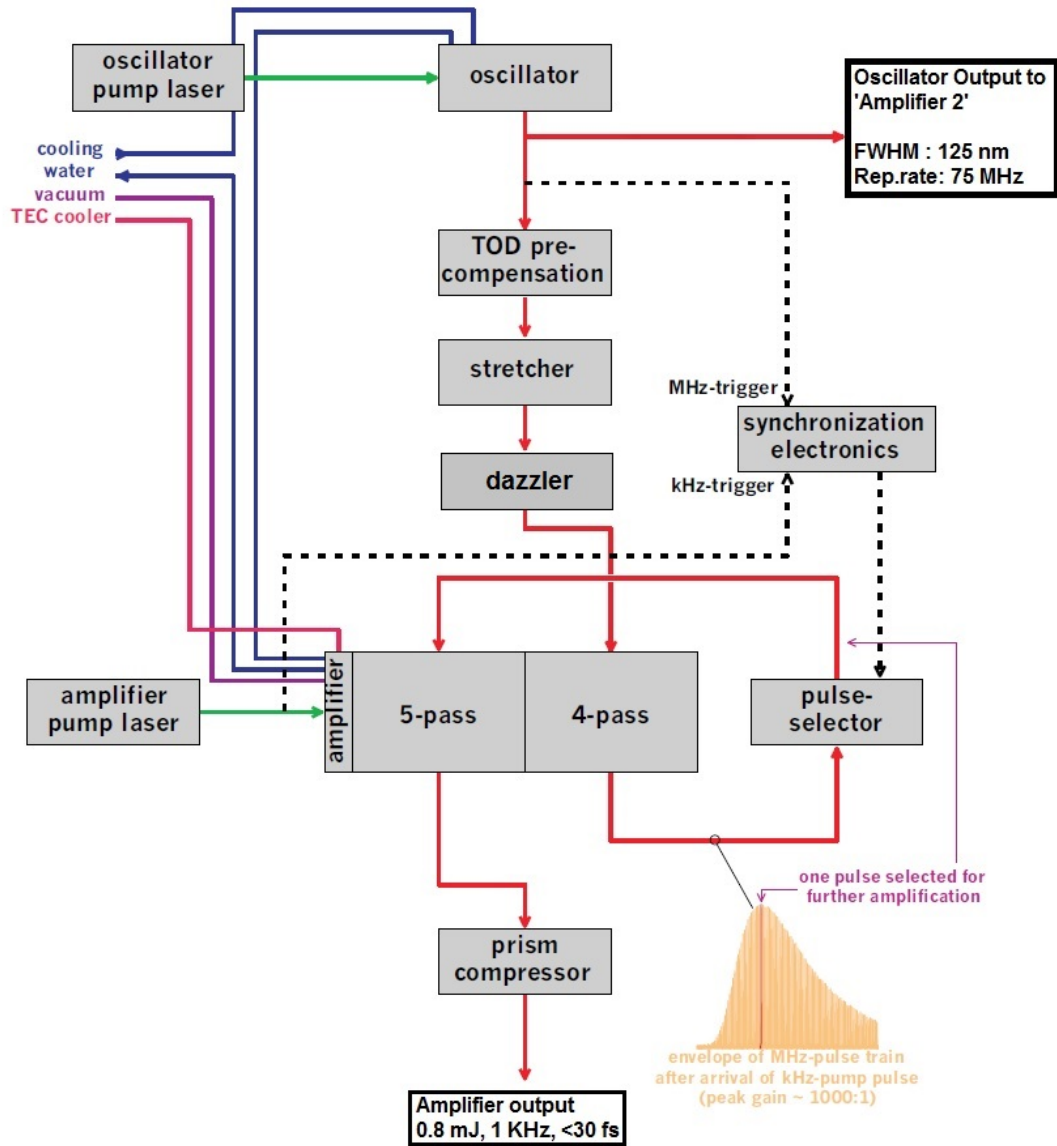


Figure 3.1: Functional block diagram of the Ti:sapphire amplifier "Femtopower-PRO, Femtolasers Produktions GmbH"

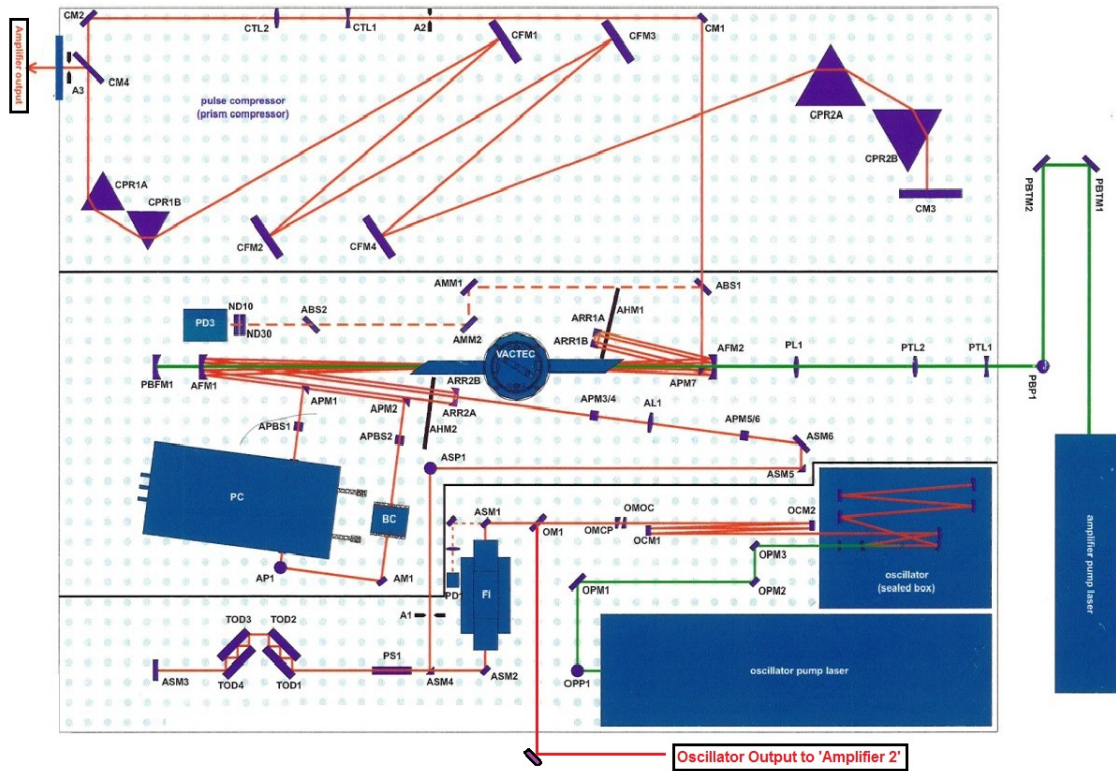


Figure 3.2: Schematic diagram of the Ti:sapphire amplifier "Femtopower-PRO, Femtolasers Produktions GmbH"

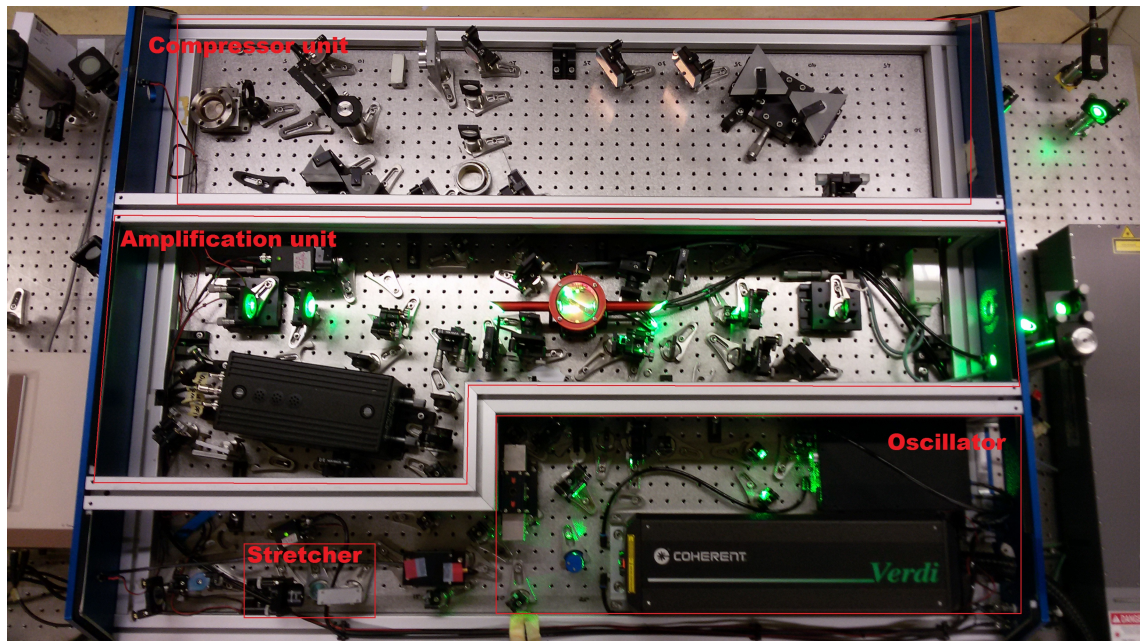


Figure 3.3: Top view image of the Ti:sapphire amplifier "Femtopower-PRO, Femtolasers Produktions GmbH"

chirped mirrors specially designed for providing third- and fourth-order dispersion control to compensate for the higher-order-dispersion of the prism compressor and all the material in the amplifier. The pulse propagates nine times through the gain region of amplifier medium. After first four passes through the crystal, a single pulse is selected out of the pulse train with a Pockel cell (PC). The selected single pulse is re-injected and amplified in another five passes. By choosing to select a single pulse after four-pass amplification, and then further amplifying has a benefit of increased pre-pulse contrast. After 9 passes, the pulses are amplified to ~ 1 mJ/pulse energy range, with a spectral width (FWHM) of > 40 nm. Pulses at 1 KHz repetition rate are selected in this manner from the 80 MHz oscillator pulse train and amplified in the amplifier unit.

3.1.2.3 Compressor

The positively chirped oscillator pulses, which are amplified in the amplification unit, are compressed in the prism-based compressor, consisting of four prisms and four chirp mirrors as shown in the Fig. 3.2 and Fig.3.3. Prism set CPR2A and CPR2B are on a linear stage to adjust the GDD to exactly compensate the positive chirp introduced by the stretcher and other optical components in the amplification unit. The pulse duration of the pulses after the compressor unit were ~ 27 fs. By moving the prism in (adding glass), we introduce more positive dispersion and by moving the prism out (removing glass), negative dispersion can be introduced. For the experiments mentioned in this thesis, we moved the prism 'in' to change the pulse duration from ~ 27 fs to ~ 550 fs. The pulse energy after the compressor unit was ~ 800 μ J.

3.1.2.4 Hollow Core Fiber (HCF)

As discussed in sections 3.1.1 and shown in Fig.3.5 (a), the initial broadband spectrum from an oscillator, after amplification narrows down to ≈ 45 nm. This limits the output pulse duration achievable from the amplifiers, which are governed by the *bandwidth* of the gain medium and the *gain narrowing* phenomena. This cannot be circumvented and to broaden the pulses, the amplifier pulses have to be broadened by spectral broadening in a gas-filled hollow fibers (HCF) followed by a compression of the broadened pulses [76]. Broadening of ultrashort laser pulses can happen because of various phenomena like *self phase modulations (SPM)*, *four wave mixing*, *cross phase modulations*, *Raman scattering* etc. However, the dominant process for spectral broadening in a gas filled hollow core fiber is self phase modulations (SPM). The physic of SPM is briefly described below.

The intensity of an ultrashort pulse with a Gaussian shape can be written as:

$$I(t) = I_0 \exp \left[-4 \ln 2 \left(\frac{t^2}{\tau^2} \right) \right] \quad (3.1)$$

where I_0 is the peak intensity, and τ is the full-width-half-maximum duration. The refractive index of a medium for high intensity pulses can be written as:

$$n(I) = n_0 + n_2 \cdot I \quad (3.2)$$

where, n_0 is the linear refractive index and n_2 is the second-order nonlinear refractive index of the medium. Now the time varying refractive index produced in the medium as the pulse propagates can be written as:

$$\frac{dn(I)}{dt} = n_2 \frac{dI}{dt} = n_2 \cdot I_0 \cdot \frac{-2t}{\tau^2} \cdot \exp \left(\frac{-t^2}{\tau^2} \right) \quad (3.3)$$

The shift in the instantaneous phase because of the variation in the refractive index can be written as:

$$\phi(t) = \omega_0 t - kz = \omega_0 t - \frac{2\pi}{\lambda_0} \cdot n(I) L \quad (3.4)$$

where, ω_0 , λ_0 and L are the carrier frequency, vacuum wavelength and the distance of propagation respectively. Now, because of the phase shift, there will be a frequency shift of the pulse. The instantaneous frequency of the pulse can be written as:

$$\omega(t) = \frac{d\phi(t)}{dt} = \omega_0 - \frac{2\pi L}{\lambda_0} \frac{dn(I)}{dt} \quad (3.5)$$

Substituting the value of $\frac{dn(I)}{dt}$ from Eqn.3.3 in Eqn.3.5 gives,

$$\omega(t) = \omega_0 + \frac{4\pi L n_2 I_0}{\lambda_0 \tau^2} \cdot t \cdot \exp \left(\frac{-t^2}{\tau^2} \right) \quad (3.6)$$

This results in the frequency shift of each part of the pulse. The leading edge shifts to lower frequencies (redder wavelengths) and the trailing edge shifts to higher frequencies (bluer wavelengths), thus broadening the pulses. The peak of the pulse is not shifted.

The HCF we used is a commercially available product (Kaleidoscope, Femtolasers Produktions GmbH). It is a noble-gas (Argon) filled hollow fiber, whose throughput is $\approx 50\%$. The output pulses of $\approx 400 \mu\text{J}$ and spectrum width $> 350 \text{ nm}$ was routinely achieved from the fiber. The HCF is followed by an all-mirror compression unit, which compressed the pulses from the HCF to $< 10 \text{ fs}$. The picture of the HCF used is shown in the Fig.3.4. The spectrum of the pulses delivered by the HCF is shown

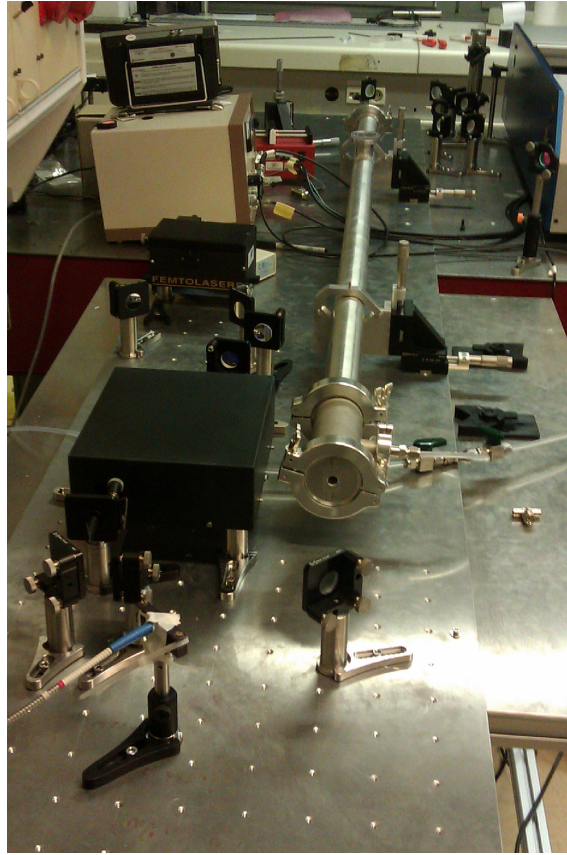


Figure 3.4: Hollow core fiber and all mirror compressor unit (black box).

in Fig.3.5(d).

3.1.3 Laser Diagnostics

Before starting an experiment the parameters of the laser beam were precisely determined. The following sections briefly lists out the apparatus and method used to characterize the laser pulses.

3.1.3.1 Pulse energy and spectrum measurement

The output power of the laser was measured using a laser power meter (Spectra Physics 407A). For precise pulse energy and pulse-to-pulse energy stability measurements, a pyroelectric detectors (J-25MB-LE & J-10MB-LE, Coherent Inc) and an energy meter (LabMax-TOP, Coherent Inc) were used, which can measure the pulse energy of every laser pulse at 1 KHz repetition rate. The spectrum of the oscillator and the amplifiers were measured by a spectrometer (USB2000+, Ocean optics). Fig.3.5(a, & d) shows the spectrum of the amplifier beam and the HCF.

3.1.3.2 Pulse profile measurement

A laser beam profiler (LaserCam –HR, Coherent Inc). was used periodically to measure the laser beam spatial intensity distribution. Fig.3.5(c & f) shows the laser beam profile of the "Amplifier 1" and the hollow-core-fiber.

3.1.3.3 Pulse width measurement

The pulse widths of the amplifier and HCF pulses were measured with a home built and commercially available second-order based auto-correlator (Femtometer, Femtolasers Produktions GmbH). The Femtometer was used in the interferometric autocorrelation mode, to measure the diffraction limited pulses from the amplifier and the sub-10 fs pulses from the HCF. To measure the stretched pulses of upto 550 fs duration, an intensity autocorrelator was built using the 10 *μm* BBO crystal from the Femtometer. Fig.3.5(b) & (e) show the autocorrelation traces of the "Amplifier 1" and the HCF.

3.2 Optical schematics

In this section the experimental setups built to perform various experiments are briefly described. The following experiments were conducted within the purview of this work:

1. Ablation and structuring on metals and bio-polymers in air environment,
2. White light generation and structuring on metals in liquid environment,
3. Ablation threshold measurements of copper and silicon in vacuum environment,
4. Electron emission measurements,
5. Ion emission measurements,
6. Neutrals emission measurements.

Ions and neutrals emission measurements were done using a time-of-flight mass spectrometer which is described in the next section.

3.2.1 Optical set-up for creating structures

Fig.3.6 shows the set-up used to produce structures on metals, semiconductor materials, and bio-polymers in air environment. The Gaussian beam from 'Amplifier 1' is focussed on the target mounted on an XYZ stage (MFA-CC, Newport Linear

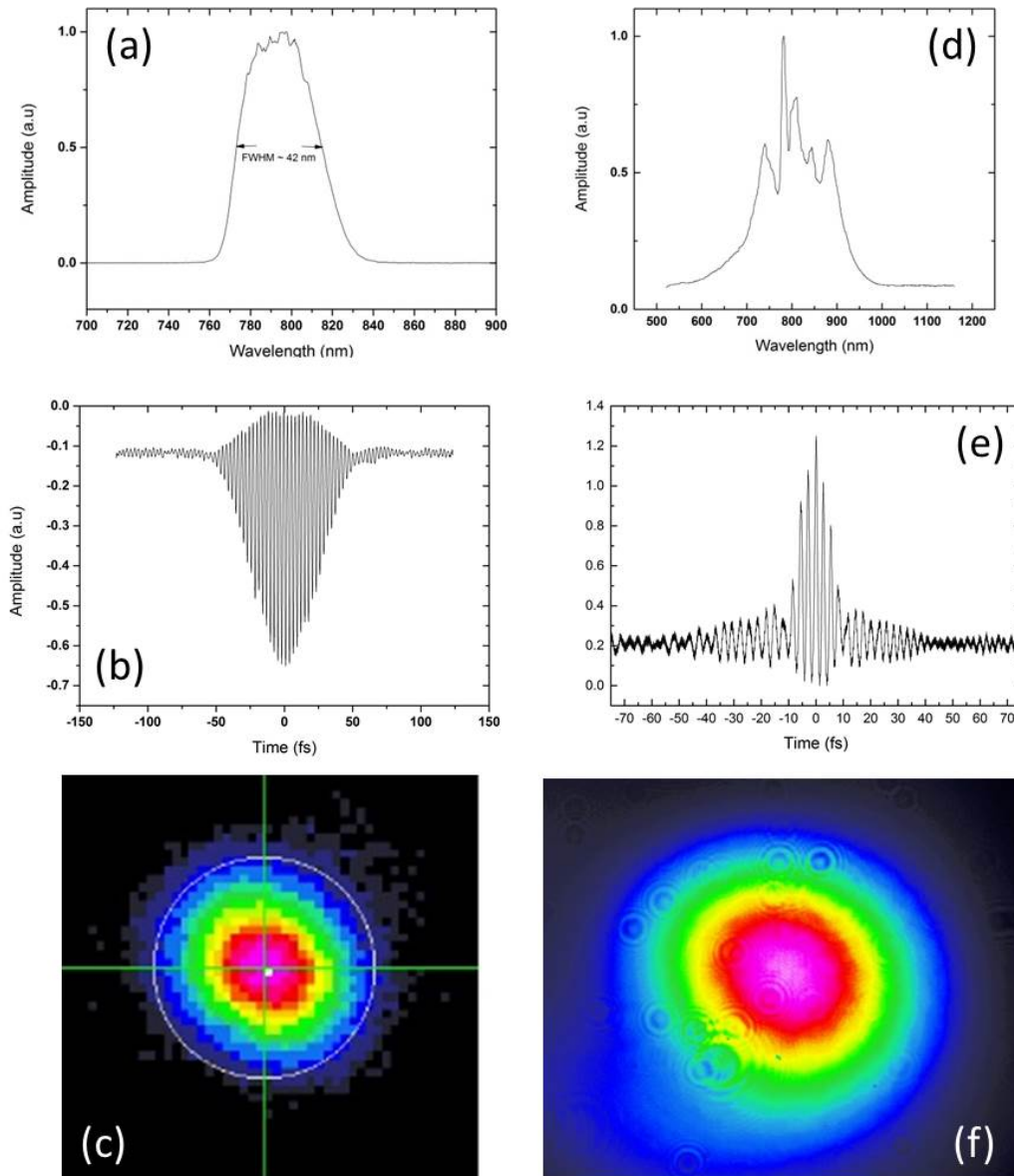


Figure 3.5: Measured laser parameters of Ti:sapphire amplifier and HCF. (a) spectrum of amplifier output pulses (b) auto-correlation trace of amplifier output pulses (c) beam profile of amplifier output pulses (d) spectrum of HCF output pulses (e) auto-correlation trace of HCF output pulses (f) beam profile of HCF output pulses

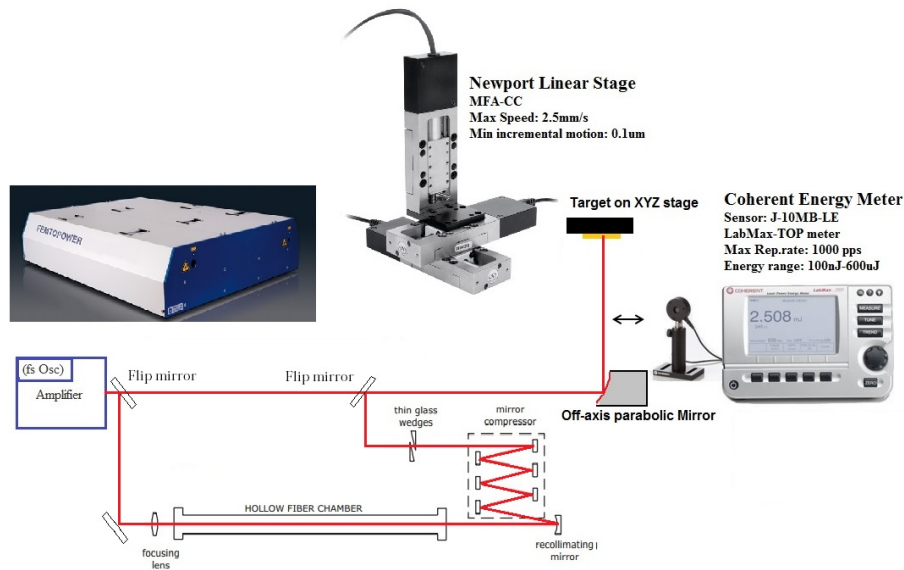


Figure 3.6: Optical set-up used for structuring and ablation threshold measurements in air environment.

stages) using an off-axis parabolic mirror of focal length 50 mm or 150 mm. The precise beam diameter on the target is determined using the method proposed by [77]. The samples can be irradiated in stationary and scanning modes with different fluences, number of pulses, and pulse durations. The energy is varied by a half-wave plate and a polarizer unit placed before the compressor unit in the amplifier. The number of pulses (spaced 1 ms apart) are extracted by controlling the internal Pockels cell of the amplifier. The pulse duration (τ) is varied by changing the dispersive path length of the compressor in the amplifier. For pulses of < 10 fs, the beam was steered into the HCF using flip mirrors as shown in the Fig.3.6.

3.2.2 Set up for White light generation and structuring in liquid environment

Figure 3.7 shows the schematic of the experimental set-up used to create white light in distilled water. The same set-up was used to create structures on metals in liquid environment. The laser beam from the amplifier (Amplifier 1) was focussed using 50 mm off-axis parabolic mirror into a cuvette of 30 mm height containing double distilled water. The cuvette was placed on a linear stage so that it can be raised or lowered so as to have the geometrical focus of the beam at various depths inside the water as measured from the top surface. The spectrum and power at the output of the cuvette was measured with a USB4000 spectrometer and a power meter. For structuring of metals in liquid environment, polished metals are placed at the bottom of the (partially) filled cuvette and the cuvette is adjusted so as to have the

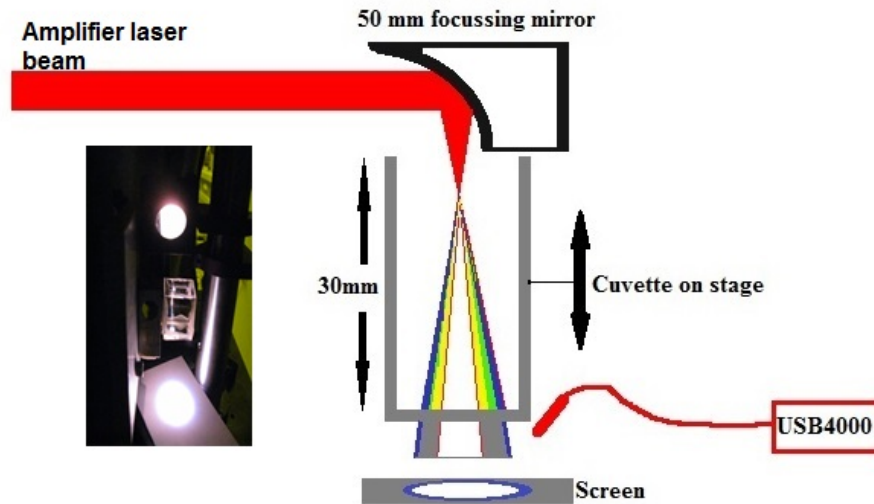


Figure 3.7: Optical set-up used for white light generation in distilled water and structuring in liquid environment.

focal point on (or few mm before) the metal surface.

3.2.3 Set up for measuring ablation thresholds in vacuum environment :

Figure 3.8 shows the schematic of the experimental set-up used to measure the ablation threshold fluence values and producing structuring in vacuum environment. The beam from the Amplifier/HCF is focussed by a 150 mm focal length off-axis parabolic mirror onto the target placed in a vacuum chamber. A rotary pump was used to evacuate the chamber. The pressure achieved was $\approx 3 \cdot 10^{-2}$ mbar.

3.2.4 Set up for measuring electron emission

For measuring the electron emission a scheme similar to the one reported in [78] was used. In the scheme for collecting the emitted electrons, the sample was mounted on the surface of a grounded electrode mounted on an XYZ stage, and a collecting copper electrode with an aperture of about 2 mm in diameter was placed 1 mm from the target surface and put under a positive potential of 0–300 V. The entire assembly was in air environment. The pump pulses were focused at normal incidence on the surface of the target using a 150 mm focal length off-axis mirror. It is assumed that the emitted electrons get attached to oxygen molecules on a nanosecond time scale [79]. Then, electrons are carried by the formed negative ions slowly moving in the applied electric field on a submillisecond time scale, thus inducing an image

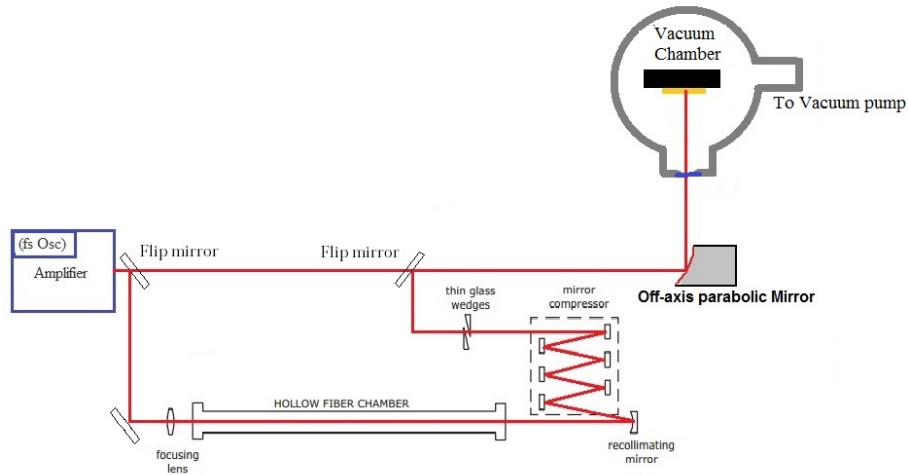


Figure 3.8: Optical set-up used for measuring ablation thresholds of silicon and copper in vacuum environment.

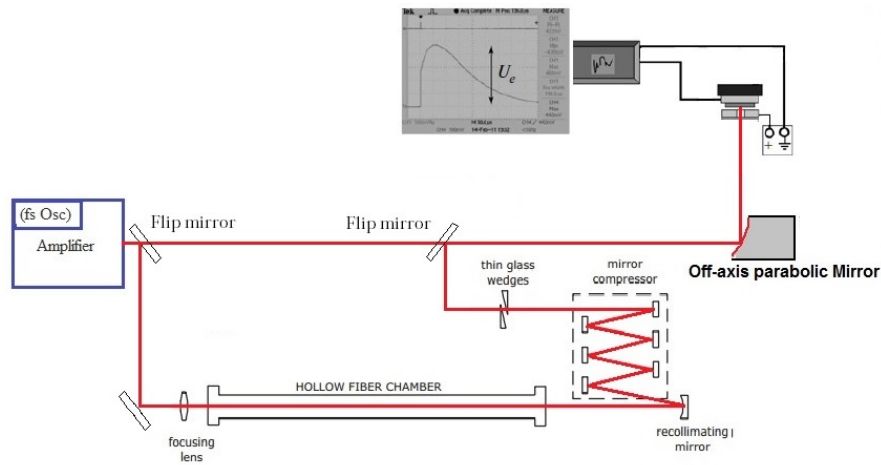


Figure 3.9: Set up for measuring electron emission in air environment.

current (potential) in the collector, which can be measured by an oscilloscope set to megaohm input impedance. It is worth noting that for doing similar experiments in high vacuum environments, the field is to be kept at 1-10 V/cm to prevent secondary electron emission. At high fluences space-charge effects might come into play. Fig.3.9 shows the schematic of the setup used to measure the electron emission.

3.2.5 Set up for measuring ion emission:

In this dissertation work, extensive investigations were done to examine the emitted ions and neutrals when an intense femtosecond laser pulse irradiates metals and semiconductors. The intention was to determine the general features of different ablation processes that take place and their dependence on laser parameters (fluence and pulse width). Fig.3.10 shows the schematic of the setup used to measure the

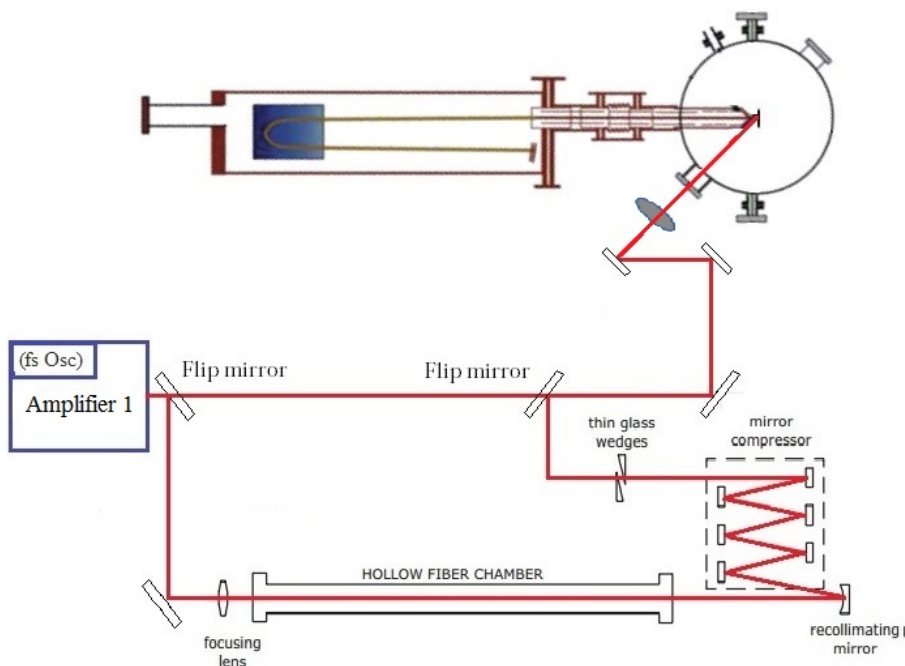


Figure 3.10: Set-up for measuring ion emission.

ion emission. Ultrashort pulses from 'Amplifier 1' or from HCF were focussed on the target mounted on a 3D stage place in an ultra-high vacuum (UHV) chamber having a base pressure of 10^{-10} Torr. The UHV chamber has a diameter of 35 cm and has an independent pumping stage which comprises of a prevacuum pump (Pfeifer-Balzars) and a turbomolecular pump (Leybold Turbovac 360). On this chamber a *time-of-flight* mass spectrometer and a high precision 3D stage was attached. The time-of-flight spectrometer has an independent pumping scheme consisting of a prevacuum pump(Alcatel) and a turbomolecular pump. After placing the targets in the chamber, the whole chamber is evacuated and baked out for 24 hours. The system is equipped with a *time-of-flight* mass spectrometer which is described in the next section. The ultrashort laser beam from the amplifier or HCF is focussed with a 40 mm focal length lens onto the target placed at 45° . The 3D stage allowed to translate the target from outside. Fig.3.13 shows the chamber, the attached *time-of-flight mass spectrometer* and the 3D stage.

3.2.6 Set up for measuring of neutral particles

In order to measure the velocity (energy) spectrum of the ejected neutral particles from the target a setup comprising of two synchronized amplifiers (amplifier 1 and amplifier 2) were used. The first laser beam (called ablation beam) is focused on the target placed at an angle of 45 degree triggering the ablation process. The ejected particles including ions and neutrals carry a typical maximum kinetic energy of a

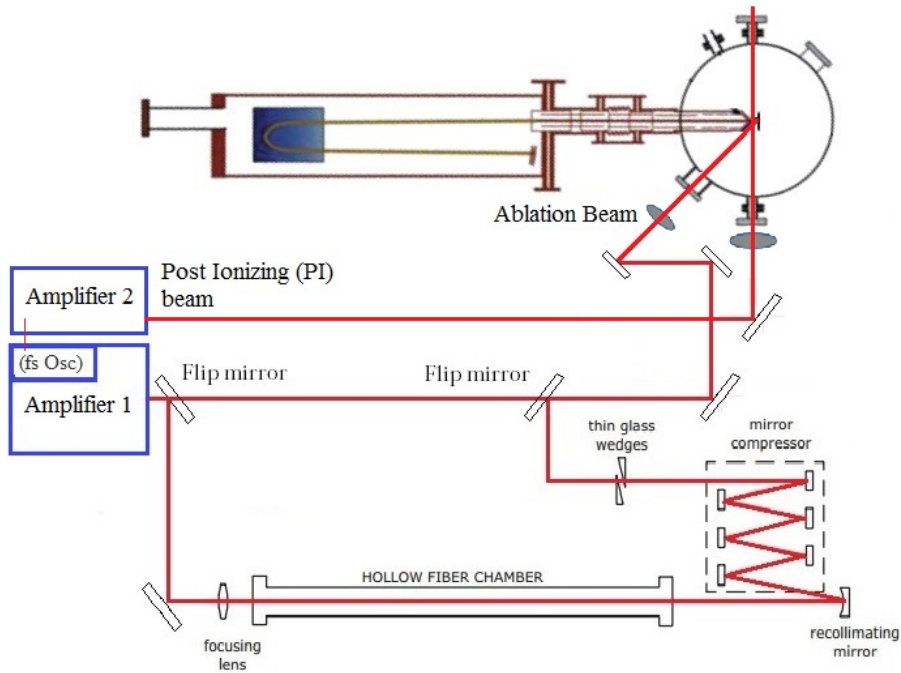


Figure 3.11: Set-up for measuring neutrals emission.

few eV. The ions are accelerated by the applied extracting voltage of about 3 kV whereas the neutrals fly with their initial kinetic energies. The second laser beam (called post ionization (PI) beam) travelling parallel to the target is focussed 1-3 mm in front of the target. The PI beam is delayed with respect to the ablation beam. The neutral particles are ionized after travelling through the focal area of the post ionizing laser beam and then they are accelerated by the applied electric field toward the extracting entrance. They are then steered towards the detector. By scanning the delay between the post ionizing pulses and ablating pulses (corresponds to TOF of the neutrals from the target surface to the focal position of the post ionizing beam) from zero to several micro second in steps of a few tens of nanosecond and measuring the total number of the ejected neutrals from the detected mass spectrum, the velocity spectrum of the neutrals can be obtained. The faster particles with higher kinetic energy arrive earlier and the slower particles are detected at later arrival times. The velocities of the neutral particles depend on the processes involved in their ejection. By measuring their velocity/energy spectrum an effort can be made to identify the processes. Fig.3.11 shows the schematic of the setup for measuring the neutrals.

3.3 Detection system and Diagnostics

3.3.1 Time of flight mass spectrometer

As discussed in chapter 2, irradiating a solid target with a laser pulse can result in emission of ions, neutrals and clusters. For analysing the emitted particles in our experiments, a reflectron type *Time-of-Flight mass spectrometer (ToF)* was used. The set-up and the working principle of a reflectron type of a ToF mass spectrometer is described below. Fig. 3.12 shows a schematic diagram of the ToF mass spectrometer. It consists of an extraction electrode, electrostatic lens system with x-y plates, field-free drift zones, a reflectron and a detector.

With Time-of-flight mass spectrometry (TOFMS), the mass-to-charge ratio of an ion or charged cluster can be determined via a time measurement. Ions are produced through interaction of femtosecond laser radiation at the surface of the target. Then, they are accelerated by a differential potential which is applied between the target and the extraction entrance. As a result of this voltage, all ions with the same charge acquire the same kinetic energy regardless of their mass. Therefore, the velocity of the ions depend on the mass-to-charge ratio; heavier particles reach lower speeds and vice versa. The time that it subsequently takes for the particle to reach a detector at a known distance is measured. By measuring the TOF of two ions with known mass and same charge, one can find the mass-to-charge ratio of all other ions which reach the detector. This way, ions and charged clusters can be directly detected using TOFMS. To detect the emitted neutral species, they were ionized by a second laser beam few mm away from the target and then detected by the TOFMS.

3.3.1.1 Working Principle of TOFMS

Assuming an ion with mass m and charge q is accelerated by extracting voltage of U_q acquires velocity v . When the length of TOFMS instrument is L the time of flight from the target to the detector can be derived from following relation:

$$U_q = \frac{1}{2}mv^2 = \frac{1}{2}m \left(\frac{L}{\Delta t} \right)^2 \quad (3.7)$$

$$\Delta t = L \sqrt{\frac{m}{2U_q}} \quad (3.8)$$

The above equation reveals clearly that the time of flight of the ion varies with the square root of its mass-to-charge ratio (i.e. for a pure material as a target the single

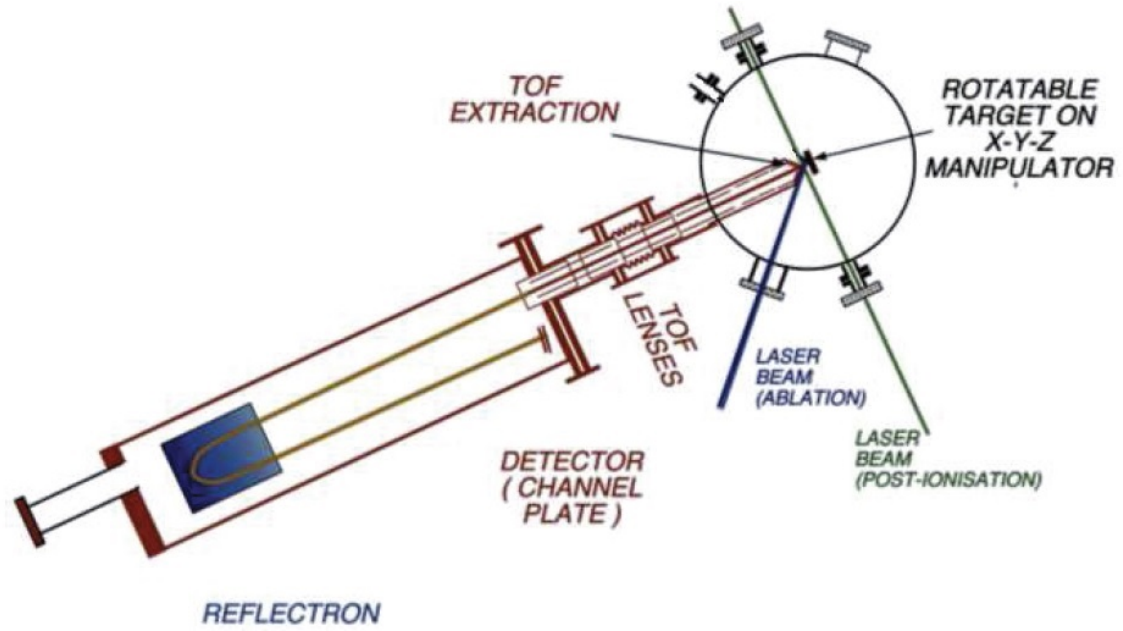


Figure 3.12: Reflectron type of *Time of Flight* mass spectrometer.

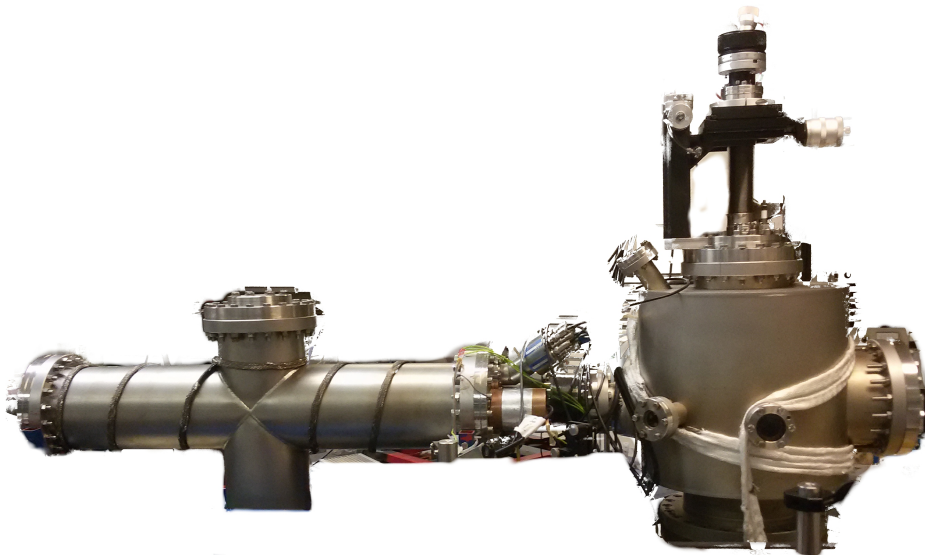


Figure 3.13: Reflectron type of *Time of Flight* mass spectrometer.

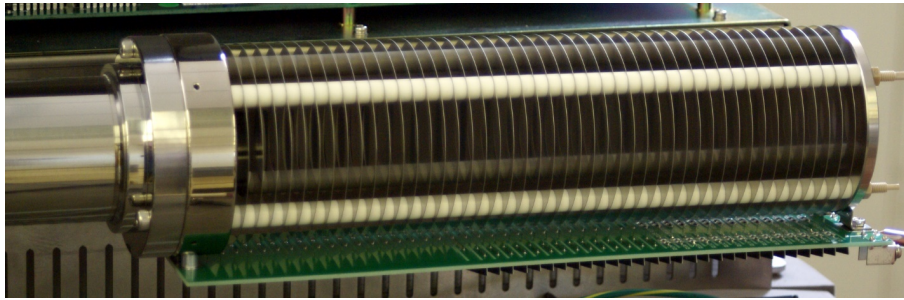


Figure 3.14: Image of *reflectron* in our TOFMS

charged clusters reach the detector later and the higher charged ions reach earlier). The time of flight can be easily converted to mass of the particle. For any set of measurement the extracting voltage and the length of TOFMS is the same. Thus, for any ion the relation between the mass and TOF can be given as follows:

$$m = k(t - t_0)^2 \quad (3.9)$$

If the TOF for two ions with different mass but the same charge is measured then the relation between the mass and TOF is exactly known. They can be written as:

$$\begin{aligned} m_1 &= k(t_1 - t_0)^2 \\ m_2 &= k(t_2 - t_0)^2 \end{aligned} \quad (3.10)$$

$$\begin{aligned} t_0 &= \frac{\sqrt{\frac{m_1}{m_2} t_2} - t_1}{\sqrt{\frac{m_1}{m_2}} - 1} \\ k &= \frac{m_1}{(t_1 - t_0)^2} = \frac{m_2}{(t_2 - t_0)^2} \end{aligned} \quad (3.11)$$

By identifying two known masses from any TOF spectrum, constants k and t_0 can be found and the TOF spectrum can be transformed into a mass spectrum.

The resolution of a TOFMS is of crucial importance. The principal physical factor which limits the resolution of a TOFMS instrument is the existence of a spread in the initial velocities of ions produced via interaction of the laser pulses with the target in a single equipotential plane of the source [80].

The time-of-flight of the ion packets is focused on the basis of energy. In the reflectron type of TOFMS, a constant electrostatic field is used to reflect the ion beam toward the detector. The more energetic ions, which are located in the leading part of ion packet, penetrate deeper into the reflectron and take a slightly longer path to the detector. Less energetic ions of the same mass-to-charge ratio, penetrate a shorter distance into the reflectron and, correspondingly, which are located at the

trailing part of ion packet, take a shorter path to the detector. Therefore, the ions which possess the same mass to charge ratio but different energies are reflected by the reflectron in such a way that they hit the surface of the detector at the same time. Simultaneous arrival of ions in this manner is often referred to as time-of-flight focus. An additional advantage to the reflectron type of TOFMS arrangement is that, twice the flight path is achieved in a given length of instrument.

3.3.2 Scanning Electron Microscope

A Scanning Electron Microscope (FEI-QUANTA 200F, Netherlands) was used extensively to analyse the morphology of the irradiated targets. A scanning electron microscope scans the surface of a sample, generally in a raster scan pattern, with a finely focused high energy electron beam to produce various signals that contain information about the sample's surface topography and composition. An image containing information about the sample's surface composition and other properties are extracted from these signals. Samples can be observed in high vacuum, in low vacuum, in wet conditions and at wide range of temperatures. The signals could be detected by a wide array of detectors: (i) secondary electron detectors, to provide surface topography information, (ii) backscattered detectors, for compositional information in both high and low vacuum modes. For imaging in SEM, atleast the surface of the sample must be electrically conductive and electrically grounded to prevent the accumulation of electrostatic charge at the surface. Metal objects require no special preparation for SEM imaging. Nonconductive specimens (bio-polymers in our case) are coated by gold/paddadium alloy (40:60) using a low-vacuum sputter coating machine.

3.3.3 Atomic Force Microscope (AFM)

An atomic-force-microscope (AFM, Cypher, Asylum Research) was used to measure the 3D surface topography after irradiating with the ultrashort laser pulses. AFM is a method of measuring surface topography on a scale from angstroms to 100 of microns. The basic imaging principle of an AFM is very simple. A sample attached to a piezoelectric positioner is rastered beneath a sharp tip, with a radius of about 10-20 nm, attached to a sensitive cantilever spring. Undulations in the surface lead to deflection of the spring, which is monitored optically. The tip is held several nanometers above the surface and usually, an employed feedback loop holds the spring deflection constant, and the corresponding movement of the piezo thus generates the image. In this work, an AFM was used to measure the height of the

high spatial frequency ripples.

3.3.4 Raman Spectroscopy

In this work, some of the targets irradiated with the ultrashort laser pulse were analysed with a Raman Spectrometer. With Raman spectroscopy, the structural, crystallographical and chemical changes, like crystallization, amorphization, bond breaking, bond weakening, cross linking, polymerization, appearance of new disorder bands for irradiated targets can be revealed. The results can be compared with the surface topographies obtained by SEM/AFM. It is also an important technique to investigate laser-induced stress distribution of processed materials. The Raman spectroscopy is performed by a Raman spectrometer (Lab Ram HR-800, Horiba Jobin-Yvon) in which a He-Ne (632.8 nm, 8 mW) laser is used as an excitation source. A 20 x objective lens is used for focusing, resulting in a spot size of $\approx 20 \mu\text{m}$. The spectral data were accumulated at a fixed grating position and collected using an air-cooled CCD camera. It is a non-destructive, non-invasive technique without the requirement of sample preparation and provides qualitative and quantitative data. When a laser interacts with materials most of the photons are elastically scattered, a process which is called Rayleigh scattering. In Rayleigh scattering, the emitted photon has the same wavelength as the primary absorbed photon. Raman Spectroscopy is based on the Raman effect, which is the inelastic scattering of photons by molecules. The Raman effect comprises a very small fraction (typically, 1:10⁷), of the incident photons. In Raman scattering, the energies of the incident and scattered photons are different. The energy of the scattered radiation is less than the incident radiation for the Stokes line and the energy of the scattered radiation is more than the incident radiation for the anti-Stokes line. The energy increase or decrease from the excitation is related to the vibrational energy spacing in the ground electronic state of the molecule and therefore, the wavenumber of the Stokes and anti-Stokes lines are a direct measure of the vibrational energies of the molecule. Raman spectroscopy measures the vibrational energies of molecules therefore for a transition to be Raman active there must be a change in polarizability of the molecule.

3.4 Summary

In this chapter, the experimental setups used for the experiments performed in this dissertation work were described. Starting from the laser source, describing how ultrashort laser pulses are produced, amplified, and characterized, the chapter detailed the setups used to measure ions and neutrals emitted from solid targets upon ultrafast laser irradiation. In case of post exposure studies, the relevant diagnostic tools used to study the exposures were discussed.

Chapter 4

Ablation Threshold Measurements

Ultrafast lasers has been of increasing interest in material processing applications due to their capability of precise micromachining of a large variety of materials: metals, semiconductors, polymers, dielectrics, biological materials etc [81]. The processes that occur when a laser pulse irradiates a material can be divided into two domains: non-thermal domain (for processes that take place up to few ps) and thermal domain (for longer durations). The laser-matter interaction processes that happen with laser pulses of duration greater than characteristic electron-phonon relaxation times ($\tau_{ep} \sim 10$ ps) seems to have been fairly understood [82, 83, 34]. However, when an ultrashort laser pulse irradiates a material, the non-thermal processes that occur depends on the class of the material irradiated as well as the intensity of the irradiation. The precise processes and the sequence of processes that take place are far from understood [83, 84]. Laser ablation refers to as removal of macroscopic amounts of material from the surface of a medium by irradiating with laser pulses. Depending on the class of the material, different processes take place preceding laser ablation. For example in metals which have abundant free electrons, absorption creates hot electrons in a cold lattice and after electron-electron scattering, electron-phonon-scattering sets in, followed by melting, boiling and ablation. To a certain extent these processes can be described by a two temperature model. In case of dielectrics and wide-bandgap semiconductors, absorption of radiation can be understood by multi-photon excitation and impact ionization with subsequent avalanche ionization. These carriers then thermalize to a Fermi-Dirac distribution while transferring their excess energy to phonons. These phonons then recombine to a Bose-Einstein distribution and thermal processes follow. It is worth mentioning that upon irradiation with high peak intensities, dielectrics can exhibit metal-like properties. Hence understanding the exact processes that take place upon femtosecond laser irradiation is a complex process involving linear and several non-linear

processes taking place simultaneously. Ablation threshold fluence, usually defined as the minimum laser fluence necessary to initiate the ablation process (material removal), is an important parameter which can give insight into the physical processes taking place in the material. Knowing the values is also necessary to deposit a defined amount of energy for precision material processing applications. The single-shot ablation threshold for ultrashort pulsed laser ablation depends on the thermal and dynamical properties of the material. In multi-pulse regime it is well established that the ablation threshold depends on the number of laser pulses exciting the same spot. The threshold fluence normally decreases with laser shot number [85, 86]. This phenomenon is referred to as material incubation, and the origin of the incubation is still under debate. The reduction in ablation threshold fluence follows a power law equation which holds for all materials [85, 87] and can be ascribed to higher energy coupling efficiency [88]. An increase of surface roughness after multi-shot irradiation due to ripples formation or accumulation of surface defects results in reduction in the reflectance [89] and thus leads to enhance the absorption and then a decrease in ablation threshold [90]. It has also been suggested that the incubation behaviour for metals can be due to the accumulation of plastic deformation resulting from laser induced thermal stress fields [87]. The ablation threshold is usually determined by inspection of the exposed area with a microscope or by detecting changes in the scattering pattern produced by a probe laser or by detecting the ion emission using time of flight spectrometers [91]. In the most frequently used method to determine the ablation threshold, the squared crater diameter is plotted as a function of the pulse fluence (F). Linear extrapolation of the plot of the squared crater diameter versus $\ln(F)$ yields the ablation threshold. The advantage of this technique is that the measurements can be performed at fluences well above threshold for which the detected fingerprint signals are clearly detectable by far-field microscopy [86]. The actual physical mechanisms of laser ablation depend on the type of materials and the irradiation properties such as laser wavelength [89], pulse duration [92–98] and repetition rate [93, 99]. Change in the repetition rate affects the ablation threshold in two respects. Increasing the repetition rate, on one hand, leads to particle shielding which reduces the absorption and thus limits the laser ablation efficiency. On the other hand it leads to heat accumulation that causes melting. The latter, especially in case of metals with a relatively low thermal conductivity, prevents the high level of precision which is achievable at lower repetition rates. Using shorter pulses makes it possible to prevent heat accumulation arising from irradiating with high repetition rate laser pulses since for pulses of a few picoseconds or shorter, heat diffusion is frozen within the interaction volume and the shock-like energy deposition leads to ablation [97]. Nevertheless, as soon as the pulse energy is increased melting cannot be avoided in multi-pulses femtosecond laser ablation processes [99].

It has been observed that the damage threshold depends on the pulse duration. For long pulses (eg. $\tau > 10$ ps), where damage on the surface of a medium results from conventional heating and melting, the damage threshold scales as $\tau^{0.5}$ with pulse duration [100, 101]. However, a deviation from this scaling has been observed for shorter pulses where damage results from plasma formation and ablation [96, 101]. Although the ablation threshold in the short pulse regime reduces with decreasing the pulse duration, this dependency is weaker than what is observed in the long pulse regime. Till date, many authors have investigated the dependence of ablation threshold fluence on various laser parameters, but most studies were limited to a particular pulse duration or number of shots or material. A comprehensive study for different type of materials under identical experimental conditions was missing. In this work a systematic study was done to investigate the influence of pulse duration on the ablation thresholds and the incubation coefficients for three different types of materials: metal (copper), semiconductor (silicon) and bio-polymer (gelatin) in 10 fs - 550 fs range. The results indicate that the threshold fluence reduce with decreasing the pulse duration. The dependence of the threshold fluence on the pulse duration was determined as $F_{th} \propto \tau^{0.05}$ for Copper, $F_{th} \propto \tau^{0.12}$ for Silicon and $F_{th} \propto \tau^{0.22}$ for Gelatin.

When a laser beam is incident on a material surface, the ablation of the material occurs only when the incident laser pulse energy exceeds a minimum value called the ablation threshold. Ablation threshold values depend on several laser and material properties. For a laser beam having a Gaussian spatial distribution, for a given number of pulses (N), and pulse energy (E_p), the ablation crater diameter (D) formed on the material can be related to the ablation threshold, $F_{th}(N)$ [77] by

$$D^2 = 2w_0^2 \ln\left(\frac{F}{F_{th}(N)}\right), \quad (4.1)$$

Where w_0 is the $1/e^2$ gaussian beam radius, and F is the peak fluence given by,

$$F = \frac{2E_p}{\pi w_0^2} \quad (4.2)$$

As can be seen from Eq.4.1, the squared ablation crater diameter goes logarithmically with the peak laser fluence (F), which is related to pulse energy E_p by Eq.4.2. This makes it possible to determine the beam radius (w_0) from a plot of the squared crater diameters (D^2) versus the logarithm of the laser pulse energy (E_p). Fig.4.1 shows the craters formed on Copper, Silicon and Gelatin when irradiated with femtosecond laser pulses. Once the spot size is known, the pulse energy values can be

converted to the fluence using Eq.4.2 and then the threshold fluence for each N ($F_{th}(N)$) of the material can be determined from the same plot by extrapolating the curve to the zero crater diameter. Fig. 4.2 shows the squared crater diameter versus fluence for Silicon when irradiated with 3, 10, 30, 100, 300, and 1000 pulses of 250 fs duration. For each shot-number the squared crater diameter shows a linear behaviour versus the logarithm of the laser fluence from which the ablation fluence threshold can be determined. Data for other pulse durations of 10 fs, 30 fs and 550 fs and for all three samples (i.e. 12 plots) were plotted (not shown here) and Fig. 4.3, Fig. 4.4 and Fig. 4.5 summarizes the results for copper, silicon and gelatin respectively. It can be seen from Fig.4.3 that the ablation threshold decreases with increasing number of pulses. This reduction of threshold can be explained in terms of the incubation model [85]. The relation between single-shot threshold fluence $F_{th}(1)$ and N -shot threshold fluence $F_{th}(N)$ has been proposed as given by

$$F_{th}(N) = F_{th}(1)N^{S-1} \quad (4.3)$$

Where S is called the incubation coefficient characteristic to the accumulation behaviour. $S = 1$ implies no incubation effect. A more elaborate model of incubation effect is given in [86]. It is clear that Eq.4.3 can be valid only upto a certain number of pulses as the threshold fluence cannot reduce indefinitely. On the other hand, for lower N (1-10 pulses), the initial condition of the sample and the peak-to-peak pulse energy variation of the laser are critical for determining accurate values. For this reason, only the data points from $N = 10$ to 300 are used for fitting in the results presented here. The below sub-sections Sec.4.1, Sec.4.2, Sec.4.3 report the experimental conditions and results in detail for Copper, Silicon and Gelatin respectively. In Sec.4.4, the dependence of the threshold fluence and the incubation coefficient on the pulse duration is reported.

4.1 Copper

A Copper sample was polished using a commercially available polishing machine (Allied High Tech Products Inc) using sand paper up to 4000 grit and finally with $0.02 \mu\text{m}$ silica suspension. Mirror-like copper sample was then irradiated in vacuum with 3, 10, 25, 50, 100, 175, 300 and 1000 pulses with varying energy and for different pulse durations (10 fs, 30 fs, 250 fs and 550 fs). The irradiated spots were analysed with optical and confocal microscopes (Fig.4.1(a,d)). Since the spots were not perfectly circular, the crater area (solid yellow line in Fig.4.1(a)) was determined for each spot using ImageJ software and the squared crater diameter was determined

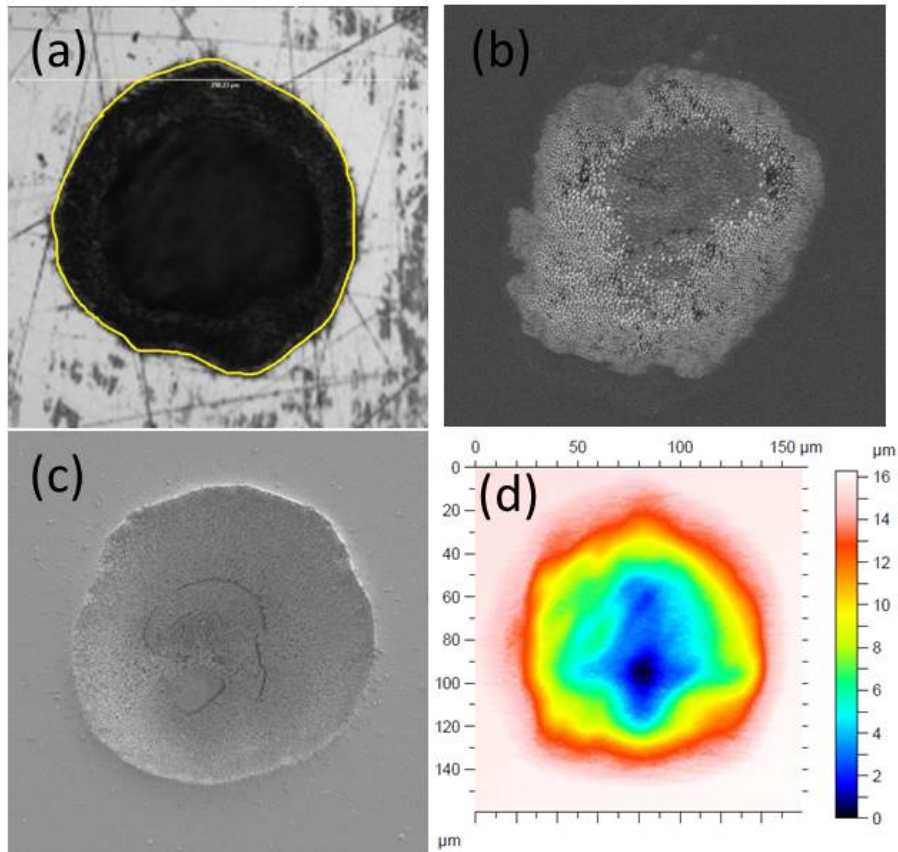


Figure 4.1: (a) Optical microscope image of spot irradiated on Copper sample with 300 pulses of $270 \mu\text{J}$ energy and 550 fs duration. (b) SEM image of Silicon sample irradiated with 100 pulses of $160 \mu\text{J}$ and 30 fs . (c) Gelatin sample irradiated with 100 pulses of $100 \mu\text{J}$ and 10 fs . (d) Confocal image of spot on Copper sample after irradiating with 300 pulses of $180 \mu\text{J}$ energy and 550 fs .

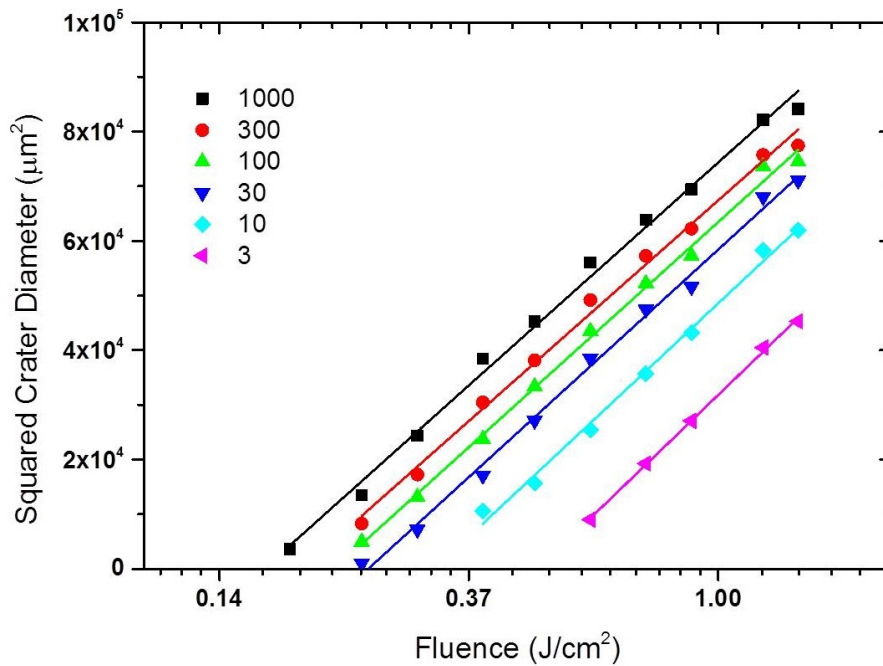


Figure 4.2: Squared crater diameters versus the laser fluence for different number of applied laser pulses on a silicon sample when irradiated with 250 fs laser pulses.

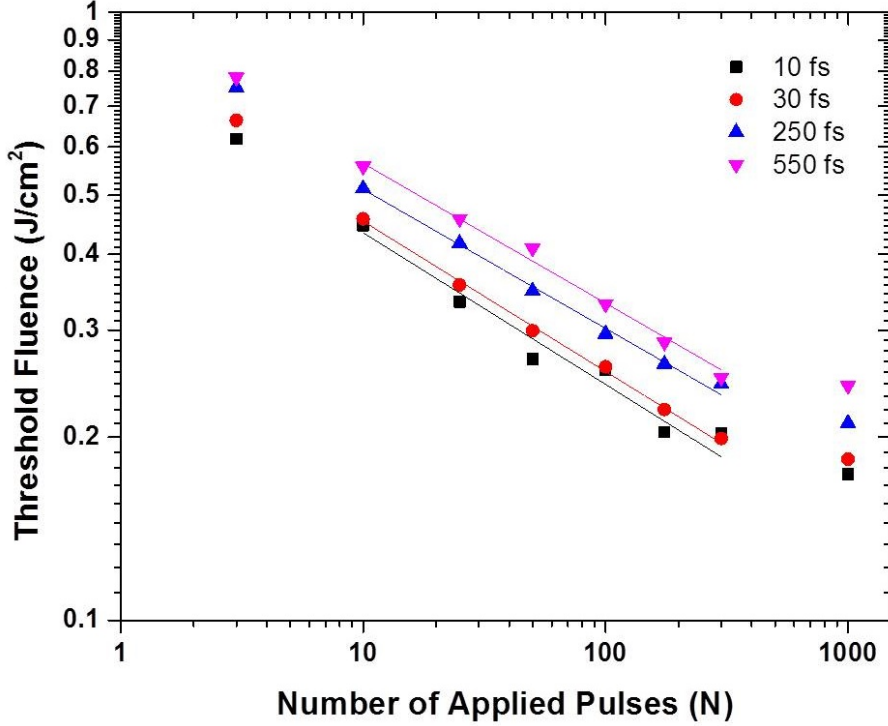


Figure 4.3: Threshold fluence versus the number of applied pulses on a Copper sample for four different pulse durations in vacuum. The solid line represents a least-square-fit using Eq.4.3, from which $S=0.75, 0.76, 0.77, 0.77$ were extracted for pulse durations 10 fs, 30 fs, 250 fs, and 550 fs respectively

by assuming it to be circular (equating it to area of a circle). Confocal images (Fig.4.1(d)) were used to identify the ablation crater accurately. The squared crater diameter was plotted against the applied pulse energy for each N and corresponding w_0 value was determined from the slope of the linear fit curves. For best fits (R^2 value $\sim 99.7\%$) the value of w_0 gradually increased from $63 \mu\text{m}$ to $72 \mu\text{m}$ as N increased from 3 to 1000. We observed this for all pulse durations and also for other metals (steel). However, for Silicon it was not significant. This makes us to conclude that there could be other mechanisms responsible for higher crater diameters at higher F and N in metals. The energy values were then converted to fluence values and the ablation threshold fluence was determined for each N by extrapolation. Table. 4.1 shows the threshold values for different N and for all 4 pulse durations. The errors associated with the threshold fluence (about 10%, not shown in the plots) arise from the error in determination of the spot size from the slope. Fig.4.3 shows the threshold fluence versus N for copper for different pulse durations. By fitting Eq.4.3 to the data points the single shot threshold fluence $F_{th}(1)$ was extracted as 0.77 J/cm^2 , 0.79 J/cm^2 , 0.86 J/cm^2 , and 0.95 J/cm^2 and the incubation coefficient S as 0.75, 0.76, 0.77, and 0.77 for pulse durations 10 fs, 30 fs, 250 fs and 550 fs respectively. The obtained ablation threshold values are slightly higher than that reported in [87] and lower than reported in [88]. In both cases, the experiments were conducted in

air, whereas we conducted our experiment in vacuum environment. To verify the reliability of the threshold values obtained in this experiment, the experiment was repeated for $N = 100$ at same focal position with an other sample polished on an other day and we observed an offset of about 15% for all pulse durations, but the dependence on pulse duration showed similar behaviour. The variation of single-shot threshold fluence with pulse duration is discussed in Sec.3.4.

4.2 Silicon

A Silicon sample was irradiated in vacuum with 3, 10, 30, 50, 70, 100, 300, 500, 700 and 1000 pulses with varying energy and for different pulse durations (10 fs, 30 fs, 250 fs and 550 fs). The irradiated spots were analysed with SEM and the ablation threshold fluence values were determined for each N by the procedure explained in Sect. 4.1. Table. 4.2 shows the ablation threshold values for different N and for all 4 pulse durations. The errors associated with the threshold fluence (not shown in the plots) arising from error in spot size measurements is about 6%. Fig.4.4 shows the threshold fluence versus N for different pulse durations. By fitting Eq.4.3 to the data points the single shot threshold fluence $F_{th}(1)$ was extracted as $0.297J/cm^2$, $0.329J/cm^2$, $0.405J/cm^2$, and $0.518J/cm^2$ and the incubation coefficient S as 0.82, 0.83, 0.84, and 0.84 for pulse durations 10 fs, 30 fs, 250 fs and 550 fs respectively. Bonse et al have reported the dependence of threshold fluence on pulse duration of Silicon for $N = 100$ pulses [92] and incubation coefficient as 0.84 with 130 fs pulses. Our results (see Table. 4.2, 4.4) match very closely with their results. However, Bonse et al conducted their experiments in air environment and we did in vacuum.

4.3 Gelatin

A Gelatin film was irradiated with 10, 25, 50, 100, 175, and 300 pulses like as described in the previous sections and the ablation threshold fluence is determined. Table. 4.3 shows the ablation threshold values for different N and for all 4 pulse durations. The errors associated with the threshold fluence (about 7%, not shown in the plots) arise from the error in determination of the spot size from the slope. Fig.4.5 shows the plot of threshold fluence versus number of applied pulses for different pulse durations. As can be clearly seen from Fig.4.5, the threshold fluence values are lower for shorter pulse durations for all N . The solid lines shows the fit curve using Eq.4.3. From the fitting, the incubation coefficient, S was determined

Table 4.1: Ablation threshold values (in J/cm^2) of Copper for different N in Vacuum as determined by the diameter regression technique for 10 fs, 30 fs, 250 fs and 550 fs. The errors (about 10%, not shown) arise from the error in determination of the spot size from the slope.

Pulse Duration (fs)	$F_{th}(3)$	$F_{th}(10)$	$F_{th}(25)$	$F_{th}(50)$	$F_{th}(100)$	$F_{th}(175)$	$F_{th}(300)$	$F_{th}(1000)$
10	0.619	0.446	0.334	0.269	0.258	0.204	0.203	0.174
30	0.664	0.457	0.356	0.299	0.261	0.222	0.199	0.184
250	0.752	0.513	0.417	0.348	0.296	0.264	0.245	0.211
550	0.781	0.557	0.457	0.409	0.331	0.286	0.251	0.243

Table 4.2: Ablation threshold values (in J/cm^2) of Silicon for different N in Vacuum as determined by the diameter regression technique for 10 fs, 30 fs, 250 fs and 550 fs. The errors (about 6%, not shown) arise from the error in determination of the spot size from the slope.

Pulse Duration (fs)	$F_{th}(3)$	$F_{th}(10)$	$F_{th}(30)$	$F_{th}(50)$	$F_{th}(100)$	$F_{th}(300)$	$F_{th}(500)$	$F_{th}(1000)$
10	0.279	0.203	0.158	0.139	0.129	0.114	0.097	0.092
30	0.334	0.228	0.187	0.172	0.155	0.131	0.120	0.109
250	0.427	0.290	0.234	0.212	0.198	0.168	0.157	0.140
550	0.552	0.365	0.283	0.262	0.236	0.207	0.190	0.173

Table 4.3: Ablation threshold values (in J/cm^2) of $20\mu m$ Gelatin film sample for different N in air as determined by the diameter regression technique for 10 fs, 30 fs, 250 fs and 550 fs. The errors (about 7%, not shown) arise from the error in determination of the spot size from the slope..

Pulse Duration (fs)	$F_{th}(10)$	$F_{th}(25)$	$F_{th}(50)$	$F_{th}(100)$	$F_{th}(175)$	$F_{th}(300)$
10	0.390	0.326	0.225	0.193	0.153	0.136
30	0.490	0.363	0.280	0.220	0.205	0.184
250	0.853	0.663	0.530	0.444	0.375	0.358
550	1.125	0.755	0.610	0.564	0.585	0.476

Table 4.4: Derived single-shot ablation threshold fluence and incubation coefficients for Copper, Silicon and 20 μm thick Gelatin film sample for different pulse durations.

Sample	$F_{th}(1)$ (J/cm^2)				S				τ dep
	10 fs	30 fs	250 fs	550 fs	10 fs	30 fs	250 fs	550 fs	
Copper	0.77	0.79	0.86	0.95	0.75	0.76	0.77	0.77	$\tau^{0.05}$
Silicon	0.297	0.329	0.405	0.518	0.82	0.83	0.84	0.84	$\tau^{0.12}$
Gelatin	0.836	0.995	1.599	1.912	0.67	0.68	0.72	0.74	$\tau^{0.22}$

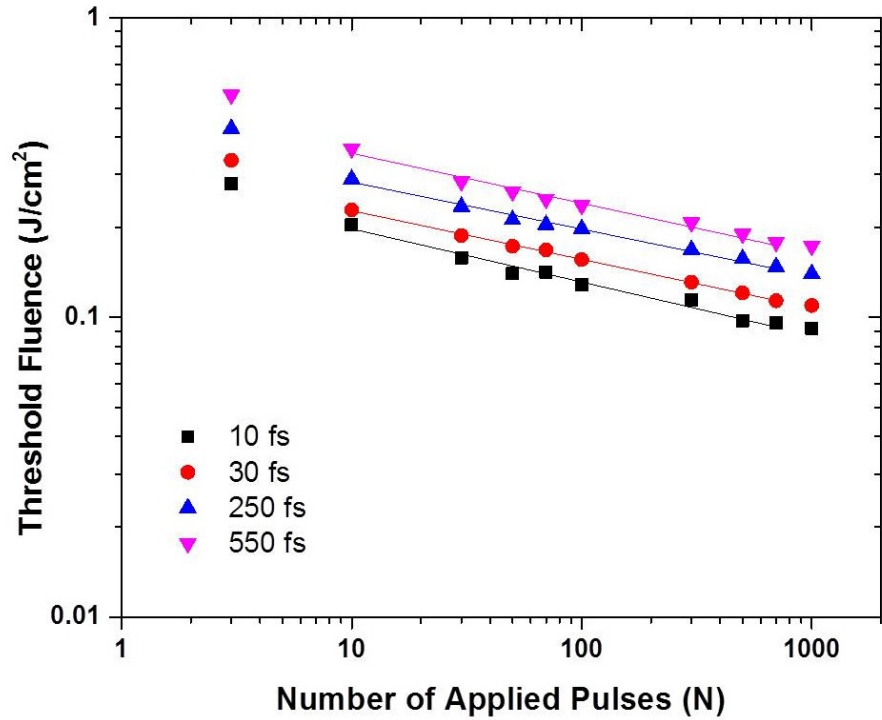


Figure 4.4: Threshold fluence versus the number of applied pulses on a Silicon sample for four different pulse durations in vacuum. The solid line represents a least-square-fit using Eq.4.3, from which $S = 0.82, 0.83, 0.84, 0.84$ were extracted for pulse durations 10 fs, 30 fs, 250 fs, and 550 fs respectively.

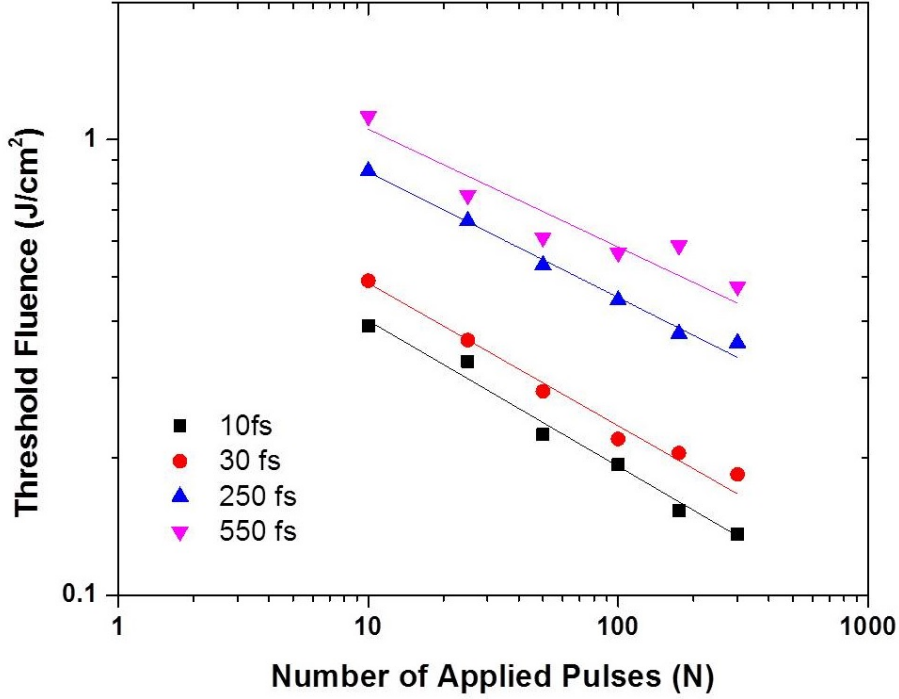


Figure 4.5: Threshold fluence versus the number of applied pulses on a Gelatin film for four different pulse durations in air. The solid line represents a least-square-fit using Eq.4.3, from which $S=0.68, 0.69, 0.72, 0.74$ were extracted for pulse durations 10 fs, 30 fs, 250 fs, and 550 fs respectively.

as 0.68, 0.69, 0.72, and 0.74 for 10 fs, 30 fs, 250 fs and 550 fs respectively, and by extrapolation of the fitted curve, single shot threshold fluences were determined as $0.83 J/cm^2, 0.99 J/cm^2, 1.59 J/cm^2,$ and $1.91 J/cm^2$ for 10 fs, 30 fs, 250 fs and 550 fs respectively. We observed that the threshold fluence depends on the concentration of the Gelatin. In this experiment we dissolved 2.0 g of Gelatin in 20 ml of millipore water. When samples are prepared with 1.6 g of Gelatin dissolved in 20 ml of water, we measured lower thresholds values, but the dependence on pulse duration was the same.

4.4 Pulse Width dependence

Table. 4.3 summarizes the results of the derived single shot threshold fluences of Copper, Silicon and Gelatin for 10 fs, 30 fs, 250 fs and 550 fs. The derived single shot threshold fluence values are then plotted as a function of the pulse duration for all three materials and is shown in Fig.4.6. It can be seen that the threshold fluence goes as $\tau^{0.05}$ for Copper and as $\tau^{0.12}$ for Silicon and as $\tau^{0.22}$ for Gelatin film. This general trend is consistent with multi-photon absorption as one of the underlying energy deposition mechanisms in these materials, with their power increasing from

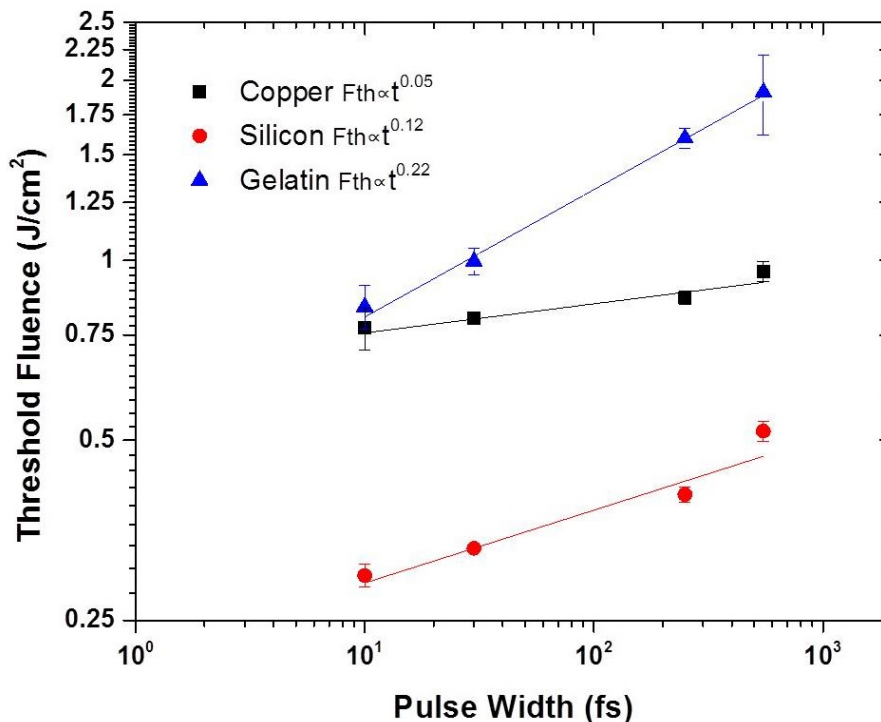


Figure 4.6: Derived single-shot threshold fluence versus pulse width for Copper, Silicon and Gelatin film samples

Copper (linear intraband or two-photon interband absorption in near-IR) to Silicon (two-photon interband absorption in near-IR) [102, 103] and 3-5 photon near-IR-photon absorption in gelatin. Since multi-photon absorption coefficient increases with increasing intensity, for the fixed laser fluence the threshold fluence decreases with the pulse width. As a result, the materials with higher powers of multi-photon absorption - transparent gelatin, to less extent, silicon - demonstrate the rising threshold fluence dependence on pulsewidth. In the case of Copper, its negligible slope indicates that one-photon intraband IR-absorption as the predominating absorption mechanism. Nevertheless though the dependence is small, a noticeable dependence on pulse duration was observed in our systematic multi-shot irradiations experiment.

4.5 Conclusions

In this chapter the results of the ablation threshold fluence measurements were presented. The dependence of ablation threshold as well as incubation coefficient on pulse duration in the range of 10 fs- 550 fs has been systematically investigated as presented, for three different types of materials: metal (Copper), semiconductor (Silicon) and biopolymer (Gelatin). Ablation threshold fluence values for multiple

pulse irradiation ranging from 3 to 1000 pulses has been reported. The ablation threshold for all investigated samples showed a decrease with pulse duration. For Copper, the threshold scales as $\tau^{0.05}$, for Silicon as $\tau^{0.12}$ and for Gelatin as $\tau^{0.22}$. The incubation coefficient of Gelatin showed a clear reduction at shorter pulse durations indicating higher incubation effect at shorter pulse durations. For Copper and Silicon the incubation coefficient is nearly constant.

Chapter 5

Time of Flight Measurements

In chapter 4, ablation threshold measurements of certain materials were presented where the ablation threshold values were derived from the crater diameter versus the fluence plots for different number of pulses, N . This method, also called Liu's method, is a widely used method to quickly determine the ablation threshold values. But the kind of particles (ions, clusters, neutrals) emitted from the materials cannot be deduced by this technique. Study of composition and expansion dynamics of femtosecond laser induced plume can provide considerable insight into the ablation mechanisms. In this section the time-of-flight measurements of various materials recorded after irradiating with femtosecond laser pulses of durations in the range 10 fs to 550 fs are presented from which the behaviour of the ejected particles can be analysed. As mentioned in the experimental section, a reflectron type of time-of-flight mass spectrometer (TOFMS) was used whose description is given in Chapter 3. The type of particles emitted (ions, clusters, neutrals) from various metals and semi-conductors were studied in detail whose results are presented in this chapter. The dependence of the flux of the emitted particles on fluence and pulse duration are presented.

Irradiating a solid target can lead to material removal from its surface. The material leaves the sample in the form of electrons, singly charged ions (monoatomic), multicharged ions, cluster of ions and neutrals. The yield of ions, clusters and neutrals depends on the target material as well as the laser parameters. Ions and charged clusters (cations) can be directly detected using a time of flight mass spectrometer, whereas neutral species can only be detected after a post ionization process.

In the below sections the TOF spectras of ions, neutrals and the velocity distribution spectras of neutral particles will be presented for few materials. The discussion part is presented at the end of the chapter.

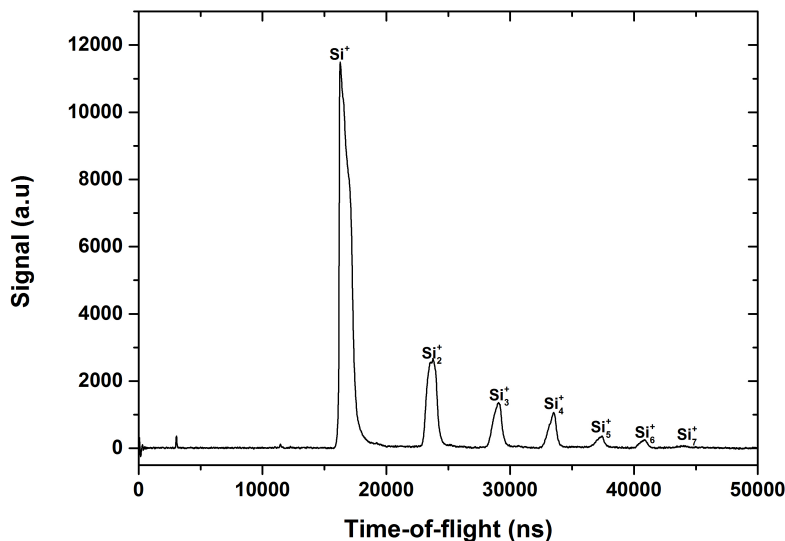


Figure 5.1: Recorded Time-of-Flight spectrum from a silicon sample at fluence of $\sim 150mJ/cm^2$.

5.1 Silicon

5.1.1 Ion/Clusters Emission

Silicon (Si) is an abundantly available element in nature which is used extensively in semiconductor industry. It has three isotopes, $_{28}Si$, $_{29}Si$ and $_{30}Si$ of which $_{28}Si$ has an abundance of $\approx 92\%$. The silicon targets used for the experiments were $< 100 >$ N-type, single side polished wafers procured from Sigma Aldrich. Fig.5.1 shows the typical TOF spectrum of silicon upon irradiation with 2000 pulses of 10 fs duration and fluence of $150mJ/cm^2$. During initial shots, the TOF spectrum shows many peaks, but with increasing N, the spectrum becomes cleaner with only Si ions and cluster peaks. The peak at 16950 ns can be identified as the silicon ion peak and the additional peaks are silicon clusters. As can be seen in the figure, silicon clusters up to Si_7^+ are clearly ejected. The transformation from time to m/q (mass over charge), referred to as *mass spectrum* in the following sections, involves identifying two known masses from the TOF spectrum and then calibrating the whole curve using Eqs.3.10 and 3.11. From Fig.5.1, we can clearly identify Si ion peak at 16950 ns and Si_5^+ cluster at 37334 ns. We can choose these two points and transform the TOF spectrum to mass spectrum. Fig.5.2 shows the corresponding mass spectrum of the TOF spectrum shown in Fig.5.1 with the vertical axis in log scale.

The area of the peaks corresponds to the abundance of the respective Si ion or clusters. The threshold fluence at which we start to observe ejected Silicon ions is

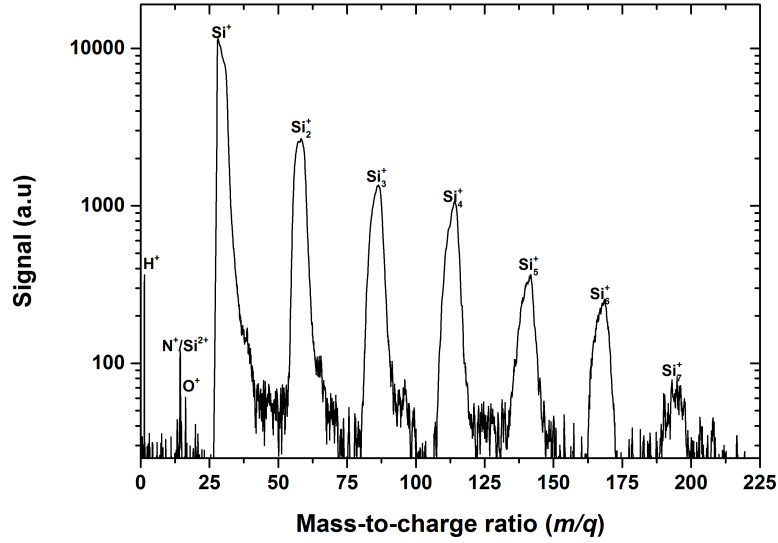


Figure 5.2: Recorded Time-of-Flight mass spectrum from a silicon sample at fluence of $\sim 150mJ/cm^2$. Vertical axis is in log scale.

$\approx 75mJ/cm^2$. This value is $\approx 15\%$ lower than the threshold value we derived from the diameter regression technique mentioned in chapter 4.

Fig.5.3 shows the yield of Si_n^+ (up to $n = 7$) at fluence of $\approx 150mJ/cm^2$. The plot in log scale is shown in the inset. It can be seen from the plot that the relative abundance of Si_n^+ ($n=1$ to 4) goes as n^{-2} and of Si_n^+ ($n=5$ to 7) as n^{-4} . This is different to that reported in [104] where the authors observed Si_n^+ clusters, for $n>3$, in high abundance with $n = 6$ having the highest amplitude. The abundance distribution was alternating between low and high with N in their case, with preferred formation of even number Si_n^+ clusters. However it should be noted that they observed this trend during the initial shots, whereas our signal is the average of 2000 pulses.

We have observed that with fluence in the range: (F_{th}) to $3x(F_{th})$, the number of silicon ions and clusters increase. However, the increase is not even for $n = 1$ to 7. The slope for $n = 1$ to 4 changes from n^{-2} to $n^{-2.4}$, the slope for $n = 5$ to 7, doesn't change. Beyond $3x(F_{th})$ fluence, the silicon ion yield increases while the observed clusters decrease. At fluence above $4x$ the threshold values, the number of clusters start to decrease drastically and instead multiply charged silicon ions show up.

Fig.5.4 shows the TOF spectrum of silicon sample at fluence of $2.2J/cm^2$. The corresponding mass spectrum is shown in Fig.5.5 in logarithmic scale.

Fig.5.6 shows the singly charged and multiply charge Si ions yield with fluence

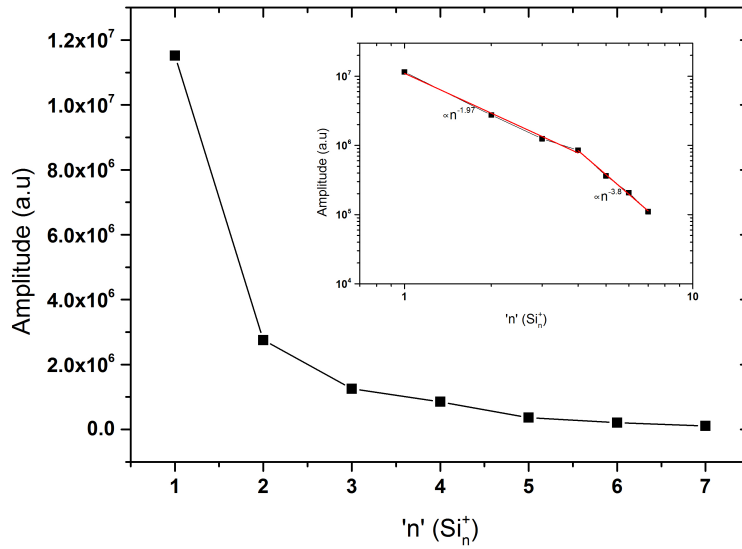


Figure 5.3: Si_n^+ yield at fluence of $\sim 150 mJ/cm^2$. Plot in the inset is in log scale.

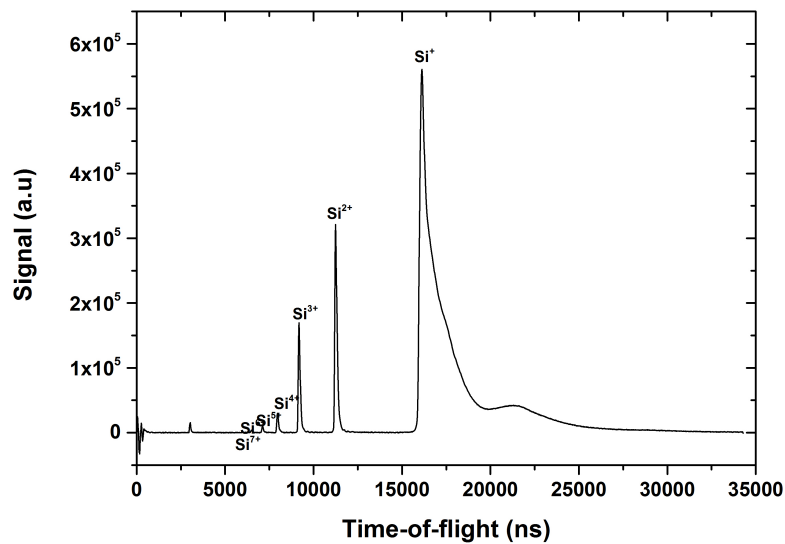


Figure 5.4: Recorded Time-of-Flight spectrum from a silicon sample at fluence of $\sim 2.2 J/cm^2$.

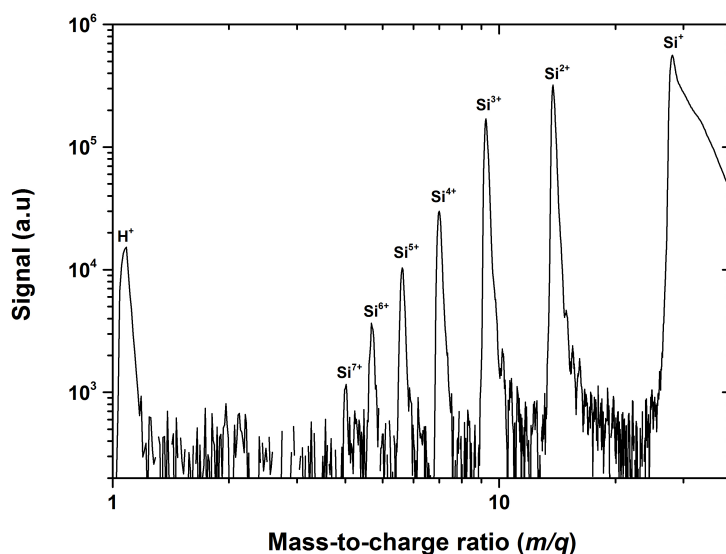


Figure 5.5: Recorded Time-of-Flight spectrum from a silicon sample at fluence of $\sim 2.2J/cm^2$.

Table 5.1: Ionization energies of Silicon.

No.of electrons	Ionization Energy (eV)
1	8.15169
2	16.34585
3	33.49302
4	45.14181
5	166.767
6	205.27
7	246.5

when irradiated with 10 fs pulses. Many interesting observations can be made from the graph. The singly charge ion signal rises sharply initially and then saturates. During the rise, it goes as F^6 indicating a 6 photon absorption. Table 5.1 shows the ionization energies of silicon [105].

As can be seen in the table, to singly ionize silicon atoms, ~ 8.15 eV is required. With photons of energy 1.55eV, it would take 6 photons, to act together to overcome the ionization energy. We noticed a F^6 dependence of singly charged silicon ion yield as shown in Fig.5.6. For doubly charging silicon atoms, an ionization energy of 16.3 eV is needed. However, we noticed only F^7 dependence on Fluence. Indicating that collisional ionization could be the dominant process to multiply ionize the silicon atoms.

The threshold fluences to start recording Si^+ , Si^{2+} , Si^{3+} , Si^{4+} with 10 fs pulses are found to be $\sim 75mJ/cm^2$, $\sim 350mJ/cm^2$, $\sim 550mJ/cm^2$, and $\sim 900mJ/cm^2$

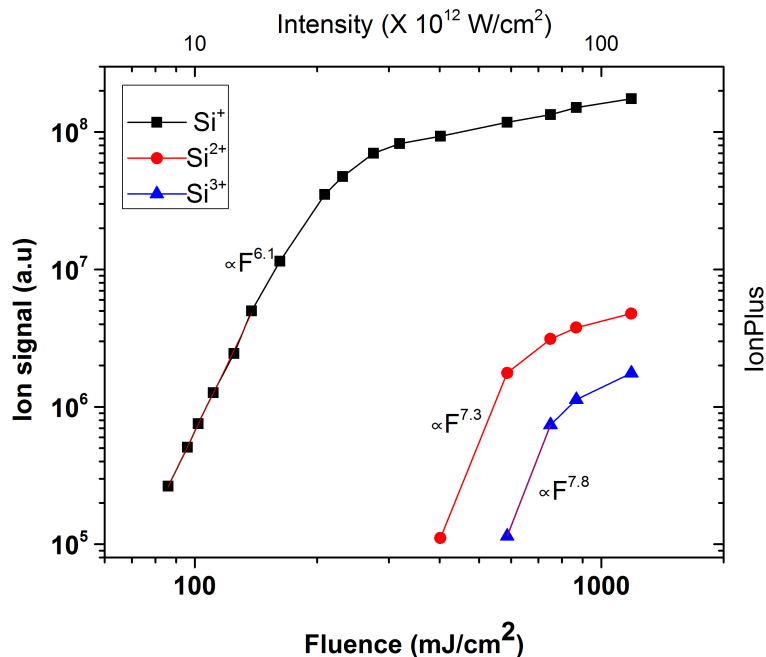


Figure 5.6: Dependence of silicon ion yield with fluence.

respectively.

The threshold fluences to start recording Si^+ , Si^{2+} , Si^{3+} , Si^{4+} for 30 fs pulses are respectively, $\sim 95 mJ/cm^2$, $\sim 380 mJ/cm^2$, $\sim 580 mJ/cm^2$, and $\sim 950 mJ/cm^2$.

Fig.5.7 shows the dependence of silicon ion yield with pulse duration, for three different fluences ($150 mJ/cm^2$, $300 mJ/cm^2$, $400 mJ/cm^2$). With the increase in fluence, the pulse duration seems to have less effect on the ion yield. This suggests the dominant process of ionization with higher fluence is impact ionization where as at lower fluence levels, multiphoton ionization is the dominant process.

5.1.2 Neutrals Emission

In order to detect the neutral particles ejected from the target a setup comprising of two synchronized amplifiers was used. The setup is shown in Fig.3.11. The first laser beam, called ablation beam is focused on the target triggering the ablation process. The emitted ions are accelerated by the applied extraction voltage of 3 kV, and the neutrals fly with their initial kinetic energies. The second laser beam, called the post ionization (PI) beam with a timing that is delayed with respect to the ablating pulses, travels parallel to the target surface and is focussed 3mm in front of the target. The neutral particles travelling through the focal volume of the post ionizing laser beam get ionized and then are accelerated by the extraction voltage and travel through the TOFMS in a similar way like that of the ions emitted by the

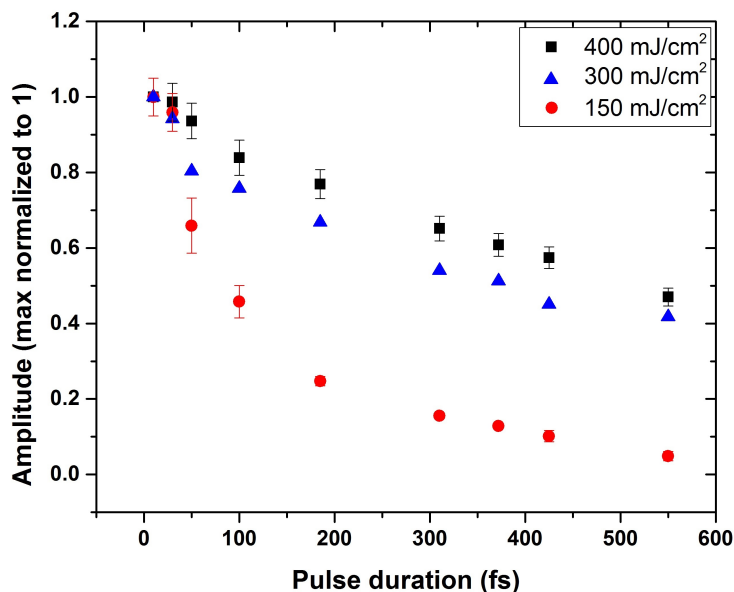


Figure 5.7: Dependence of silicon ion yield on pulse duration.

Table 5.2: Abundance of silicon dimers.

	$^{28}\text{Si} + ^{28}\text{Si}$	$^{28}\text{Si} + ^{29}\text{Si}$	$^{28}\text{Si} + ^{30}\text{Si}$	$^{29}\text{Si} + ^{29}\text{Si}$	$^{29}\text{Si} + ^{30}\text{Si}$	$^{30}\text{Si} + ^{30}\text{Si}$
Mass (a.u)	56	57	58	58	59	60
Calculated abundance	74%	15.5%	8.6%	0.8%	0.9%	0.2%
Measured abundance	73%	16.6%		9.7%	not measurable	not measurable

ablation process.

Fig.5.8 shows the typical mass spectrum of Si neutrals, The ablated neutrals were ionized with the post-ionizing laser beam (from Amplifier 2) passing 3 mm in front and parallel to the target. The delay between the ablation pulse and the post-ionizing pulse is $2 \mu\text{s}$ in this case. The resolution of the reflectron TOFMS is high enough to resolve one unit of atomic mass (see inset in Fig.5.8). Thus, the TOFMS can easily separate the different isotopes of any element even heavy elements. From this highly resolved mass spectrum the abundance of different isotopes can be obtained. The results show that the abundance of Si isotopes with atomic mass of 28, 29, and 30 is 86%, 9% and 5% respectively.

Fig.5.9 shows the mass spectrum of the emitted dimers and trimers. It is interesting to notice the formation of dimers and trimers with all three isotopes of silicon. But owing to the different abundance values of ^{28}Si , ^{29}Si and ^{30}Si , the probability of different dimers/trimers formation is different. Table 5.2 shows the probability of forming different dimers, calculated purely based on their abundance, and the experimentally measured values. The calculated values match with the experimentally measured values.

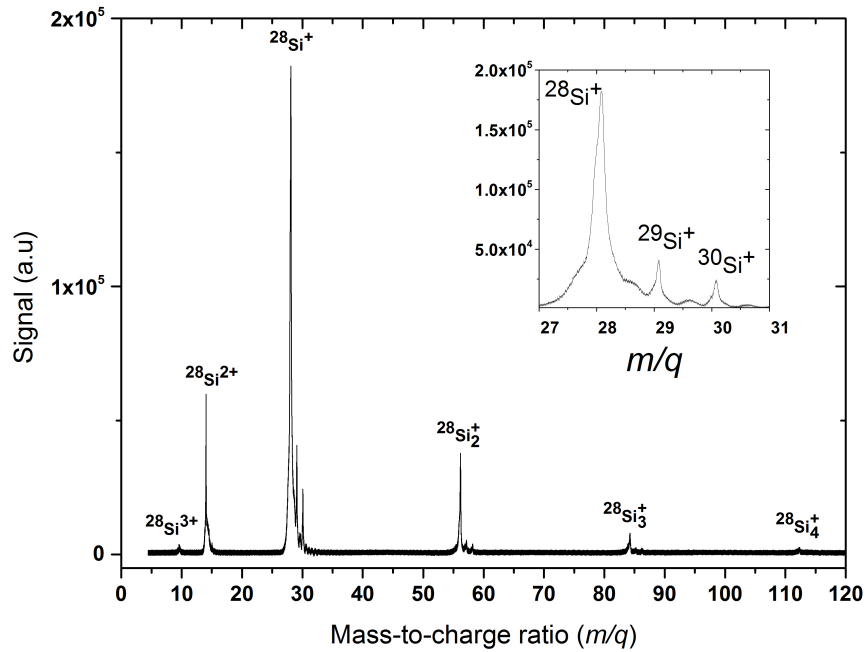


Figure 5.8: Time of flight spectrum of neutrals emitted from silicon target upon irradiation by 10 fs laser pulses and $\approx 500 \text{ mJ/cm}^2$.

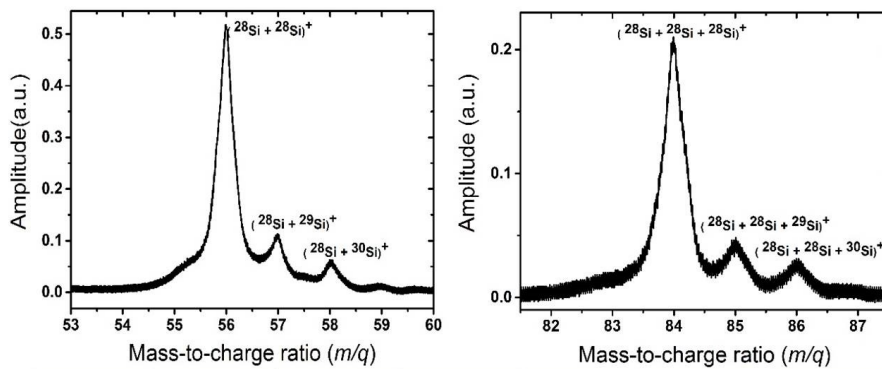


Figure 5.9: Mass spectrum of the emitted dimers and trimers when silicon is irradiated with 10 fs pulses.

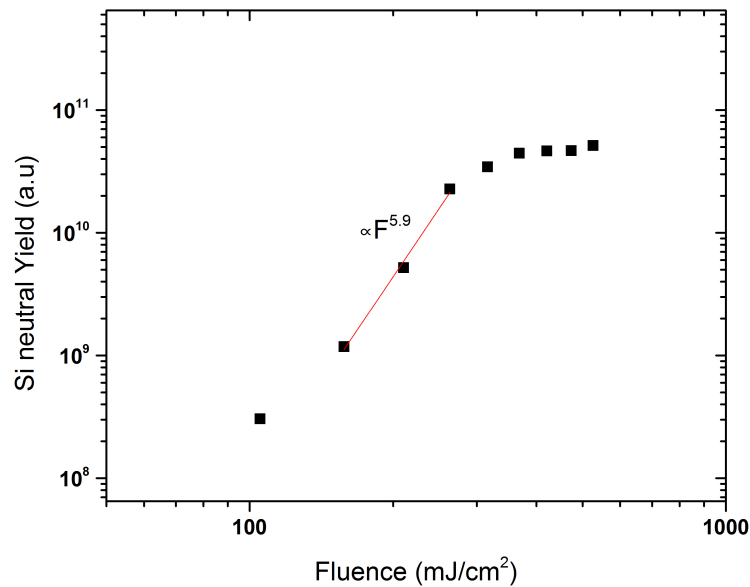


Figure 5.10: Dependence of neutrals emission on fluence when irradiated with 10fs laser pulses.

Fig.5.10 shows the silicon neutral emission with laser fluence when irradiated with 10 fs. As can be seen from the figure, the dependence of the neutrals yield on fluence goes as F^6 in the fluence range $\sim 100\text{-}300 \text{ mJ/cm}^2$. This dependence is strikingly similar to that of ion dependence on fluence.

5.1.3 Velocity spectrum

The velocity (energy) spectrum of the neutral particles ejected from the target can be obtained by recording the neutral signal as a function of the delay between the ablating pulses and the post ionizing pulses. This delay corresponds to the time the neutrals take to travel from the target surface to the focal position of the post ionizing beam. By scanning the delay between the two laser pulses from zero to several micro second in steps of a few tens of nanoseconds and measuring the total number of the ejected neutrals from the detected mass spectrum, the velocity spectrum of the neutrals can be obtained. In order to measure a reliable velocity spectrum a few points should be considered.

1. To convert the TOF spectrum of neutrals to their velocity or kinetic energies, the distance between the target and the post ionizing beam focus must be known precisely. Therefore this distance has to be precisely determined.

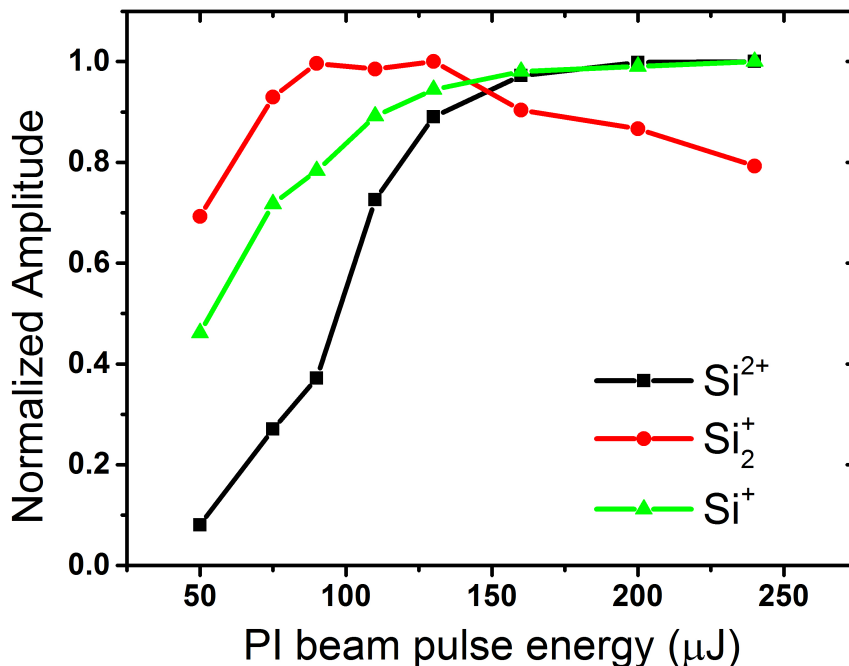


Figure 5.11: Dependence of number of neutrals ionized by the PI beam with respect to PI pulse energy.

2. To measure the exact amount of emitted neutral all of the neutrals at the focal volume of the PI beam have to be ionized by the PI pulse. Therefore, the post-ionizing pulse should be intense enough. In order to verify if this criterion is met, we studied the influence of post-ionizing pulse energy on the detected neutrals. Fig.5.11 shows that as the post-ionizing pulse energy increases the Si^+ , Si^{2+} signal becomes stronger and then for pulse energies over $200 \mu J$ the signal is saturated indicating that all neutrals have been ionized at this intensity level.

The dimer signal (Si_2^+ signal) also increases first with pulse energy but eventually decreases at higher pulse energies. This is due to the fragmentation and decomposition of the dimer particles into single atoms and contributes to the single or doubly charged signals. For all velocity spectrum measurements reported in this thesis, we used post ionizing pulse energy of $>200 \mu J$, and therefore ensuring that all neutral particles are ionized at the focal volume.

Fig.5.12 shows the velocity spectrum of the neutrals emitted when irradiated with $170 mJ/cm^2$ and $290 mJ/cm^2$ of 10 fs duration.

For better visualization, the velocity spectrum is presented as a function of the delay time between the ablation beam and the PI beam, which is the time the neutrals take to travel from the target to the post ionizing point. This helps to distinguish the different peaks and ascribe them to different processes taking place. However, one can easily convert the neutral's TOF spectra to the velocity or kinetic energy

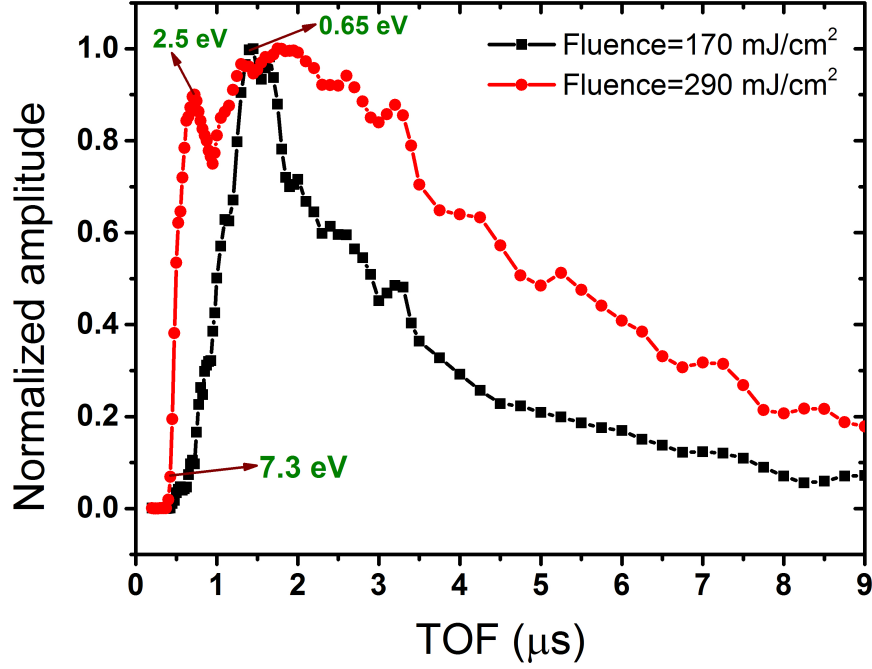


Figure 5.12: Time of flight distribution of silicon neutrals when irradiated with 10 fs pulses.

spectra using the following relations¹

$$f(v) = f(t) \frac{t^2}{x} \quad (5.1)$$

and,

$$f(E) = f(t) \frac{t^3}{mx^2} \quad (5.2)$$

Where, E is the kinetic energy, m is the mass of the neutral atoms and $f(E)$ is the calculated number of neutrals having kinetic energy E .

¹ $v = x/t, dv = \frac{x}{t^2} dt = \frac{v^2}{x} dt; f(t).dt = f(v)dv; f(v) = \frac{f(t)dt}{dv} = f(t) \frac{x}{v^2}; \text{and } E = mv^2/2; E = mx^2/2t^2; dE = mv dv, dE = \sqrt{2mE} dv; f(E)dE = f(v)dv; f(E) = f(v) \frac{1}{\sqrt{2mE}}; \text{or } f(E) = f(t) \frac{t^3}{mx^2}$

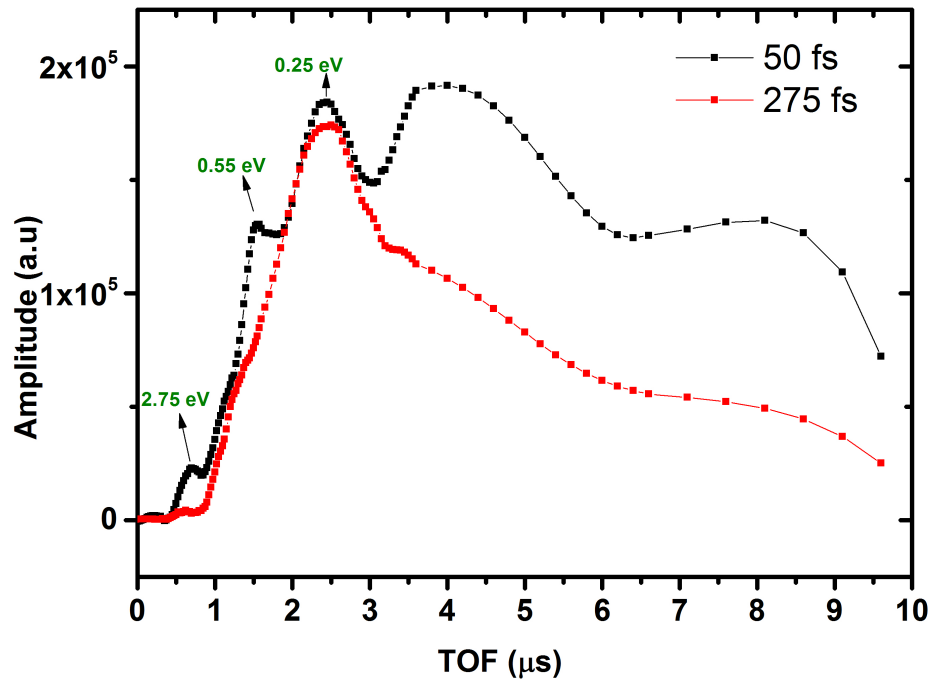


Figure 5.13: Time-of-flight distribution of silicon neutrals when irradiated with pulses of 50 fs and 275 fs and fluence of $\approx 290 \text{ mJ/cm}^2$.

Fig.5.12 and Fig.5.13 shows the TOF distribution of Si neutrals with fluence and pulse duration respectively. It can be seen from the figure that the neutral distribution depends strongly on both fluence and pulse duration of the laser pulses. At fluence of 290 mJ/cm^2 , it can be noticed that the TOF distribution obtained with 10 fs pulses shows two peaks. One sharp peak at $0.72 \mu\text{s}$ corresponding to neutrals having 2.5 eV (or velocity of 4.2 km/s), which can be attributed to the fast process or non-thermal processes and the other peak at $\sim 1.41 \mu\text{s}$, corresponding to 0.65 eV neutrals or 2.1 km/s velocities.

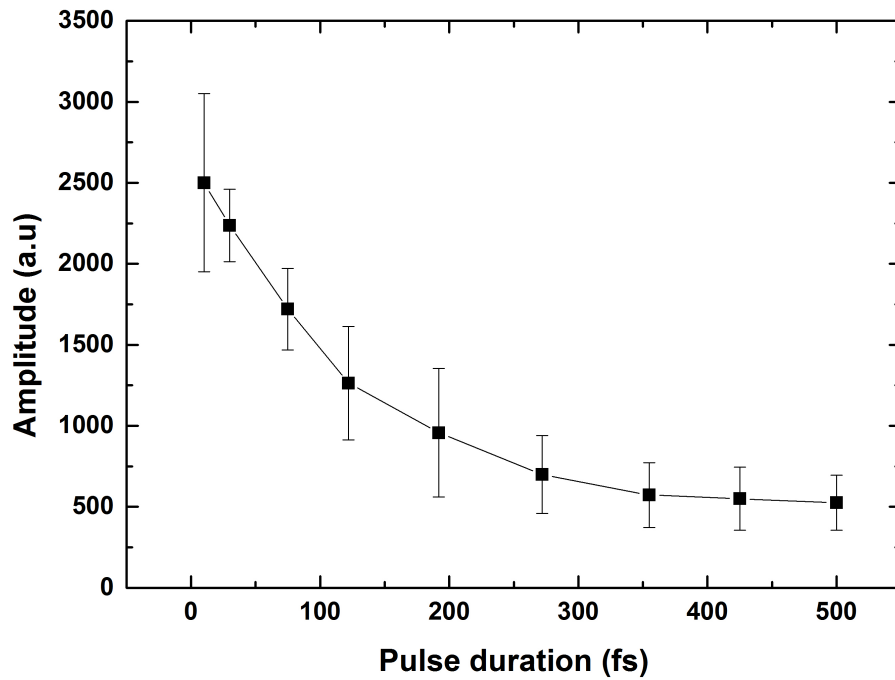


Figure 5.14: Silicon neutrals yield with pulse duration when irradiated with pulses of $\approx 200mJ/cm^2$.

Fig.5.14 shows the neutrals yield with pulse duration when the ablating beam fluence was $200 mJ/cm^2$. By increasing the fluence, the neutral signal is masked by the ion signal making it difficult to estimate the neutral yield, but roughly it could be observed that the yield is more or less the same for all pulse durations.

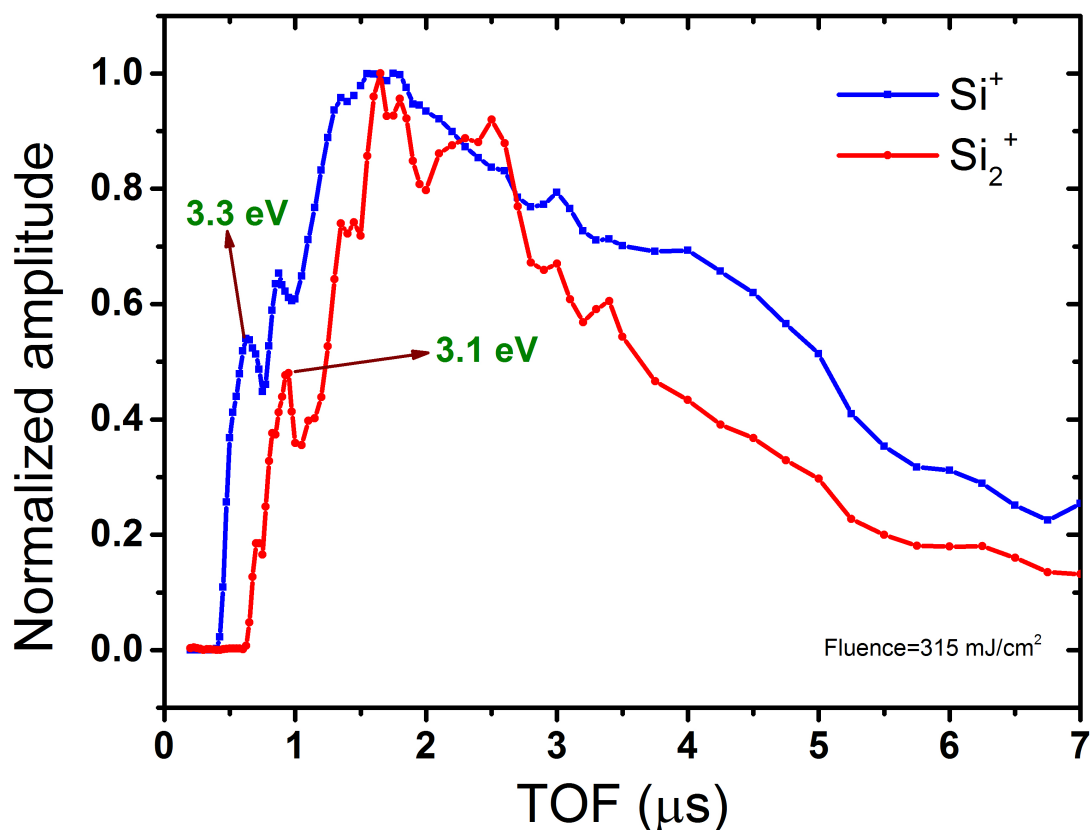


Figure 5.15: Silicon and silicon dimer yield when irradiated with pulses of $\approx 315 \text{ mJ/cm}^2$.

Fig.5.15 shows the spectrum of singly charged Si atom and singly charged Si dimer. The fastest silicon atoms and silicon dimers have been detected at TOF of 450 ns and 650 ns respectively giving a ratio of $\sqrt{2}$.

5.2 Copper

Copper is a chemical element with atomic number 29. It is found as a pure metal in nature. Copper was the first metal to be smelted or cast into a shape in a mold or purposefully alloyed with another metals by humans as early as 4000 BC. It is good conducting metal and is extensively used in a wide variety of applications even now. There are 29 isotopes of copper, of which isotopes ^{63}Cu and ^{65}Cu are stable with ^{63}Cu comprising approximately 69% of naturally occurring copper. The copper samples used in the TOF experiments are 1 mm foils (metal basis, 99.99% purity, Alfa Aesar GmbH) cut to 1x1 mm size and mechanically polished to mirror like surfaces.

5.2.1 Ion Emission

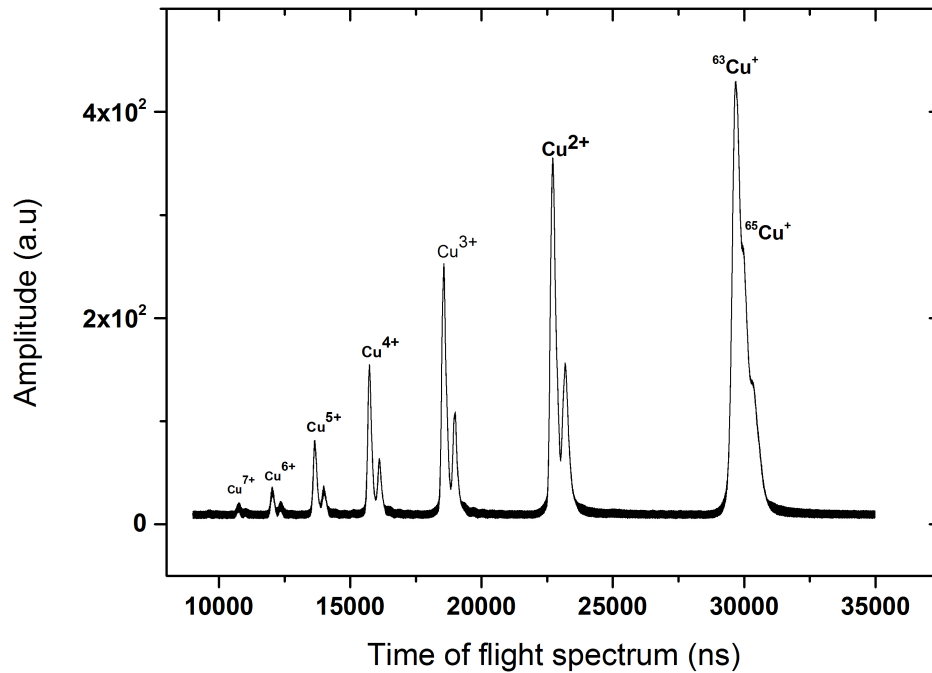


Figure 5.16: Time-of-flight mass spectrum of copper sample when irradiated with 10 fs pulses of fluence $\approx 1.4J/cm^2$.

Fig.5.16 shows the typical TOF spectrum of Cu obtained when irradiated with 10 fs pulses and fluence of $1.4J/cm^2$. As can be seen in the figure, Cu singly charged and multi-charged signals upto $q=8$ can be detected at this fluence range. In comparison with silicon, copper signal didnot show cluster peaks at any fluence range. Indicating that cluster formation is typical in semiconductors.

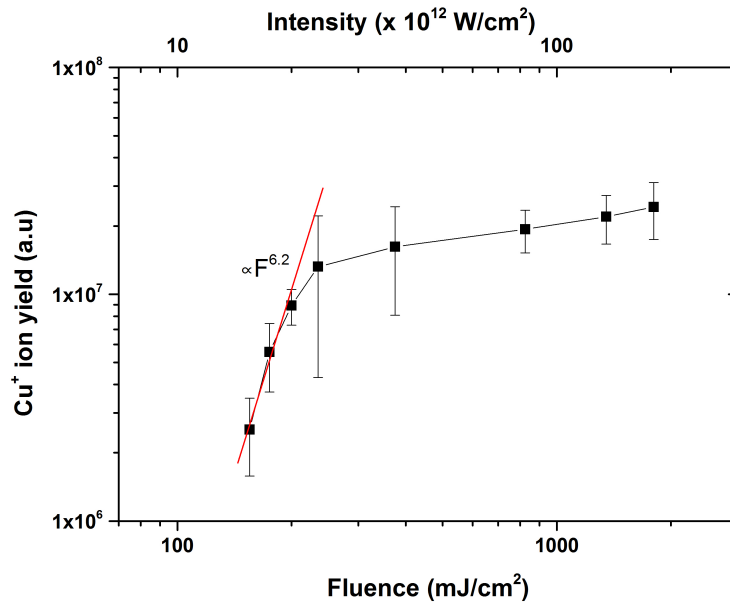


Figure 5.17: Dependence of copper ion yield on fluence.

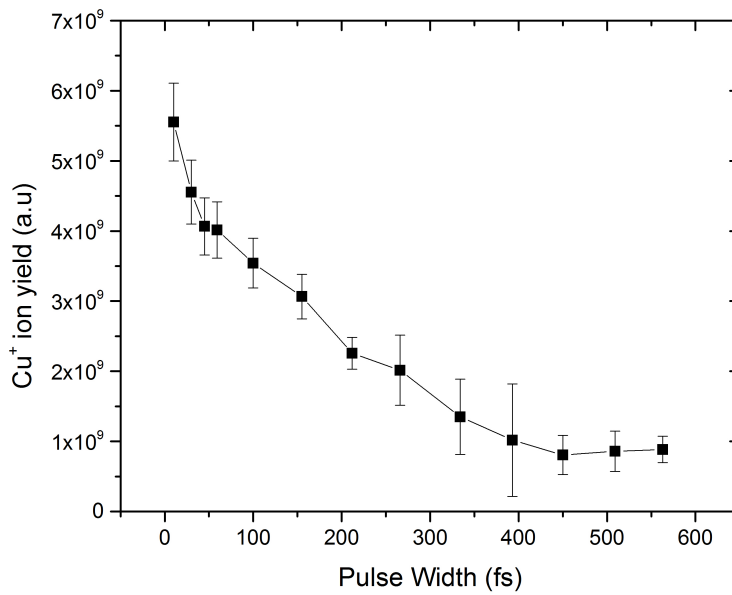


Figure 5.18: Dependence of copper ion yield on pulse duration when the fluence is ~ 200 mJ/cm².

Fig.5.17 and Fig.5.18 shows the dependence of singly charged Cu ions signal on fluence and pulse duration respectively. It should be mentioned that for some reason the fluctuations in ion signal with copper sample was very high. Another sample that showed such fuctuations was gold sample, while signal from samples like silver, titanium and aluminium was very stable.

5.2.2 Neutral Emission

Fig.5.19 shows the time-of-flight spectrum of Cu neutrals. It should be noted that the doubly charged copper signals seen are a result of the neutrals being doubly ionized by the PI beam and not the singly charged ions emitted by ablation being ionized again at the PI beam focus. Since the ions emitted by the sample will see the extraction voltage, they will acquire much higher velocities and pass through the reflectron.

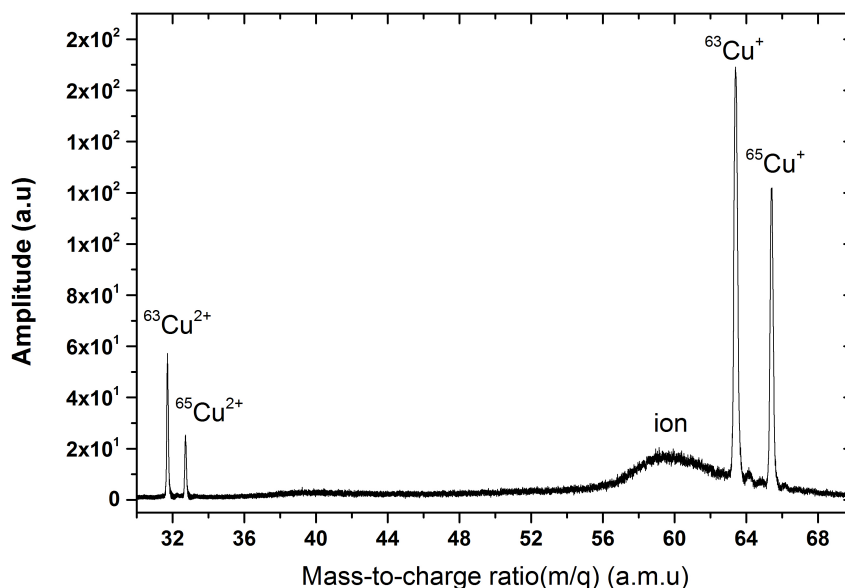


Figure 5.19: Time-of-flight mass spectrum of neutral copper atoms emitted from copper sample when irradiated with 10 fs pulses of fluence $\approx 500 \text{ mJ/cm}^2$.

5.2.3 Velocity spectrum

Fig.5.20 shows the time-of-flight distribution spectrum of Cu neutrals. It can be seen in the figure that the fast peaks observed in copper are not very prominent than that observed in other samples. Though not prominent, two peaks at 3.25 eV and 1.16 eV are consistently seen in all the measurements.

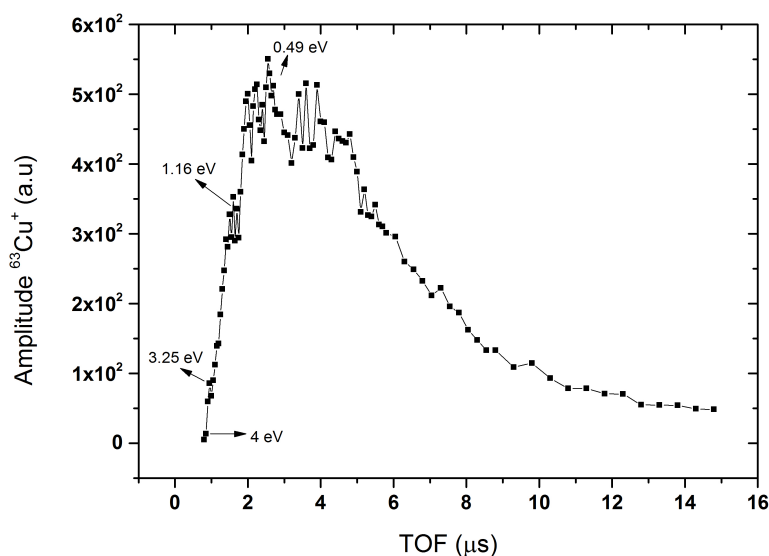


Figure 5.20: Time-of-flight mass spectrum of neutral copper atoms emitted from copper sample when irradiated with 10 fs pulses of fluence $\approx 250 \text{ mJ/cm}^2$.

5.3 Titanium

Titanium with atomic number 22 and 5 stable isotopes ^{46}Ti , ^{47}Ti , ^{48}Ti , ^{49}Ti , ^{50}Ti is an extensively used metal because of its corrosion resistance and highest strength-to-density ratio. Fig.5.21 shows the ion spectra recorded by the time-of-flight spectrometer of the titanium sample. 5.22 shows the pulse duration dependence of the ejected singly charged and doubly charged ions. It can be seen that the doubly charged ion emission is strongly dependent on the pulse duration. 5.23 shows the time of flight mass spectrum of titanium neutrals. The peaks corresponding to 5 isotopes can be clearly seen and their abundance can be measured. The abundance was found to be 7.5%, 7%, 73.4%, 6.5%, and 5.6%. The reflectron settings were so chosen that the original ions travel through the reflectron and are not reflected, thus the ion signal is suppressed and the neutral signal is free of background ion signal.

5.3.1 Ion Emission

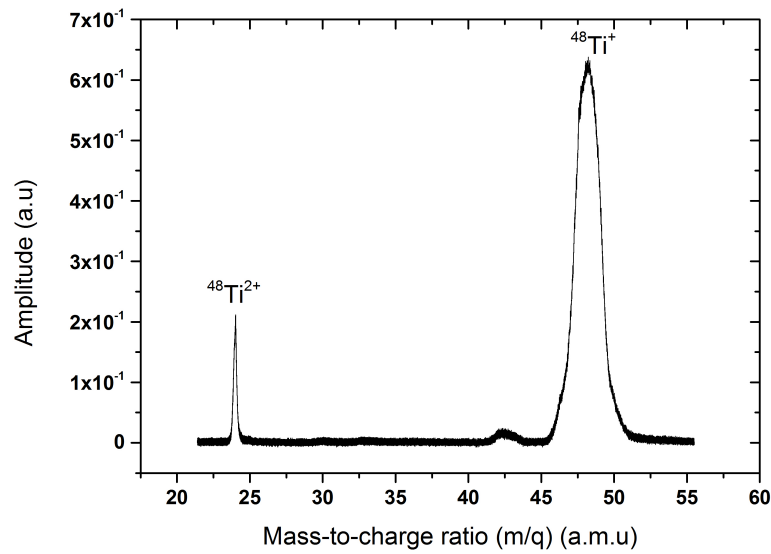


Figure 5.21: Time-of-flight mass spectrum of titanium sample when irradiated with 10 fs pulses of fluence $\approx 500 \text{ mJ/cm}^2$.

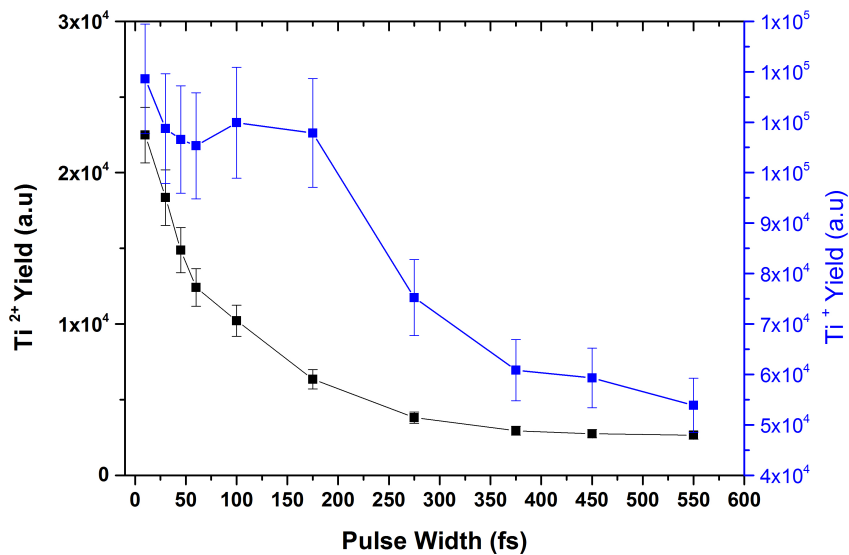


Figure 5.22: Pulse duration dependence of titanium singly and doubly charged ion emission when irradiated with pulses of fluence $\approx 500 \text{ mJ/cm}^2$.

5.3.2 Neutral Emission

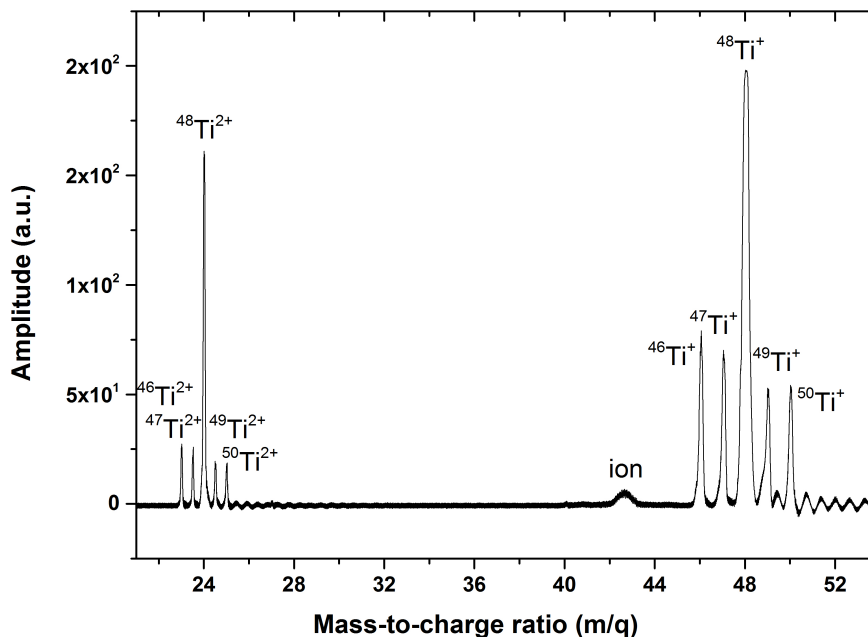


Figure 5.23: Time-of-flight mass spectrum of neutral atoms emitted from titanium sample when irradiated with 10 fs pulses of fluence $\approx 140 \text{ mJ/cm}^2$.

5.3.3 Velocity spectrum

5.24 shows the velocity spectrum of titanium neutrals when the ablation beam fluence was 140 mJ/cm^2 . The post ionizing pulse energy was $> 250 \mu\text{J}$ to ensure all the neutrals at the focal volume are ionized. The time-of-flight distribution of neutrals shows a remarkable triple-peak structure: two pronounced high energy non-thermal peaks corresponding to kinetic energies of 7 eV and 3 eV representing velocity groups which can be attributed to two ultrafast electronic processes of Coulomb explosion and rapid plasma formation; and a peak which according to its kinetic energy of 0.3 eV can be attributed to the thermal processes. Coulomb explosion is a violent ablation process resulting in ejection of particles with the highest kinetic energies upto 10 eV. By increasing the ablation fluence, the thermal peaks becomes broader and eventually covers the gentle peak making it harder to distinguish between different distinct processes.

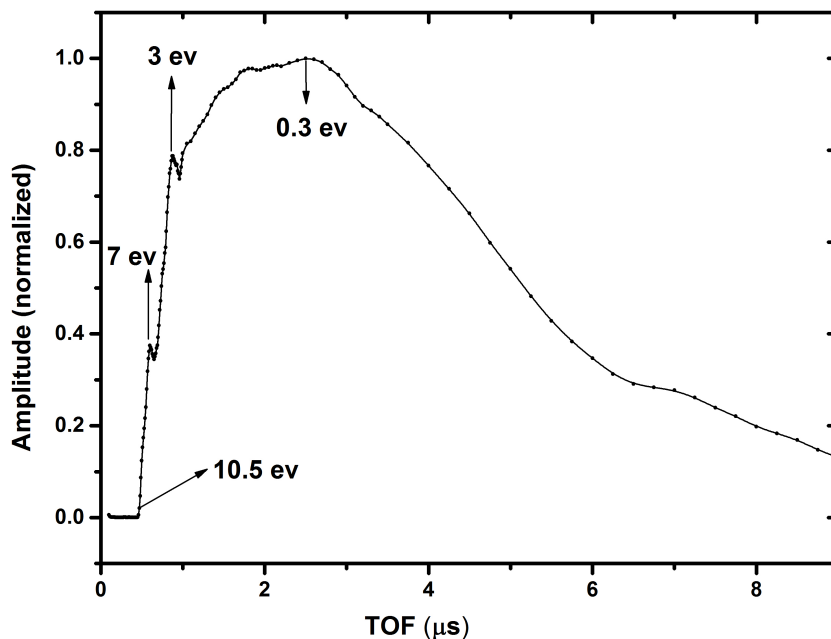


Figure 5.24: Time-of-flight distribution of titanium neutrals emitted when irradiated with 10 fs pulses of fluence $\approx 140 \text{ mJ/cm}^2$.

5.4 Silver

Silver is a metallic element with atomic number 47 and two stable isotopes ^{107}Ag and ^{109}Ag with ^{107}Ag being slightly more abundant. Fig.5.25 shows the dependence of ion emission with pulse duration. It can be seen that as the fluence is increased, the ion emission becomes insensitive to pulse durations indicating that for shorter pulse durations multiphoton process is a dominant process, but as the fluence is increased other processes like impact ionization becomes the dominant process. Fig.5.26 and Fig.5.27 shows the time-of-flight mass spectrum of neutral atoms emitted from silver sample when irradiated with 10 fs pulses of fluence $\approx 300 \text{ mJ/cm}^2$ and the velocity spectrum of Ag neutral atoms when irradiated with 10 fs pulses at two different fluence values respectively. Fig.5.28 shows the total neutral yield (obtained by integrating the time-of-flight distribution curve from 0 - 10 μs) for two different fluences.

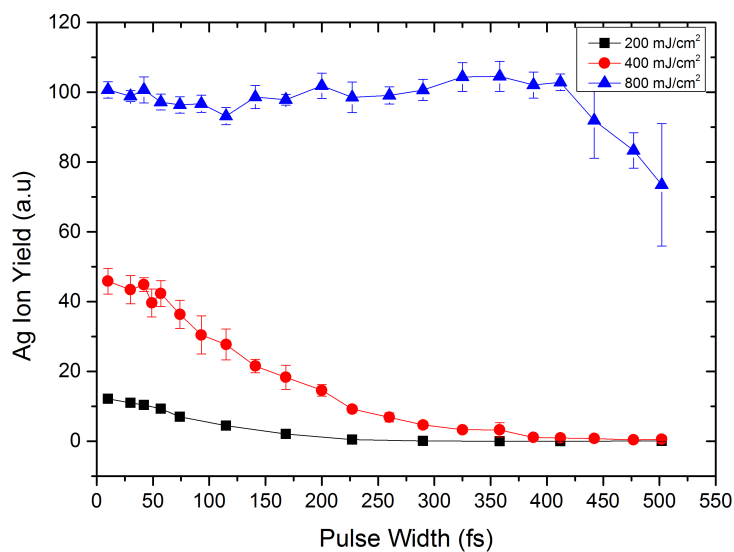


Figure 5.25: Dependence of Ag ion emission on pulse duration.

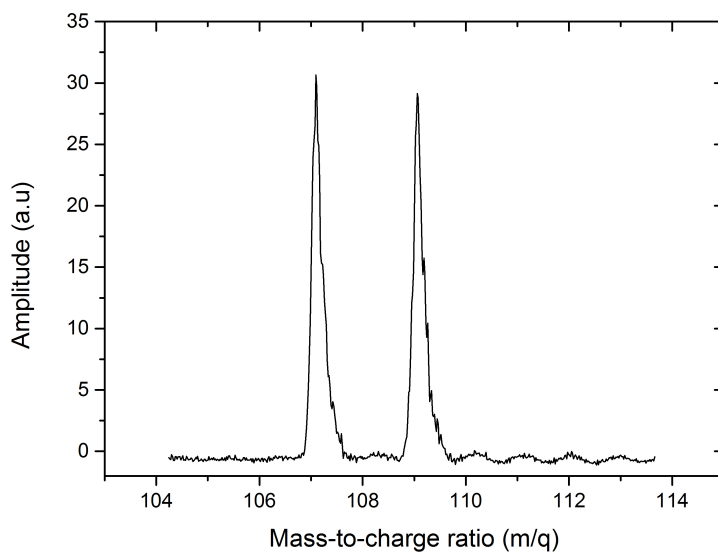


Figure 5.26: Time-of-flight mass spectrum of neutral atoms emitted from silver sample when irradiated with 10 fs pulses of fluence $\approx 300 \text{ mJ/cm}^2$.

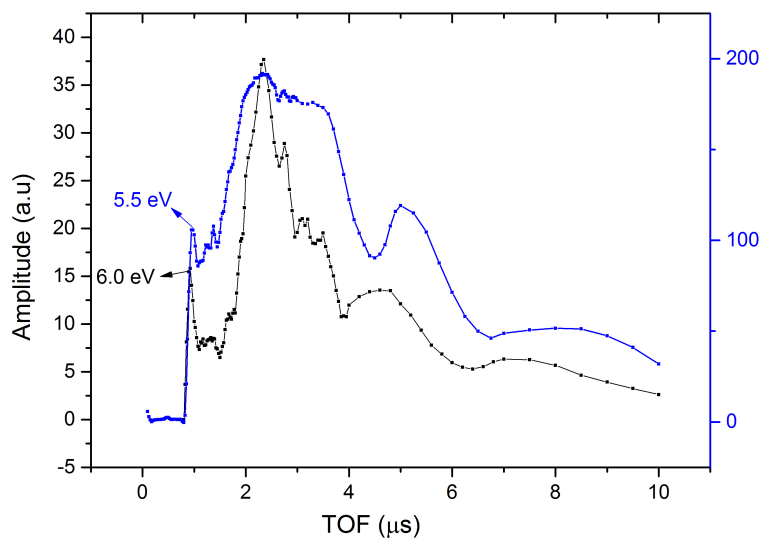


Figure 5.27: Velocity distribution of Ag neutral atoms when irradiated with 350 mJ/cm^2 (blue curve) and 200 mJ/cm^2 (black curve)

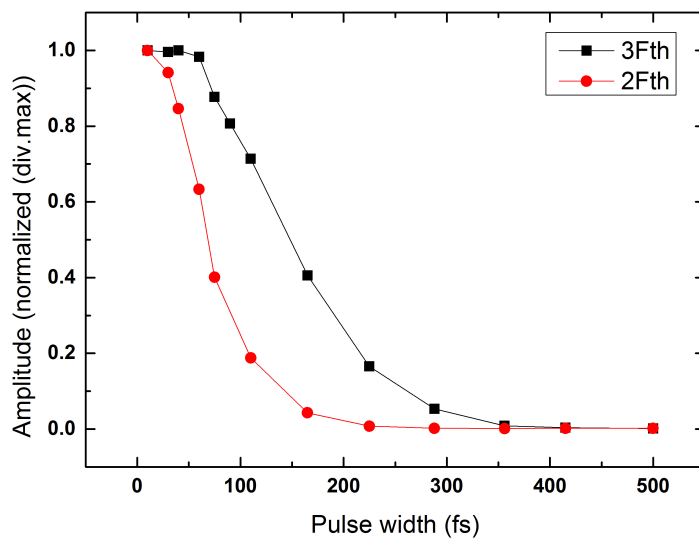


Figure 5.28: Dependence of Ag neutral emission on pulse duration.

5.5 Discussion

The nature of processes which govern the interaction of ultrashort laser radiation with materials can be a complex interplay between ultrafast processes and thermal processes. Ultrafast processes occur before thermalization between the atoms and

the hot electrons can take place. Two interesting examples of this class of phenomena are ultrafast melting (UFM) and Coulomb explosion (CE). For UFM the photoexcited high density electron-hole plasma causes destabilization of the lattice, and the material melts in a time less than 1 ps [24], and CE can occur when parts of the lattice become charged due to stripping of their outer valence electrons. The repulsive electrostatic energy, initially stored in the charged region, leads to a local state with ultra high pressure and stress. During the relaxation process, part of the potential energy propagates into the surrounding region while the remainder is converted into kinetic energy, resulting in a Coulomb explosion. Within less than 1.0 ps, a nanometer-sized hole on the surface is formed. This happens under this assumption that the electrons are removed sufficiently fast so that the solid cannot replenish them and thus, a localized region of the surface can become charged [106]. As far as laser ablation is concerned, in particular, CE is of interest.

Based on the results presented in the above sections, we can attempt to address the fundamental questions on the formation and emission of different species emitted when an ultrashort laser pulse irradiates a sample. Primarily the following observations can be directly made:

1. The dependence of ion emission from silicon (Fig.5.6) and copper (Fig.5.17) with fluence look very similar. For fluences in the range F_{th} to $3x F_{th}$, the ion yield goes as F^6 indicating a 6 photon absorption for both silicon and copper in this fluence range. We can infer that multi-photon absorption process can take place in metals too. It could also be stated that semiconductors exhibit metal like behaviour when irradiated with ultrashort laser pulses, thereby removing the distinction between the type of material. However, it should be noted that I^6 yield doesn't necessarily indicate a 6-photon absorption process and can be a result of other processes.
2. Like ions, the neutral emission of silicon (Fig.5.10) too goes as F^6 . (This trend is observed in metals too).
3. At low fluences, the yield of ions (Fig.5.7 in Si, Fig.5.18 in Cu, Fig.5.22 in Ti, Fig.5.25 in Ag) and neutrals (Fig.5.14 in Si, Fig.5.28 in Ag) with pulse duration look very identical. Is this identical behaviour of ion and neutral emission with fluence and pulse duration indicate that the emission of both these species a result of a same mechanism?
4. For doubly charging silicon atoms, an ionization energy of 16.3 eV is needed. However, we noticed only F^7 dependence on Fluence. Indicating that collisional ionization could be the dominant process to multiply ionize the silicon atoms. However, this is valid only if we assume that doubly ionizing is a two step process.
5. As the fluence increases, the dependence of ion yield on pulse duration becomes minimal. As shown in Fig.5.25, somewhere between 5 -10 times the threshold flu-

ence the ion emission doesn't depend on the pulse duration anymore atleast until 400 fs. This again suggests that the collisional ionization becomes the dominant process at fluences in the range 5-10 times the threshold fluences. Below this value, multi-photon absorption is the dominant process.

6. For the materials investigated in this work, in a particular fluence range, the emitted neutrals showed distinct peaks (Fig.5.12 in Si, Fig.5.20 in Cu, Fig.5.24 in Ti, Fig.5.27 in Ag) in the velocity spectrum corresponding to energies upto 10 eV. The origin for the emission of neutrals with such high energies is a subject of deep interest.

As shown in Fig.5.12, at lower fluence of 170 mJ/cm^2 the interaction of ultrashort radiation with Si, for example, leads to heating the lattice and consequently to thermal ablation emitting silicon neutral atoms and clusters. The velocity distribution reveals a peak at 0.65 eV which cannot be attributed to a fast ablation process. At higher fluence of 290 mJ/cm^2 in addition to the thermal peak another gentle peak appears in the velocity spectrum. This peak corresponds to a kinetic energy of 2.5 eV (or velocity of 4.2 km/s). Observing this peak and higher kinetic energies up to 8 eV in the velocity spectrum presents good evidence to conclude that fast ablation process like Coulomb explosion takes place. An observation that support the CE mechanism is the momentum scaling for the particles. Fig. 5.15 shows the spectrum of single charged Si atom in comparison with single charged Si dimer (once again note that these are neutral atoms or dimers ionized by PI beam). Since the Si dimer has a mass twice larger than Si atom therefore its TOF spectrum should be recorded basically $\sqrt{2}$ times later than that of Si atom, if they are both formed by CE mechanism. This can be clearly seen in fig.5.15. The fastest silicon atoms and silicon dimers have been detected at TOF of 450 ns and 650 ns respectively giving the ratio very close to $\sqrt{2}$. Unfortunately clusters are not observed in metals to put forward a similar argument.

Comparing the velocity spectrum of Si atom at two different fluences in Fig.5.12 and Fig.5.15 reveals two facts. 1) The gentle peak ascribed to fast process shifted to higher kinetic energy (from 0.25 eV to 3.3 eV) with increasing ablating fluence. This behaviour is observed in all the samples investigated. It is reasonable to expect such behaviour since in a fast ablation process, for instance CE, higher deposition of laser light energy leads to higher density of local charge in the exposed area and then results in more violent explosion and thus faster ejected particles. 2) The fast process peak becomes less pronounced with increasing the fluence since for higher fluences the thermal peak becomes much broader that it covers the gentle fast process peak and thus it is not practically feasible to distinguish these two different peaks.

In ultrafast laser ablation experiments, ions with kinetic energy of several tens of

eV have been observed [23] whereas we observed the neutral's maximum kinetic energies in the range of only several eV. If ions and neutrals are emitted by the same underlying mechanism, then their velocities are expected to be in the same order. So probably the emitted neutral particles are formed from the original ions (in the bulk and during the emission process), which are neutralized by electron capture in the vicinity of the surface. So the velocities of charged particles following disintegration by CE will be determined by the repulsive Coulomb forces, while neutral particles which are ejected as neutrals from the surface obtain their velocities by collisions with fast ions and velocities of neutrals formed by 'ion capturing an electron' is determined by the velocity of the ion at the time of capturing an electron and becoming a neutral [24]. However, in the thermal regime many different mechanisms have been proposed to explain the ablation process. An example of these mechanisms is phase explosion. Particles ejected through the thermal process are very slow carrying only a fraction of eV kinetic energy.

As mentioned earlier, our studies on time-of-flight measurements showed that the thresholds for atomic emission is $\sim 15\%$ smaller than the threshold measured by Liu's method, where microscopic removal of materials and formation of surface structures is seen by SEM or optical microscope. Correlating these fluence values suggest that atomic emission starts much before any observable surface structuring takes place.

5.6 Conclusion

In this chapter the results of our time-of-flight measurements of various materials recorded after irradiating with femtosecond laser pulses of durations in the range 10 fs to 550 fs are presented. The dependence of ion and neutral emission with fluence and pulse duration showed similar trend. The recorded velocity spectras of silicon and metals, like copper, titanium and silver, showed multiple high energy peaks that could be attributed to fast processes like CE and ultrafast melting. However since ions are emitted with energies of few KeV [23] and maximum energies of neutrals recorded is only few eV, probably the emitted neutral particles are formed from the original ions, which are neutralized by electron capture in the vicinity of the surface.

Chapter 6

Laser Induced Structuring

In the last decade fabrication of micro and nanostructures on a wide variety of materials using ultrafast lasers has become quite promising for a number of applications. Different kinds of structures are formed when a femtosecond laser irradiates a material. The most well known are regular arrays of conical microstructures and periodic ripples. Fig.6.1 shows the images of the conical structures and periodical ripples formed on Steel, Titanium and Silicon after irradiation with femtosecond laser pulses. Which kind of structures form on the surface depends strongly on the laser parameters, particularly the laser fluence and the number of pulses. With conical structures, silicon exhibits a strong reduction of incident light reflection, which is why it is named as *black silicon*[107]. This can enhance the efficiency of photovoltaic solar cells[108]. Similar structures can be produced on the surface of any material. Surfaces with such structures exhibit superhydrophobicity due to lotus effect and these surfaces can be used to produce self-cleaning products[109]. Another kind of structures that are formed by ultrafast laser irradiation is periodic ripples or laser-induced periodic surface structures (LIPSS). Two kinds of ripples are formed: ripples with spatial periods slightly less than the laser wavelength and ripples whose spatial periods are significantly smaller than the incident laser wavelength. We did a systematic investigation to characterize the formation of these laser induced periodic structures and their dependence on laser parameters. In the next section the results from titanium metal are reported.

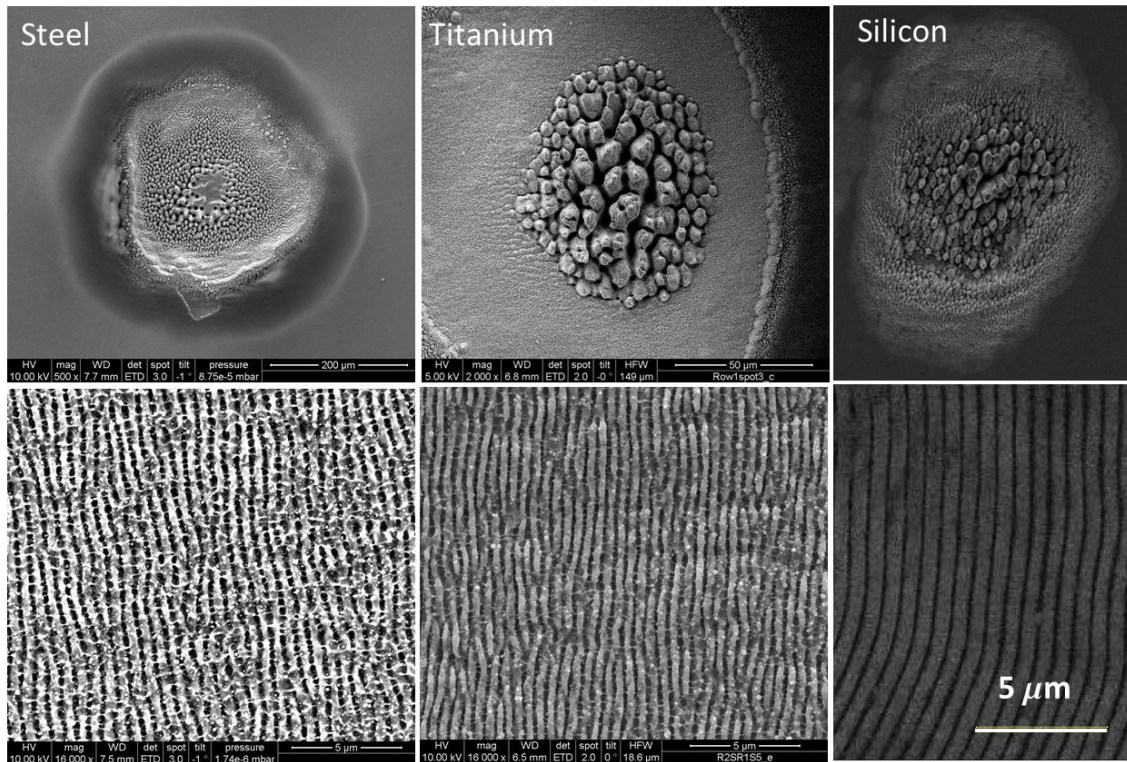


Figure 6.1: SEM micrographs of a Steel, Titanium and Silicon after irradiating with IR fs-laser pulses. Top row shows the formed conical structures and the bottom row shows the laser induced periodic ripples

6.1 Laser Induced Periodic Surface Structures on Titanium

IR fs-laser pulses have been applied successfully for the formation of surface gratings (or ripples) in air with an orientation perpendicular to the laser polarization and periods in the range $\approx \lambda$ [110–112, 62, 63, 48] widely referred to as laser-induced periodic surface structures (LIPSS). Their origin is supposed to be related to the excitation of surface plasmon-polaritons (SPP) [52, 113, 114], which are transverse magnetic (TM) waves [63, 112, 62]. However, recently observed high-spatial-frequency-LIPSS (HSFLs) on metals with orientation parallel to the laser polarization [56, 57, 115] cannot be explained via SPP excitation, existing at the negative real part of material dielectric function, or by other surface electromagnetic modes existing at the positive real part of the material dielectric function [52, 114]. In fact for example, the real part of the dielectric function of aluminum (Al) is strongly negative in the vis-IR range [116, 42], supporting only SPP (i.e. TM-modes) with wavelength values close to the exciting laser wavelengths. Therefore, it was supposed that the origin of HSFLs formation lies in the formation of cavitation instabilities in the melted surface layer [56, 57]. Recently, principally different HSFLs generation mechanism

has been proposed [117], considering multi-shot minor fs-laser oxidation of titanium (Ti) surface and third-harmonic generation at the oxidized surface to explain HSFLs appearance with periods down to one tenth of the employed fs-laser wavelengths within the common interference model [52, 113]. Another problem in understanding the origin of HSFLs with orientation parallel to the laser polarization is their distribution on the surface. Some authors reported homogeneously distributed structures [115], but in the other studies it was found that the HSFLs grow along stripes separated by distances exactly equal to the low-spatial-frequency-LIPSS (LSFLs) periods [56, 57]. Since these two types of nanoripples have been studied separately, it is still unclear whether they are connected or independent of each other. The aim of this work is to identify the common rules for femtosecond laser-induced periodic surface structures and resolve any ambiguities in the known literature data. Since LSFLs were extensively studied, we will aim to concentrate on HSFLs while constantly comparing the HSFLs with LSFLs which are also produced under exactly similar experimental conditions. We choose titanium due to its high importance in biological and medical applications, where control of morphology at nanoscale is required [118].

6.1.1 Fluence dependence

In previous studies of sub-100 nm HSFLs on titanium, HSFLs have been observed at fluences significantly lower than the single-shot ablation threshold $F_{abl} \approx 300 \text{ mJ/cm}^2$ at $\lambda \approx 800 \text{ nm}$ [119]. For instance, in work of Bonse et al. [115] a value of $F \approx 0.05 - 0.09 \text{ J/cm}^2$ with the number of pulses $N = 50$ under static irradiation has been reported. While in the work of Golosov et al. [56] a value of $F \approx 0.018 \text{ J/cm}^2$ at $N \approx 700$ in scanning regime has been reported. The periodicity in both cases was in the same range of $\Lambda \approx 50 - 150 \text{ nm}$. In the latter case parallel nanoripples were formed inhomogeneously, i.e. along separate stripes, being periodically ordered with distances of about $\Lambda \approx 0.5 - 0.6 \text{ }\mu\text{m}$. In our experiments, after irradiation of the titanium film and bulk samples with laser pulses ($\lambda = 800 \text{ nm}$, $\tau = 30 \text{ fs}$) in scanning mode with scan speed of 0.2 mm/s ($N \approx 220$), the formation of HSFLs was observed in the center of the irradiated region within a narrow fluence range of 30 mJ/cm^2 to 45 mJ/cm^2 (Fig. 6.2). Above a fluence value of 45 mJ/cm^2 only the formation of LSFLs was observed. However on mechanically polished bulk samples, at few regions where the surface is rough, LSFLs were observed at fluence values below 45 mJ/cm^2 . Moreover, it was found that the quality of nanogratings is much better on mirror-like titanium film sample than on mechanically polished bulk titanium.

The periodicity of HSFLs as a function of fluence on a titanium thin film is shown

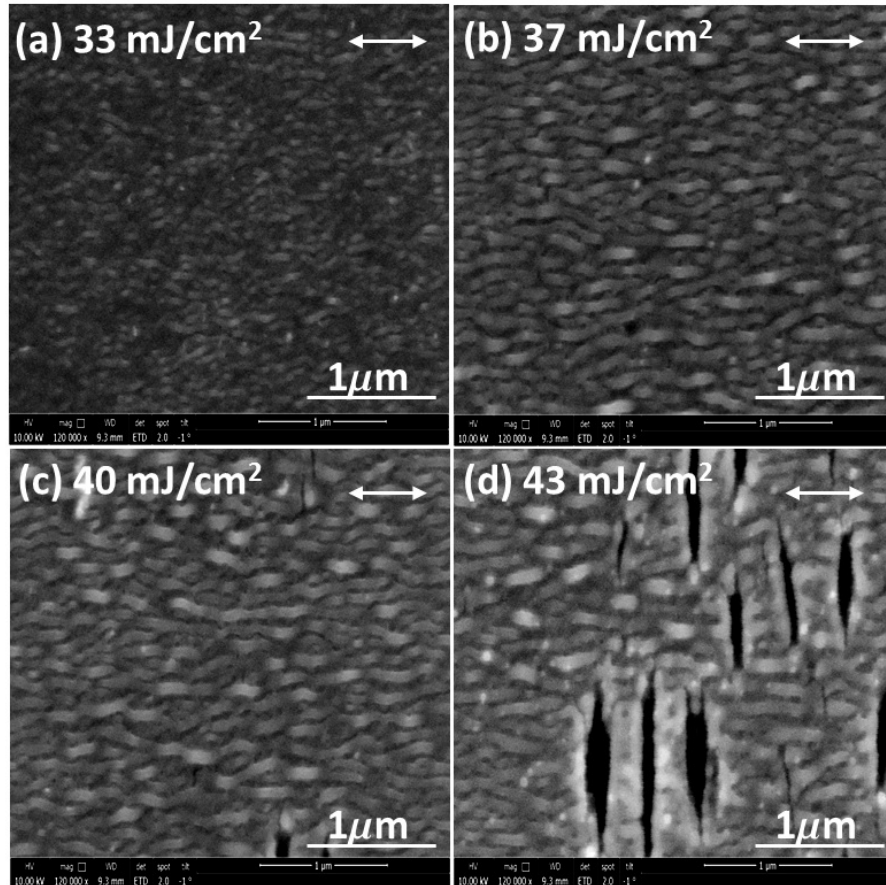


Figure 6.2: SEM micrographs of a titanium film surface after irradiation by IR fs-laser pulses ($\lambda = 800$ nm, $\tau = 30$ fs, $\nu = 1$ kHz) in the scanning mode with scanning speed of 0.2 mm/s ($N \approx 220$) at various fluence values. The double-headed arrow indicates the direction of the laser beam polarization.

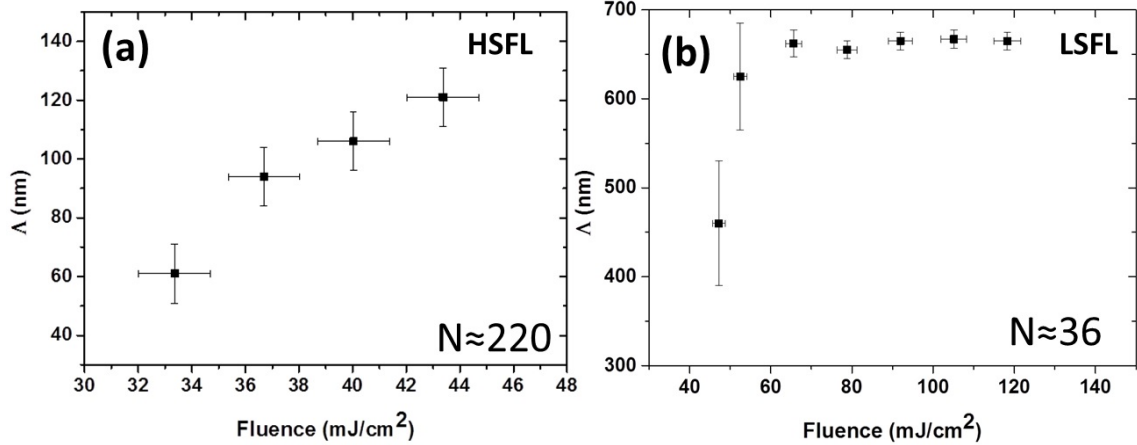


Figure 6.3: Dependence of (a) HSFLs and (b) LSFLs periodicity on Fluence, formed on a titanium film surface when irradiated with $\tau=30$ fs pulses and (a) $V=0.2$ mm/s ($N \approx 220$) (b) $V=0.6$ mm/s ($N \approx 36$).

in Fig. 6.3(a). Similar values of periodicity and fluence range were observed in a bulk sample. However, in stationary mode, with $N = 30$, we observed the formation of HSFLs at slightly higher fluence values of 60 mJ/cm^2 to 80 mJ/cm^2 . The higher threshold value for the formation of HSFLs in stationary mode is attributed to a lower number of pulses. Therefore, the so-called incubation law (dependence of threshold values on number of irradiated pulses)[88] [20] is also relevant for HSFLs formation. On the other hand, when the titanium film is irradiated by 30 fs pulses using a 50 mm focusing mirror at a scanning speed of 0.6 mm/s ($N \approx 36$), the LSFLs periodicity increases from 460 nm to 665 nm, as a function of the fluence, (as shown in Fig. 6.3(b)). It was observed that within a fluence range of $\sim 20 \text{ mJ/cm}^2$, the periodicity increases from a lower value of ~ 460 nm to a saturation value of ~ 665 nm. With $N \approx 36$ and fluence values $> 120 \text{ mJ/cm}^2$, the film in the central region of irradiation is totally ablated. Compared to HSFLs, which exhibit a slow and monotonous rise of periodicity with fluence, LSFLs exhibit a step-like increase in periodicity. Similar results of LSFLs periodicity dependence on fs-laser fluence have been reported by others [63, 115, 114, 120, 43, 121].

6.1.2 Scanning Speed / Pulse Number Dependence

Figure 6.4 shows SEM micrographs of HSFLs on a titanium film formed after irradiation at a fixed fluence of 42 mJ/cm^2 and pulse duration of 30 fs, as a function of scanning speed in the range of 0.2 mm/s - 2.5 mm/s.

Figure 6.5 shows SEM micrographs of LSFLs formed on a titanium film surface after irradiation using a 50 mm focal length mirror at a fixed fluence of 65 mJ/cm^2 and a pulse duration of 30 fs as a function of the scanning speed. As can be seen in

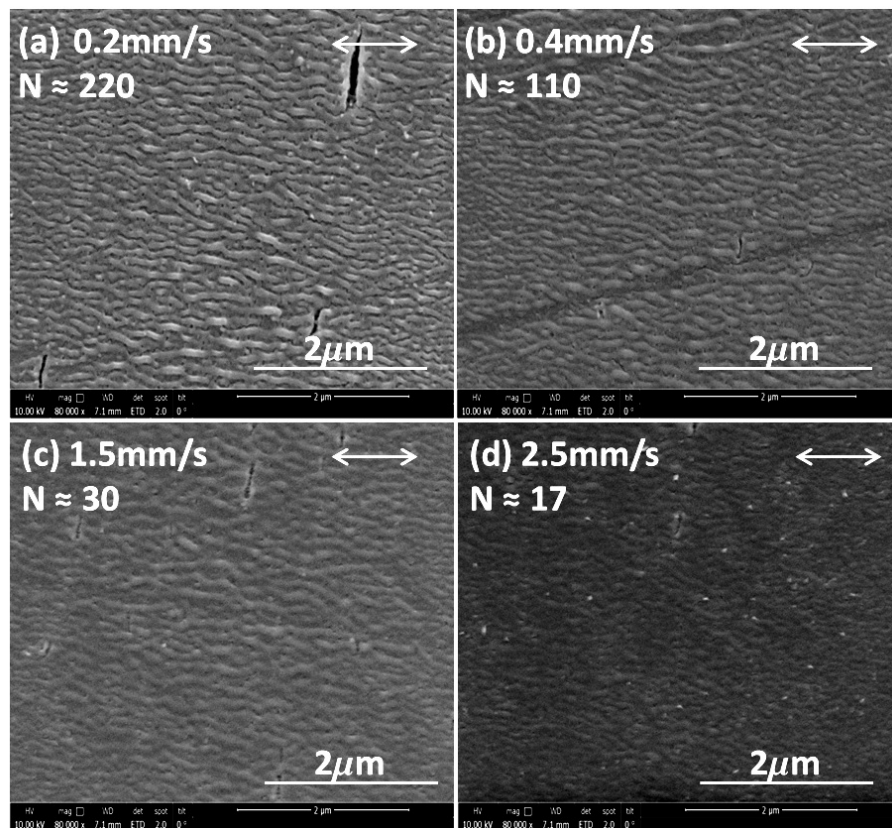


Figure 6.4: SEM micrographs of titanium film irradiated by IR fs-laser pulses at $F=42 \text{ mJ/cm}^2$, $\tau=30 \text{ fs}$, with scan speed (pulse number) variation in the range 0.2 mm/s - 2.5 mm/s ($N=17 - 220$). The double-headed arrow indicates the direction of the laser beam polarization.

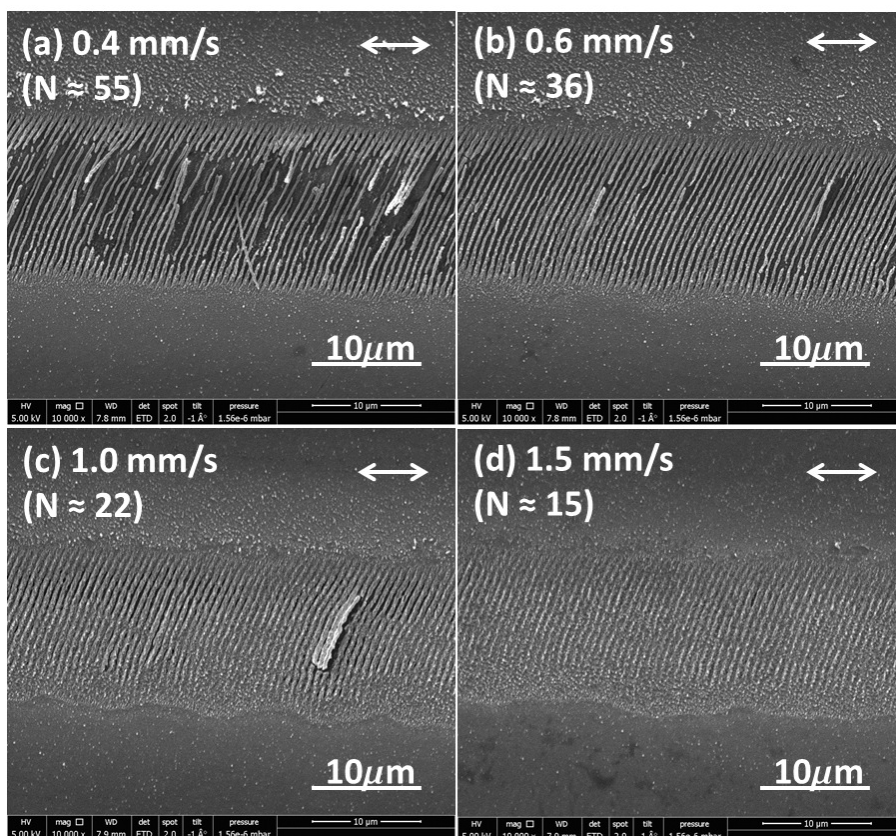


Figure 6.5: SEM micrographs of titanium film irradiated by IR fs-laser pulses at $F=65 \text{ mJ/cm}^2$, $\tau=30 \text{ fs}$, with scanning speed/pulse number variation range $0.4 \text{ mm/s} - 1.5 \text{ mm/s}$ ($N=55 - 15$). The double-headed arrow indicates the direction of the laser beam polarization.

Fig. 6.5, at a scanning speed of 0.6 mm/s , the ripples are fully developed and all the material between the ripples is completely removed up to the substrate. At a scanning speed of 0.4 mm/s the central area of irradiation is ablated, and at scanning speeds of 1.5 mm/s and above, the ripples are less pronounced. The dependence of LSFLs and HSFLs periodicity on scanning speed is shown in Fig. 6.6.

The periodicity of HSFLs monotonously increases from $\sim 90 \text{ nm}$ to $\sim 120 \text{ nm}$ when the scanning speed is increased from 0.2 mm/s to 0.8 mm/s ($N \approx 220 - 55$) and is constant in the scanning speed range of $0.8 \text{ mm/s} - 2.5 \text{ mm/s}$ ($N \approx 55 - 18$) (Fig. 6.6(a)). However this parameter rather strongly affects the quality of HSFLs and weakly affects the periodicity. In particular, the best quality of HSFLs were achieved at scanning speeds corresponding to $N \approx 50 - 220$ at $F = 42 \text{ mJ/cm}^2$. In stationary mode, homogeneous HSFLs were achieved at $F \approx 70 \text{ mJ/cm}^2$ and $N \approx 10 - 100$. At $N < 10$ the HSFLs are weakly ordered and have small height, while at $N > 100$ they degrade. On the contrary, as shown in fig. 6.6(b), the periodicities of LSFLs reduce with pulse number in a clearly defined manner, which is consistent with previous reports [62, 121, 61]. The red curve in fig. 6.6(b) is an exponential decay

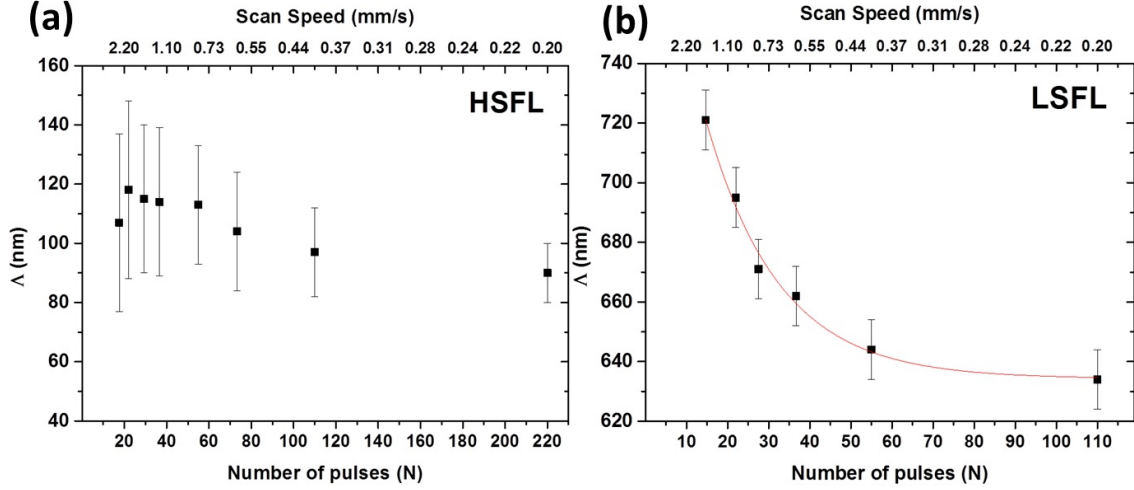


Figure 6.6: Dependence of (a) HSFLs and (b) LSFLs periodicity on scanning speed (pulse number) formed on a titanium film surface when irradiated with $\tau=30$ fs pulses and (a) $F=42$ mJ/cm^2 (b) $F=65$ mJ/cm^2

curve fitted to guide the eye. Recently, a new model describing such N -dependent LSFLs periodicity in terms of variable surface roughness and SPP scattering has been proposed [121].

6.1.3 Pulse Duration Dependence

In this work, LIPSS parameters were characterized for the first time as a function of pulse widths, providing a novel type of dependence for its characteristics. Fig. 6.7 shows the SEM micrographs of formed HSFLs in the central area of irradiation on a titanium film when irradiated with a fixed fluence of $F = 42$ mJ/cm^2 , scanning speed of 0.2 mm/s ($N \approx 220$) and for pulse durations in the range 10 fs – 550 fs. As shown in Fig. 6.7(f), when the titanium film is irradiated with pulses of 550 fs duration and fluence of 42 mJ/cm^2 , the ripples appear isolated and with pulses of duration below 400 fs, they are fully formed.

It is observed that as the pulse duration is lowered, HSFLs formation is more prominent (Fig. 6.7). We checked the pulse width dependence for bulk titanium sample and the same behavior was observed. Additionally, heights of HSFLs on bulk and film samples are in the same range of about 30 nm (Fig. 6.8). Fig. 6.9 shows the SEM micrographs of LSFLs formed in the central area of irradiation on a titanium film when irradiated with fixed fluence of $F = 65$ mJ/cm^2 , scanning speed of 0.6 mm/s ($N \approx 36$) for pulse durations in the range 30 fs – 550 fs.

The most important finding in this section is the decrease of the HSFLs periodicity with pulse duration. This is shown in Fig. 6.10 for $F = 42$ mJ/cm^2 and $N \approx 220$,

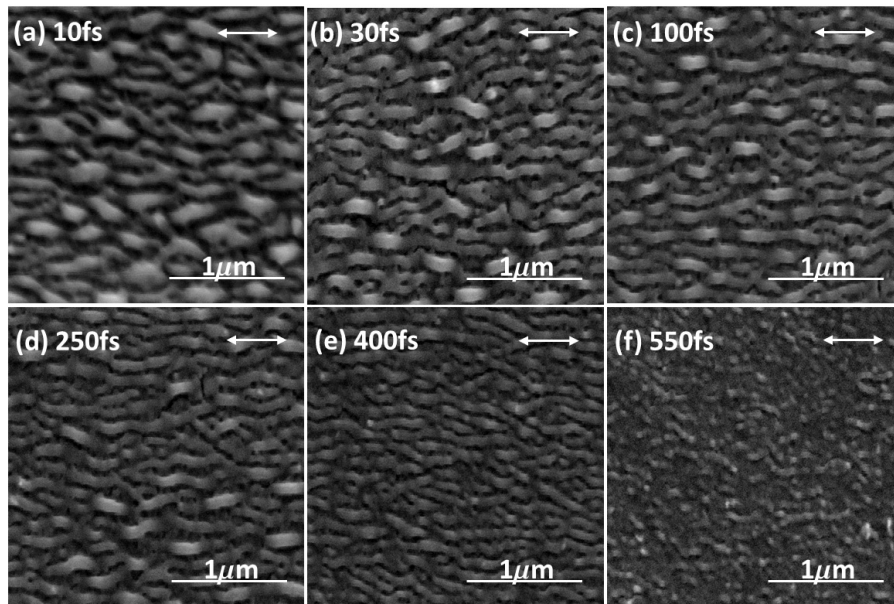


Figure 6.7: SEM micrographs of HSFLs on titanium film surface when irradiated by IR fs-laser pulses with $F \approx 42 \text{ mJ/cm}^2$ and scan speed of 0.2 mm/s ($N \approx 220$) of different pulse durations. The double-headed arrow indicates the direction of the laser beam polarization.

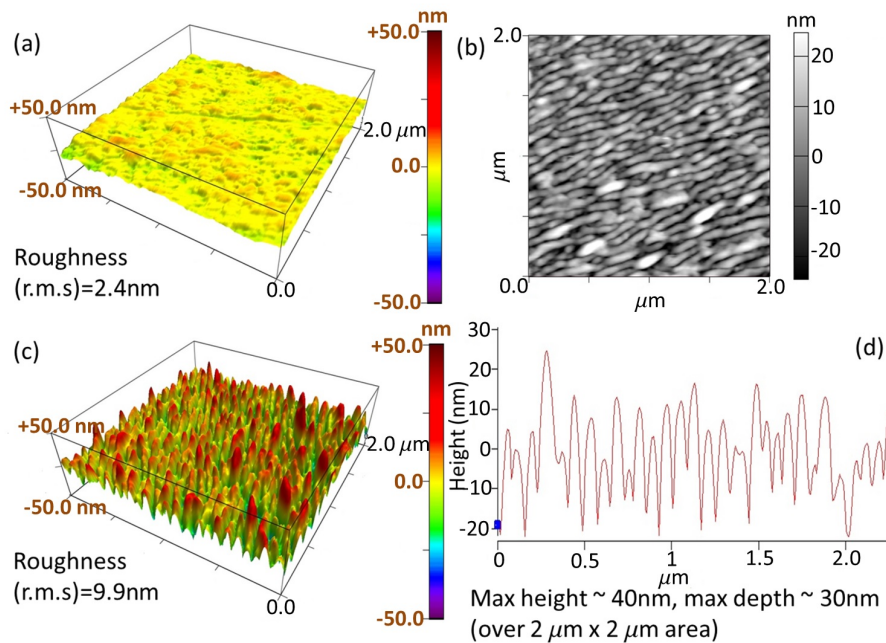


Figure 6.8: AFM images of titanium film (a) unexposed area, (b) 2D image of nano-ripples (c) 3D image of nano-ripples (d) Height profile of nano-ripples, after irradiating by IR fs-laser pulses with $F = 36 \text{ mJ/cm}^2$, $\tau = 30 \text{ fs}$, $N \approx 220$.

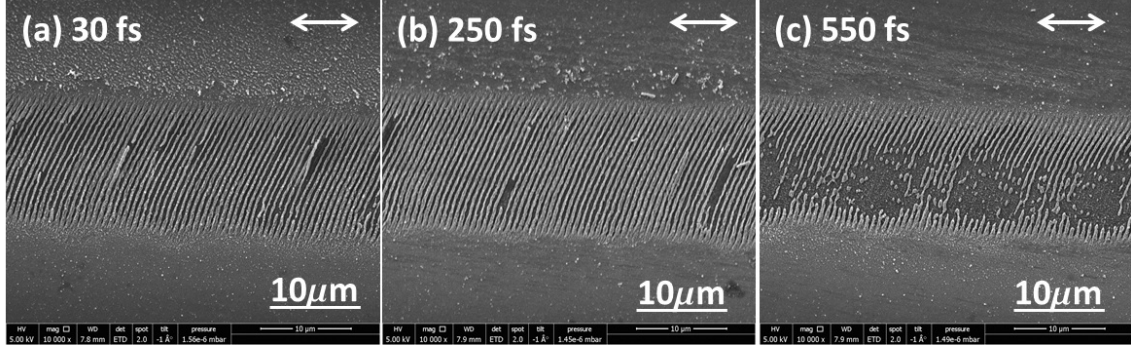


Figure 6.9: SEM micrographs of LSFLs on titanium film surface when irradiated by IR fs-laser pulses with $F \approx 65 \text{ mJ/cm}^2$ and scan speed of 0.6 mm/s ($N \approx 36$) at different pulse durations. The double-headed arrow indicates the direction of the laser beam polarization.

where a relatively moderate decay of the period can be seen. However the periodicity of LSFLs was found to be independent on pulse duration. The periodicity of LSFLs when irradiated with $F = 65 \text{ mJ/cm}^2$ in scanning mode corresponding to $N \approx 36$ pulses is $\sim 660 \text{ nm}$ for pulses of duration in the range of $30 - 550 \text{ fs}$. This strongly suggests that the physical processes for formation of these two types of ripples are of different nature.

The measurements of LSFLs topology at different pulse durations revealed strong dependence of their structure quality (Fig. 6.9) rather than their periodicity (Fig. 6.10).

6.1.4 Wavelength Dependence

To study the dependence of LSFLs and HSFLs periodicity on the laser wavelength, we irradiate mirror like titanium film surface by both fundamental (800 nm) and second harmonic (400 nm) of the Ti:Sa laser in the range of $F = 30 - 50 \text{ mJ/cm}^2$, and $\tau = 30 - 550 \text{ fs}$ in the scanning mode at scanning speeds of $0.2 - 2.5 \text{ mm/s}$. In excellent accordance with the interference model, LSFLs exhibit linear dependence of periodicity with wavelength, in agreement with reported experimental observations [111, 122]. When irradiated with a set of chosen experimental parameters ($\lambda = 800 \text{ nm}$, $F = 48 \text{ mJ/cm}^2$, scanning speed = 0.2 mm/sec ($N \approx 220$), $\tau = 30 \text{ fs}$), the periodicity of LSFLs is found to be $\Lambda_{LSFLs} \sim 620 \text{ nm}$. Under similar conditions, when irradiated with 400 nm laser pulses, the periodicity of LSFLs was found to be $\Lambda_{LSFLs} \sim 300 \text{ nm}$ (Fig. 6.11(a)). However, the ranges of HSFLs periods for both wavelengths (800 nm and 400 nm) was found to be in the same range of $50 - 150 \text{ nm}$, depending on the other laser parameters (Fig. 6.11(b) and Fig. 6.2(a)-1(d)). For example, $\Lambda_{HSFLs} \sim 62 \text{ nm}$, when $\lambda = 800 \text{ nm}$, $F = 33 \text{ mJ/cm}^2$, $N \approx 220$, $\tau \sim 30 \text{ fs}$, and $\Lambda_{HSFLs} \sim 65 \text{ nm}$ when $\lambda = 400 \text{ nm}$, $F = 25 \text{ mJ/cm}^2$, $N \approx 220$, $\tau \sim 30 \text{ fs}$.

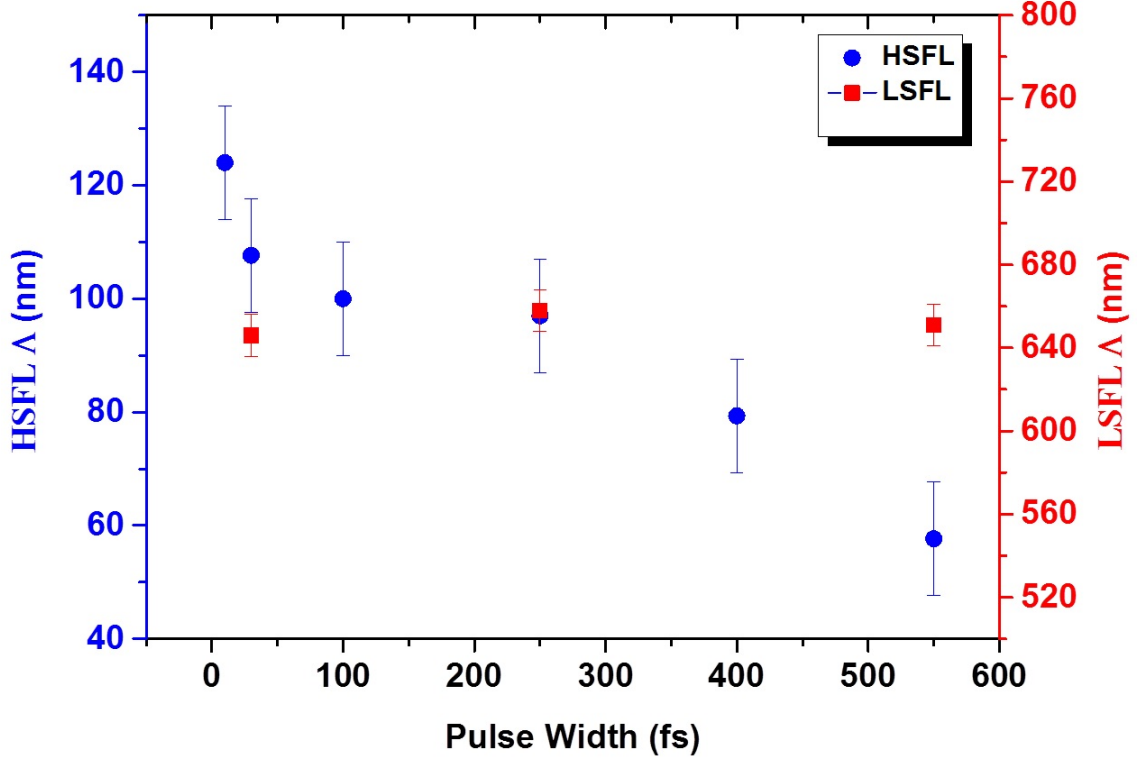


Figure 6.10: Periodicity dependence of HSFLs (black dots, left axis) and LSFLs (red dots, right axis) on pulse duration on a titanium film surface in scanning mode with: $N \approx 220$, $F = 42 \text{ mJ/cm}^2$ for HSFLs and $N \approx 36$, $F = 65 \text{ mJ/cm}^2$ for LSFLs.

This is in striking contrast with experimental observations in [117], demonstrating a monotonous increase of HSFLs periodicity with laser wavelength ($\lambda \approx 1.4 - 2.2 \mu\text{m}$). However in the experiments in [117] the photoexcitation conditions were not kept identical over the spectral range.

6.1.5 Polarization Dependence

The comparison of LSFLs and HSFLs ridges orientation exhibit a similar picture at different wavelengths, fluences, pulse durations, shots numbers and thickness of sample. LSFLs and HSFLs are always perpendicular to each other. In general, HSFLs are always parallel to the laser polarization (Fig. 6.12) (see also Table 1 in [115]), while LSFLs are perpendicular to the laser polarization (Fig. 6.2(d), Fig. 6.5, and Fig. 6.9) as usually observed [123].

6.1.6 Surface-roughness Dependence

In order to reveal possible correlation between LSFLs and HSFLs we also compared titanium surfaces with different roughness quality. In Fig. 6.8(a) the roughness of

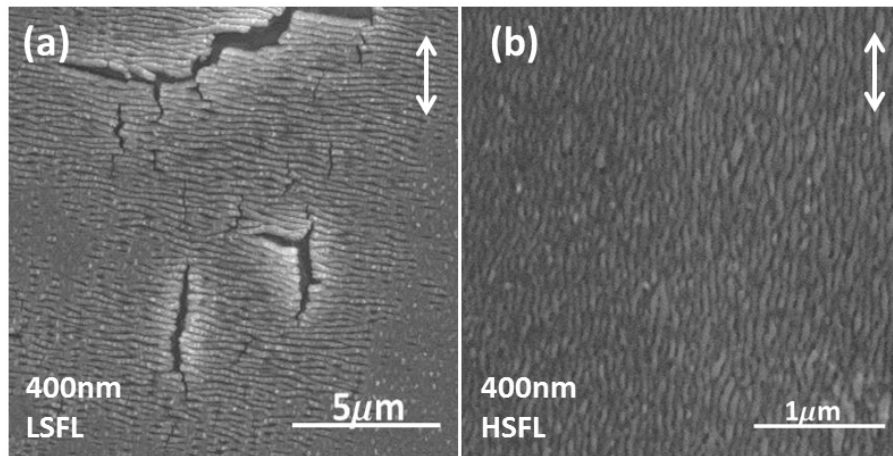


Figure 6.11: SEM micrographs of (a) LSFLs and (b) HSFLs formed on a titanium film surface after irradiation with $\lambda = 400 \text{ nm}$, $F = 25 \text{ mJ/cm}^2$, $N \approx 220$, $\tau \sim 30 \text{ fs}$ pulses. The double-headed arrow indicates the direction of the laser beam polarization.

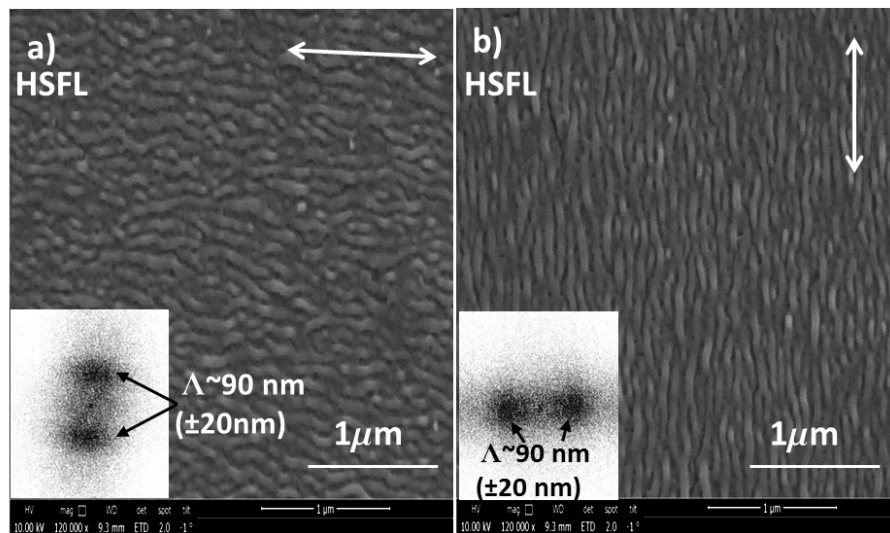


Figure 6.12: SEM micrographs of HSFLs formed on a titanium film after irradiation with IR laser pulses with $F = 36 \text{ mJ/cm}^2$, $N \approx 220$, $\tau = 30 \text{ fs}$. The double-headed arrow indicates the direction of the laser beam polarization. The corresponding 2D Fourier transformations of SEM micrographs are shown in the insets.

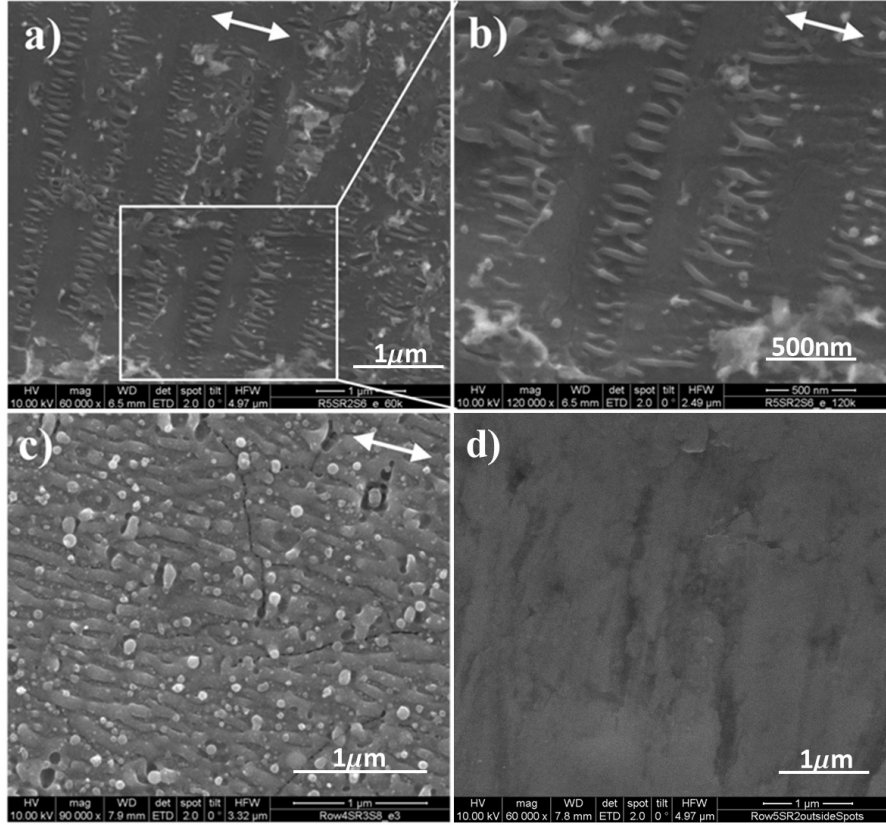


Figure 6.13: SEM micrographs of HSFLs on bulk titanium surface when irradiated by 30 fs IR laser pulses with (a, b) $F \approx 60 \text{ mJ/cm}^2$, $N = 70$ (c) $F \approx 80 \text{ mJ/cm}^2$, $N = 20$ (d) un-exposed area. The double-headed arrow indicates the direction of the laser beam polarization.

initial surface of mirror-like Ti film is presented, indicating absence of any nano-tranches. Fig. 6.13(d) shows SEM micrograph of the initial roughness of bulk titanium surface. Indeed, in case of mirror-like surface quality only homogeneously distributed HSFLs are formed at any fluence values in agreement with some previous studies [57]. However, presence of initial tranches on the bulk titanium surface leads to coexistence of LSFLs and HSFLs at near-threshold fluences $F \approx 60 \text{ mJ/cm}^2$ at $N = 70$ (Fig. 6.13(a) and 12(b)) in agreement with the other previous studies [114, 56]. At higher fluences of $F \approx 80 \text{ mJ/cm}^2$ at $N = 20$ the HSFLs fill the irradiated area homogeneously and almost independent of the nanoroughness (Fig. 6.13(c)). On the other hand, as mentioned in Sec. 3.1, the threshold fluence for formation of LSFLs is lower on rough titanium surface compared to mirror like titanium surface, which is in good agreement with a previous study [124]. It should be noted that the periodicity of LSFLs is about half near the threshold and are referred to as ‘fine ripples’ in [124].

Table 6.1: Main dependences of LIPPS period on laser parameters.

	Wavelength	Fluence	No.of Pulses	Pulse duration
LSFLs (\perp to pol.)	Dependent	Dependent	Dependent	Not dependent
HSFLs (\parallel to pol.)	Not dependent	Dependent	weakly dependent	Dependent

6.1.7 Discussion

In order to provide a systematic, qualitative overview of these experimental results, we summarize the observations in Table 6.1, where one can see that LSFLs and sub-100-nm HSFLs generated on titanium surface irradiated in air environment exhibit an opposite trend with varying basic laser parameters. These laser parameters were proven to be of major significance in the process of LSFLs formation. In particular, the interference model implies linear explicit dependence on the laser wavelength [52] with some nonlinear influence arising from dispersion of the dielectric function and the number of shots via grating coupling [62]. However, HSFLs are much less dependent on these two parameters as LSFLs does.

In spite of the fact that generally both LSFLs and HSFLs exhibit a fluence-dependent periodicity, the characters of the dependencies are quite different. According to the literature data, the periods of LSFLs are changed slowly at high fluences [63, 43] and dropped by two times near the threshold of their formation [112, 43, 121], which is in good agreement with our data for LSFLs. All these variations of LSFLs periodicity occur in the fluence range of $0.04 - 0.12 J/cm^2$ (Fig. 6.3(b)), comparing to LSFLs generation range of $0.08 - 0.35 J/cm^2$ reported in [115], where in the latter case the lower fluence limit represents minute spallation and higher fluence limit represents deep fragmentation ablation thresholds for titanium, according to the constant spallation and linear fragmentation yields of atomic emission recorded in our optical emission studies of ablative plumes and previous studies [119]. In contrast to LSFLs, HSFLs exhibit significant dependency on laser fluence (Fig. 6.3) below the spallative ablation threshold, where intense sub-surface cavitation occurs [56, 57]. Also, smaller but clear dependence on pulse duration of HSFLs has been found, whereas LSFLs periodicity does not depend on pulse duration. Thus, bearing in mind that intensity is $I = F/\tau$, the dependence of the periodicity on intensity for HSFLs is even more rapid as compared with LSFLs. In particular, the fitting of $\Lambda(F)$ and $\Lambda(\tau)$ dependencies are $\Lambda \sim F^{1.5 \pm 0.6}$ (Fig. 6.3(a)) and $\Lambda \sim \tau^{0.20.1}$ (Fig. 6.10) gives nonlinear dependence $\Lambda \sim I^{1.7 \pm 0.7}$. The non-linear character of this dependence apparently depends on fs-laser energy deposition and electron dynamic details, which have to be understood yet for titanium, using, e.g., the pulse width dependency of spallation and fragmentation ablation thresholds [125]. An additional problem for

the interference model arises when one needs to explain why LSFLs and HSFLs with crossed orientations can co-exist in the same surface area. Such cross oriented structures, which are both LSFLs, have been observed in double pulse experiments also [126, 127]. According to the interference model [52, 113, 114] LIPSS with parallel orientation to the laser polarization requires real part of the photo-excited dielectric function of the metal, $\Re(\varepsilon_m) > -1$. Hence, in air environment with dielectric function ε_d ($\Re(\varepsilon_d) \approx 1$) only separate formation of LSFLs at $\Re(\varepsilon_m) < -1$ and HSFLs at $\Re(\varepsilon) > -1$ is expected [52, 113, 114, 128, 129]. However, according to the experimental results of our present and previous studies [56, 57], regimes where LSFLs and HSFLs co-exist were revealed. Moreover, very recently another SPP-based model of HSFLs formation was reported [117] where nanoripples are created on a titanium foil by exploiting laser induced oxidation and in situ generation of third harmonic of Ti:sapphire laser operating at wavelengths in the range of $1.4 - 2.2\mu m$. The observed HSFLs period which is in the order of one tenth of the irradiating laser wavelengths was explained by excitation of short-wavelength SPP by the generated third-harmonic-radiation at the oxidized interface with much higher refractive index of titanium oxides. However, the laser-induced 10-nm thick oxide layer can affect only wavelengths of sub-wavelength longitudinal surface electromagnetic waves (surface plasmons) with $\Re(\varepsilon_m) \rightarrow -\Re(\varepsilon_d)$, which are strongly localized in the metal and dielectric near the interface within the corresponding penetration depths d and D given by Eqs. (2,3), comparing to presumably transverse near-wavelength surface polaritons at $\Re(\varepsilon_m) \ll -\Re(\varepsilon_d)$, which usually exhibit sub-micron depths in the boundary dielectric medium [129].

$$d \approx \frac{\lambda}{2\pi} \sqrt{\frac{\varepsilon_m + \varepsilon_d}{\varepsilon_m^2}} \quad (6.1)$$

$$d \approx \frac{\lambda}{2\pi} \sqrt{\frac{\varepsilon_m + \varepsilon_d}{\varepsilon_d^2}} \quad (6.2)$$

Moreover, the ultimate wavelength of surface plasmons in corresponding surface plasmon resonance, given by the condition $\Re(\varepsilon_m) = -\Re(\varepsilon_d)$, is not directly scalable with the incident laser wavelength, i.e., is hardly affected by the third-harmonic radiation [130]. Also, we have mentioned in the introduction, that HSFLs on Ti have been previously observed as two different types: (i) combination of LSFLs and HSFLs [56]; or (ii) only HSFLs [115]. Our detailed analysis of fluence dependence reveals both these types at slightly different conditions. In particular, under irradiation of bulk Ti by $N \approx 30$ laser pulses with duration of $\tau \approx 30fs$ and fluence of $F < 60mJ/cm^2$ the HSFLs appear only inhomogeneously (Fig. 6.13(a,b)). The periodicity of HSFLs in this case is about $\Lambda \approx 70nm$ and width of each stripe is about

200 nm. The periodicity is stable in this range of fluences, but increases rapidly up to $\Lambda \approx 140\text{nm}$ at higher fluence $F \approx 80\text{mJ/cm}^2$, where spallative ablation starts to destroy HSFLs (see also [115]). The increased values of period correspond to homogeneously distributed nanoripples (Fig. 6.13(c)). Importantly, we did not observe any inhomogeneous HSFLs formation on mirror-like Ti film, where only homogeneous HSFLs formation was observed. Such a strong dependence of HSFLs type on surface quality can be explained in terms of the interference model of LSFLs formation. In case of rough surface with a lot of initial trenches (“sources” of light scattering) (Fig. 6.13(d)), they provide SPP excitation and interference pattern formation around themselves. These patterns usually are stable from pulse to pulse, if the local fluence in the interference maxima is not too high to produce new deep trenches, i.e. when it is lower than the corresponding LSFLs formation threshold. In this case the laser energy is absorbed many times along narrow separated stripes. The opposite is true when the initial surface is smooth with nano-roughness growing randomly from pulse to pulse, which does not provide fixed interference pattern, resulting in emerging of maxima on new places after each shot. Therefore, a surface without single “sources” for SPP cannot exhibit formation of inhomogeneous HSFLs. One possible mechanism for the formation of sub-100-nm HSFLs structures on titanium surface under femtosecond pulses irradiation can be the previously proposed cavitation-instability mechanism [114, 56] which is based on intense reversible and irreversible pre-spallation sub-surface boiling (thermally-induced cavitation). This results in relief restoration at the sub-threshold fluences and surface swallowing at fluences approaching the corresponding spallation threshold [102, 131]. It predicts formation of sub-surface nanobubbles in the molten surface layer along each narrow and long interference surface stripe formed via interference of the incoming light with excited SPP. At higher fs-laser fluences, exceeding the ripple formation threshold, such sub-surface nanobubbles are merged together into a longitudinal vapor nanocavity along the stripe, then expelling the top liquid overlayer and making a spallative ripple trench. At lower fluences such nanobubbles can make longitudinal self-organized sequences of tightly spaced, separated closed nanovoids (nanospikes at sub-threshold fluences [56]) or separated open nanovoids (nanopores at near-threshold fluences [56, 132]) through their collective repulsive interaction [133], which finally remain frozen in the quasi-regular structures. Indeed, in such regime, surface is heated along narrow stripes resulting in formation of LSFLs at local fluences higher than ablation threshold or HSFLs at fluences lower than the ablation threshold [56, 57]. Our present experiments support this mechanism. At higher fluences ($F > 80\text{mJ/cm}^2$), HSFLs represent aligned open nanovoids (Fig. 6.14). At higher exposures open nanovoids are merged into trenches, forming LSFLs. The same broken voids were noticed for HSFLs on aluminum [56] indicating the uni-

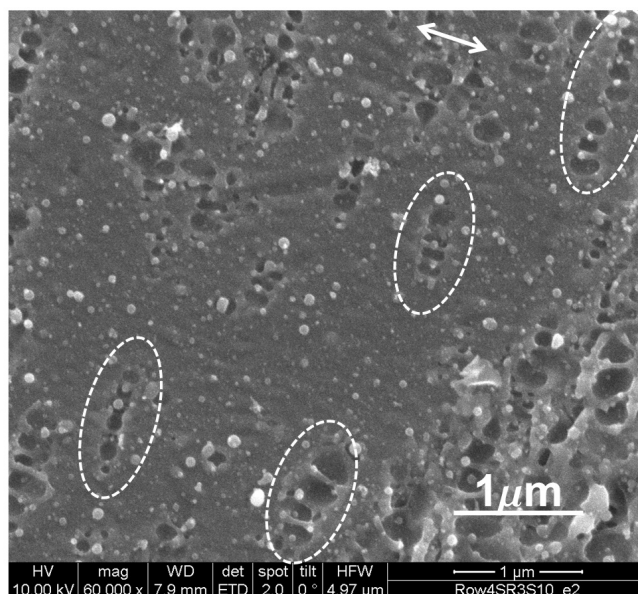


Figure 6.14: SEM micrographs of HSFLs on bulk titanium surface when irradiated by 30 fs IR laser pulses with $F \approx 80 \text{ mJ/cm}^2$, $N = 5$. The double-headed arrow indicates the direction of the laser beam polarization.

versal character of this mechanism. Indeed, sub-surface cavitation under ultrashort laser irradiation is the universal effect for different materials [134, 135].

6.2 Structuring in liquid environment and Raman Analysis

Laser-ablation of metals in liquids is responsible for enhanced heat conduction, confinement of plasma expansion, intensified acoustic pressure, thermodynamic nucleation, phase transition and kinetic growth of nanostructures [136, 137]. With the help of this technique, morphology of the material could be easily modified with the development of debris-free nano and micro-structures. Another benefit of this technique is an enhancement of chemical reactivity. The chemical reactivity of most of the liquids with materials during laser irradiation results into the formation of oxides, hydro-oxides and metalalcohols [138, 139].

We studied the formation of nano structures on the surface of Tin and Titanium after irradiating them with femtosecond laser pulses in ethanol as an ambient environment [140, 141]. The effect of fluence and pulse duration on the formation of nanostructures in liquid environment is studied and is compared with the exposures done in air environment. Particularly, the topographical differences and the chemical changes to the surface has been studied.

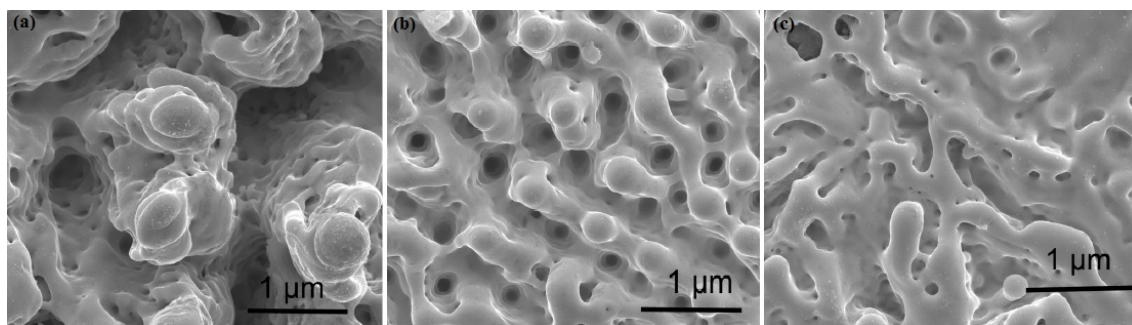


Figure 6.15: SEM micrographs of Tin surface after irradiating with 1000 pulses of ~ 30 fs duration and fluence of (a) $4.7 J/cm^2$ (b) $7.1 J/cm^2$ and (c) $9.4 J/cm^2$.

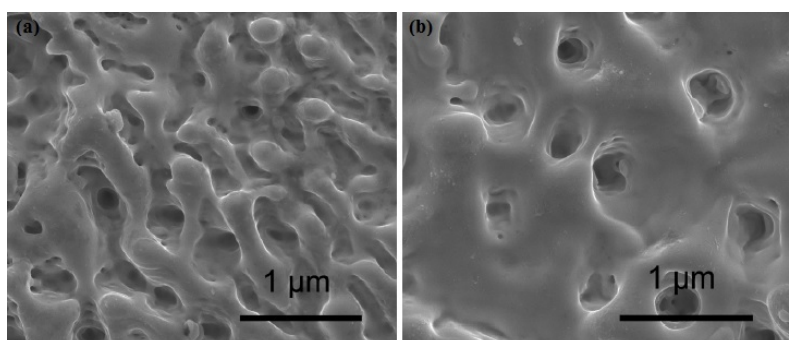


Figure 6.16: SEM micrographs of Tin surface after irradiating with 1000 pulses of $\sim 11.6 J/cm^2$ and (a) ~ 30 fs and (b) ~ 250 fs.

Fig.6.15 shows the SEM images of Tin(Sn) surface after irradiating with 1000 pulses of 30 fs duration with varying fluences. In the SEM images, it can be seen that columnar structures with globules with an average diameter of ~ 800 nm at the top are formed at $4.7 J/cm^2$ and with increase in fluence, the globule diameter decreases whereas the number of structures increase. Further increasing in fluence results in melting of these columnar structures.

Fig.6.16 shows the SEM images on the surface after irradiating with 1000 pulses of $\sim 11.6 J/cm^2$ and ~ 30 fs (Fig.6.16(a)) and ~ 250 fs (Fig.6.16(b)). As can be seen in the images that with higher pulse duration pulses, the structures seem to have melted but some deep craters are formed.

6.2.1 Raman spectrographs

Fig.6.17 shows the Raman spectrograms obtained from the surface of Sn after irradiating with pulses of varying fluence (Fig.6.17(a)) and pulse durations (Fig.6.17(b)). Several structural modifications in the Sn after the exposures can be noticed. The un-exposed surface or the surface irradiated with $4.7 J/cm^2$ doesn't show any bands. However, peaks at $475 cm^{-1}$, $631 cm^{-1}$ and $775 cm^{-1}$ are noticed for higher fluence irradiated samples. These correspond to the A_{1g} , E_g and B_{2g} vibrational modes of

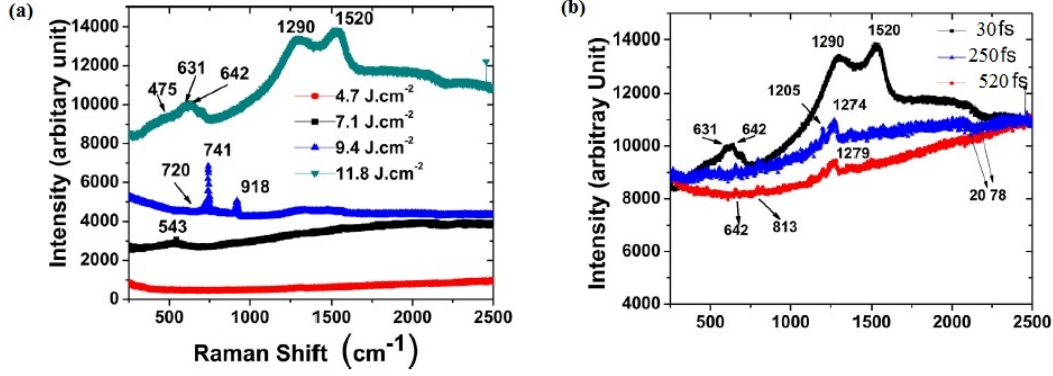


Figure 6.17: Raman spectrographs of the sample irradiated with ultrashort laser pulses in ethanol environment (a) with varying fluence (b) with varying pulse widths

Sn [142]. The peaks identified at 1520 cm^{-1} corresponds to C=C stretching mode [143] and the peak at 1290 cm^{-1} corresponds to $\text{C}_6\text{H}_5 - \text{C}$ stretching mode[143]. The band appearing at 740 cm^{-1} corresponds to the functional group of C_2H_5 Sn of C-H symmetric mode[143]. The peak identified at 918 cm^{-1} represents an existence of symmetric COC stretching mode[143]. This indicates that Sn has been structurally significantly modified after exposure in ethanol. Appearance of more bands at higher fluences could be a consequence of higher energy deposition. Fig.6.17(b) shows the Raman spectrographs when the sample is irradiated with different pulse durations. At higher pulse durations some of the peaks identified at wavenumber 631 cm^{-1} , and 1520 cm^{-1} disappear completely and represent the dissociation of E_g vibrational mode and C=C stretching mode [143]. With higher pulse durations, there is more time for the laser beam to deposit energy and because of enhanced thermal effects some bands dissociate and some bands become weaker.

6.3 Some observations

In the scope of this work structures were produced extensively on many metals and semiconductors. It serves no purpose to put all the results here, but some observations are briefly presented in this section.

6.3.1 Structuring with 10 fs laser pulses

Fig.6.18 (a) and (b) shows the SEM micrographs of LSFLs obtained on Titanium surface when irradiated with 30 fs pulses (spectrum with full width at 10th of maximum is $\sim 90 \text{ nm}$) and 10 fs pulses (spectrum with full width at 10th of maximum is $\sim 350 \text{ nm}$) under identical fluence conditions. The corresponding FFT images are

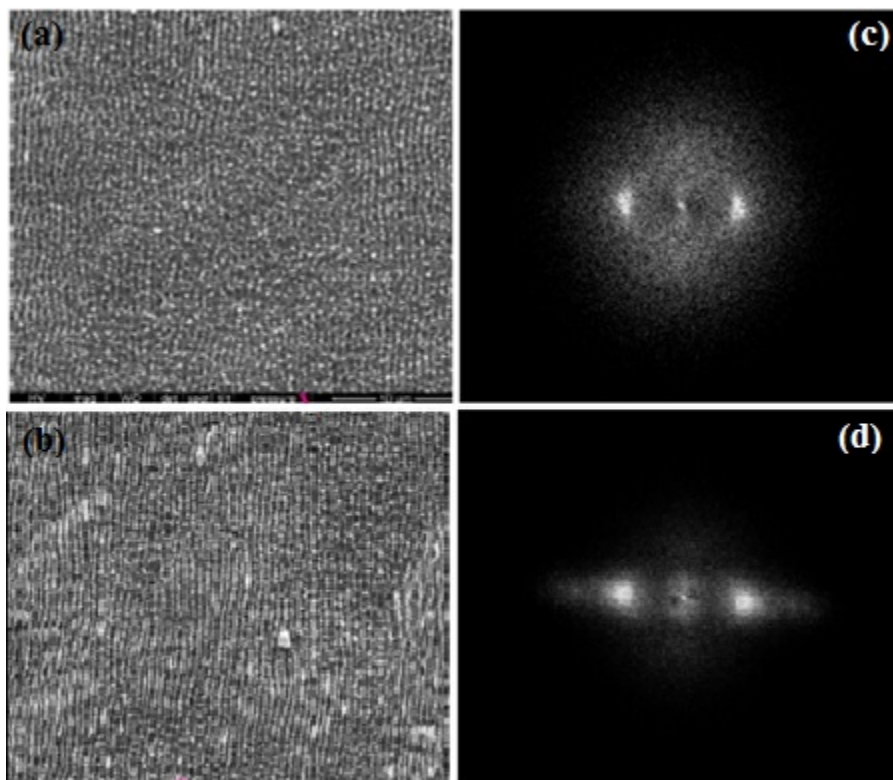


Figure 6.18: SEM micrographs of LSFLs obtained on Titanium surface with (a) 30 fs pulses and (b) 10 fs pulses under identical fluence conditions. The corresponding FFT images are shown in (c) and (d) respectively.

also shown Fig.6.18 (c) and (d). It can be clearly seen from the FFT images that the ripples periodicity range is broader for 10 fs case than that observed for 30 fs pulses.

6.3.2 Structures formed on titanium surface at higher repetition rate

Most of the experiments on LIPSS reported in literature were done with Ti:sapphire laser running at 1 KHz. To test the influence of repetition rate, we produced the structures on mirror like titanium film with repetition rates upto 500 KHz using commercially available extended cavity Ti:sapphire oscillator (XL, Femtolasers Produktions GmbH), capable of delivering pulses of 600 nJ at 1 MHz repetition rate. Fig.6.19 shows the SEM micrographs of structures formed on mirror like titanium film sample when irradiated with pulses of 40 mJ/cm^2 and at fixed scanning speed of 2.5 mm/sec, which corresponds to $N \sim 20$ pulses for 1 KHz repetition rate. As can be seen in the figure, at 1KHz repetition rate, the results are identical to those obtained with the amplifier running at 1 KHz. The HSFLs are produced until the laser repetition rate is 25 KHz (corresponding to $N = 1000$ pulses). At 50 KHz

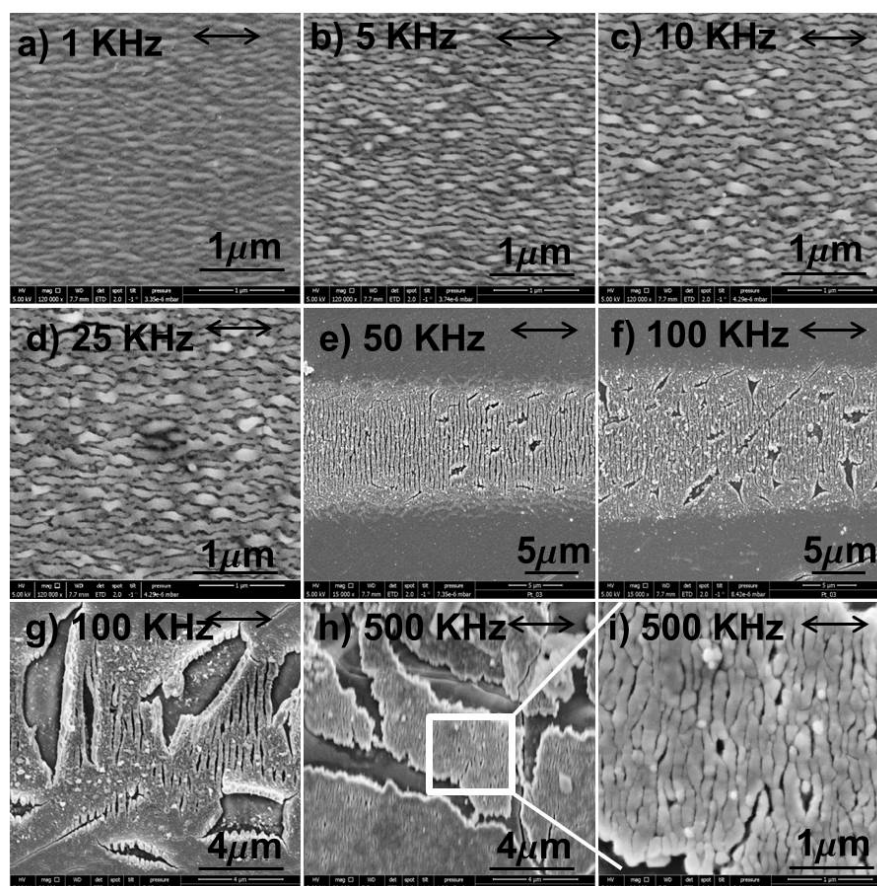


Figure 6.19: SEM micrographs of structures formed on mirror like titanium film sample when irradiated with pulses of 40 mJ/cm^2 and at fixed scanning speed of 2.5 mm/sec , which corresponds to ~ 20 pulses for 1 KHz repetition rate.

repetition rate ($N = 2000$), the HSFLs totally disappear and LSFL kind of structures form perpendicular to the laser polarization. In Sec.6.1.1 we have shown that HSFLs have a Fluence threshold window of $(30 - 50) \text{ mJ/cm}^2$, only within which HSFLs are formed. Below this value, no HSFLs can be seen, and above which LSFLs form. Similarly, with number of pulses too, HSFLs have a threshold. It need a few pulses so as to see them in SEM imaging and maximum number of pulses seem to be between 1000 and 2000. However, it should be noted that its not just the number of pulses that is changing here, but also the spacing between the incoming laser pulses. At 1 KHz repetition rate, the pulses are spaced 1 ms apart and at 500 KHz , they are $2 \mu\text{s}$ apart. So the dynamics and incubation coefficients could be very different.

6.3.3 Split in periodicity

When silicon was irradiated with 30 pulses of 30 fs duration and the SEM image taken at the central area is Fourier transformed (FFT), we observed a split in the

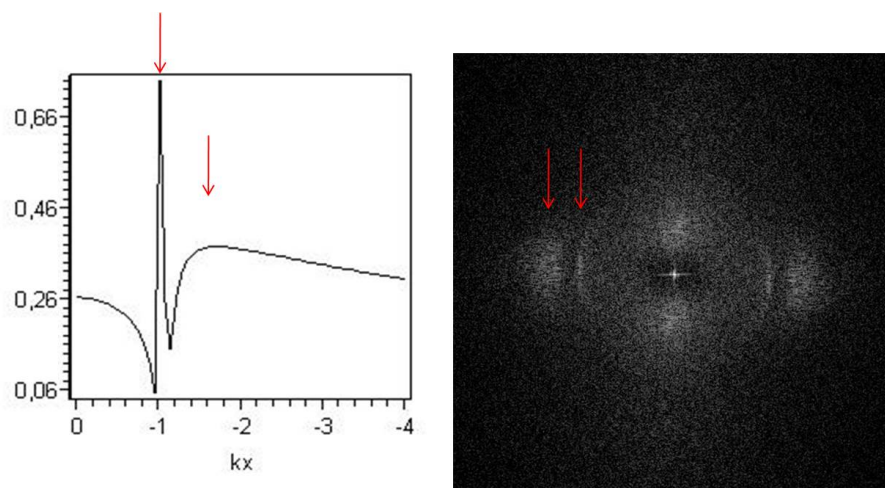


Figure 6.20: (a) Efficacy factor η as a function of normalized LIPSS wave vector for the direction parallel (k_x) to the polarization vector. (b) FFT image of the SEM image obtained on surface of silicon irradiated with 30 pulses of 30 fs duration and 500 mJ/cm^2

main peak. A similar split can be simulated using Sipe model if we take the dielectric function as: $\varepsilon = -6 + i10$. Fig.6.20 shows the FFT image and the η curve as described in the Sipe model. The high negative value of -6 of the real part of the dielectric constant seems unrealistic, but Derrien et.al and Danilov et.al have reported that Silicon can indeed have such transient optical constants when irradiated with ultrashort pulse. This validates the theory of 'interferometric' model.

6.3.4 Nano tips formation on Aluminium

Nanoantennas (tips) were fabricated on an aluminum surface by using two fs-laser pulses of fluence 0.85 J/cm^2 . The two pulses were spaced few seconds apart. After the first laser pulse an irregular array of round spallative pits with a surface density of $\sim 10^7$ appears on the surface 6.21(a & b). Their edges have widths of about 100 nm, their bottom appears semispherical and are about 100 nm deep. They could be a result of intense sub-surface nanovoid generation (homogeneous nucleation) in the melted surface layer. Such pits with prominent edges respond to EM fields in the optical range as plasmonic nanolenses, providing excitation and sub-diffraction focussing of SPPs in their centers. The focussing in plasmonic lenses exposed by fs-laser pulses of 0.85 J/cm^2 results within each pit a formation of a single nanojet 6.21(c), related to material expulsion and its ultrafast cooling. We created such nanojets and studied the electron emission from such nano tips by irradiating the surface with a third fs laser pulse and recording the electron emission. Our results show a 28-fold enhancement of the electron photoemission from such surfaces. The results are reported in [144]

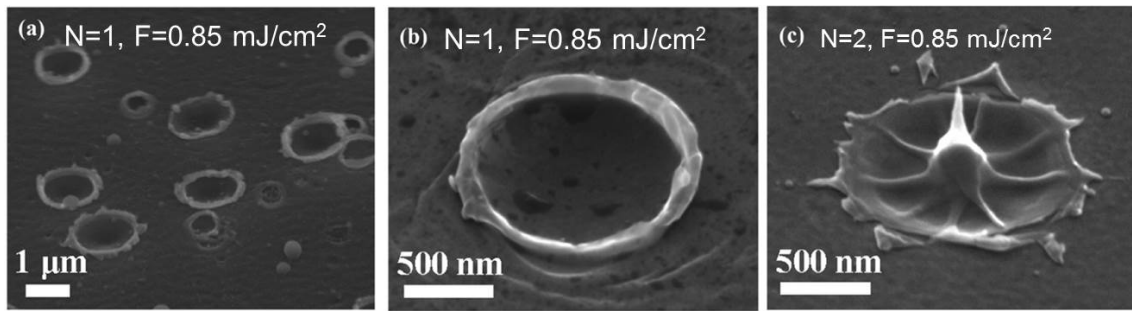


Figure 6.21: SEM micrographs of structures formed on Aluminium upon 1 and 2 pulse irradiation.

6.4 Summary and Conclusions

In this work the near wavelength structures (LSFLs), and sub-100-nm structures (HSFLs) were made on different type of materials in air and liquid environment, but systematic measurements were done in air environment on titanium film and bulk samples by irradiating the surface with linearly polarized femtosecond (fs) laser pulses. In scanning mode with scanning speed of 0.2 mm/s ($N \approx 220$), and $\tau = 30$ fs, HSFLs form parallel to the laser polarization within a narrow fluence range of 30 mJ/cm^2 to 45 mJ/cm^2 , and the periodicity increases with fluence. With number of pulses, the periodicity of HSFLs do not show a clear trend, but the periodicity of LSFLs reduces exponentially. The periodicities of both types of LIPSS demonstrate opposite pulse duration and wavelength dependencies, which suggest their origins are different and cannot be explained by the interference model developed for explaining the formation of LSFLs. The self-organization model looks more promising to explain the formation of LIPSS.

Chapter 7

Laser Induced Structuring on Bio-Polymer Films

In regenerative medicine the goal is to promote tissue regeneration and healing after injury or disease. It requires the use of a temporary porous matrix in order to guide the regeneration of tissue to the desired shape and is achieved through a delivery of cells in tissue engineered scaffolds designed to provide a biometric micro environment conducive to cell adhesion, proliferation, differentiation and host tissue integration. It must also be noted that for a scaffold to be successful it need to become vascularised so that the adhered cells have access to nutrients and oxygen for their survival. Dense cavitation and bubbling phenomenon yield micro/nano-foaming when biopolymer thin films from collagen and gelatine are irradiated with laser pulses [145, 146]. It is hypothesized that such artificially created scaffolds matrix may be seeded with cells which are then encouraged to develop into the desired tissue. Scaffolds, constructed from biocompatible polymers (gelatin, collagen and their blends), have been developed for the needs of skin tissue replacements [147]. A scaffold requires many characteristics in order to be a successful replacement. The main requirements for engineered scaffolds are: (i) bio-compatibility, (ii) produced from biodegradable materials, (iii) high surface area for cell attachment, and (iv) good mechanical integrity suitable for treatment handling. Therefore, biopolymers collagen and gelatin can be selected from within a group of biomaterials, since both these materials are biomimetic due to their specific chemical, physical, and biological properties [148, 149]. These biopolymers, collagen and gelatin already exist in the human body. Collagen is one of the key structural proteins found in the extracellular matrices of many connective tissues like cartilages, bones, blood vessels, the gut, and inter-vertebral discs. Two techniques can be distinguished for production of collagen biomaterials: one is based on decellularization of the collagen matrix keeping the

original ECM structure, while the other is related with extraction, purification and polymerization of collagen to form a functional scaffold. Most present research is aimed at the optimization of collagen-based biomaterials for medical applications by improving mechanical strength, biodegradability or delivery characteristics. Gelatin is a derivative of collagen which does not exhibit anti-genicity. Elastin is a key structural protein found in the extracellular matrix (ECM). It is the dominant part of the elastic fiber. Above mentioned biopolymers may be used as appropriate host materials and applied as a substrate which could directly interact with cells and reveal very good adhesion. However, this is not the only requirement which has to be fulfilled for the preparation of the appropriate scaffolds for cell growth and controlled cell behaviour. Surface topography has been shown to be a key issue in cell's proliferation. Scaffold design should mimic the *in vivo* tissue micro-architecture and cellular micro-environment. The microstructure and the mechanical properties of biomaterials influence the scaffold bioactivity [150–154]. It is specified that the tissue regeneration depends on pores size with optimum, ranging from 5 μm in neovascularization to 100–350 μm in bone regeneration, providing adequate space for cell seeding, growth and proliferation [152].

Scaffolds can be prepared by a number of techniques: either chemical or physical. Chemical techniques include solvent-casting particulate-leaching, gas foaming, freeze drying, solution casting and phase separation [155–158]. Whereas, physical techniques are based on laser sintering [159, 160] and laser enhanced surface modification [161]. Scaffolds produced by solvent-casting particulate-leaching cannot guarantee interconnection of pores because this is dependent on whether the adjacent salt particles are in contact. Furthermore, skin layers are formed during evaporation, and agglomeration of salt particles makes controlling the pore size difficult. For gas foaming, it has been reported that only 10–30% of the pores were interconnected. The presence of residual organic solvent is the most significant problem facing these techniques due to the risks of toxicity and carcinogenicity it poses to cells. In contrast to all known chemical techniques for scaffold designing, femtosecond laser enhanced surface modification is an attractive approach since it is noncontact and is normally completed in one step that does not require any additional chemicals or materials. Another benefit of the laser based techniques is that this approach does not require vacuum conditions or the use of organic solvents. A primary concern when applying laser pulses to thin film of biomaterials is the potential for undesirable thermal effects. Advantages using femtosecond laser for material modification include high precision with negligible collateral damage and heat affected zones [162]. It has been found that the biomaterial surface topography influences the ability of cell adhesion and interaction, which is critically

important for achievement of optimal bioactivity. The cell migration is one of the important cellular activities for cell–cell and cell–extracellular matrix interactions, which involve as a main role in the mechanism of cell proliferation on the matrix. Laser-ablated micro-grooves have been used to modify the surface characteristics of biomaterials and influence cellular behaviour. These laser-micro grooves have been used to promote contact guidance, a phenomenon where cells align themselves and migrate along the grooves. The modified response of the cells to these different laser treated surfaces is clearly detectable. It is evident that the induction of roughness, facilitated cell orientation. Surface topography has been shown to influence the cellular functions. Micro- and nano-structures influence the cells adhesion, spreading, proliferation, migration, and differentiation of different cell types. Many experimental studies have demonstrated that different type of cell's like nerve, osteoblasts, fibroblast cells attach easily and migrate with a preference to surfaces with rough microstructure. One hypothesis is associated with the relation of surface roughness to improvement of effective surface area. Thus making the surface roughness (Ra) as one of the important material surface properties. In the literature two scales for roughness estimation is adapted: micro (1-100 μ m) and nano (bellow 100nm) roughness [163]. The micro and nanoscale irregularities show to regulate the cell behaviour selectively. Depending on the size of the surface undulations different cells activities are triggered [164]. Another important surface property is its wettability. The initial response of cell behaviour is governed by the hydrophobicity/hydrophilicity of the material surface. The surface is categorized to be hydrophilic when the water contact angle is $< 90^\circ$, and hydrophobic when the water contact angle is $> 90^\circ$. When the contact angle have values more than 150° , the surface is ascribed as superhydrophilic.

The surface topographical properties, at nanoscale, affect the cells interaction process. The main factors of cell-behaviour which are mainly influenced by the nanostructured surface are: cell's orientation, morphology and disposition. The evolution of cell proliferation reveals that the cells do react to hydrophobic and hydrophilic surfaces and are strongly dependent on surface morphology. Many reports have emphasized on the role of extra cellular matrix (ECM) topography in orientation of cell migration. Nanoroughness of materials is one of the properties which closely correspond with the origin of the extracellular matrix. However, the actual mechanism of contact guidance and selective cell adhesion on the laser grooves is a complex process of chemical and topographical stimuli. Change in the surface roughness affects the cells receptivity due to the change in extra cellular matrix protein adsorption on micro grooved surfaces. Cells mobility is governed by integrin-mediated focal adhesions [165, 166]. They tend to adapt focal adhesions in dependence to

deviations in the surface structure, internal physical strengths present in the ECM microenvironment and molecular properties. Cell locomotion occurs at the leading edge, when a membrane protrusion has emerged by small focal adhesions in order to make an initial contact with the ECM. Changes in local integrin adhesion force, influences cell membrane stretching and cell movement, thus affecting its response to surface roughness. In focal adhesions, the mechanical tension that cells experience, as a consequence of surface irregularities, causes conformational changes to focal adhesion proteins which lead to mechano-sensing and adhesion signalling.

The control over nanostructures can be particularly powerful in controlling cell behaviour. Cells do react strongly to the surfaces; they adhere, spread, and change their shape depending on the geometry of the features [167]. The process of creation of nanofiber scaffolds will enable tissue engineering applications that require precise placement of cells in an organized pattern on a substrate having geometric constraints. Previous studies have shown that laser irradiation is a suitable method for production of thin layer of biomaterial porous matrix [168]. However, there is scarce information about the ability of the method to influence the scaffold matrix microstructure. Within the scope of my phd work, I actively collaborated with the group in Institute of Electronics-Bulgarian Academy of Sciences to demonstrate the effectiveness of application of femtosecond laser pulses for successful modification of surfaces of gelatin, collagen and collagen–elastin thin films, for creation of micro and nanoscale structures, and to study the thin film structure evolution dependence on laser parameters. Experimental measurements of the effects of femtosecond laser irradiation parameters on pores shape, pore wall morphology, and interconnectivity between pores, which are important for cell seeding, migration, growth, mass transport, gene expression, and new tissue formation in three dimensions, were compared for different biomaterial surfaces. We investigated the surface morphology of single and multiple shots irradiated thin films of different biomaterials and show how the interaction of multiple overlapping pulses with different pulse durations influence the surface roughness. The appropriate microarchitecture for scaffolds made of porous foam of gelatin and collagen induced by femtosecond laser modification was determined. It is also vital to determine the right combination of laser parameters to obtain the desired surface morphology and quality. To achieve this, appropriate settings of laser intensity, pulse number, and pulse duration are critical. We report, herein, the optimal laser parameters for creation of surface matrix on biopolymer films to promote the greatest degree of cell proliferation and the successful cell culture results on collagen–elastin porous matrix. However, to better control the surface modification process using ultrashort laser pulses it is necessary to understand the fundamental formation mechanism of these small surface features,

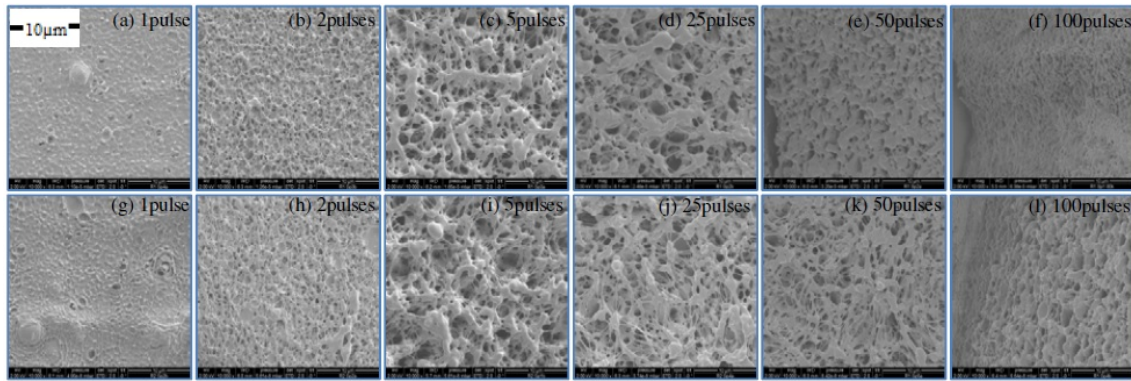


Figure 7.1: SEM images of gelatin thin films after irradiation with 30fs pulses (a to f) and 500fs pulses (g to l). Fluence: $3J/cm^2$

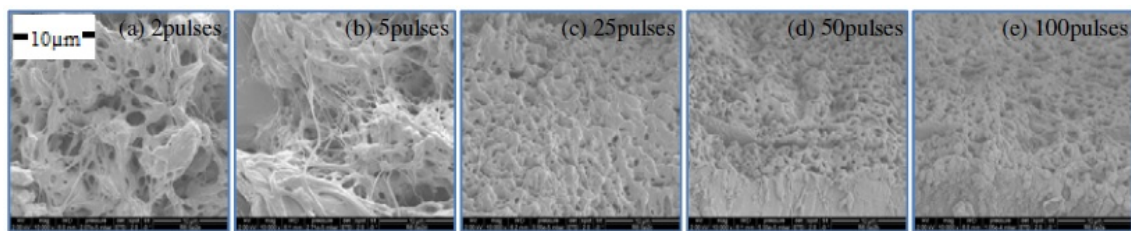


Figure 7.2: SEM images of gelatin films after irradiation with a 5ps pulse. Fluence: $3J/cm^2$

which is still largely not understood.

7.1 Pulse number and pulse duration dependence

Limited information is available on the interaction of high energy ultrashort laser pulses with thin biomaterial films. Laser induced nanometer scale biomaterial matrix formation can be controlled by varying the number of applied pulses, pulse duration, and laser fluence. The control over nanostructures can be particularly powerful for controlling cell proliferation. The data reported here extends the existing information about ultra-short laser pulse biomaterial modification. Our study shows that, low ($< 1 J/cm^2$) and medium ($1 - 5 J/cm^2$) laser fluence levels and small number of laser shots (< 5 pulses) are most suitable conditions for producing nanoporous surface modification. To study the pulse number and pulse duration dependence on surface modifications self-standing gelatin films of $\approx 100 \mu m$ thickness were prepared and irradiated with femtosecond laser pulses from a Ti:sapphire laser amplifier as shown in Fig.3.6. When irradiated with pulses with a fixed fluence of $3J/cm^2$, in subject of pulse duration (30 fs, 500 fs and 5 ps) and number of pulses (1, 2, 5, 25, 50 and 100) the gelatin films were modified like as shown in Figs.7.1 & Fig.7.2. Fig.7.1 shows the SEM images of the irradiated regions when the sample is irradiated with

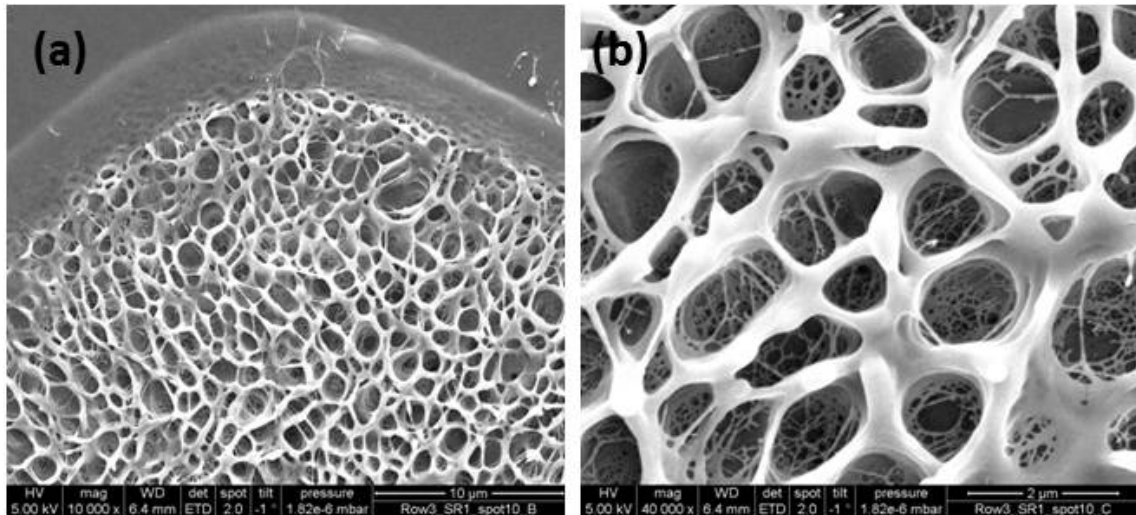


Figure 7.3: SEM images of single pulse irradiated collagen-elastin film at $\lambda = 800$ nm, $\tau = 30$ fs, $F = 3.92$ J/cm².

30 fs (Fig.7.1 a to f) and 500 fs (Fig.7.2 g to l) pulses. Fig.7.1 clearly shows the onset of formation of a network of interconnected micro-pores with the number of irradiated pulses. We can clearly distinguish the onset of surface modification which starts by irradiation with 1 pulse, and after irradiation with more than 25 pulses the surface modification transforms to ablation of the fine structures.

The mechanism of the foaming surface is not a classical ablation process leading to a clean etching. It clearly proceeds by a dense bubble nucleation followed by a fast expansion because of strong pressure effects. The process leads to a submicrometer-sized bubble nucleation of tissue with negligible heat transfer and collateral damage. The gas formed by laser ablation may play an important role in the pressure equilibration inside the bubbles. It clearly proceeds by a fast expansion because of strong pressure effects. In addition, owing to the expansion of the heated plasma, a high pressure transient propagates radially from the laser induced optical breakdown (LIOB) center into the surrounding environment. The investigations of the samples revealed the presence of a liquid phase during the formation of the nanomatrix. Evidence of this fact is the presence of small interconnections which indicate a flow of molten material between the separate pores. The water content of the collagen films is also important to be considered since it is a source of vapor and vapor pressure when bubbles form. Collagen films contain 15% of water [165, 166]. The ablation reproducibility obtained with fs laser assisted method could be exploited to produce reliable microstructure features in a broad range of biopolymers. Currently there are still many uncertainties regarding the optimum requirements for a scaffold in tissue engineering. Some of them are related to the scaffold pore size and porosity. Controlling the processing of biocompatible biopolymer based matrices may lead to a better understanding of the cellular requirements necessary

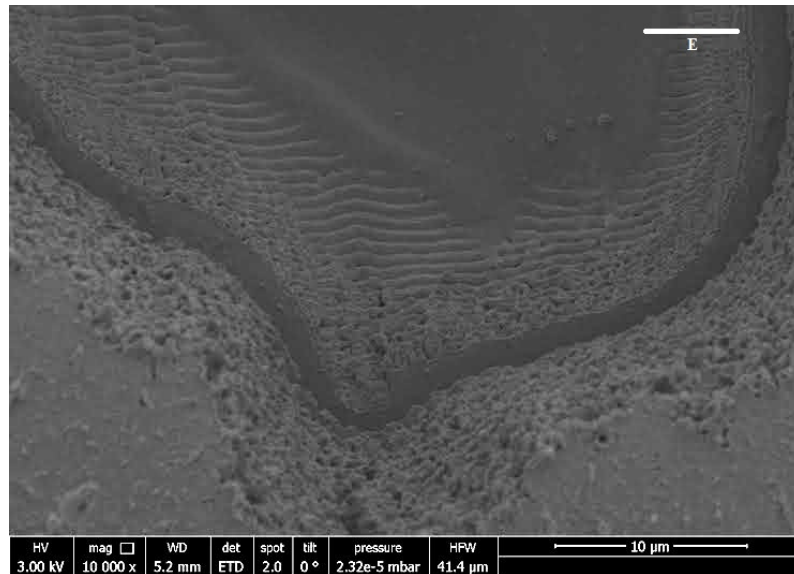


Figure 7.4: SEM image of Chitosan sample when irradiated with 50 pulses of 30 fs and fluence $3J/cm^2$.

for successfully regenerating new tissue scaffolds.

In the many bio-polymers we investigated we did not observe the formation of periodic structures. However, when Chitosan sample is irradiated with 50 pulses of 30 fs duration and $3 J/cm^2$, in the center, most of the sample is ablated, but where a thin layer of the material is still present, LSFLs with periods ~ 730 nm were observed parallel to the polarization as shown in the Fig.7.4.

7.2 Conclusions

The results presented show capability of tuning the micro-pores dimensions by controlling the number of ultrashort pulses, pulse duration, and laser fluence. Our study shows that a large variety of nano- and micro-pores can be controllably produced on biomaterials by varying femtosecond laser irradiation parameters. Femtosecond laser modification is able to produce a biopolymer porous matrix that mimic in part the structure and biological function of the extracellular matrix and can be potentially used for controlling cell behaviour. It is tunable and can be used to design structures that affect cell proliferation, viability, and spreading. It was demonstrated that surface topography has an important effect on cells mobility and that cells are able to reorganize themselves in relation to surface nanofeatures.

Chapter 8

White Light Generation in Water

The interaction of intense laser light with matter continues to be a topic of considerable interest due to a host of nonlinear optical effects associated with it, and one process which clearly and visually shows the manifestation of these nonlinear optical effects is the supercontinuum emission (SCE) or white-light generation. When intense pulses of infrared light interacts with transparent condensed matter or gases its spatial and temporal profiles are strongly modified by self-focusing/defocusing and self-phase modulations respectively, resulting in spectral broadening of the pulses whose wavelengths can span from the ultraviolet to the near infrared. Since its initial discovery in 1970 by Alfano and Shapiro using pico-second pulses in glass medium [169], the supercontinuum generation has been extensively investigated in different media: solids [170, 171], liquids [172–174], gases [175, 176], macromolecular media [177] etc. In 1983, Fork et al, generated the femtosecond supercontinuum by focusing 80 fs pulses into ethylene glycol [172]. Generation of supercontinuum in water by femtosecond laser pulses is a simple technique and is studied by various groups [173, 178]

Filamentation is an important process in SCE [175]. When a laser pulse with peak power higher than the critical power P_{cr} ($P_{cr} = 3.77\lambda^2/8\pi n_o n_2$, where n_o and n_2 denote, linear and nonlinear refractive indices of the medium respectively) propagates through a medium, because of optical Kerr effects, it self-focus. As the pulse self-focus, if the intensity is high enough, the molecules ionize eventually producing a plasma. The produced plasma now defocuses the pulse and thus limits the peak intensity. This self-focusing and defocussing effect results in a series of self-foci points (channel) along the propagation path known as “filaments”. During this filamentation process, because of different mechanisms like self-phase modulations (SPM), self-steepening, four-wave mixing, multi photon excitation (MPE) etc, the laser pulse transforms into white light. This phenomenon has applications in opti-

cal pulse compression, optical parametrical amplification, time-resolved broadband spectroscopy etc. Despite a wide variety of applications, and extensive theoretical and experimental investigations over last 4.5 decades, it is modest to say that the filamentation process and the associated white light generation have not fully been understood yet. The main reason for this is due to a number of several non-linear effects happening at the same time and the theoretical treatment should involve a number of coupled nonlinear effects. White light generation in water with propagation of intense laser pulses has been investigated by several authors, however, to the best of our knowledge, a systematic study on the dependence of pulse duration on spectral broadening and the efficiency of the white light generated under different focusing conditions is not studied. This study aims to focus on this issue.

The setup for generating the white light is explained in Sec.3.2.2 and illustrated in Fig.3.7. Pulse energy is changed by the half-wave plate placed before the compressor. The half-wave plate and the prisms placed at Brewster angle in the compressor together act as an attenuator. The pulse width is changed by adjusting the dispersion in the compressor.

Fig.8.1 shows the spectrum recorded at the output of the cuvette for different pulse energies. The symmetrical broadening of the spectrum around the incident laser wavelength (800 nm with FWHM $\sim 42nm$) is attributed to self-phase modulations (SPM) arising from Kerr non-linearity. The asymmetric component in the blue spectral region is attributed to processes like four-wave mixing, self-steepening[179], plasma formation[169] etc. It can be seen from the Fig.8.1 that beyond 300 μJ the spectral conversion doesn't rise as steep and almost saturates.

The white light spectrum recorded at fixed input energy of 500 μJ and different pulse durations is shown in Fig.8.1. The spectrum shows that at pulse durations >120 fs, there is only symmetric component of self-phase modulations present in the spectrum. As the pulse duration is reduced the asymmetric component of the spectrum on the blue side increases drastically. It can also be noticed that unlike the saturation effect seen with energy, there is no saturation of the conversion seen as the pulse duration is reduced.

To see the effect of the focussing geometry and the optimal distance of focussing in the water to generate efficient white light, we focussed the input beam at different depths inside the water by moving the cuvette, which is on a linear stage, by known distances. Fig.8.3 shows the spectras recorded with varying focal depths. The cuvette is first moved so as to have the focus on the surface of the water. Then it is raised in steps of 1 mm so as to have the geometrical focus inside the water at various depths in steps of 1 mm. As can be seen in Fig.8.3, the maximum broadening

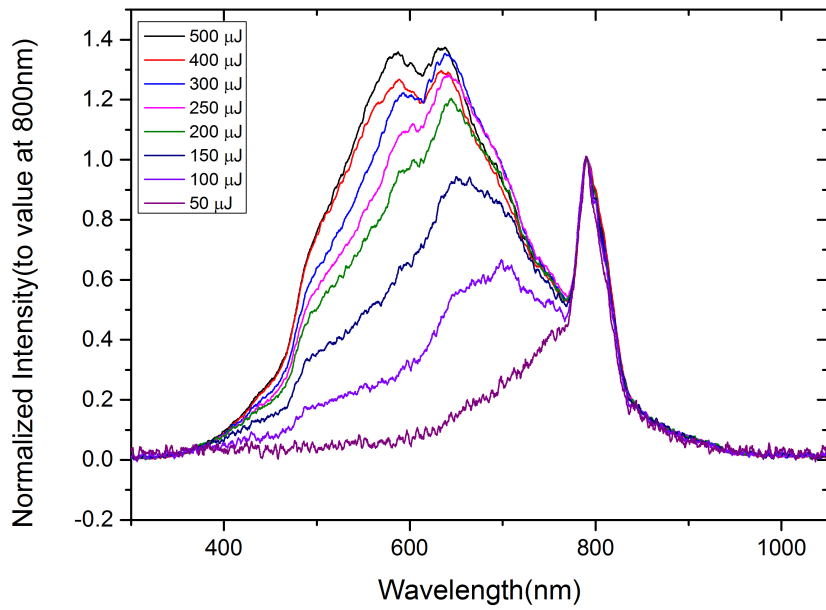


Figure 8.1: SCE spectra from water when incident with 30 fs laser pulses at 1 KHz repetition rate with different energies.

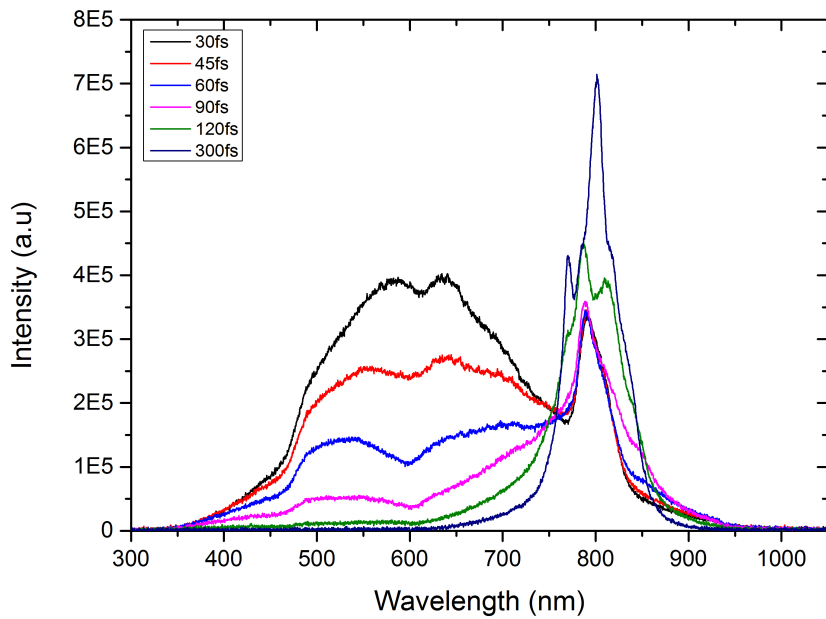


Figure 8.2: SCE spectra from water when incident with fs pulses of duration 30-300fs.

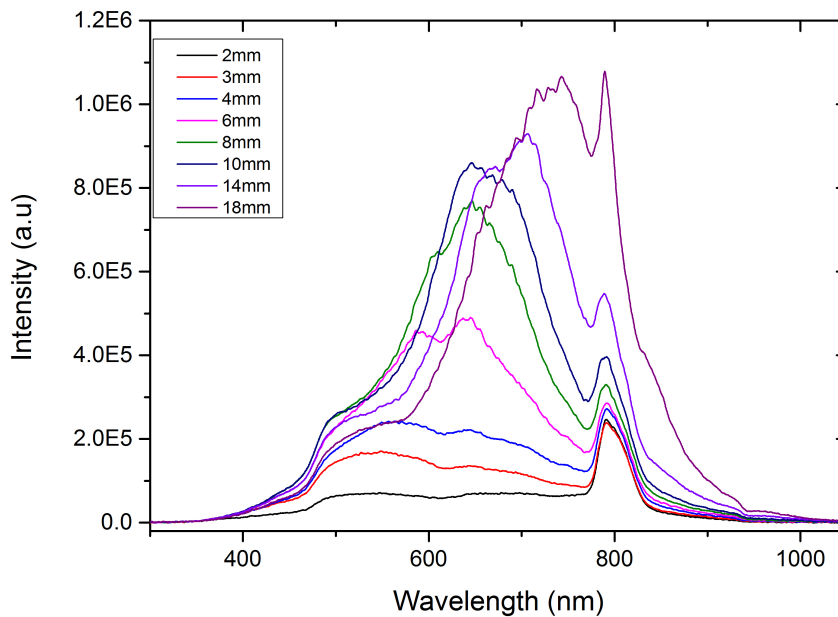


Figure 8.3: SCE spectra from water when incident with 30 fs laser pulses when focussed at different depths from the top surface.

happens when the geometrical focal point is set between 6 and 8mm. Fig.8.4 shows the images of filamentation formed inside the water. It can be seen that as the geometrical focal point is increased, the filamentation channel becomes quite long. When the focal point is set to 18 mm from the top surface, the channel hits the bottom of the cuvette damaging it instantly.

Fig.8.5 shows the efficiency of the white light generated in the water when the incident laser beam is focussed at different focal depths. A colored glass band pass filter (Thorlabs-FGS900) which has 75% transmission in the 300 - 750 nm spectral range is used to block the incident laser radiation. The transmitted white light power is measured with a power meter and is plotted against the geometrical focal depths. This is done for three different pulse durations to see the effect of pulse duration on the conversion efficiency. Efficiency with and without the filter is shown in the figure. It can be seen that the efficiency of white light is about 20% for pulses of duration 30 fs. For pulses of twice the width, the efficiency drops by half. This demonstrates the importance of pulse duration. It can also be seen in Fig.8.5 that the overall power transmitted increases with the geometrical focal distance. This is because of the formation of long filament channels at higher focal depths which reduces the transmission losses. Also it can be seen that shorter pulses have less transmission losses than longer pulses.

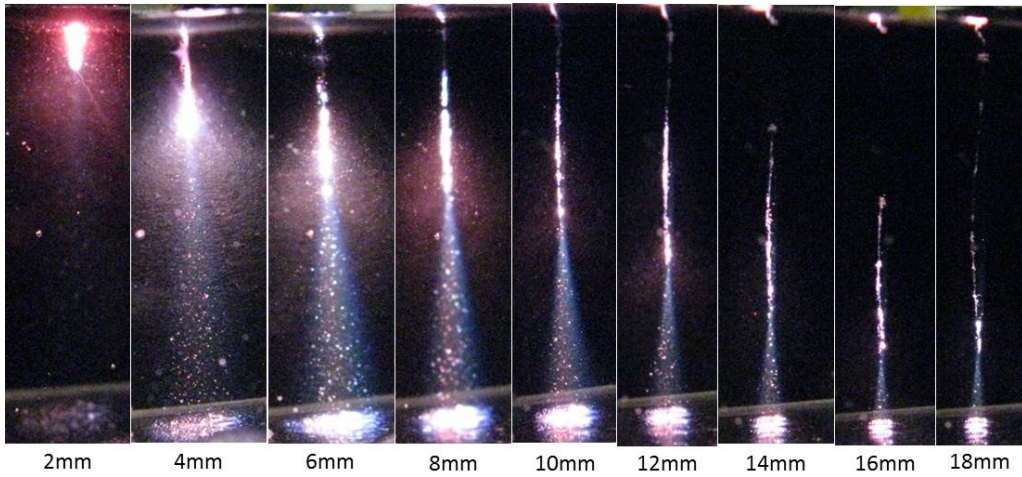


Figure 8.4: Images of filamentation in water when incident with 30 fs laser pulses when focussed at different depths from the top surface.

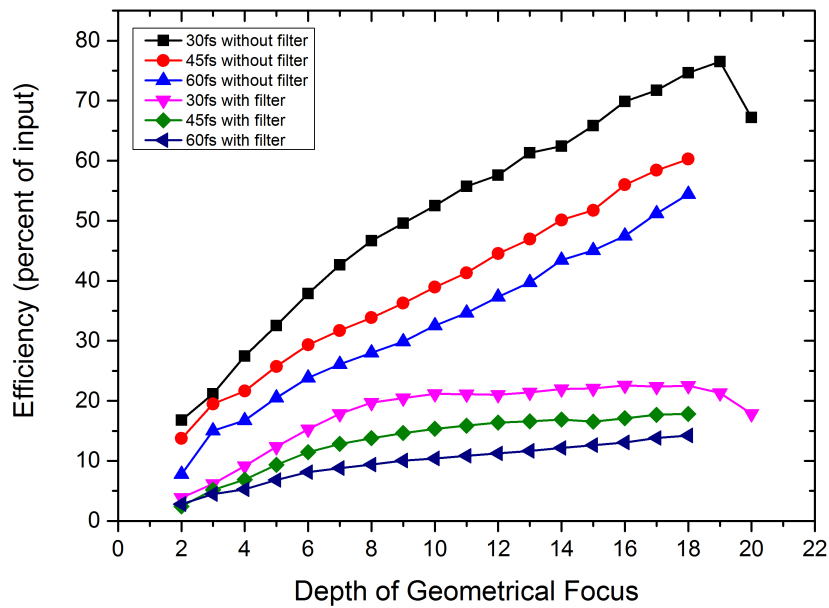


Figure 8.5: Efficiency of white light generated in water when incident with 30 fs laser pulses at different depths. Set 1 is colored glass band pass filter (Thorlabs-FGS900), which has 75% transmission in 300 - 750nm range.

8.1 Conclusions

White light (or Super continuum) is generated in distilled water with ultrashort laser pulses of 30 fs to 300 fs duration. Efficient white light is generated with pulses of shortest duration. The saturation effect seen with increasing input energy is not seen with reducing pulse widths. The efficiency of the white light generated is maximum when the geometrical focal depth is about 6-8 mm. Efficiency $>20\%$ is achieved with ~ 30 fs pulses.

Chapter 9

Conclusions

In this thesis, ablation of materials, formation of periodic micro- and nano-structures on metals and semi-conductors, and structuring on bio-polymer films upon femtosecond laser pulse irradiation was studied in details. *Ablation threshold fluence* is an important parameter to be known for precise material processing applications. Knowing the values can also give insight into the physical processes taking place in the material. In this work, the threshold values has been determined for copper, silicon and gelatin bio-polymer samples for multiple pulse irradiation ranging from 3 to 1000 pulses. The ablation threshold for all investigated samples showed a decrease with pulse duration. For Copper, the threshold scales as $\tau^{0.05}$, for Silicon as $\tau^{0.12}$ and for Gelatin as $\tau^{0.22}$.

The dynamics of particles that are emitted (ions, clusters and neutrals) when irradiated with pulses as short as 10 fs was studied using the reflectron type of mass spectrometer. The results of our time-of-flight measurements of various materials are presented. The dependence of ion and neutral emission with fluence and pulse duration showed similar trend. The recorded velocity spectra of silicon and metals, like copper, titanium and silver, showed multiple high energy peaks that could be attributed to fast processes like CE and ultrafast melting. However ions are emitted with energies of few KeV [23] and maximum energies of neutrals recorded is only few eV. Since the probability of slow moving ions capturing an electron is higher, we can conclude that probably the emitted neutral particles are formed from the ejected ions neutralized by electron capture in the vicinity of the surface.

Laser induced periodic surface structures (LIPSS) were produced on metals and semi-conductors and the dependence of their formation on laser parameters were studied in detail. In particular, near wavelength structures (LSFLs), and sub-100-nm structures (HSFLs) were made on a mirror like titanium surface by irradiating it with linearly polarized femtosecond (fs) laser pulses in air environment. In scanning

mode with scanning speed of 0.2 mm/s ($N \approx 220$), and $\tau = 30$ fs, HSFLs form parallel to the laser polarization within a narrow fluence range of $30mJ/cm^2$ to $45mJ/cm^2$, and the periodicity increases with fluence. With number of pulses, the periodicity of HSFLs do not show a clear trend, but the periodicity of LSFLs reduces exponentially. The periodicities of both types of LIPSS demonstrate opposite pulse duration and wavelength dependencies, which suggest their origins are different and cannot be explained by interference model developed for LSFLs.

Dense cavitation and bubbling phenomenon yield micro/nano-foaming when biopolymer films like collagen and gelatin are irradiated with laser pulses. It is hypothesized that such artificially created scaffold matrix may be seeded with cells which then are encouraged to develop into the desired tissue. Extensive experiments were done to study the formation of the scaffolds under irradiation of femtosecond laser pulses. The results presented show capability of tuning the micro-pores dimensions by controlling the number of ultrashort pulses, pulse duration, and laser fluence. Our study shows that a large variety of nano- and micro-pores can be controllably produced on biomaterials by varying femtosecond laser irradiation parameters.

One process which clearly and visually shows the manifestation of nonlinear optical effects taking place when an ultrashort laser pulse is irradiated on a condensed media is the supercontinuum emission (SCE) or white-light generation. SCE is generated in distilled water with ultrashort laser pulses of 30 fs to 300 fs duration. Efficient white light is generated with pulses of shortest duration. The saturation effect seen with increasing input energy is not seen with reducing pulse widths. The efficiency of the white light generated is maximum when the geometrical focal depth is about 6-8 mm in the medium. Efficiency $>20\%$ is achieved with ~ 30 fs pulses.

A note on the use of sub-10 fs pulses: We have extensively used the sub-10 fs pulses in our ablation and structuring experiments. With the experience we gained, we tried to address the following questions. Does the extension from 50 fs to sub-10 fs bare any advantages for material processing applications? Do we see any new ablation processes with sub-10 fs pulses? How easy it is to use sub-10 fs pulses and are the drawbacks significantly more than the advantages.

In our experiments on ablation threshold measurements and TOF measurements, we didnot notice any really new phenomenon by using sub-10 fs pulses. It was only a logical extension of what we observed with pulses of about 100 fs - 30 fs. Be it the ablation threshold values or the emission of atomic species, the reduction in pulse duration scaled in accordance with what we observed in going from 500 fs to 30 fs. Surface structures produced with sub-10 fs pulses on different materials also didnot show any unique patterns. On the other hand generating and using the

sub-10 pulses exhibits experimental challenges. Over the years, Ti:sapphire lasers delivering pulses of few mJ and ~ 25 fs, have become robust enough and can run for many hours with constant specifications. Controlling the dispersion of these pulses is also easy. However, the case with sub-10 fs pulses generated from hollow-core-fibers is different. The spectrum needed to achieve sub-10 fs pulses is huge and hence the dispersion management becomes quite complex. Moreover, since the fiber core is only 100 - 200 μm in diameter, mechanical stability is an issue. To have stable gas pressure inside the hollow-core-fiber is also important. It has a direct consequence on the spectrum and hence the pulse duration. Any changes, like the input power or beam pointing or the gas pressure will have a direct effect on the pulse duration. So using such pulses for experiments will require very controlled environment with live monitoring of pulse duration at all times during the experiments. So the suitability of sub-10 fs pulses for material processing applications is questionable.

Bibliography

- [1] T.H. Maiman, *Nature* **187**(4736), 493 (1960)
- [2] D. Strickland, G. Mourou, *Optics Communications* **56**, 219 (1985)
- [3] A. Stingl, R. Szipöcs, M. Lenzner, C. Spielmann, F. Krausz, *Opt. Lett.* **20**(6), 602 (1995)
- [4] M. Hentschel, R. Kienberger, C. Spielmann, G.A. Reider, N. Milosevic, T. Brabec, P. Corkum, U. Heinzmann, M. Drescher, F. Krausz, *Nature* **414**(6863), 509 (2001)
- [5] A. Baltuska, T. Udem, M. Uiberacker, M. Hentschel, E. Goulielmakis, C. Gohle, R. Holzwarth, V.S. Yakovlev, A. Scrinzi, T.W. Hansch, F. Krausz, *Nature* **421**(6923), 611 (2003)
- [6] C. Phipps (ed.), *Laser Ablation and its Applications* (Springer US, 2007)
- [7] L. Keldysh, *JETP* **20**, 1307 (1965)
- [8] L. Perelomov, V. Popov, M. Terentev, *Sov.Phys.JETP* **23**, 924 (1966)
- [9] E. Carpane, D. Höche, P. Schaaf, *Fundamentals of Laser-Material Interactions* (Springer Berlin Heidelberg, 2010), vol. 139, pp. 21–47
- [10] D. Pines, P. Nozières, *The Theory of Quantum Liquids* (Benjamin, 1966)
- [11] W. Lotz, *Zeitschrift für Physik* **216**(3), 241 (1968)
- [12] W. Lotz, *J. Opt. Soc. Am.* **60**(2), 206 (1970)
- [13] P.B. Allen, *Phys. Rev. Lett.* **59**, 1460 (1987)
- [14] S.I. Anisimov, B.L. Kapeliovich, T.L. Perel'man, *Soviet Physics, JETP* **39**, 375 (1974)
- [15] B. Rethfeld, *Phys. Rev. Lett.* **92**, 187401 (2004)
- [16] A. Kaiser, B. Rethfeld, M. Vicanek, G. Simon, *Phys. Rev. B* **61**, 11437 (2000)
- [17] J. Denavit, *Physics of Fluids* **22**(7), 1384 (1979)

- [18] M. Huang, F. Zhao, Y. Cheng, N. Xu, Z. Xu, *Phys. Rev. B* **79**, 125436 (2009)
- [19] S. Tokita, S. Inoue, S. Masuno, M. Hashida, S. Sakabe, *Applied Physics Letters* **95**(11), 111911 (2009)
- [20] J. Reif, F. Costache, S. Eckert, M. Henyk, *Applied Physics A* **79**(4), 1229 (2004)
- [21] R. Stoian, D. Ashkenasi, A. Rosenfeld, E.E.B. Campbell, *Phys. Rev. B* **62**, 13167 (2000)
- [22] H. Dachraoui, W. Husinsky, *Phys. Rev. Lett.* **97**, 107601 (2006)
- [23] W.G. Roeterdink, L.B.F. Juurlink, O.P.H. Vaughan, J. Dura Diez, M. Bonn, A.W. Kley, *Applied Physics Letters* **82**(23), 4190 (2003)
- [24] H. Dachraoui, W. Husinsky, *Applied Physics Letters* **89**(10), 104102 (2006)
- [25] H. Dachraoui, W. Husinsky, G. Betz, *Applied Physics A* **83**(2), 333 (2006)
- [26] A.A. Rukhadze, K.Z. Rukhadze, V.P. Tarakanov, *Technical Physics* **53**(2), 264 (2011)
- [27] V.Y. Bychenkov, V.F. Kovalev, *Plasma Physics Reports* **32**(11), 973 (2006)
- [28] S. Sakabe, M. Hashida, S. Tokita, S. Namba, K. Okamuro, *Phys. Rev. B* **79**, 033409 (2009)
- [29] N.M. Bulgakova, R. Stoian, A. Rosenfeld, I.V. Hertel, E.E.B. Campbell, *Phys. Rev. B* **69**, 054102 (2004)
- [30] R. Stoian, A. Rosenfeld, D. Ashkenasi, I.V. Hertel, N.M. Bulgakova, E.E.B. Campbell, *Phys. Rev. Lett.* **88**, 097603 (2002)
- [31] A. Vella, B. Deconihout, L. Marrucci, E. Santamato, *Phys. Rev. Lett.* **99**, 046103 (2007)
- [32] N.M. Bulgakova, I.M. Burakov, Y.P. Meshcheryakov, R. Stoian, A. Rosenfeld, I.V. Hertel, *Journal of Laser Micro/Nanoengineering* **2**, 76 (2007)
- [33] K. Sokolowski-Tinten, C. Blome, C. Dietrich, A. Tarasevitch, M. Horn von Hoegen, D. von der Linde, A. Cavalleri, J. Squier, M. Kammler, *Phys. Rev. Lett.* **87**, 225701 (2001)
- [34] K.H. Leitz, B. Redlingshfer, Y. Reg, A. Otto, M. Schmidt, *Physics Procedia* **12, Part B**, 230 (2011)
- [35] B.N. Chichkov, C. Momma, S. Nolte, F. von Alvensleben, A. Tünnermann, *Applied Physics A* **63**(2), 109 (1996)

- [36] T.Q. Qiu, C.L. Tien, *Int. J. Heat Mass Transfer* **35**, 719 (1992)
- [37] L. Jiang, H.L. Tsai, *Journal of Heat Transfer* **127**, 1167 (2005)
- [38] M. Birnbaum, *Journal of Applied Physics* **36**, 3688 (1965)
- [39] C.S. Nathala, A. Ajami, A.A. Ionin, S.I. Kudryashov, S.V. Makarov, T. Ganz, A. Assion, W. Husinsky, *Opt. Express* **23**(5), 5915 (2015)
- [40] A.Y. Vorobyev, V.S. Makin, C. Guo, *Journal of Applied Physics* **101**(3), 034903 (2007)
- [41] F. Keilmann, Y.H. Bai, *Applied Physics A* **29**(1), 9 (1982)
- [42] E.V. Golosov, A.A. Ionin, Y.R. Kolobov, S.I. Kudryashov, A.E. Ligachev, S.V. Makarov, Y.N. Novoselov, L.V. Seleznev, D.V. Sinitsyn, *Nanotechnologies in Russia* **6**(3), 237 (2011)
- [43] K. Okamuro, M. Hashida, Y. Miyasaka, Y. Ikuta, S. Tokita, S. Sakabe, *Phys. Rev. B* **82**, 165417 (2010)
- [44] J. Bonse, J. Krüger, S. Höhm, A. Rosenfeld, *Journal of Laser Applications* **24**(4), 042006 (2012)
- [45] D. Haneman, R. Nemanich, *Solid State Communications* **43**(3), 203 (1982)
- [46] J. Bonse, M. Munz, H. Sturm, *Journal of Applied Physics* **97**(1), 013538 (2005)
- [47] E.M. Hsu, T.H.R. Crawford, H.F. Tiedje, H.K. Haugen, *Applied Physics Letters* **91**(11), 111102 (2007)
- [48] Q. Wu, Y. Ma, R. Fang, Y. Liao, Q. Yu, X. Chen, K. Wang, *Applied Physics Letters* **82**(11), 1703 (2003)
- [49] J. Reif, F. Costache, M. Henyk, S.V. Pandelov, *Applied Surface Science* **197–198**, 891 (2002)
- [50] D. Ashkenasi, A. Rosenfeld, H. Varel, M. Wähmer, E. Campbell, *Applied Surface Science* **120**(1–2), 65 (1997)
- [51] D.C. Emmony, R.P. Howson, L.J. Willis, *Applied Physics Letters* **23**(11), 598 (1973)
- [52] J.E. Sipe, J.F. Young, J.S. Preston, H.M. van Driel, *Phys. Rev. B* **27**, 1141 (1983)
- [53] S.E. Clark, N.C. Kerr, D.C. Emmony, *Journal of Physics D: Applied Physics* **22**(4), 527 (1989)

- [54] S.A. Wilson, J.R. Zimbelman, Journal of Geophysical Research **109**, E10003 (2004)
- [55] R. Cuerno, A.L. Barabási, Phys. Rev. Lett. **74**, 4746 (1995)
- [56] A. Ionin, S. Kudryashov, A. Ligachev, S. Makarov, L. Seleznev, D. Sinitsyn, Journal of Experimental and Theoretical Physics **94**(4), 266 (2011)
- [57] A.A. Ionin, S.I. Kudryashov, S.V. Makarov, L.V. Seleznev, D.V. Sinitsyn, A.E. Ligachev, E.V. Golosov, Y.R. Kolobov, Laser Physics Letters **10**(5), 056004 (2013)
- [58] T. Okada, H. Kawahara, Y. Ishida, R. Kumai, T. Tomita, S. Matsuo, S. Hashimoto, M. Kawamoto, Y. Makita, M. Yamaguchi, Applied Physics A **92**(3), 665 (2008)
- [59] E.M. Hsu, T.H.R. Crawford, C. Maunders, G.A. Botton, H.K. Haugen, Applied Physics Letters **92**(22), 221112 (2008)
- [60] J.F. Young, J.S. Preston, H.M. van Driel, J.E. Sipe, Phys. Rev. B **27**, 1155 (1983)
- [61] J. Bonse, J. Krüger, Journal of Applied Physics **108**(3), 034903 (2010)
- [62] M. Huang, F. Zhao, Y. Cheng, N. Xu, Z. Xu, ACS Nano **3**(12), 4062 (2009). PMID: 20025303
- [63] J. Bonse, A. Rosenfeld, J. Krüger, Journal of Applied Physics **106**(10), 104910 (2009)
- [64] G. Miyaji, K. Miyazaki, Opt. Express **16**(20), 16265 (2008)
- [65] G. Miyaji, K. Miyazaki, Applied Physics Letters **91**(12), 123102 (2007)
- [66] F. Garrelie, J.P. Colombier, F. Pigeon, S. Tonchev, N. Faure, M. Bounhalli, S. Reynaud, O. Parriaux, Opt. Express **19**(10), 9035 (2011)
- [67] E. Gurevich, Applied Surface Science **278**, 52 (2013). Laser materials processing for micro and nano applications, E-MRS 2012 Symposium V
- [68] O. Varlamova, J. Reif, S. Varlamov, M. Bestehorn, *Self-organized Surface Patterns Originating from Laser-Induced Instability* (Springer International Publishing Switzerland, 2015)
- [69] Y. Kuramoto, T. Tsuzuki, Progress of Theoretical Physics **55**(2), 356 (1976)
- [70] G. Sivashinsky, Acta Astronautica **6**(5), 569 (1979)
- [71] M. Kardar, G. Parisi, Y.C. Zhang, Phys. Rev. Lett. **56**, 889 (1986)

- [72] D.E. Spence, P.N. Kean, W. Sibbett, *Opt. Lett.* **16**(1), 42 (1991)
- [73] P.F. Curley, C. Spielmann, T. Brabec, F. Krausz, E. Wintner, A.J. Schmidt, *Opt. Lett.* **18**(1), 54 (1993)
- [74] B. Proctor, F. Wise, *Applied Physics Letters* **62**(5), 470 (1993)
- [75] R. Szipöcs, C. Spielmann, F. Krausz, K. Ferencz, *Opt. Lett.* **19**(3), 201 (1994)
- [76] M. Nisoli, S.D. Silvestri, O. Svelto, R. Szipöcs, K. Ferencz, C. Spielmann, S. Sartania, F. Krausz, *Opt. Lett.* **22**(8), 522 (1997)
- [77] J.M. Liu, *Opt. Lett.* **7**(5), 196 (1982)
- [78] A.A. Ionin, S.I. Kudryashov, S.V. Makarov, P.N. Saltuganov, L.V. Seleznev, D.V. Sinitsyn, A.R. Sharipov, *JETP Letters* **96**(6), 375 (2012)
- [79] L. Bruschi, M. Santini, G. Torzo, *Journal of Physics B: Atomic and Molecular Physics* **17**(6), 1137 (1984)
- [80] B. Mamyrin, V. Karataev, D. Shmikk, V. Zagulin, *JETP* **37**(1), 82 (1973)
- [81] J. Cheng, C. sheng Liu, S. Shang, D. Liu, W. Perrie, G. Dearden, K. Watkins, *Optics & Laser Technology* **46**, 88 (2013)
- [82] J. Reif, *Springer Series in Materials Science* **191**, 29 (2014)
- [83] J. Reif, in *Laser-Surface Interactions for New Materials Production*, edited by A. Miotello and P. M. Ossi (Springer Berlin Heidelberg, 2010) **130**, 19 (2010)
- [84] W. Kautek, O. Armbruster, *Springer Series in Materials Science* **191**, 42 (2014)
- [85] Y. Jee, M.F. Becker, R.M. Walser, *J. Opt. Soc. Am. B* **5**(3), 648 (1988)
- [86] Z. Sun, M. Lenzner, W. Rudolph, *Journal of Applied Physics* **117**(7), (2015)
- [87] P. Mannion, J. Magee, E. Coyne, G.O. Connor, T. Glynn, *Applied Surface Science* **233**, 275 (2004)
- [88] J. Byskov-Nielsen, J.M. Savolainen, M. Christensen, P. Balling, *Applied Physics A* **101**(1), 97 (2010)
- [89] C. McDaniel, A. Flanagan, G.M.O. Connor, *Applied Surface Science* **295**, 1 (2014)
- [90] B. Neuenschwander, B. Jaeggi, M. Schmid, A. Dommann, A. Neels, T. Bandi, G. Hennig, *Proc. SPIE* **8607**, 86070D (2013)
- [91] M. Hashida, S. Namba, K. Okamuro, S. Tokita, S. Sakabe, *Phys. Rev. B* **81**, 115442 (2010)

- [92] J. Bonse, S. Baudach, J. Krüger, W. Kautek, M. Lenzner, *Applied Physics A* **74**(1), 19 (2002)
- [93] F.D. Niso, C. Gaudiuso, T. Sibillano, F. Mezzapesa, A. Ancona, P. LugarÃ, *Physics Procedia* **41**, 698 (2013)
- [94] H.O. Jeschke, M.E. Garcia, M. Lenzner, J. Bonse, J. Krüger, W. Kautek, *Applied Surface Science* **197**, 839 (2002)
- [95] H.O. Jeschke, M.E. Garcia, *Applied Surface Science* **197**, 107 (2002)
- [96] B.C. Stuart, M.D. Feit, S. Herman, A.M. Rubenchik, B.W. Shore, M.D. Perry, *J. Opt. Soc. Am. B* **13**(2), 459 (1996)
- [97] M. Lenzner, J. Krüger, S. Sartania, Z. Cheng, C. Spielmann, G. Mourou, W. Kautek, F. Krausz, *Phys. Rev. Lett.* **80**, 4076 (1998)
- [98] I. Artyukov, D. Zayarniy, A. Ionin, S. Kudryashov, S. Makarov, P. Saltuganov, *JETP Letters* **99**(1), 51 (2014)
- [99] F.D. Niso, C. Gaudiuso, T. Sibillano, F.P. Mezzapesa, A. Ancona, P.M. Lugarà, *Opt. Express* **22**(10), 12200 (2014)
- [100] J. Byskov-Nielsen, J.M. Savolainen, M. Christensen, P. Balling, *Applied Physics A* **103**(2), 447 (2011)
- [101] B.C. Stuart, M.D. Feit, A.M. Rubenchik, B.W. Shore, M.D. Perry, *Phys. Rev. Lett.* **74**, 2248 (1995)
- [102] A. Ionin, S. Kudryashov, L. Seleznev, D. Sinitsyn, A. Bunkin, V. Lednev, S. Pershin, *Journal of Experimental and Theoretical Physics* **116**(3), 347 (2013)
- [103] P. Danilov, A. Ionin, S. Kudryashov, S. Makarov, A. Rudenko, P. Saltuganov, L. Seleznev, V. Yurovskikh, D. Zayarny, T. Apostolova, *Journal of Experimental and Theoretical Physics* **120**(6), 946 (2015)
- [104] A. Bulgakov, I. Ozerov, W. Marine, *Applied Physics A* **79**(4), 1591 (2004). URL [j](#)
- [105] D.R. Lide (ed.), *CRC Handbook of Chemistry and Physics, 96th Edition. Section 10, Atomic, Molecular, and Optical Physics; Ionization Potentials of Atoms and Atomic Ions* (CRC Press. Boca Raton, Florida, 2015)
- [106] H.P. Cheng, J.D. Gillaspay, *Phys. Rev. B* **55**, 2628 (1997)
- [107] J.E. Carey, C.H. Crouch, M. Shen, E. Mazur, *Opt. Lett.* **30**(14), 1773 (2005)

- [108] W. Fang, C. Changshui, H. Huili, L. Songhao, *Applied Physics A* **103**(4), 977 (2011)
- [109] A.Y. Vorobyev, C. Guo, *Journal of Applied Physics* **117**(3), 033103 (2015)
- [110] S. Bashir, M.S. Rafique, W. Husinsky, *Nuclear Instruments and Methods in Physics Research Section B: Beam Interactions with Materials and Atoms* **275**, 1 (2012)
- [111] A. Borowiec, H.K. Haugen, *Applied Physics Letters* **82**(25), 4462 (2003)
- [112] E.V. Golosov, A.A. Ionin, Y.R. Kolobov, S.I. Kudryashov, A.E. Ligachev, S.V. Makarov, Y.N. Novoselov, L.V. Seleznev, D.V. Sinitsyn, A.R. Sharipov, *Phys. Rev. B* **83**, 115426 (2011)
- [113] S.A. Akhmanov, V.I. Emel'yanov, N.I. Koroteev, V.N. Seminogov, *Soviet Physics Uspekhi* **28**(12), 1084 (1985)
- [114] J.Z.P. Skolski, G.R.B.E. Römer, J. Vincenc Obona, A.J. Huis in ápost Veld, *Journal of Applied Physics* **115**(10), 103102 (2014)
- [115] J. Bonse, S. Höhm, A. Rosenfeld, J. Krüger, *Applied Physics A* **110**(3), 547 (2013)
- [116] C. Guo, G. Rodriguez, A. Lobad, A.J. Taylor, *Phys. Rev. Lett.* **84**, 4493 (2000)
- [117] X.F. Li, C.Y. Zhang, H. Li, Q.F. Dai, S. Lan, S.L. Tie, *Opt. Express* **22**(23), 28086 (2014)
- [118] K. Bazaka, R.J. Crawford, E.P. Ivanova, *Biotechnology Journal* **6**(9), 1103 (2011)
- [119] M. Ye, C.P. Grigoropoulos, *Journal of Applied Physics* **89**(9), 5183 (2001)
- [120] N. Yasumaru, K. Miyazaki, J. Kiuchi, *Applied Physics A* **81**(5), 933 (2005)
- [121] A.A. Ionin, S.I. Kudryashov, S.V. Makarov, A.A. Rudenko, L.V. Seleznev, D.V. Sinitsyn, V.I. Emel'yanov, *Laser Physics Letters* **12**(2), 025902 (2015)
- [122] M. Huang, F. Zhao, Y. Cheng, N. Xu, Z. Xu, *Opt. Express* **16**(23), 19354 (2008)
- [123] O. Varlamova, F. Costache, J. Reif, M. Bestehorn, *Applied Surface Science* **252**(13), 4702 (2006). Proceedings of the European Materials Research society 2005 - Symposium-J: Advances in Laser and Lamp Processing of Functional Materials EMRS 2005 Symposium {JProceedings} of the European Materials Research Society 2005

- [124] T. Tomita, K. Kinoshita, S. Matsuo, S. Hashimoto, Applied Physics Letters **90**(15), 153115 (2007)
- [125] I.A. Artyukov, D.A. Zayarniy, A.A. Ionin, S.I. Kudryashov, S.V. Makarov, P.N. Saltuganov, JETP Letters **99**(1), 51 (2014)
- [126] E.V. Barmina, A.A. Serkov, E. Stratakis, C. Fotakis, V.N. Stolyarov, I.N. Stolyarov, G.A. Shafeev, Applied Physics A **106**(1), 1 (2012)
- [127] S. Höhm, M. Herzlieb, A. Rosenfeld, J. Krüger, J. Bonse, Opt. Express **23**(1), 61 (2015)
- [128] E.V. Golosov, A.A. Ionin, Y.R. Kolobov, S.I. Kudryashov, A.E. Ligachev, Y.N. Novoselov, L.V. Seleznev, D.V. Sinitsyn, Journal of Experimental and Theoretical Physics **113**(1), 14 (2011)
- [129] J.W. Yao, C.Y. Zhang, H.Y. Liu, Q.F. Dai, L.J. Wu, S. Lan, A.V. Gopal, V.A. Trofimov, T.M. Lysak, Opt. Express **20**(2), 905 (2012)
- [130] H. Raether, *Surface Plasmons on Smooth and Rough Surfaces and on Gratings* (Springer Berlin Heidelberg, Berlin, Heidelberg, 1988), chap. Surface plasmons on smooth surfaces, pp. 4–39
- [131] J.M. Savolainen, M.S. Christensen, P. Balling, Phys. Rev. B **84**, 193410 (2011)
- [132] A. Vorobyev, C. Guo, Applied Surface Science **253**(17), 7272 (2007)
- [133] P.B. JOHNSON, P.W. GILBERD, Y. MORRISON, C.R. VAROY, Modern Physics Letters B **15**(28n29), 1391 (2001)
- [134] S.I. Ashitkov, N.A. Inogamov, V.V. Zhakhovskii, Y.N. Emirov, M.B. Agranat, I.I. Oleinik, S.I. Anisimov, V.E. Fortov, JETP Letters **95**(4), 176 (2012)
- [135] C. Wu, L.V. Zhigilei, Applied Physics A **114**(1), 11 (2014)
- [136] E. Barmina, M. Barberoglou, V. Zorba, A. Simakin, E. Stratakis, C. Fotakis, G. Shafeev, J. Optoelectron. Adv. Mater. **12**, 496 (2010)
- [137] G. Yang, Progress in Materials Science **52**(4), 648 (2007)
- [138] H.W. Kang, H. Lee, A.J. Welch, Journal of Applied Physics **103**(8), 083101 (2008)
- [139] S.C. Singh, R.K. Swarnkar, R. Gopal, Journal of Nanoparticle Research **11**(7), 1831 (2009)
- [140] S. Bashir, M.S. Rafique, C.S. Nathala, W. Husinsky, Applied Surface Science **290**, 53 (2014)

- [141] S. Bashir, M.S. Rafique, C.S. Nathala, W. Husinsky, *Applied Physics A* **114**(1), 243 (2014)
- [142] P. Sangeetha, V. Sasirekha, V. Ramakrishnan, *Journal of Raman Spectroscopy* **42**(8), 1634 (2011)
- [143] F. Parker, *Trends in Biochemical Sciences* **9**(6), 289 (1983)
- [144] M.A. Gubko, W. Husinsky, A.A. Ionin, S.I. Kudryashov, S.V. Makarov, C.R. Nathala, A.A. Rudenko, L.V. Seleznev, D.V. Sinitsyn, I.V. Treshin, *Laser Physics Letters* **11**(6), 065301 (2014)
- [145] S. Lazare, V. Tokarev, A. Sionkowska, M. Wiśniewski, *Applied Physics A* **81**(3), 465 (2005)
- [146] S. Lazare, R. Bonneau, S. Gaspard, M. Oujja, R. Nalda, M. Castillejo, A. Sionkowska, *Applied Physics A* **94**(4), 719 (2008)
- [147] L. Kolacna, J. Bakesova, F. Varga, E. Kostakova, L. Planka, A. Necas, D. Lukas, E. Amler, V. Pelouch, *Physiol. Res.* **56**, S51 (2007)
- [148] J.A. Burdick, R.L. Mauck (eds.), *Biomaterials for Tissue Engineering Applications* (Springer Vienna, 2011)
- [149] C.N. Grover, R.E. Cameron, S.M. Best, *Journal of the Mechanical Behavior of Biomedical Materials* **10**, 62 (2012)
- [150] X. Liao, H. Zhang, T. He, *J. Nanomaterials* **2012**, 6:6 (2012)
- [151] A. Sionkowska, J. Kozłowska, *International Journal of Biological Macromolecules* **52**, 250 (2013)
- [152] V. Hovhannisyan, A. Ghazaryan, Y.F. Chen, S.J. Chen, C.Y. Dong, *Opt. Express* **18**(23), 24037 (2010)
- [153] Y. Liu, S. Sun, S. Singha, M.R. Cho, R.J. Gordon, *Biomaterials* **26**(22), 4597 (2005)
- [154] R.A. Boerboom, K.N. Krahn, R.T. Megens, M.A. van Zandvoort, M. Merckx, C.V. Bouten, *Journal of Structural Biology* **159**(3), 392 (2007)
- [155] H.J. Chung, T.G. Park, *Advanced Drug Delivery Reviews* **59**(4–5), 249 (2007).
Matrices and Scaffolds for Drug Delivery in Tissue Engineering
- [156] G. Chen, T. Ushida, T. Tateishi, *Macromolecular Bioscience* **2**(2), 67 (2002)
- [157] N. Bhardwaj, S.C. Kundu, *Biotechnology Advances* **28**(3), 325 (2010)

- [158] A.R.C. Duarte, J.F. Mano, R.L. Reis, *Journal of Bioactive and Compatible Polymers* **24**(4), 385 (2009)
- [159] J.M. Williams, A. Adewunmi, R.M. Schek, C.L. Flanagan, P.H. Krebsbach, S.E. Feinberg, S.J. Hollister, S. Das, *Biomaterials* **26**(23), 4817 (2005)
- [160] S. Lohfeld, M. Tyndyk, S. Cahill, N. Flaherty, V. Barron, P. McHugh, *Journal of Biomedical Science and Engineering* **3**, 138 (2010)
- [161] R. Narayan, P. Goering, *MRS Bulletin* **36**, 973 (2011)
- [162] J. Krüger, W. Kautek, *Polymers and Light* (Springer Berlin Heidelberg, Berlin, Heidelberg, 2004), chap. Ultrashort Pulse Laser Interaction with Dielectrics and Polymers, pp. 247–290
- [163] P. Slepicka, N.S. Kasalkova, J. Siegel, Z. Kolska, L. Bacakova, V. Svorcik, *Biotechnology Advances* **33**(6, Part 2), 1120 (2015). BioTech 2014 and 6th Czech-Swiss Biotechnology Symposium
- [164] K. Anselme, P. Davidson, A. Popa, M. Giazzon, M. Liley, L. Ploux, *Acta Biomaterialia* **6**(10), 3824 (2010)
- [165] R. Major, K. Maksymow, J. Marczak, J. Lackner, M. Kot, B. Major, *Bulletin of the Polish Academy of Sciences Technical Sciences* **60**, 337 (2012)
- [166] P. Pholpabu, S. Kustra, H. Wu, A. Balasubramanian, C. Bettinger, *Biomaterials* **39**, 164 (2015)
- [167] A. Vogel, N. Linz, S. Freidank, G. Paltauf, *Phys. Rev. Lett.* **100**, 038102 (2008)
- [168] E.A. Brujan, K. Nahen, P. Schmidt, A. Vogel, *Journal of Fluid Mechanics* **433**, 251 (2001)
- [169] R.R. Alfano, S.L. Shapiro, *Phys. Rev. Lett.* **24**(11), 584 (1970)
- [170] S. Tzortzakis, L. Sudrie, M. Franco, B. Prade, A. Mysyrowicz, A. Couairon, L. Bergé, *Phys. Rev. Lett.* **87**(21), 213902 (2001)
- [171] A. Dharmadhikari, F. Rajgara, N.C. Reddy, A. Sandhu, D. Mathur, *Opt. Express* **12**(4), 695 (2004)
- [172] R.L. Fork, W.J. Tomlinson, C.V. Shank, C. Hirlimann, R. Yen, *Opt. Lett.* **8**(1), 1 (1983)
- [173] S. Sreeja, C. Leela, V.R. Kumar, S. Bagchi, T.S. Prashant, P. Radhakrishnan, S.P. Tewari, S.V. Rao, P.P. Kiran, *Laser Physics* **23**(10), 106002 (2013)

- [174] P. Vasa, M. Singh, R. Bernard, A.K. Dharmadhikari, J.A. Dharmadhikari, D. Mathur, *Applied Physics Letters* **103**(11), 111109 (2013)
- [175] A. Braun, G. Korn, X. Liu, D. Du, J. Squier, G. Mourou, *Opt. Lett.* **20**(1), 73 (1995)
- [176] P.B. Corkum, C. Rolland, T. Srinivasan-Rao, *Phys. Rev. Lett.* **57**(18), 2268 (1986)
- [177] C. Santhosh, A. Dharmadhikari, J. Dharmadhikari, K. Alti, D. Mathur, *Applied Physics B* **99**(3), 427 (2010)
- [178] Q. Yuan-Dong, W. Dan-Ling, W. Shu-Feng, G. Qi-Huang, *Chinese Physics Letters* **18**(3), 390 (2001)
- [179] A.L. Gaeta, *Phys. Rev. Lett.* **84**, 3582 (2000)



Chandra Sekher Reddy Nathala

Donaufelderstrasse 73/4/4, Vienna, 1210, Austria

Email: ncsr1975@gmail.com

EDUCATION

- Pursuing Ph.D at Vienna Technical University. Expected date of completion: Feb 2016.
- Master of Technology (M.Tech) in “Laser Science and Applications” from Devi Ahilya University, Indore, India. (1998 – 2000)
- Master of Science (M.Sc) in “Physics” from Osmania University, Hyderabad, India. (1995 – 1997)
- Bachelor of Science (B.Sc) from Osmania University, Hyderabad, India. (1992 – 1995)

PROFESSIONAL EXPERIENCE

Femtolasers, Vienna, Austria

March'07 – Present

Laser Engineer, Sr.Laser Engineer (Prod., and R&D)

Responsibilities:

1. Building different models of ultrafast oscillators [<7 fs oscillators, High power, Extra broadband, Carrier Envelope Phase (CEP) Stabilized etc] and amplifiers.
2. Installation and service of company products at customer site,
3. Participate in company's ongoing research projects,
4. Individually develop new products,
5. Documentation,
6. Training customers/users/new employees on current products,
7. Interact with worldwide customer base and support them in technical questions.

Laser Science Services (I) Pvt Ltd, Mumbai, India

July'05– Feb'07

Manager (Tech Support)

- Laser Science Services (India) Pvt Ltd, is an exclusive representative in India for Coherent Inc, Continuum, Quantronix, Thales Lasers, Femto Lasers, Ropher Scientific etc.)
- Laser Science also has an In-house production unit.

Responsibilities:

- Overall in charge of the production unit,
- Building Nd:Yag and Co2 based laser cutting machines,
- Installation and maintenance of complex scientific systems,
- Discussing with various scientific and industrial customers about their laser requirements and experimental setups,
- Training and supervision of new incoming colleagues and technicians.

Tata Institute of Fundamental Research, Mumbai, India. July'03 – June'05

Scientific Officer (C)**Responsibilities:**

- Overall in-charge of the laser systems in the lab (lab houses 10Hz, 20 TW Ti:Sapphire laser from Thales Lasers; 10Hz, 0.5TW laser from Continuum Inc; 1KHz, 1mJ, 20fs laser from Quantronix; Ti:Sa oscillators from FemtoLasers, Coherent, KM Labs; solid-state pump lasers from Coherent, Thales, Continuum etc and different laser diagnostic equipments)
- Participate in on-going research projects of the lab. Research interests of the group include: Intense laser plasma interactions, white light generation, and Non-Linear optics.
- Build lasers and laser diagnostic systems, and
- Set-up experiments and train graduate students on lasers and laser based equipments.

Laser Science Services (I) Pvt Ltd, Mumbai, India

Jan'00 – June'03**Laser Engineer****Responsibilities:**

- Installation and Maintenance of Coherent's Ar+ lasers, diode pumped solid state lasers, tunable femto-second lasers, OPO's, Continuum's flash lamp pumped solid-state nano-second and pico-second lasers, Ti:sapphire based amplifiers from Thales, Kimmon electric company's He-Cd lasers, and laser based diagnostic equipment.

While working as Laser Engineer, visited the following places, during 2000 to 2003:

- 1.Coherent Laser Group, CA, USA, for training on Water cooled Ar+ lasers, diode pumped frequency doubled Nd:YVO4 laser (Verdi), Ti:Sa Femto-second Oscillator (Mira) and OPO.
- 2.Continuum Inc, CA, USA, and Continuum, Paris, France, for training on nano-second and pico-second Nd:YAG lasers,
- 3.Thales Lasers, Paris, France, for training on 7 Terawatt Ti:Sa amplifier and pump lasers.
- 4.Quanta Systems, Milan, Italy, for training on Nd:YAG Lasers.
- 5.Kimmon Electric Company, Japan for training on He-Cd lasers.

PUBLICATIONS

- *Experimental study of fs-laser induced sub-100-nm periodic surface structures on titanium.* Optics Express, 2015. **23**(5): p. 5915-5929.
- *Enhancement of ultrafast electron photoemission from metallic nanoantennas excited by a femtosecond laser pulse.* Laser Physics Letters, 2014. **11**(6): p. 065301.
- *Defined nano-structuring with ultrashort pulses in gelatin biopolymer films for tissue-engineering.* MATEC Web of Conferences, 2013. **8**: p. 03009.
- *The formation of nanodimensional structures on the surface of Tin exposed to femtosecond laser pulses in the ambient environment of ethanol.* Applied Surface Science, 2014. **290**: p. 53-58.
- *Highly efficient white light generation from barium fluoride.* Optics Express, 2004. **12**(4): p. 695-700.
- *Controlling the porosity of collagen, gelatin and elastin biomaterials by ultrashort laser pulses.* Applied Surface Science, 2014. **292**: p. 367-377.
- *Estimation of ultrashort laser irradiation effect over thin transparent biopolymer films morphology.* in *Eighteenth International School on Quantum Electronics: Laser Physics and Applications*. 2015. International Society for Optics and Photonics.
- *Microfluorometric detection of catecholamines with multiphoton-excited fluorescence.* Applied optics, 2004. **43**(12): p. 2412-2417.

CERTIFICATES

- Post Graduate Diploma in Computer Applications (PGDCA) – (1997 – 1998)

PERSONAL PROFILE

- Date of Birth : 16th June 1975
- Nationality : Indian